Statistical approach to astrophysical flows in star forming clouds : towards the stellar initial mass function

Etienne Jaupart

To cite this version:

Etienne Jaupart. Statistical approach to astrophysical flows in star forming clouds : towards the stellar initial mass function. Astrophysics [astro-ph]. Université de Lyon, 2021. English. NNT : 2021LYSEN021 . tel-03367068

HAL Id: tel-03367068
https://theses.hal.science/tel-03367068v1

Submitted on 6 Oct 2021

Numéro National de Thèse : 2021LYSEN021

Thèse de Doctorat de l'Université de Lyon

opérée par

l'École Normale Supérieure de Lyon

École Doctorale N^{o}52
École Doctorale de Physique et d'Astrophysique de Lyon

Discipline : Physique
Spécialité : Astrophysique

Soutenue publiquement le 08 Juillet 2021

par Étienne JAUPART

Statistical approach to astrophysical flows in star forming clouds: towards the stellar initial mass function.

-

Approche statistique des écoulements astrophysiques dans les nuages hôtes de la formation stellaire : vers la fonction de masse initiale des étoiles.

Devant le jury composé de :

Pascal TREMBLIN	Physicien	CEA Saclay	Rapporteur
Thierry PASSOT	Directeur de recherche	Obs. Cote d'Azur	Rapporteur
Laure SAINT-RAYMOND	Professeure	ENS de Lyon	Examinatrice
Philippe ANDRÉ	Physicien	CEA Saclay	Examinateur
Gilles CHABRIER	Directeur de recherche	ENS de Lyon	Directeur

Remerciements

Par où commencer ..? Cette thèse étant l'achèvement de mes années d'études et de mes années lyonnaises, il est certain que j'ai beaucoup de monde à remercier. J'espère que toutes ces personnes se retrouveront dans ces (quelques) lignes.

A tout seigneur tout honneur je tiens à remercier mon directeur, Gilles, de m'avoir d'abord accueilli pour un "petit stage de 4 mois" lors de ma 4eme année d'école, puis de m'avoir permis de changer de sujet et de faire ma thèse avec lui. Bien que nous ne soyons pas toujours d'accord sur qui devrait jouer dans l'équipe de France de rugby, j'ai passé de très bonnes années à tes côtés durant lesquelles j'ai beaucoup appris sur une vaste gamme de sujets (pas toujours reliés aux sciences). En parlant de seigneur, je voudrais aussi remercier Stéphanie qui, bien qu'elle ne dirige pas de recherche, gère magnifiquement l'équipe Astro-ENS et est notre véritable directrice à tous ; te côtoyer pendant ces années a été un réel plaisir. Que ce soit par ta gentillesse ou ta personnalité tu participes pleinement à l'excellente ambiance qui règne dans l'équipe dont tu es le ciment.

Viennent, bien entendu, ensuite les collègues et amis du CRAL. Guillaume qui par ton enthousiasme et ton énergie permets à tous de se sentir chez lui dans cette équipe et es toujours d'une aide précieuse sur les questions scientifiques. Tu es, je pense, le vrai plus de cette équipe et un atout majeur pour les jeunes stagiaires et thésards. A toi Benoit, qui reste quelqu'un de bien même si tu supportes l'OM et m'as battu au concours de 3 points, je tenais à te dire merci pour ces années de bonne ambiance et rigolades. Il est toujours intéressant d'avoir ton point de vue que ce soit en sciences ou sur le basket (sur le foot un peu moins). Un grand merci à toi aussi, Christophe, pour ces années à travailler avec toi en recherche comme en enseignement et pour avoir été assez gentil, il y a 7 ans maintenant, pour me mettre une note sympa aux oraux de l'ENS. Tes vannes me manqueront même si nous allons continuer à collaborer lors de mon post-doc avec François. A Jeremy, merci d'avoir supporter mes blagues, écouter mes idées et participer à de nombreuses discussions scientifiques. Enfin merci à tous les autres permanents, Gerard, Isabelle, Jean-François, Rolf, Thomas qui ont toujours été très gentils et accueillants.

Après (ou avant ?) les permanents viennent bien entendu mes potes thésards devenus pour certains post-docs et pour l'un d'entre eux permanent (Ca va Flo ?). Merci à Quentin, ma grosse couenne, pour ces années de bons délires à l'école et d'échanges scientifiques. On s'est suivi à coup de percu' bien placées et de montages photos pixélisées avec jeux de mots bien nuls. Tu m'as permis de développer mes idées en les confrontant à tes remarques, toujours pertinentes, et de me défouler en me prêtant une oreille quand j'avais besoin de râler. A Maxime, sans doute l'une des personnes les plus gentille et bienveillante que j'ai jamais rencontré, je voulais aussi te dire un grand merci. Au delà de la science (Schmolu c'est compliqué), ton côté humain m'a beaucoup touché, tu es vraiment un gars génial. A Ugo et ses chansons et dessins, à Charlet (Arthur de son prénom) pour ses vieux memes, à Pierre pour nos discussions et les pizza à 13h00 précise et à Timothée et ses monologues sur les algorithmes portables sur GPU, je voulais dire merci d'avoir égayé mes années au CRAL. Enfin, last but not least, merci à mon bonobo-brother, Florian ou Big-Flo, grand frère de thèse étant devenu un très bon ami. Côté recherche tu m'as permis de travailler avec toi et l'équipe d'Exeter et j'ai beaucoup apprécié nos échanges. Mais plus important encore, de nos premiers entrainements et matchs de basket (dédicace à Augustin) à la conférence à St Malo, j'ai passé de super moments à tes côtés. J'attends que tu décroches une ERC pour m'inviter chez toi dans ton labo à Toulouse (pas de pression).

Mais je ne dois pas cette thèse uniquement à l'entourage scientifique et amical que j'ai eu dans mon laboratoire. Si mes années lyonnaises, avant et pendant la thèse, se sont si bien déroulées c'est grace à tous mes amis : de Lyon bien sur, mais aussi ceux de Paris, des Landes et des autres coins de France.

Parmi les Lyonnais, je voulais remercier Laureline et JM que j'ai rencontrés lors de mes premiers jours à Lyon il y a 7 ans et qui ont été d'incroyables amis lors de ces dernières années et j'espère les prochaines. Merci de m'avoir accompagné lors de mon périple en Californie (je sais que tu as toujours la photo Lolo). La bise à vos 2 ours et à votre petite reine Elely. Merci aussi à Clément et Sophie, toujours disponible pour aller voir des matchs à Gerland, à Décines, dans les bars dont on a parfois repeint les plafonds avec nos bières ou chez nous. A vos côté j'ai appris à faire des pizza, des croissants ou des super roulades. A ceux qui m'ont accompagné au cours de ma scolarité, Victor San et ses muffins tops, Arsène et ses avirons, Clelia et ses tirages d'oreilles, Antoine et ses 46 discussions dans sa tête, Louis Villa (aka le bolossé), Louis Vignoli et ses renards, Yacouba et le business, la team h bar-terrasse : Pascalie le sage, Corneliu d'une autre planète , Pricou et ses histoires, et mon énorme poulaga Louis Monier (faut qu'on fasse signer ce contrat au Yac), merci à tous d'avoir fait que ces années lyonnaises soient mémorables. Merci à Lulu et Guillaume pour les soirées KL et les mojitos (pas ceux au rhum Charette, faut pas abuser), avec vous la période Covid a été beaucoup moins pesante. A ceux du basket à l'ENS, Bordy Mathieu (Mathieu), Betsch, Jean, Seb la frite, Tristan, Miary, Antoine (ou Jacob selon les réseaux), mon poulet Romain Bucci, mon autre poulet Quentin RF et sa beauce-mobile (qui ne faisait pas d'ombre à celle de Betsch), Augustin, Octavie et Mathilde, merci d'avoir été là sous les paniers et en dehors. Aux autres avec qui j'ai fait du sport à l'école, le rugby avec notamment Coco-Tib, Jimmy, ce bon vieux Gatien Polly et Francis ; le volley (qui l'eut cru) avec Remi et son vieux rap et Richard et ses discours ; le MMA avec Mathieu, merci de m'avoir aidé à me maintenir en forme et m'amuser. A mon club de judo, le judo club de Gerland et ses deux directeurs : Rose et Vincent Valente, merci pour ces chaleureuses années dans cette veritable petite famille du judo lyonnais.

Je voudrais remercier les gens avec qui j'ai vécu dans ma mega coloc' avec mon Zouk-Machine (Benjamin L.), Joan (ou Jojo) que j'aurais pu mettre dans le basket mais mes chevilles gardent des rancunes (ca vaut pour vous aussi Mathieu et Miary), et notre Naomi (ou Nomi chez elle).

Bien entendu, merci aussi à Camille et Lucille, vous aussi faites partis des personnes les plus gentilles et bienveillantes que j'ai rencontré dans ma vie. Merci pour le template de ce manuscrit, les soirées KL ou celle à St-Bo dans la piscine. On se revoit chez les belges pour des fritttttttes et à votre mariage ou je suis témoin (je crois). Enfin merci aussi à Benjamin G., Guiseli, que j'ai d'abord rencontré à Paris mais qui m'a copié et suivi à Lyon (sisi ça s'est passé comme ça). On se reverra à Groffliers ou à Montpellier.

Viennent, bien entendu, ensuite les amis de Paris et des Landes. Merci à ma sista Camille T.-B., Guillaume, Marine, Simon, Kevin A., d'avoir été là quand je rentrais sur Paris et d'être restés proches malgré la distance. Merci à toi Yannick et ta Camille, on se connait depuis le collège et tu es toujours disponible pour m'accueillir chez vous ou venir à Lyon, partir faire du ski ou aller voir un Angleterre-France à Twickenham. A la famille de ma Noémie et ses amis Landais, merci de votre accueil très chaleureux et des moments de détente que j'ai pu partager avec vous pendant nos vacances ou voyages ensembles.

Enfin, merci mon frère d'une autre mère, Yoann L., mon Yoyo, d'être toujours là et de continuer d'être ce mec drôle et attachant, toujours dans le gourmand croquant; viril mais correct comme ils diraient. Merci aussi Solène (Soso), pour ta bonne humeur, nos voyages tous les 4 ensembles et surtout de supporter nos bétises.

Merci aussi bien entendu à ma famille à qui je dois qui je suis, mes deux parents Brigitte et Claude et mon frère Pascal, pour leur éducation, leur soutien et leur amour inconditionnel évidement partagé.

Et puis, finalement, qu'aurait été ma thèse sans toi Noémie, ma Nono, avec qui je partage ma vie depuis ces 4 dernières années. Tu es toujours là pour moi et tout ce que je te dois ne pourrait pas tenir sur ces quelques lignes. Merci pour tout mon loup.

Résumé

Les étoiles se forment au sein de grands nuages moléculaires, dans des sous-régions de haute densité. De telles augmentations locales de densité sont attribuées à des mouvements turbulents supersoniques qui sont connus pour générer des structures désorganisées, d'apparence aléatoire et évolutives. Ces structures denses et complexes sont des germes appropriés pour la condensation locale du gaz par gravitation et les astrophysiciens modernes s'efforcent de comprendre leur rôle dans le processus de formation des étoiles.

La description la plus courante des fluctuations de densité dans les nuages moléculaires repose sur la phénoménologie de la turbulence isotherme sans gravitation. Dans ce cas, le champ de densité est lognormal et sa variance est proportionnelle à $\mathcal{M}^2$, où $\mathcal{M}$ est le nombre de Mach. Des observations et des simulations numériques ont toutefois montré que, dans les nuages hôtes de la formation d'étoiles, la fonction de densité de probabilité (PDF) s'écarte d'une forme lognormale et développe une queue en loi de puissance prééminente à des valeurs de densité élevées, une caractéristique qui a été identifiée comme la signature de la gravité. Les études théoriques se sont concentrées sur les parties gravitationnellement instables d'un nuage et ont été basées sur des modèles analytiques d'effondrement gravitationnel invariant d'échelle et/ou des arguments *géométriques*. Elles ont conduit à des valeurs asymptotiques pour les exposants de queues en loi de puissance, mais n'ont pas permis d'obtenir une description statistique complète des fluctuations de densité dans les parties gravitationnellement stables et instables d'un nuage. En outre, à l'exception des simulations numériques de Girichidis et al. (2014), ces études traitent la PDF comme une propriété statique et ne s'intéressent pas à son évolution dans le temps.

Dans cette thèse, nous avons exploré de nouveaux cadres théoriques, et, nous l'espérons, plus élaborés, afin d'obtenir de nouvelles perspectives sur la physique complexe qui sous-tend la formation des étoiles et des outils pour la décrire. Deux communautés différentes se sont penchées sur les systèmes dynamiques complexes et hautement non linéaires. Dans le domaine de la turbulence, l'approche statistique pour les *milieux compressibles* remonte à la célèbre formulation initiale pour les écoulements incompressibles (Batchelor, 1953). Cependant, les progrès concernant la PDF des fluctuations de densité dans les écoulements turbulents ont été plus lents. Un grand nombre d'efforts ont porté sur les fluides incompressibles et ce n'est que récemment qu'un cadre théorique robuste a été mis à disposition pour les fluides compressibles par Pan et al. (2018, 2019a,b), mais sans gravité. En cosmologie, l'étude des fluctuations de densité primordiales et de la formation ultérieure de structures sous l'effet de la gravité a conduit au développement d'un vaste cadre statistique (voir par exemple Peebles 1973; Monaco 1998).

Nous espérons que cette thèse constitue un pas vers une description des statistiques des mouvements aléatoires (turbulents) des fluides sous l'influence de la gravité. Dans un sens, ce travail relie les formalismes qui ont été développés dans les domaines distincts de la turbulence et de la cosmologie. Dans un autre sens, il vise à améliorer notre compréhension du rôle joué par les structures turbulentes dans le processus de formation des étoiles. Elle se concentre sur les statistiques de densité et de vitesse dans les nuages moléculaires et plus particulièrement sur leur évolution dans le temps.

Nous abordons d'abord la question de savoir comment extraire les propriétés statistiques du champ de densité 3D à partir des observations qui révèlent un champ de densité 2D projeté. Nous quantifions quelles variables d'intérêt peuvent être dérivées des observations et comment elles sont liées à celles du champ de densité 3D sous-jacent. Nous étudions ensuite la pertinence d'une approche statistique pour l'étude des nuages moléculaires. En effet, que ce soit pour les observations ou les simulations numériques, une seule réalisation (image instantanée) d'un nuage est disponible. Pour qu'une approche statistique soit pertinente, le nuage doit être suffisamment grand pour que l'information statistique soit fiable. Nous clarifions et définissons rigoureusement ce que l'on entend par "suffisamment grand" à l'aide de la théorie ergodique et appliquons nos résultats aux nuages de Polaris et d'Orion B. Enfin, nous appliquons le même formalisme à d'autres caractéristiques (observationnelles ou numériques) des nuages moléculaires. Les observations ne peuvent pas dévoiler toute la complexité de la structure interne de ces nuages. Elles fournissent des estimations robustes des caractéristiques *globales*, telles que la masse totale et la taille, et il est utile d'évaluer comment celles-ci peuvent être utilisées pour obtenir des estimations précises d'autres quantités physiques globales pertinentes pour la dynamique des nuages, telles que l'énergie gravitationnelle totale et le paramètre du viriel. Nous obtenons ensuite l'équation régissant l'évolution des statistiques du champ de densité dans les nuages hôtes de la formation d'étoiles. Plus précisément, nous étudions les évolutions temporelles de la PDF, de la fonction d'auto-covariance (ACF) et de la longueur de corrélation du champ de densité. Nous développons en détail une théorie analytique pour les statistiques des fluctuations de densité dans les nuages moléculaires sous les effets combinés de la turbulence supersonique et de l'auto-gravité. La théorie repose sur les propriétés générales des solutions aux équations couplées de Navier-Stokes pour les mouvements des fluides et à l'équation de Poisson pour la gravité. Elle étend les approches précédentes en tenant compte de la gravité et en traitant la PDF comme une variable dynamique et non stationnaire. Nous dérivons rigoureusement les équations de transport pour la PDF et l'ACF en présence d'un champ magnétique, déterminons leur évolution dans le temps et résolvons le seuil de densité au-dessus duquel la gravité affecte fortement et finit par dominer la dynamique de l'écoulement. Les résultats et diagnostics théoriques sont comparés aux données de plusieurs nuages moléculaires ainsi qu'aux résultats de simulations numériques. Enfin, nous décrivons une étape vers une amélioration des théories analytiques modélisant la fonction de masse initiale en nous appuyant sur les résultats obtenus précédemment.

Abstract

Stars are formed in high density subregions embedded in larger molecular clouds. Such local density enhancements are attributed to supersonic compressible turbulent motions which are known to generate disorganized, random-looking and evolving structures. These dense and intricate structures are suitable seeds for gravitation-driven condensation and modern astrophysicists are striving to understand their role in the star formation process.

The most common description of density enhancement in molecular clouds relies on the phenomenology of isothermal gravitation-less turbulence. In this case, the density field is lognormal and its variance is proportional to $\mathcal{M}^2$, where $\mathcal{M}$ is the Mach number. Observations and numerical simulations have shown, however, that, in star forming clouds, the probability density function (PDF) deviates from a lognormal form and develops a preeminent power law tails at high density values, a feature which has been identified as the signature of gravity. Theoretical studies have been focussed on the gravitationally unstable parts of a cloud and have been based on analytical models of scale-free gravitational collapse and/or *geometrical* arguments. They have led to asymptotic values for power-law tail exponents but have fallen short of a complete statistical description of density fluctuations in both gravitationally stable and unstable parts of a cloud. In addition, with the exception of the numerical simulations of Girichidis et al. (2014), these studies treat the PDF as a static property and do not deal with its evolution through time.

In this thesis, we have explored new, and hopefully more elaborate, theoretical frameworks in order to obtain new insights on the complex physics behind star formation and tools to describe them. Two different communities have been at work on highly non linear and complex dynamical systems. In turbulence, the statistical approach for *compressible media* can be traced back to the famous initial formulation for incompressible flows (Batchelor, 1953). However, progress on the PDF of density fluctuations in turbulent flows has been slower. A large number of efforts have dealt with

incompressible fluids and it is only recently that a robust theoretical framework has been made available for compressible ones by Pan et al. (2018, 2019a,b) but without gravity. In cosmology, the study of primordial density fluctuations and the subsequent formation of structures due to gravity has lead to the development of a vast statistical framework (see e.g Peebles 1973; Monaco 1998).

It is hoped that this thesis is one step toward a description of the statistics of random (turbulent) fluid motions under the influence of gravity. In one sense, this work connects formalisms that have been developed in the distinct fields of turbulence and cosmology. In another sense, it is aimed at improving our understanding of the role played by turbulent structures in the star formation process. It is focussed on the statistics of density and velocity in molecular clouds and more specifically on how they evolve with time.

We first tackle the issue of how to extract statistical properties of the 3D density field from the observed 2D projected density field. We quantify which variables of interest can be derived from observations and how they are related to those of the underlying density field. We then study the relevance of a statistical approach to the study of molecular clouds. Indeed, be it for observations or numerical simulations, only one realization (one snapshot) of a cloud is available. For a statistical approach to be meaningful, the cloud must be large enough for statistical information to be reliable. We clarify and define rigorously what is meant by "large enough" using ergodic theory and apply our results to the Polaris and Orion B clouds. Finally we apply the same formalism to other characteristics (observational or numerical) of molecular clouds. Observations cannot unravel the full complexity of the inner structure of these clouds. They do provide robust estimates of *bulk* characteristics, such as total mass and size, and it is useful to assess how these can be used to obtain accurate estimates of other global physical quantities of relevance to cloud dynamics, such as the total gravitational (binding) energy and the virial parameter. We then obtain the equation governing the evolution of statistics of the density field in star forming clouds. More specifically, we study the time evolutions of the density PDF, the auto-covariance function of the density field and its associated correlation length. We develop in detail an analytical theory for the statistics of density fluctuations in star-forming molecular clouds under the combined effects of supersonic turbulence and self-gravity. The theory relies on general properties of solutions to the coupled Navier-Stokes equations for fluid motions and the Poisson equation for gravity. It extends previous approaches by accounting for gravity and by treating the PDF as a dynamical variable, not a stationary one. We derive rigorously transport equations for the PDF and ACF with a magnetic field present, determine how they evolve with time and solve for the density threshold above which gravity strongly affects and eventually dominates the flow dynamics. The theoretical results and diagnostics are compared to data on several molecular clouds as well as to the results of numerical simulations. Finally, we describe a step towards an improved analytical theory for the Initial Mass Function relying on the previous obtained results.

Contents

Introduction

Chapter 1

Tools

Chapter 2
Column densities as tracers of the underlying density field: the link with observation

Chapter 3

Relevance of a statistical approach

Chapter 4

Evolution of the statistics of the density field in star forming clouds

Chapter 5

Towards the stellar initial mass function (IMF)

2 Cosmological mass functions 140

3 From the cosmological to the stellar mass functions 148

Introduction

Contents

Stars and celestial objects have always been a source of fascination for mankind. The Sun, the Moon and the planets of our solar system are undoubtedly the most accessible ones to the human eye but many others have been marveled at since the Antiquity. The Milky Way stretches across the whole sky and has been at the origin of countless myths. Constellations, comets and nebulae have been given names and used as beacons. Archaeologists have found evidence that celestial objects have been thoroughly studied and classified by astronomers of the Babylonian, Egyptian empires but also in early Chinese, Indian and Meso-American societies. The name "Milky Way" was borrowed, via the Latin *via lactea*, from the ancient Greek word for "milky circle" and has its origins in Greek mythology. In the most common account, Zeus, who wished to make Heracles immortal, made him suck at the breast of Hera, who was asleep. As Hera was pulling Heracles off her breast, milk squirted out and spread across the sky, forming the Milky Way. Democritus and Anaxagoras had argued that the Milky Way is made of a multitude of stars that cannot be singled out with the naked eye but it took Galileo and his telescope to demonstrate, in 1610 AD, that this is indeed true. It was not until the 20th century that the general structure and composition of stars was finally understood. Thanks to the development of quantum mechanics and special relativity, it became possible to describe the microscopic states of matter and probe stars. In 1919, Jean Baptiste Perrin and Arthur Eddington first proposed that the sun is fueled by nuclear reactions within its core. A few years after, in 1925, Cecilia Payne-Gaposchkin discovered that the sun, a fairly typical star, is primarily made of Hydrogen and Helium. Edwin Hubble's discoveries in the 1920s and 1930s led to a revised classification of astronomical objects. In particular, nebulae were recognized as "island universes" similar to our own galaxy but extremely distant. Other nebulae, relatively close by, provided unmistakable evidence that interstellar space is far from empty. Scanning the sky over a large spectral range, and in particular at infrared and radio frequencies, subsequently revealed the abundance and richness of structures in the universe.

The study of star formation in its modern form is recent, but the main ideas can be traced back to the Renaissance when the Aristotelian worldview became challenged. Among others, Tycho Brahe took issue with the notion of an immutable sky. He demonstrated the translunar nature of the supernova of 1572 and a comet that appeared in 1577, noting that a nearby object should appear to change position relative to the background sky depending on the observatory location (the parallax phenomenon). The major advance came with the rebuttal of geocentrism by Copernicus, Galileo and Kepler on the basis, in particular, of Tycho Brahe's observations. On the one hand, the heliocentric framework made it much simpler to describe planet motions, but, on the other hand, one had to deal with the Jupiter's satellites that Galileo had discovered. From then on, the formation of the solar system ceased to be a theological concern and became an object of scientific study. Descartes, in his Treatise on the World and Light (written in the early 1630s and published posthumously in 1664), which was taken up later by Kant in 1755 in his General History of Nature and Theory of the Heavens, conjectured that the Sun and the planets have the same origin and were formed from a single nebula that contracted. According to him, the Sun formed in the centre of the nebula and planets condensed in a nebular disc around it. Laplace refined and improved this scenario in 1796. The primitive solar nebula saw its rotation accelerate as it was contracting, generating a disc that revolved around a dense central core (Marquis de Laplace, 1835). This disc became unstable as it was cooling and split into rings that later collapsed into planets, and the core became the Sun. In 1902, James Jeans realized that stars do not form in isolated nebulae but in giant unstable ones, known today as molecular clouds, as a result of gravitational collapse (Jeans, 1902). Since then, the huge advances of the last 40 years in observational astrophysics have shown that the star and planet forming interstellar medium is far more complex than previously thought. High resolution images provided by space telescopes such as Spitzer, Hubble or Herschel, have revealed that molecular clouds host very intricate and disorganized narrow structures such as filaments and are shaped by the interaction between turbulence, gravitation and magnetic fields.

Modern astrophysicists are striving to understand the role played by the disorganized, random-looking and evolving structures of molecular clouds in the star formation process. This thesis is part of this effort and is focussed on the statistics of density and velocity in these clouds and more specifically on how they evolve with time.

1 The interstellar medium.

1.1 A variety of structures in our Galaxy.

According to our current understanding, our galaxy must be viewed as a hierarchy of structures of different sizes. To describe a diverse population over such an enormous size range, astrophysists have introduced several characteristic length-scales. The parsec (pc) is a unit of distance that is roughly equal to 3 light-years (and in kilometers 1 pc $= 3.08\,10^{13}$ km) and corresponds to the typical distance between stars. The astronomical unit (1 UA $\simeq 150\,10^{6}$ km) is the average distance between the Earth and the Sun and hence is suited to the study of planetary systems. For stellar objects, appropriate scales for length (distance) and mass are the solar radius $R_\odot \simeq 700\,000$ km and mass $M_\odot = 2\,10^{30}$ kg, respectively.

At the largest (galactic) scale, our Galaxy is made of a central spherical bulge, a rotating disc with a radius of about 20 kilo-parsecs, a stellar halo and probably also a dark matter halo. Within the disc, density waves generate spiral arms. At the other end of the hierarchy of structures, at scales of the order of a hundred astronomical units, stars and their planetary systems are the elementary constituents of the galactic disc. At intermediate scales, the interstellar medium (ISM), which is mainly confined to the galactic disc, consists of dust and gas in different physical states. The galactic components continuously interact with one another. On the one hand, the interstellar medium and stars continuously exchange mass and energy whilst, on the other hand, galactic tides transfer energy to smaller scale components.

1.2 Where stars are formed.

The interstellar medium plays a key role in the evolution of a galaxy. It is in its densest regions that the gravitational collapse of giant (molecular) gas clouds generates stars (Jeans, 1902). This medium is therefore highly heterogeneous and its interactions with the other components of the galactic system are only part of the picture. How its constituents interact with one another must be ascertained as well.

1.3 Density and chemical composition.

As a whole, the ISM is a rather sparse environment, where the particle number density varies between a few $\overline{n} \sim 10^{-3}$ to $\overline{n} \sim 10^{4}$ units per centimeter cube (cc). But it is also enormous, so that the amount of material sampled by a line of sight, typically $N = 10^{21}$ particules per cm square, is sufficiently large for very weak phenomena to become measurable. In particular, the hydrogen spectral line or 21-centimeter line, which corresponds to the transition between two hyperfine levels of the neutral hydrogen atom, is detected in the ISM. This transition is due to a spin flip of the hydrogen electron which emits a photon at a wave-length of 21 cm (1420 MHz) and is extremely difficult to observe on Earth. It is of the utmost importance because it is a characteristic feature of the hydrogen atom. Astronomers denote the neutral hydrogen atom by $\mathrm{H_I}$.

Save for heavy elements that are generated in stars, the chemical composition of interstellar gas is inherited from primordial nucleosynthesis. In terms of mass fraction, it is a mixture of 70% hydrogen and 28% helium, with carbon, oxygen and nitrogen making up most of the remaining 2%. Helium is chemically inert and intimately coupled to hydrogen by collisions, so one may treat the mixture as a hydrogen gas with an enhanced mean mass of particles. Hydrogen is found in ionized atomic form (noted $\mathrm{H_{II}}$ by astronomers), neutral form $\mathrm{H_I}$ and molecular form $\mathrm{H_2}$, but the latter is difficult to detect owing to its weak emission amplitude. Ionized hydrogen is observed in the visible range thanks to the Hα recombination spectral line at 656.3 nm. Transitions between these species occur in different locations depending on local conditions.

Dust is a very minor, but crucial, component of the ISM. It accounts for about half of the residual 2% mass fraction and plays an extremely important role in the chemical and thermal evolution of the ISM. Dust can be detected because it interacts with light and is responsible for the "dark" clouds that are masking stars (see Chapter **1**).

1.4 Various phases

Far from being homogeneous, the interstellar gas has different phases with different temperatures and densities due to a competition between heating and cooling processes.

In a pioneering study of the ISM phase structure, Field et al. (1969) have suggested the coexistence of two different phases in thermodynamical equilibrium. A first one is called the Warm Neutral Medium (WNM) and corresponds to average number density $\overline{n} \sim 0.25$ cc^{-1} and temperature $T \sim 8000$ K. The second one, called the Cold Neutral Medium (CNM), is denser with $\overline{n} \sim 25$ cc^{-1} and colder with $T \sim 80$ K. Hydrogen is principally in its neutral atomic form $\mathrm{H_I}$ in both phases and is revealed by the 21-centimeter spectral line. At higher pressures corresponding to higher particle densities $\overline{n} \gtrsim 100$ cc^{-1}

and lower temperatures $T \lesssim 20$K, there is also a molecular hydrogen phase (H_2). At higher pressures still and in the environment of massive O-stars, with particle densities $\overline{n} \sim 1 - 10^4$ cc^{-1} and temperatures $T \sim 10\,000$ K, hydrogen may be found in ionized form (H_{II}) in some regions. Finally, hot bubble gas around supernovae form a highly out of equilibrium phase where hydrogen is ionized (McKee & Ostriker, 1977), called the Hot Ionized Medium (HIM). All these different phases are in constant interaction with one another.

1.5 Magnetic field

Observations of Zeeman effects in spectral lines (see Chapter **1**), synchrotron emission and light polarization testify to the existence of a magnetic field in which the ISM is immersed. This magnetic field has a large scale structure parallel to spiral arms with an intensity of about 1.4 micro-Gauss (μG). It also has a disordered component of the order of 5 μG which is therefore dominant, especially in dense regions of the ISM.

2 Molecular clouds

As mentioned in the previous section, molecular clouds are relatively dense and cold media where hydrogen and other chemical species form molecules. Because of their relatively high densities and small temperatures, they are where stars form. They are bathed in larger clouds of atomic hydrogen and hence, strictly speaking, cannot be studied in isolation. One must instead take into account energy that is supplied from larger scales, by the differential rotation of the galaxy for example. Other energy sources operate at stellar scales, such as the winds of young stars for example. The number of processes that are active in molecular clouds is so large that it would take many pages to describe them, so that we shall limit ourselves to brief presentations of key observations and theoretical results. The interested reader may find more information in recent reviews (Klessen & Glover, 2016; Ballesteros-Paredes et al., 2020).

2.1 Difficulties with observations

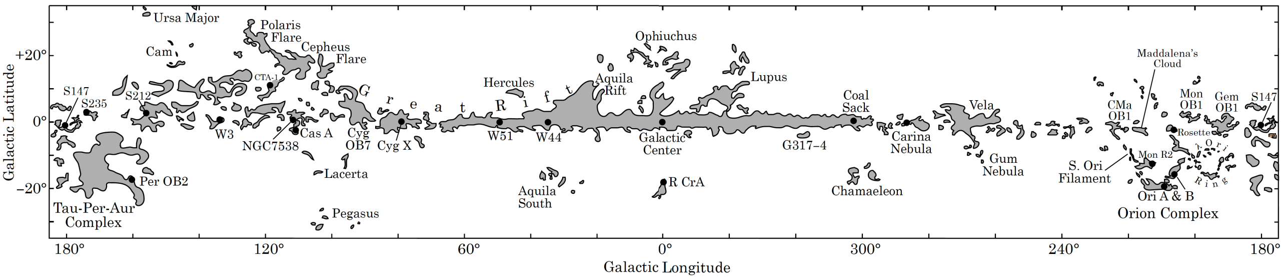

FIGURE 1 Schematic distribution of molecular cloud complexes in the Milky Way. Molecular clouds are revealed by the spectral line associated with the ^{12}CO rotational transitions. Data from (Dame et al., 2001).

Molecular gas is mostly made of dihydrogen H_2, a symmetric molecule with only weak rotational and vibrational transitions, which makes it difficult to detect. In order to track molecular matter, one relies instead on several carbon monoxide isotopes, ^{12}CO, ^{13}CO, $C^{18}O$, whose rotational transitions occur at radio frequencies (see Chapter **1**). Their total abundance with respect to dihydrogen is extremely small, of the order of $7\,10^{-5}$, but they are believed to be well coupled to H_2, so that they provide information on this elusive molecule (Dame et al., 2001). They therefore allow us to detect and study molecular clouds (see Fig 1).

Dense molecular regions can also be detected thanks to the phenomenon called extinction. This phenomenon, which has long been known to astronomers, is linked to the absorption and scattering of electromagnetic radiation by dust (and gas) along the line of sight between emitter and observer. Its effects on visible light is to mask stars that lie behind the absorbing dust (and gas), so that large portions of sky appear dark and starless. In Chapter **1**, we explain in greater detail how one determines the properties of molecular clouds.

What is perhaps most striking is that the two spectral lines of ^{12}CO and ^{13}CO coupled with knowledge of CO spectroscopy are sufficient to infer that dark clouds (*i.e.* those that are seen as dark islands in visible maps of the sky) is cold ($T < 20$ K) and dense ($n > 10^2 \mathrm{cc}^{-1}$) and furthermore that their CO contents are low relative to H_2, $[\mathrm{CO}]/[\mathrm{H}_2] < 10^{-4}$.

2.2 Transient structures

Molecular clouds and their complex structures are currently thought to be rather transient. Hartmann et al. (2001) realized that a long-lived molecular cloud should lie next to older stars that formed from it. However, in most star-forming regions with large concentrations of molecular gas, the typical age of stars is of the order of 1 to 3 million years (Ballesteros-Paredes et al., 1999). This age is shorter than the characteristic travel time of a particle at the speed given by the velocity dispersion in the cloud. This time, known as the crossing time, is the characteristic time for turbulence in the cloud as well as that for the significant deformation of a non self-gravitating cloud (Frisch, 1995). This suggests that, on the one hand, molecular clouds appear and disappear rather quickly and that, on the other hand, star formation is not bound to happen in slowly evolving, isolated and inert clouds, but is instead triggered by shocks that form within turbulent molecular gas. Once stars are born, they heat up and disperse the surrounding gas, thereby limiting the lifetime of a cloud in its molecular state.

2.3 Characteristic scales and filamentary substructures

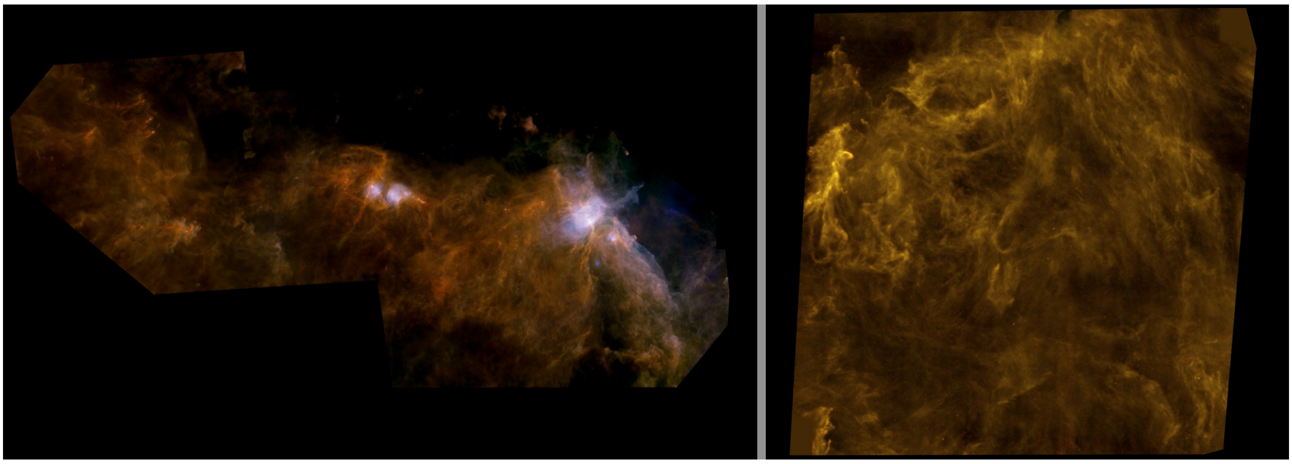

FIGURE 2 Molecular clouds in the Gould Belt observed with the Herschel telescope (André et al., 2010). Left: Orion B (Galactic longitude ~ 210°), a cloud of active star formation. Right: The Polaris Flare (Galactic longitude ~ 120°) with little or no sign of star formation. Note that the two clouds host a hierarchy of interwoven disorganized substructures.

Molecular cloud sizes span a very large range, from ~ 1 pc to ~ 100 pc. Embedded in these clouds is a hierarchy of interwoven substructures with fairly similar characteristics (from a statistical point of view). These substructures show up as sheet-like, filamentary and clump-like objects that do not seem to be part of large well organized structures, as can be seen in Fig. 2. This chaotic aspect is often attributed to turbulence (see next section). Surprisingly though, the average radial size of filaments is almost always the same, on the order of 0.1 pc, irrespective of the parent cloud properties (Arzoumanian et al., 2011; André, 2017; André et al., 2019), although the subject is still a matter of debate concerning whether this is also the most probable (characteristic) size of filamentary structures (Panopoulou et al., 2017).

2.4 Complex thermodynamics

The thermodynamics of the ISM and in particular of its molecular phase is extremely complicated due to the many physical processes that may generate or absorb heat (see Klessen & Glover 2016 for a more complete review).

2.4.1 Heating

In sparse ISM, the photo-electronic effect and UV radiation are extremely powerful heat sources. UV radiation, for example, can either dissociate molecules (like H_2) or be absorbed by them. In the former case, the kinetic energies of atoms produced by molecular fission are on average higher than the average thermal agitation speed of the other gas constituents.

In the molecular phase, gas is dense enough so that it is protected from UV radiation. In this case, there are several other heat sources. Cosmic rays made of particles produced in high energy events, such as protons, electrons, positrons or nuclei (see e.g. Jaupart et al. 2018), release energy by ionizing the gas. In the turbulent cloud, collisions and dissipation in shocks also generate heat. These two processes are the major sources of heat in molecular clouds. In addition, many chemical reactions are exothermic, such as the formation of a new chemical bond between two hydrogen nuclei in a H_2 molecule. In subsonic, gravitationally collapsing regions, such as low mass pre-stellar cores, adiabatic (isentropic) compression can be a major source of heat and may well overwhelm the others.

2.4.2 Cooling

In the molecular phase, the emission of rotational spectral lines by CO isotopes is one of the main energy sinks. In addition, gas is coupled to dust grains at the densities of the molecular phase, which acts as a thermostat and provides a lot of cooling power.

2.4.3 Overall effects

In the molecular phase where densities are large ($n > 10^2$ /cc) and temperatures are low ($T \sim 10$ K), cooling from dust and molecular transitions compensates for the heat that is released by the various sources mentioned above. At high densities, $n \sim n_{\mathrm{ad}} = 10^{10}$ cm^{-3}, gas becomes opaque to its own radiation and heats up (Masunaga & Inutsuka, 2000; Machida et al., 2006; Vaytet et al., 2013, 2018). In these conditions, the gas equation of state, $P \propto \rho^\gamma$, where P is pressure and ρ is density, is best described by isothermal conditions ($\gamma = 1$) with perhaps an over-isothermal polytropic exponent ($\gamma > 1$) at high density.

2.5 Turbulent motions

Molecular motions in the ISM are responsible for the broadening of spectral lines by the Doppler effect, which provides a measurement tool (see Chapter **1**).

2.5.1 Non thermal motions

These measurements allow the determination of the gas temperature ($T < 20$ K) but they are also sensitive to non thermal motions. Typical velocity values for these motions are of the order of 1 km/s and hence are much larger than the typical thermal velocity (sound speed), $c_{\mathrm{s}} \simeq 0.2$ km/s. These non thermal velocities have been measured in a large number of molecular clouds and are shown as a function of the parent cloud size in Fig. 3. There is a relationship between size and velocity, but it is affected by a large scatter (about a factor of 10) about $v_{\mathrm{NT}} \sim 1$ km/s $(L/1\ \mathrm{pc})^{1/2}$. These scalings are called the Larson relations in the honor of astronomer Richard Larson. We discuss in more detail various explanations for this velocity scale dependence in Chapter **4**.

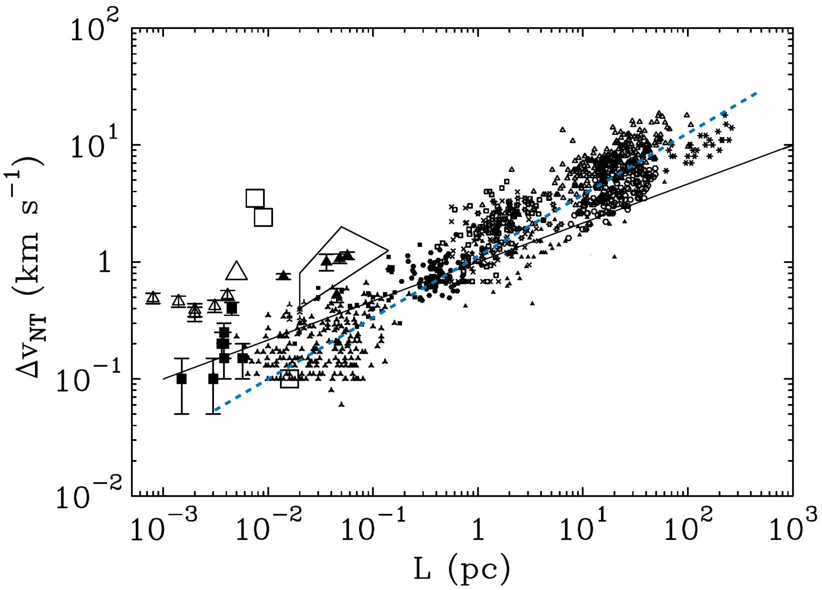

FIGURE 3 Scalings of the non thermal velocity dispersion as a function of molecular cloud size. Cloud properties are inferred from their ^{12}CO ($J = 1 - 0$) spectral line emissions. The black solid and dashed lines indicate scalings $v_{\mathrm{NT}} \propto L^{1/3}$ and $v_{\mathrm{NT}} \propto L^{1/2}$, respectively. These velocity-dispersion - size scalings are called Larson relations in the honor of astronomer Richard Larson. This figure is taken from Hennebelle & Falgarone (2012).

2.5.2 Reynolds number and turbulence

The dynamic regime of fluid motions is characterized by a dimensionless number R_{e} called the Reynolds number, which weighs the respective contributions of advection and viscous dissipation to momentum. For a system of characteristic size L, velocity U and kinematic viscosity ν, the Reynolds number is :

$$R_{\mathrm{e}} = \frac{UL}{\nu}. \tag{1}$$

At high Reynolds number $R_{\mathrm{e}} \gg 1$, any flow disturbance gets amplified significantly before viscous dissipation acts to dampen it. In such conditions, flow structures appear disorganized and chaotic, a phenomenon called turbulence. This complex and fundamental phenomenon has defied theoreticians and experimentalists for more than a century and remains an extremely active field of research today. For details and current understanding of this phenomenon, we refer the reader to the excellent book of Frisch (1995).

In molecular clouds, the Reynolds number is estimated to be in a $10^5 - 10^8$ range, indicating highly turbulent motions (Chandrasekhar, 1949; Von Weizsäcker, 1951). In fact, the Larson relations (see Fig. 3) are believed to be due to turbulence. Moreover, as these non thermal velocities exceed the typical sound speed, the Mach number $\mathcal{M} = v_{\mathrm{NT}}/c_{\mathrm{s}}$ is greater than one and turbulence is supersonic. Under such conditions, shocks develop in association with local increases of density.

2.5.3 Compressible, isothermal turbulence

Supersonic turbulence is characterized by a density field that is disorganized and chaotic with structures that are strongly reminiscent of those of molecular clouds (see Fig. 2 and Fig. 4 taken from Kritsuk et al. 2007).

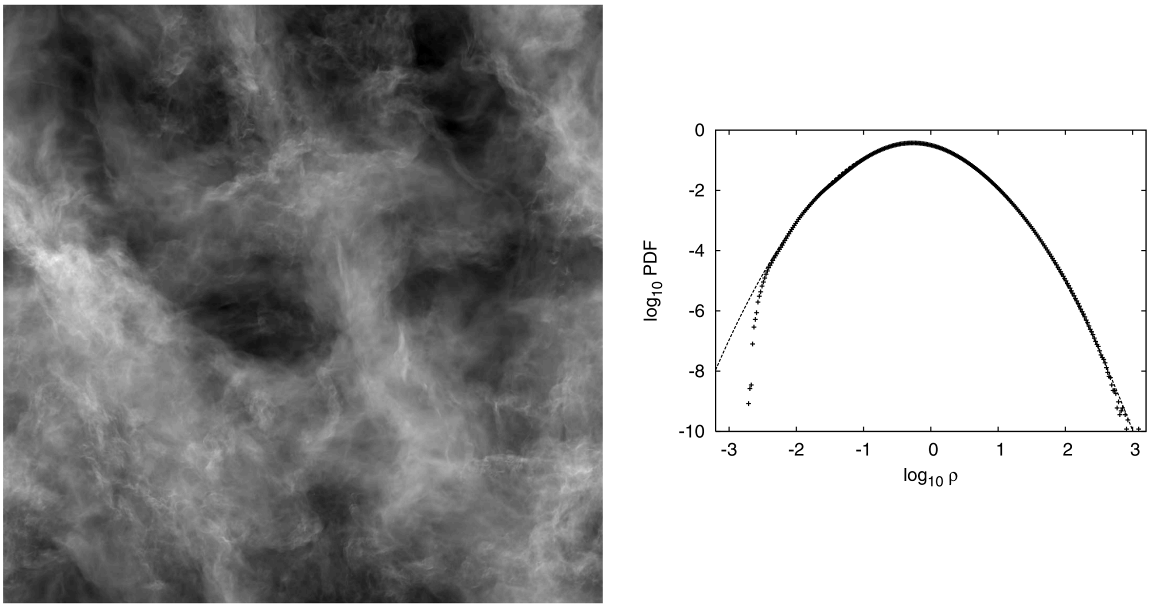

FIGURE 4 Density structures and statistics from numerical simulations of isothermal compressible turbulence. Left: Snapshot of the logarithm of the projected density field along one of the axis of the simulation Box. Right: PDF of the logarithm of the density field. The dotted line is a Gaussian fit to the data points shown as small crosses. The density field is disorganized and chaotic and exhibits structures that are strongly reminiscent of those of molecular clouds. Its PDF appears lognormal, *i.e* the PDF of its logarithm appears Gaussian. Both pictures are taken from Kritsuk et al. 2007.

In experiments and numerical simulations of isothermal compressible turbulence, the probability density function (PDF, see Chapter **1**) of the density field ρ is found to be lognormal, implying that the PDF of the logarithm of ρ is Gaussian, as shown in Fig. 4. A heuristic explanation of this result was given by Vazquez-Semadeni (1994). An isothermal shock of Mach number $\mathcal{M}$ is associated with a local density enhancement ρ_+ over the post-shock density ρ_- which is proportional to $\mathcal{M}^2$, *i.e.*, $\rho_+ = \mathcal{M}^2\rho_-$. Density fluctuations are due to a random succession of passing shocks. This produces a random distribution of density enhancement factors, which become additive for the density logarithm. Thus, owing to the central limit theorem, one ends up with a normal (Gaussian) distribution function for the logarithmic density. This elegant model should be taken as heuristic because the central limit theorem only applies to independent random variables and it is not clear that shocks in a sequence are independent of one another.

The variance σ_s^2 of the Gaussian density logarithm $s = \ln(\rho/\overline{\rho})$ is a function of the Mach number $\mathcal{M}$:

$$\sigma_s^2 = \ln\left(1 + (b\mathcal{M})^2\right) \tag{2}$$

where prefactor b in front of the Mach number, $b\mathcal{M}$, is a parameter that depends on the ratio between the compressive and solenoidal modes of the turbulent forcing (see Chap. **1** and Federrath et al. 2008).

3 Fundamentals of core and star formation

It is now recognized that stars are due to the gravitational collapse of dense regions in giant (molecular) gas clouds, *i.e.* form out of the condensation of interstellar gas. In hindsight, this model may seem rather obvious and simple but it developed out of quite a few physical principles and theoretical calculations clarifying the role of gravity as the main driving force. In spite of the many complicating factors that must be added to it, it covers many key aspects of star formation and remains central to our current understanding. The increasingly sophisticated models that have been put forward rely on the same core principles and it is useful to review them.

3.1 Newtonian Gravity

3.1.1 Attraction of point masses

In his seminal work entitled Mathematical Principles of Natural Philosophy (*Philosophiae naturalis principia mathematica*) published in 1687, Isaac Newton laid the foundations of modern physics. Drawing on the work of Kepler in particular, he set out a new world system and introduced the law of universal gravitation. According to this law, two point masses attract each other with a force that is inversely proportional to the square of the distance between them and parallel to the line segment that joins them. Moreover, the attraction that a body of mass m exerts on another body of mass m' is proportional to the product $m\,m'$. Thus, $\boldsymbol{F}_{m;m'}(d)$, the force exerted by point mass m on m' lying at a distance d is:

$$\boldsymbol{F}_{m;m'}(d) = G\frac{m\,m'}{d^2}\boldsymbol{e}_{m;m'}, \tag{3}$$

where $G \simeq 6.67\,10^{-11}$ m^3 kg^{-2} s^{-1} is the universal gravitational constant, and $\boldsymbol{e}_{m;m'}$ is a unit vector pointing towards m along the direction that joins m and m'. As this is true for all mass m', one may define the gravitational field generated by m at any position $\boldsymbol{x}$, where the reference frame has its origin at the position of m:

$$\boldsymbol{\mathcal{G}}_m(\boldsymbol{x}) = -G\frac{m}{|\boldsymbol{x}|^3}\boldsymbol{x}. \tag{4}$$

One can then rewrite the force acting on any particle of mass m' immersed in the gravitational field generated by m as follows:

$$\boldsymbol{F}_m = m'\,\boldsymbol{\mathcal{G}}_m. \tag{5}$$

With this new principle, Newton was able to derive Kepler's laws of motion of planets and account for the revolution of the Moon around the Earth, thereby establishing the universal character of gravity. We note that the law of universal gravitation is a principle and as such cannot be derived from more primitive laws. It is validated by its success in describing the Universe. As we know now from the work of Albert Einstein, this law is not perfectly correct but is an excellent approximation to describe the motion of material particles in curved space-time, provided that the mass curving space-time is "small enough" so that the curvature is weak and provided that particles move at velocities that are small compared to the speed of light.

3.1.2 Continuous media and Poisson equation

The quantity that characterizes the attraction generated by a point mass is the gravitational field. For a set of N point masses with masses m_i at positions $\boldsymbol{x}_i$, the resulting gravitational field $\boldsymbol{\mathcal{G}}^{(N)}$ at point $\boldsymbol{x}$ is simply the sum of the all the individual fields $\boldsymbol{\mathcal{G}}_{m_i}$:

$$\boldsymbol{\mathcal{G}}^{(N)}(\boldsymbol{x}) = \sum_{i=1}^{N}\boldsymbol{\mathcal{G}}_{m_i}(\boldsymbol{x}) = -G\sum_{i=1}^{N}\frac{m_i}{|\boldsymbol{x}-\boldsymbol{x}_i|^3}\left(\boldsymbol{x}-\boldsymbol{x}_i\right), \tag{6}$$

because of the principle of addition of forces. This gravitational field can be interpreted as the gradient of a quantity called the gravitational potential Φ_G:

$$\begin{aligned}
\boldsymbol{\mathcal{G}}^{(N)}(\boldsymbol{x}) &= -\boldsymbol{\nabla}_{\boldsymbol{x}}\Phi_G^{(N)}, && (7)\\
\Phi_G^{(N)} &= G\sum_{i=1}^{N}\frac{m_i}{|\boldsymbol{x}-\boldsymbol{x}_i|}, \text{ and where } \boldsymbol{\nabla}_{\boldsymbol{x}} \text{ is the usual Nabla operator,} && (8)\\
\boldsymbol{\nabla}_{\boldsymbol{x}}\Phi_G &= \frac{\partial\Phi_G}{\partial x}\boldsymbol{e}_x + \frac{\partial\Phi_G}{\partial y}\boldsymbol{e}_y + \frac{\partial\Phi_G}{\partial z}\boldsymbol{e}_z, && (9)
\end{aligned}$$

and where the notation $\boldsymbol{\nabla}_{\boldsymbol{x}}$ indicates that derivatives are carried out with respect to $\boldsymbol{x}$. In a material media with a large number of material particles, one usually switches from a discrete description of matter to a continuous one, where the mass distribution is described by density ρ. Density $\rho(\boldsymbol{x})$ corresponds to the mass contained in an infinitesimal volume $\mathrm{d}\boldsymbol{x}$ around position $\boldsymbol{x}$, $\mathrm{d}M$:

$$\mathrm{d}M = \rho(\boldsymbol{x})\mathrm{d}\boldsymbol{x}. \tag{10}$$

For a set of N point masses m_i at positions $\boldsymbol{x}_i$, density is:

$$\rho^{(N)}(\boldsymbol{x}) = \sum_{i=1}^{N} m_i\delta\left(\boldsymbol{x}-\boldsymbol{x}_i\right), \text{ where } \delta \text{ is Dirac distribution.} \tag{11}$$

Then the gravitational potential Φ_G generated by these particles satisfies the following partial differential equation:

$$\Delta\Phi_G^{(N)} = 4\pi G\rho^{(N)}, \text{ where } \Delta \text{ is the Laplacian operator } \Delta = \frac{\partial^2}{\partial x^2}+\frac{\partial^2}{\partial y^2}+\frac{\partial^2}{\partial z^2}. \tag{12}$$

with the boundary condition that $\Phi_G \to 0$ when $|\boldsymbol{x}| \to 0$. In fact, the solution for a single point mass m_1 is:

$$\Phi_G^{(1)}(\boldsymbol{x}) = G\frac{m_1}{|\boldsymbol{x}-\boldsymbol{x}_1|}, \tag{13}$$

which is the Green function for the partial differential equation 12. For a continuous description of a medium with density $\rho(\boldsymbol{x})$, the gravitational potential generated by the mass distribution is the solution of *Poisson equation*:

$$\Delta\Phi_G = 4\pi G\rho. \tag{14}$$

with the boundary condition that $\Phi_G \to 0$ when $|\boldsymbol{x}| \to 0$. In terms of the gravitational field $\boldsymbol{\mathcal{G}}$, this leads to two partial differential equation equations:

$$\begin{aligned}
\nabla\cdot\boldsymbol{\mathcal{G}} &= -4\pi G\rho && (15)\\
\nabla\times\boldsymbol{\mathcal{G}} &= 0. && (16)
\end{aligned}$$

3.1.3 Gravitational potentials and fields of homogeneous distributions.

We are now able to calculate gravitational potentials and fields for any distribution of matter. In general, however, solutions to the Poisson Equation are rarely obtained in closed form and must be found by numerical methods. Only in a few special cases can an explicit solution be obtained.

This is the case for a homogeneous sphere of radius R_0 and uniform density $\rho = \rho_0$. In this case, choosing the origin of reference frame at the center of the sphere, one easily shows that:

$$\begin{aligned}
\Phi_G(\boldsymbol{x}) &= \frac{4\pi G\rho_0}{6} R_0^2 \left(\frac{r^2}{R_0^2} - 3 \right), \text{ for } r = |\boldsymbol{x}| \le R_0, \\
\Phi_G(\boldsymbol{x}) &= -\frac{4\pi G\rho_0}{3} \frac{R_0^3}{r}, \text{ for } r = |\boldsymbol{x}| \ge R_0,
\end{aligned} \tag{17}$$

which corresponds to the following gravitational field:

$$\begin{aligned}
\boldsymbol{\mathcal{G}}(\boldsymbol{x}) &= -\frac{4\pi G\rho_0}{3} \boldsymbol{x} = -G\frac{M(r)}{r^3}\boldsymbol{x}, \text{ for } r = |\boldsymbol{x}| \le R_0, \\
\boldsymbol{\mathcal{G}}(\boldsymbol{x}) &= -\frac{4\pi G\rho_0}{3} \frac{R_0^3}{r^3}\boldsymbol{x} = -G\frac{M(R_0)}{r^3}\boldsymbol{x}, \text{ for } r = |\boldsymbol{x}| \ge R_0,
\end{aligned} \tag{18}$$

where

$$M(r) = \int_{S(r)} \rho \mathrm{d}\boldsymbol{x} = \frac{4\pi}{3}\rho_0 r^3, \text{ is the mass enclosed in a sphere of radius } r. \tag{19}$$

As may be seen from Eq. 17, equipotential surfaces, *i.e* surfaces such that $\Phi_G = cst$, are concentric spheres. As a consequence, the gravitational field is in the radial direction, as can be seen in Eq. 18. Written in terms of $M(r)$, equations 18 are also valid for a heterogeneous cloud with spherical symmetry, *i.e* such that iso-density surface are concentric spheres.

It is also possible to obtain the gravitational potential and field of a homogeneous ellipsoid, which has fewer symmetries than the sphere and therefore allows some generalization of the previous results. The outward surface of an ellipsoid $\mathcal{E}(a_i)$ is defined, for a proper choice of coordinate system (x, y, z), by:

$$\left(\frac{x}{a_1}\right)^2 + \left(\frac{y}{a_2}\right)^2 + \left(\frac{z}{a_3}\right)^2 = 1, \tag{20}$$

where $a_i > 0$ are the lengths of the three principal axes of the ellipsoid. When all the a_i's are set equal to the same R_0, one retrieves of course the equation for a sphere of radius R_0. The study of an ellipsoidal gravity field and its stability has attracted many renowned scientists. To name but a few, Newton, Laplace, MacLaurin, Dirichlet, Dedekind, Riemann and Poincare have all tackled this topic. It can be shown that the potential *inside* a homogeneous ellipsoid of density ρ_0 and principal axes lengths a_i is (Chandrasekhar, 1969):

$$\begin{aligned}
\Phi_G(\boldsymbol{x}) &= \pi G\rho_0 \left(I - \sum_{i=1}^{3} A_i x_i^2 \right), \text{ where,} \\
I &= a_1\, a_2\, a_3 \int_0^\infty \frac{\mathrm{d}u}{\Delta(u)}, \text{ with }, \Delta(u)^2 = (a_1^2+u)(a_2^2+u)(a_3^2+u), \\
A_i &= a_1\, a_2\, a_3 \int_0^\infty \frac{\mathrm{d}u}{(a_i^2+u)\Delta(u)},
\end{aligned} \tag{21}$$

The corresponding gravitational field is:

$$\boldsymbol{\mathcal{G}}(\boldsymbol{x}) = -2\pi G\rho_0 \, \mathrm{Diag}\,[A_1, A_2, A_3] \cdot \boldsymbol{x}, \tag{22}$$

where, $\mathrm{Diag}\,[A_1, A_2, A_3]$ is a 3×3 diagonal matrix with coefficients (A_1, A_2, A_3). It may be seen that equipotential surfaces are concentric ellipsoids that verify the equation:

$$\sum_{i=1}^{3} A_i x_i^2 = c_0. \tag{23}$$

Thus, their three principal axes are the same as those of the starting ellipsoid $\mathcal{E}(a_i)$.

3.2 Two descriptions of fluid motions

One can track fluid motions in two different ways. One can choose to follow material particles (in a Lagrange perspective) or one can make snapshots of the velocity field for all the fluid particles (in a Euler perspective). In the former description, the position of a material fluid particle P is tracked by vector $\boldsymbol{f}(P,t)$. The Lagrange variables are time t and the position $\boldsymbol{\mathcal{R}}$ of P at a reference time t_0, which serves as an identifier label for the particle. These variables are independent. In the latter description, instead of tracking fluid particles, one remains at some fixed point Q of the reference frame. Point Q is identified by vector $\boldsymbol{x}$ and the velocity of the fluid particle that is at Q at time t is $\boldsymbol{v}(\boldsymbol{x},t)$. The Euler variables are $\boldsymbol{x}$, the position of the observation point and time t. These variables are also independent.

3.3 Homologous collapse: free-fall time scale

Let us now describe the evolution of a spherically symmetric, pressure-less and initially homogeneous cloud. No external driving force or field is acting on it, so that the cloud retains spherical symmetry attributes throughout. The cloud evolution is governed by the following equation:

$$\begin{aligned} \frac{\mathrm{D}\boldsymbol{v}}{\mathrm{D}t} &= \boldsymbol{\mathcal{G}}(\boldsymbol{x}) = -\frac{GM(r)}{r^3}\boldsymbol{x}, & (24)\\ \frac{\mathrm{D}\rho}{\mathrm{D}t} &= -\rho\boldsymbol{\nabla}\cdot\boldsymbol{v} & (25)\end{aligned}$$

where

$$\frac{\mathrm{D}}{\mathrm{D}t} = \left.\frac{\partial}{\partial t}\right|_{\boldsymbol{x}} + (\boldsymbol{v}\ \cdot\boldsymbol{\nabla}) \tag{26}$$

is the Lagrangian derivative, and where ρ and $\boldsymbol{v}$ are the fluid density and velocity, respcetively. Eq. 24 and Eq 25 account for the conservation of momentum and mass, respectively. Solving for the field equation is not straightforward with a Eulerian description and is much simpler with the Lagrangian one. Each particle is identified by its initial position $\boldsymbol{\mathcal{R}}$ and is at $\boldsymbol{f}(\boldsymbol{\mathcal{R}},t)$ at some later time t. At $t=0$, one therefore has $\boldsymbol{f}(\boldsymbol{\mathcal{R}},t=0)=\boldsymbol{\mathcal{R}}$.

3.3.1 Lagrangian description and mass conservation

In the Lagrangian description, mass conservation is readily solved for with the first Lagrangian integral:

$$\rho(\boldsymbol{\mathcal{R}},t) = \frac{\rho_0}{J(\boldsymbol{\mathcal{R}},t)} \tag{27}$$

where ρ_0 is the initial uniform density and $J(\boldsymbol{\mathcal{R}},t)$ is:

$$J(\boldsymbol{\mathcal{R}},t) = \det\left(\frac{\partial\boldsymbol{f}}{\partial\boldsymbol{\mathcal{R}}}\right). \tag{28}$$

We are dealing with a spherically symmetric system so that it is sufficient to track each particle with the norm of its position f:

$$f(\boldsymbol{\mathcal{R}},t) = |\boldsymbol{f}(\boldsymbol{\mathcal{R}},t)|. \tag{29}$$

Furthermore, every particle initially at the same radial distance $\mathcal{R} = |\boldsymbol{\mathcal{R}}|$ evolves in the same manner. We can then write Eq (24) in its Lagrangian form, taking into account spherical symmetry:

$$\frac{\mathrm{D}^2 f}{\mathrm{D}t^2} = -\frac{GM(f)}{f^2}, \tag{30}$$

where, in the Lagrangian description:

$$\frac{\mathrm{D}}{\mathrm{D}t} = \left.\frac{\partial}{\partial t}\right|_{\boldsymbol{\mathcal{R}}}. \tag{31}$$

We can then also prove that the mass under particles with Lagrangian identifier $\mathcal{R}$ is constant:

$$\frac{\mathrm{D}M(f)}{\mathrm{D}t} = 0. \tag{32}$$

Indeed, this mass is the mass included in the spatial domain $\mathcal{D}_t(\mathcal{R})$ delimited by particles with Lagrangian identifier $\mathcal{R}$:

$$M(f) = \int_{\mathcal{D}_t(\mathcal{R})} \rho \,\mathrm{d}\,\boldsymbol{x}. \tag{33}$$

Going from Eulerian to Lagrangian coordinates, one obtains:

$$M(f) = \int_{\mathcal{D}_0(\mathcal{R})} (\rho(\boldsymbol{\mathcal{R}}, t) J(\boldsymbol{\mathcal{R}}, t)) \;\mathrm{d}\;\boldsymbol{\mathcal{R}} = \int_{\mathcal{D}_0(\mathcal{R})} \rho_0 \,\mathrm{d}\;\boldsymbol{\mathcal{R}} = \frac{4\pi}{3}\rho_0 \mathcal{R}^3. \tag{34}$$

3.3.2 Solving the equation of motion

We can now perform a first integration of (30). This gives:

$$\frac{1}{2}\left(\frac{\mathrm{D}f}{\mathrm{D}t}\right)^2 - \frac{GM(\mathcal{R})}{f(\mathcal{R}, t)} = E(\mathcal{R}), \tag{35}$$

where $E(\mathcal{R})$ is an energy per unit mass and is independent of time. This yields:

$$v = \frac{\mathrm{D}f}{\mathrm{D}t} = \mathrm{sgn}(v_0)\sqrt{\frac{8\pi G\rho_0 \mathcal{R}^3}{3f} + 2\,E(\mathcal{R})} \tag{36}$$

where v_0 is the initial velocity of particles at radial distance $\mathcal{R}$ and where $\mathrm{sgn}(v_0)$ is the sign function equal to -1 if $v_0 \leq 0$ and equal to 1 if $v_0 > 0$. Now if the initial velocity field has homogeneous gradients, *i.e.* if the following condition is met:

$$v_0(\mathcal{R}) = \frac{\mathrm{D}f}{\mathrm{D}t}(\mathcal{R}, t = 0) = \alpha\mathcal{R}, \tag{37}$$

it follows that:

$$E(\mathcal{R}) = E_0 \mathcal{R}^2, \text{ with } E_0 = \frac{\alpha^2}{2} - \frac{4\pi}{3} G\rho_0 \tag{38}$$

We then have

$$\frac{\mathrm{D}\,(f/\mathcal{R})}{\mathrm{D}t} = \mathrm{sgn}(v_0)\sqrt{\frac{8\pi G\rho_0}{3}\frac{\mathcal{R}}{f} + 2\,E_0} \tag{39}$$

or, in terms of the reduced variable $x = (f/\mathcal{R})$,

$$\frac{\mathrm{D}x}{\mathrm{D}t} = \mathrm{sgn}(v_0)\sqrt{\frac{8\pi G\rho_0}{3}\frac{1}{x} + 2\,E_0}. \tag{40}$$

This shows that x is only a function of time t. Then, due to spherical symmetry, one has $\boldsymbol{f}(\boldsymbol{\mathcal{R}},t) = \boldsymbol{\mathcal{R}} \times x(t)$, which yields $J(\boldsymbol{\mathcal{R}},t) = x(t)^3$ and:

$$\rho(\boldsymbol{\mathcal{R}},t) = \frac{\rho_0}{x(t)^3} \tag{41}$$

As a consequence, the cloud remains homogeneous with uniform density at all times. This is referred to as a homologous collapse sequence.

Carrying out the same analysis for an initial ellipsoidal cloud with principal axes lengths a_i, $\mathcal{E}(a_i)$ is more involved. Indeed, as we saw earlier, equipotential surfaces are not simple homothetic contractions of the initial bounding ellipsoid $\mathcal{E}(a_i)$, but they are concentric ellipsoids with the same principal axis. This implies that the collapse is not a homothetic process, implying that the bounding ellipsoid of the cloud is not simply given by some $\mathcal{E}(\alpha a_i)$ with $\alpha < 1$. However, if the cloud is homogeneous initially and if the initial velocity field does not act to generate heterogeneities, the cloud density will remain uniform throughout collapse because $\boldsymbol{\mathcal{G}}(\boldsymbol{x})$ is linear in $\boldsymbol{x}$. In general, the principal axes will contract in different ways so that the cloud remains ellipsoidal but with different aspect ratios.

3.3.3 Dynamical regimes

One may define three different regimes using Eq 40.

- If $v_0 \leq 0$ initially, $x(t)$ decreases with time and the cloud is collapsing.

There are two other regimes if $v_0 > 0$ at $t = 0$.

- One regime is such that $v_0 > 0$ and $E_0 \geq 0$. In this case, the kinetic energy is initially larger than the gravitational binding energy, so that $x(t)$ keeps increasing at all times and the cloud expands.
- A last regime is obtained when $v_0 > 0$ and $E_0 < 0$. In this case, the initial kinetic energy is smaller than the gravitational binding energy and $x(t)$ first increases up to the following value:

$$x_{\max} = \frac{4\pi G\rho_0}{-3\,E_0} = \frac{4\pi G\rho_0}{3\,|E_0|} > 1 \tag{42}$$

  and then decreases. In this regime, therefore, the cloud initially expands but eventually collapses due to its own gravity.

This an important result. Gravity always acts to promote collapse, but, if the cloud is expanding initially, it will first expand and will only collapse if gravity is strong enough. Moreover, if the cloud initial expansion is fast enough, it will simply never collapse.

3.3.4 "Standard" initially motionless free fall: the free fall time.

The standard calculation from which one derives the free fall time

$$\tau_{\mathrm{ff},0} = \sqrt{\frac{3\pi}{32\pi G\rho_0}} \tag{43}$$

relies on the assumption of an initially motionless state, $v_0(\boldsymbol{\mathcal{R}}) = 0$, i.e. $\alpha = 0$ in Eq. (37). Eq (40) then becomes:

$$\frac{\mathrm{d}x}{\mathrm{d}t} = -\sqrt{\frac{8\pi G\rho_0}{3}\left(\frac{1}{x} - 1\right)}, \tag{44}$$

which is solved by setting $x(t) = \cos^2(\beta(t))$ and obtaining the following equation for $\beta(t)$

$$\frac{\mathrm{d}\beta}{\mathrm{d}t} \times \cos^2(\beta(t)) = \sqrt{\frac{8\pi G\rho_0}{3}}. \tag{45}$$

This yields:

$$\beta + \frac{1}{2}\sin(2\beta) = \sqrt{\frac{8\pi G\rho_0}{3}} \times t. \tag{46}$$

This solution is defined up to $\tau_{\mathrm{ff},0}$ such that $x(\tau_{\mathrm{ff},0}) = 0$, corresponding to $\beta(\tau_{\mathrm{ff},0}) = \pi/2$ and

$$\tau_{\mathrm{ff},0} = \sqrt{\frac{3\pi}{32\pi G\rho_0}}. \tag{47}$$

One can then obtain $J(\boldsymbol{\mathcal{R}}, t) = \cos^6(\beta(t))$ and also $\boldsymbol{\nabla} \cdot \boldsymbol{v}$:

$$\boldsymbol{\nabla} \cdot \boldsymbol{v} = \frac{1}{J(\boldsymbol{\mathcal{R}}, t)} \frac{\mathrm{d}J}{\mathrm{d}t} = -\sqrt{24}\sqrt{4\pi G\rho(t)}\,\sin(\beta(t)). \tag{48}$$

We can then go back to a Euler description and obtain the radial component of the velocity field at radial distance r, v_r:

$$v_r = -\sqrt{\frac{8}{3}}\sqrt{4\pi G\rho(t)}\,\sin(\beta(t)) \times r \tag{49}$$

At short times, we note that:

$$\beta(t) = \sqrt{\frac{4\pi G\rho_0}{24}} \times t + \mathcal{O}(t^2) \tag{50}$$

giving:

$$\boldsymbol{\nabla} \cdot \boldsymbol{v} = -4\pi G\rho_0 t = -4\pi G\rho t \tag{51}$$

3.4 Virial equilibrium

In the example given above, there are no stable situations. The cloud either ends up collapsing or expands indefinitely. This is because (1) we have restricted ourselves to purely radial motions and (2) we have not considered other types of support such as pressure. With more complex collapse dynamics, solutions become much more involved than the previous one. However, one can still study the evolution of global quantities such as the cloud volume to gain insights into the dynamics. Instead of the volume, one usually studies quantity I, which is the moment of inertia for the distribution of gas in some volume Ω_t that may evolve with time and which is defined as follows:

$$I = \int_{\Omega_t} \rho(\boldsymbol{x}, t)|\boldsymbol{x}|^2 \mathrm{d}\boldsymbol{x}, \tag{52}$$

where, usually, the origin of positions $\boldsymbol{x}$ is taken at the center of mass of the distribution. This quantity gives information on the size of the cloud but also, and this is important, on the distribution of material within it. For example, redistributing material whilst keeping volume Ω_t in the same shape may lead to a change in I. Therefore, a change of I does not necessarily imply a change of shape or size of a cloud. If the gas cloud Ω_t collapses in all three directions (as in the precedent examples), however, I will necessarily decrease. Thus, a decrease of I is a necessary condition for collapse in the three directions but not a sufficient one. It is quite easy to construct situations such that I decreases just by redistributing material inside the cloud, even if the cloud is globally static or expanding in one or more directions. Nevertheless, a decreasing I is a necessary condition for collapse, so that it is valuable to study how I evolves in order to rule out collapse in all three directions.

3.4.1 Evolution of the moment of inertia

To follow the evolution of moment of inertia I, it is instructive to focus on its second derivatives:

$$\frac{\mathrm{D}^2 I}{\mathrm{D}t^2} = \int_{\Omega_0} (\rho J(\boldsymbol{\mathcal{R}}, t)) \frac{\mathrm{D}^2 |\boldsymbol{f}(\boldsymbol{\mathcal{R}}, t)|^2}{\mathrm{D}t^2} \mathrm{d}\boldsymbol{\mathcal{R}} = \int_{\Omega_t} \rho \left(\boldsymbol{v}^2 + \boldsymbol{x} \cdot \frac{\mathrm{D}\boldsymbol{v}}{\mathrm{D}t} \right) \mathrm{d}\boldsymbol{x}, \tag{53}$$

where we have switched from Eulerian description to a Lagrangian one and vice versa to obtain the last two integrals. Then, for the following equation of motion:

$$\rho \frac{\mathrm{D}\boldsymbol{v}}{\mathrm{D}t} = -\boldsymbol{\nabla} P + \rho \boldsymbol{\mathcal{G}}, \tag{54}$$

where P is pressure, we obtain

$$\frac{\mathrm{D}^2 I}{\mathrm{D}t^2} = 2E_\mathrm{k} - \int_{\Omega_t} \boldsymbol{x} \cdot \boldsymbol{\nabla} P \mathrm{d}\boldsymbol{x} + \int_{\Omega_t} \rho \boldsymbol{x} \cdot \boldsymbol{\mathcal{G}} \mathrm{d}\boldsymbol{x} \tag{55}$$

where

$$E_\mathrm{k} = \frac{1}{2} \int_{\Omega_t} \rho \boldsymbol{v}^2 \mathrm{d}\boldsymbol{x} \text{ is the kinetic energy of the distribution } \Omega_t. \tag{56}$$

Using Leibnitz rule and Stokes theorem, we further obtain

$$\frac{\mathrm{D}^2 I}{\mathrm{D}t^2} = 2E_\mathrm{k} + 3 \int_{\Omega_t} P \mathrm{d}\boldsymbol{x} - \int_{\partial\Omega_t} P \boldsymbol{x} \cdot \mathrm{d}\boldsymbol{S} + \int_{\Omega_t} \rho \boldsymbol{x} \cdot \boldsymbol{\mathcal{G}} \mathrm{d}\boldsymbol{x}. \tag{57}$$

The last term is

$$\int_{\Omega_t} \rho \boldsymbol{x} \cdot \boldsymbol{\mathcal{G}} \mathrm{d}\boldsymbol{x} = \frac{1}{2} \int_{\Omega_t} \rho(\boldsymbol{x}) \Phi_G(\boldsymbol{x}) \mathrm{d}\boldsymbol{x} = E_G. \tag{58}$$

Recognizing the (thermal) internal kinetic energy of a perfect gas

$$3 \int_{\Omega_t} P \mathrm{d}\boldsymbol{x} = \int_{\Omega_t} 3\rho \frac{k_\mathrm{B} T}{m} \mathrm{d}\boldsymbol{x} = \int_{\Omega_t} \rho v_\mathrm{th}^2 \mathrm{d}\boldsymbol{x} = 2E_\mathrm{th}, \tag{59}$$

where k_B is Boltzmann constant, m is the mass of gas particles and $v_\mathrm{th} = c_\mathrm{s}$ is the thermal velocity (sound speed). This reduces to

$$\frac{\mathrm{D}^2 I}{\mathrm{D}t^2} = 2E_\mathrm{k} + 2E_\mathrm{th} + E_G - \int_{\partial\Omega_t} P \boldsymbol{x} \cdot \mathrm{d}\boldsymbol{S}. \tag{60}$$

One may neglect the surface term on the r.h.s. of this equation to obtain:

$$\frac{\mathrm{D}^2 I}{\mathrm{D}t^2} = 2E_\mathrm{k} + 2E_\mathrm{th} + E_G. \tag{61}$$

Then, provided that $\frac{\mathrm{D}^2 I}{\mathrm{D}t^2} < 0$, the cloud is said to be unstable and it is assumed that it will collapse eventually. At *virial equilibrium*, $\frac{\mathrm{D}^2 I}{\mathrm{D}t^2} = 0$, the two kinetic energy components $2E_\mathrm{k} + 2E_\mathrm{th}$ exactly compensate for the gravitational bounding energy $E_G < 0$:

$$2E_\mathrm{k} + 2E_\mathrm{th} = -E_G. \tag{62}$$

3.4.2 Virial parameter

In a *homogeneous, isothermal and spherical cloud*, the surface term in Eq.60 is such that:

$$\int_{\partial\Omega_t} P\boldsymbol{x}\cdot \mathrm{d}\boldsymbol{S} \text{ exactly compensates for the thermal energy } 2E_{\mathrm{th}} \tag{63}$$

so that one is left with:

$$\frac{\mathrm{D}^2 I}{\mathrm{D}t^2} = 2E_{\mathrm{k}} + E_G = M\left\langle \boldsymbol{v}^2\right\rangle - \frac{3}{5}G\frac{M^2}{R} = M\left(\left\langle \boldsymbol{v}^2\right\rangle - \frac{4\pi}{5}\rho_0 G R^2\right), \tag{64}$$

where ρ_0 is the uniform density, $\left\langle \boldsymbol{v}^2\right\rangle$ is some average non thermal velocity, R is the cloud radius and M its mass. One defines virial parameter α_{vir} as follows:

$$\alpha_{\mathrm{vir}} = \frac{2E_{\mathrm{k}}}{|E_G|} = \frac{5\left\langle \boldsymbol{v}^2\right\rangle}{4\pi\rho_0 G R^2}. \tag{65}$$

For $\alpha_{\mathrm{vir}} > 1$, the cloud is not bound and is expected to expand, whereas it is bound and expected to collapse for $\alpha_{\mathrm{vir}} < 1$. The case $\alpha_{\mathrm{vir}} = 1$ corresponds to equilibrium.

3.5 The Jeans criterion

In his pioneering work, Jeans (1902) studied the stability of a homogeneous, isothermal and initially inert cloud with density $\overline{\rho}$. Using a linear stability analysis, he showed that any disturbance with wave number k less than

$$k_J = \frac{\sqrt{4\pi G\overline{\rho}}}{c_{\mathrm{s}}} \tag{66}$$

grows exponentially. He further showed that the fastest growing modes, corresponding to vanishing k, have growth rate $\tau^{-1} \simeq \sqrt{4\pi G\overline{\rho}} \simeq 2\tau_{\mathrm{ff}}(\overline{\rho})^{-1}$. He interpreted this result as follows. An isothermal cloud of size R is unstable against gravitational collapse if it is larger than the typical wave-length:

$$R > \lambda_J = \frac{2\pi}{k_J} = c_{\mathrm{s}}\sqrt{\frac{\pi}{G\overline{\rho}}}. \tag{67}$$

Chandrasekhar (1951a) added turbulence to the physical setup and showed that the Jeans length must be modified as follows:

$$\lambda_J = \frac{2\pi}{k_J} = \sqrt{c_{\mathrm{s}}^2 + \frac{1}{3}\boldsymbol{v}^2}\sqrt{\frac{\pi}{G\overline{\rho}}}. \tag{68}$$

where $\boldsymbol{v}^2$ is the dispersion of turbulent velocities. Thus, turbulence provides an additional support to stabilize dense regions against collapse.

3.6 Overview of low mass star formation

Low-mass stars, with masses of less than a few $M_\odot$, are the most abundant ones in the Universe. It is widely accepted that their formation proceeds in three main stages (André et al., 2000).

In the pre-stellar phase, the parent molecular cloud is mainly composed of molecular hydrogen at a temperature of about 10 K and undergoes local isothermal collapse in regions where the thermal support is not strong enough to counteract gravity. Condensation generates a pre-stellar core with a universal density profile $\rho \propto r^{-2}$ (Foster & Chevalier, 1993). During this phase, temperature remains almost constant as gravitational energy is radiated away by thermal emission from the dust. At the end of the phase, collapse stops when density reaches the typical value $n \sim n_{\mathrm{ad}} = 10^{10}$ cm^{-3}. At such high density values, the core region is opaque to its radiation. The cloud core is now in a quasi-static equilibrium with typical density $n_1 \sim 10^{12}$ cm^{-3}. This has been called the first Larson core. Radiation cannot escape, and hence the core enters a phase of adiabatic contraction, which leads to a temperature increase. One should note here that the adjective "adiabatic" is misleading as the core is in fact generating heat. It is a common abuse of language and one should use "isentropic" instead. When temperatures reach 2000 K, H_2 dissociates in an endothermic reaction and a second collapse phase begins. Once H_2 has been completely dissociated, the new core, called the second Larson core, undergoes a slow adiabatic contraction. It now has a typical density of $n_2 \sim 10^{23}$ cm^{-3} and stretches over a few solar radii $R_\odot$.

After the formation of the second Larson core, the proto-stellar phase begins. During this phase, the protostar mass increases by accretion of the free-falling envelope. Conservation of the angular momentum during collapse leads to the formation of an accretion disk, also called a protoplanetary disk, which is most likely birthplace of planets. Simultaneously, a fraction of the mass is being ejected from the system by bipolar outflows (Bachiller, 1996) that are probably driven by magnetic fields. Finally, at the end of this phase, the proto-star has become dense and massive enough to trigger nuclear reactions in its core: it is now a star.

4 Mass functions

A mass function (MF) describes the number density of objects per mass interval. These functions are the cornerstones as well as the starting points of statistical studies of cosmological and astrophysical populations. In his pioneering study, Salpeter (1955) defined the stellar mass function as follows:

$$\xi(m) = \frac{\mathrm{d}n}{\mathrm{dlog}(m)}. \tag{69}$$

where n is the the number of stars per unit volume at time t and per mass interval m. The stellar initial mass function (IMF) pertains to the mass of stars at their creation. More details on mass functions can be found in Chapter **5**.

The IMF provides an essential link between the evolutions of galaxies and stars and determines the chemical, light and baryonic contents of the universe (Chabrier, 2003). It is used in almost all numerical models of star formation as a closure equation for the evolution of sub-grid regions. Two key questions remain: *what determines the IMF and does the IMF remain unchanged as the universe evolves ?*

Mass functions were first investigated in cosmology (see Monaco 1998; Zentner 2007 for reviews), and the formalism that was developed was adapted to stellar scales by Hennebelle & Chabrier (2008); Hopkins (2012a,b). These models are successful in explaining the shape and the rather universal character of the IMF over a wide range of stellar cluster conditions in Milky-Way like environments. They are based on an *initial* lognormal distribution for the statistically homogeneous fluctuating density field, which is appropriate for turbulence in compressible media. Observations have shown, however, that, in star forming clouds, probability density functions (PDF) deviate from a lognormal form and develop preeminent power law tails at high density values, a feature which has been identified as the signature of gravity

5 Motivation for this work.

Stars are formed in high density subregions embedded in larger molecular clouds. Such local density enhancements are attributed to supersonic compressible turbulent motions which are known to generate disorganized, random-looking and evolving structures. These dense and intricate structures are suitable seeds for gravitation-driven condensation and modern astrophysicists are striving to understand their role in the star formation process. Thanks to observations from cutting edge space telescopes, high resolution numerical simulations and theoretical advances, our knowledge of the density fields of molecular clouds and their statistics has greatly improved. On the numerical side, the development of increasingly refined methods has made it possible to account for an increasing number of physical effects and to probe the star formation environment with increasing resolution. From a theoretical point of view, simplified, but elaborate, models have led to a better understanding of the physical processes involved in star formation. More precisely, they have allowed us to separate between processes that are essential to the evolution of molecular clouds and those that are comparatively minor contributors.

The most common description of density enhancement in molecular clouds relies on the phenomenology of isothermal gravitation-less turbulence. In this case, the density field is lognormal and its variance is proportional to $\mathcal{M}^2$, where $\mathcal{M}$ is the Mach number. Observations and numerical simulations have shown, however, that, in star forming clouds, the probability density function (PDF) deviates from a lognormal form and develops a preeminent power law tails at high density values, a feature which has been identified as the signature of gravity. This thesis includes a review of the most important attempts at explaining this feature and at introducing it in models of star formation. Theoretical studies have been focussed on the gravitationally unstable parts of a cloud and have been based on analytical models of scale-free gravitational collapse and/or *geometrical* arguments. They have led to asymptotic values for power-law tail exponents but have fallen short of a complete statistical description of density fluctuations in both gravitationally stable and unstable parts of a cloud. In addition, with the exception of the numerical simulations of Girichidis et al. (2014), these studies treat the PDF as a static property and do not deal with its evolution through time.

Considerable improvement of numerical capabilities has occurred in parallel with theoretical advances on basic physical processes. In studies of turbulence, theoretical work have continued to refine description tools and to guide the numerical exploration of the phenomenon. Thus, in astrophysics, the current trend is to run numerical simulations that tackle various physical effects with varying amplitudes and varying degrees of resolution. Results can rarely account for observations over the whole range of dimensions and physical properties of real astrophysical systems. They are extremely useful exploration tools and provide unprecedented insights into many aspects, but they are costly, time consuming and have a huge ecological impact. For example, a large proportion of the Australian and German Max Planck Institutes CO_2 emissions are generated by supercomputers, to an extent that depends on the source of their electricity (Stevens, 2020).

In this thesis, we have explored new, and hopefully more elaborate, theoretical frameworks in order to obtain new insights on the complex physics behind star formation and tools to describe them. Two different communities have been at work on highly non linear and complex dynamical systems. In turbulence, the statistical approach for *compressible media* can be traced back to the famous initial formulation for incompressible flows (Batchelor, 1953). Chandrasekhar (1951b,a) for example, studied the dynamics of the density field for homogeneous and isotropic turbulence. However, progress on the PDF of density fluctuations in turbulent flows has been slower. A large number of efforts have dealt with incompressible fluids and it is only recently that a robust theoretical framework has been made available for compressible ones by Pan et al. (2018, 2019a,b). This framework relies on the formalism developed by Pope (1981, 1985) and Pope & Ching (1993) in which the PDF of any quantity is expressed as the conditional expectation of its time derivatives. Pan et al. (2019b) was able to derive a theoretical formulation of the density fluctuation PDF at steady state *from first principles*, but without gravity. In cosmology, the study of primordial density fluctuations and the subsequent formation of structures due to gravity has lead to the development of a vast statistical framework (see e.g Peebles 1973; Monaco 1998).

It is hoped that this thesis is one step toward a description of the statistics of random (turbulent) fluid motions under the influence of gravity. In one sense, this work connects formalisms that have been developed in the distinct fields of turbulence and cosmology. In another sense, it is aimed at improving our understanding of the role played by turbulent structures in the star formation process.

It is focussed on the statistics of density and velocity in molecular clouds and more specifically on how they evolve with time. On the one hand, it leads to new tools for studying and describing the statistics of astrophysical flows which should be useful to both observers and numerical specialists. On the other hand, it aims to improve our understanding of the evolution of the statistics of velocity and density fields and to develop a new approach on how gravitational collapse gets initiated and proceeds in dense Molecular Clouds.

This thesis is organized as follows.

In Chapter **1**, we present some theoretical tools that are relevant to the present study. We first give a review of probability theory and of the statistical tools that will be used throughout this thesis. We then briefly review what information is obtained from observations and how it is obtained. Finally, we summarize a set of numerical simulations due to Federrath & Klessen (2012, 2013) that will allow us to test our theoretical formulation.

In Chapter **2**, we tackle the issue of how to extract statistical properties of the 3D density field from the observed 2D projected density field. We quantify which variables of interest can be derived from observations and how they are related to those of the underlying density field.

In Chapter **3**, we study the relevance of a statistical approach to the study of molecular clouds. Indeed, be it for observations or numerical simulations, only one realization (one snapshot) of a cloud is available. For a statistical approach to be meaningful, the cloud must be large enough for statistical information to be reliable. We clarify and define rigorously what is meant by "large enough" using ergodic theory and apply our results to the Polaris and Orion B clouds. Finally we apply the same formalism to other characteristics (observational or numerical) of molecular clouds. Observations cannot unravel the full complexity of the inner structure of these clouds. They do provide robust estimates of *bulk* characteristics, such as total mass and size, and it is useful to assess how these can be used to obtain accurate estimates of other global physical quantities of relevance to cloud dynamics, such as the total gravitational (binding) energy and the virial parameter.

In Chapter **4**, we study the evolution of statistics of the density field in star forming clouds. More specifically, we study the time evolutions of the density PDF, the auto-covariance function of the density field and its associated correlation length. We develop in detail an analytical theory for the statistics of density fluctuations in star-forming molecular clouds under the combined effects of supersonic turbulence and self-gravity. The theory relies on general properties of solutions to the coupled Navier-Stokes equations for fluid motions and the Poisson equation for gravity. It extends previous approaches by accounting for gravity and by treating the PDF as a dynamical variable, not a stationary one. We derive rigorously transport equations for the PDF and ACF with a magnetic field present, determine how they evolve with time and solve for the density threshold above which gravity strongly affects and eventually dominates the flow dynamics. The theoretical results and diagnostics are compared to data on several molecular clouds as well as to the results of numerical simulations.

Chapter **5** describes a step towards an improved analytical theory for the Initial Mass Function relying on the results of the previous chapters.

A final Chapter is devoted to the conclusion.

1 Chapter
Tools

Contents

Appendices

1 Elements of probability theory

The aim of this thesis is to use a statistical approach to study the apparently disorganized structures of astrophysical flows. To this end, it is useful to recall a few basic notions of probability theory.

1.1 A first approach to the notion of probabilities

Observations of many phenomena occurring in apparently random fashion show that certain averages tend to a constant value as the number of observations increases. Moreover, these values do not seem to depend on any particular subset of events, provided it is large enough. For example, it is intuitively known that if we throw dice a very large number of times, it is highly likely that we will find about as many 1s or 6s. The purpose of probability theory is to formalize these issues and investigate the properties of averages in relation to probabilities of events. The probability of some event A is a real value $\mathbb{P}(A)$, which can be interpreted in the so-called relative-frequency framework as follows: if one performs a large enough number of experiments N and event A occurs N_A times, one expects that $\mathbb{P}(A) \simeq N_A/N$. It is clear, however, that this statement is imprecise as we do not really know what is meant by "large enough" or "expects", or even what "$\simeq$" stands for. In an attempt to solve this issue, one may introduce the *relative-frequency* definition of probability as the limit of the frequency of occurrence as the number of experiments tends to infinity (von Mises, 1957):

$$\mathbb{P}(A) = \lim_{N \to \infty} \frac{N_A}{N}. \tag{1.1}$$

However, if this definition seems to specify what is meant by "large enough", it presupposes the existence of a limit and cannot be used in practice to evaluate the accuracy of the prediction made by ratio N_A/N for a finite number N of experiments. It is worth noting at this point that this lack of precision cannot be totally avoided, but, as will be seen below, it is possible to give working definitions developed logically from clearly defined axioms that can be applied to real problems.

1.2 Axiomatic of probability theory and set theory

We introduce here the formalism introduced by Kolmogorov (von Plato, 2005) which is considered the most correct approach to probability theory today. For a complete review of this approach, we refer to the excellent book of Papoulis & Pillai (1965) and only mention what is needed for the present work. This approach formalizes both the concept of events as subsets of a (larger) set and the notion of probability as a measure on this set. This measure can intuitively be interpreted as the size of a subset.

1.2.1 Elements of set theory

We will only briefly review the basic notions of set theory here, mainly in order to clarify the terminology of probability theory.

We first start by introducing the so-called universal or possibility set Ω, whose elements are called elementary events. As mentioned above, an event is described as some subset A of Ω and if in any trial outcome ω is an element of $A \subseteq \Omega$, one states that event A occurs. The first two trivial subsets and events are Ω itself, sometimes called the "sure event" (occurs at every trial), and the empty set $\emptyset$ sometimes called impossible event. From now on, we shall refer to "events" in order to use the language of probability theory but will keep in mind that the word really stands for subsets.

A natural procedure is to construct from two events A_1 and A_2 either the event such that either one of these events occurs or the event such that both occur simultaneously. For example in a dice experiment, from the events $A_1 =$ *the dice gives 2*, $A_2 =$ *the dice gives 4*, one may wish to consider event $A_{1+2} =$ *the dice gives 2 or 4*. This is easily accomplished in set theory with the union $\cup$ and intersection $\cap$ operations. Thus, from two events A_1 and A_2, one considers the union $A_1 \cup A_2$, sometimes noted $A_1 + A_2$ as the event such that either A_1 or A_2 occurs, both not being necessarily exclusive. Moreover, one also constructs the intersection $A_1 \cap A_2$, sometimes noted $A_1\,A_2$, as the event such that A_1 and A_2 both occur simultaneously. Two events A_1 and A_2 are then called mutually exclusive if the occurrence of one prevents the occurrence of the second one, which is written as $A_1 \cap A_2 = \emptyset$. Another natural operation is to introduce the event opposite to A, noted $\overline{A}$, such that A and $\overline{A}$ are mutually exclusive and their union is the universal set Ω. This operation is the complementation operation in set theory.

1.2.2 Probability space

As discussed above, the set of events $\mathcal{A}$ (which is a set of subsets of Ω) we seek to deal with must possess several properties highlighted below:

- $\mathcal{A}$ is not empty (it contains Ω and $\emptyset$),
- $\mathcal{A}$ is closed under complementation: If A is in $\mathcal{A}$, then so is its complement $\overline{A}$,
- $\mathcal{A}$ is closed under countable unions: If $(A_n)_{n\in J}$ is a countable collection of elements of $\mathcal{A}$, then so is their union $\cup_{n\in J} A_n$,
- $\mathcal{A}$ is closed under countable intersections: If $(A_n)_{n\in J}$ is a countable collection of elements of $\mathcal{A}$, then so is their intersection $\cap_{n\in J} A_n$.

We note that item 4 is a consequence of item 2 and 3 by De Morgan's law, and as such does not need to be included as a property of $\mathcal{A}$. All these properties provide $\mathcal{A}$ with the structure of a σ-Algebra, as named in set theory.

The last item one needs to set up is the probability associated to each events in $\mathcal{A}$. Given that $\mathcal{A}$ is a σ-Algebra, it possesses the properties required to be endowed with a *probability measure* $\mathbb{P}$ (or law) which is a function defined on $\mathcal{A}$ with values in the $[0, 1]$ interval, such that:

- $\mathbb{P}$ is positive: $\mathbb{P}(A) \geq 0$, $\forall A \in \mathcal{A}$,
- $\mathbb{P}$ is normalized: $\mathbb{P}(\Omega) = 1$,
- $\mathbb{P}$ is σ-additive: If $(A_n)_{n\in J}$ is a countable collection of *disjoint* elements of $\mathcal{A}$, $\mathbb{P}\left(\cup_{n\in J} A_n\right) = \sum_{n\in J} \mathbb{P}(A_n)$.

Triplet $(\Omega, \mathcal{A}, \mathbb{P})$ is then called a probability space.

1.2.3 Simple properties

From the properties of normalization and σ-additivity, we deduce that, for each event A ($\subseteq \Omega$), $\mathbb{P}(A) \leq 1 = \mathbb{P}(\Omega)$ and $\mathbb{P}(\overline{A}) = 1 - \mathbb{P}(A)$. Furthermore as $\mathbb{P}(\Omega) = 1$, $\mathbb{P}(\emptyset) = 0$, implying that the impossible event has probability 0, as expected.

Moreover the probabilities of the union and intersection of *any* events A_1 and A_2 are related by the equation $\mathbb{P}\left(A_1 + A_2\right) + \mathbb{P}\left(A_1\,A_2\right) = \mathbb{P}\left(A_1\right) + \mathbb{P}\left(A_2\right)$. And two events A_1 and A_2 are said to be independent if $\mathbb{P}\left(A_1\,A_2\right) = \mathbb{P}\left(A_1\right)\,\mathbb{P}\left(A_2\right)$.

1.2.4 Conditional probability

Once the probability $\mathbb{P}(B)$ of a given event $B \in \mathcal{A}$ is known and not zero, it is possible to create a new probability measure on $\mathcal{A}$, called conditional probability relative to B and noted $\mathbb{P}(A|B)$ for any events A defined by

$$\mathbb{P}(A|B) = \frac{\mathbb{P}(A\,B)}{\mathbb{P}(B)}, \qquad \forall A \in \mathcal{A}. \tag{1.2}$$

Considering two events A and B and constructing the conditional probability relative to both of them, it is straightforward to deduce from Eq. (1.2) that : $\mathbb{P}(A\,B) = \mathbb{P}(A|B)\mathbb{P}(B) = \mathbb{P}(B|A)\mathbb{P}(A)$. This yields:

$$\boxed{\mathbb{P}(B|A) = \frac{\mathbb{P}(A|B)\mathbb{P}(B)}{\mathbb{P}(A)},} \tag{1.3}$$

which is known as Bayes' formula.

1.2.5 Random variables

The notion of random variable allows one to deal with a measure in probability space through a relation with a measurable space, for example $\mathbb{R}$ (or $\mathbb{R}^n$). The interest of this association, in the case where the measurable space is $\mathbb{R}$ (or $\mathbb{R}^n$), is that one can assign a number (or mutliplet) to the abstract result of an experiment, such as "heads" or "tails" for example, that allows one to treat in a unified way similar experiments using different terminologies. Consider first the case of a scalar random variable. The measurable space $(\mathbb{R}, \mathcal{B}, \mu)$ is usually endowed with Lebesgue's measure μ and $\mathcal{B}$ is Borel's σ-Algebra which contains all the $\mathbb{R}$ interval. A random variable X is then a map $X : \Omega \to \mathbb{R}$, which attributes a real number $X(\omega)$ to each elementary event $\omega \in \Omega$.

In order to benefit from the properties of the measurable space $(\mathbb{R}, \mathcal{B}, \mu)$, random variable X should be such that the preimage of every integral $I_x =]-\infty, x]$ is an element of the σ-Algebra $\mathcal{A}$: $A_x = X^{-1}(I_x) \in \mathcal{A}$ and X is said to be a measurable function. In other words, the events of $\mathcal{A}$ are mapped onto the events in $\mathcal{B}$. This can be generalized to $\mathbb{R}^n$ in a straightforward manner.

1.3 (Cumulative) Distribution function

1.3.1 Definition

The mapping of events in $\mathcal{A}$ on those of $\mathcal{B}$ allows one to define a probability measure on $\mathbb{R}$ (hence not a Lebesgue's measure), $\mathbb{P}_X$, which is defined as $\mathbb{P}_X(X(A)) = \mathbb{P}(A)$ for every A in $\mathcal{A}$. The notation $\mathbb{P}_X$ serves as a reminder that this depends on the choice of X and it is called law of the random variable X.

Applied to the interval $I_x =]-\infty, x]$, $\mathbb{P}_X(I_x) = \mathbb{P}\left(X^{-1}(I_x)\right)$ defines a function of the real variable x, labelled F_X and called (cumulative) distribution function of random variable X:

$$F_X(x) = \mathbb{P}_X(I_x) = \mathbb{P}\left(X^{-1}(I_x)\right). \tag{1.4}$$

The value of this function at a given x is the probability that the outcome of a trial ω yields $X(\omega) \leq x$. By abuse of language and notation, one can state that $F_X(x) = \mathbb{P}\left(X \leq x\right)$ is the probability that the outcome of a trial is smaller than x.

1.3.2 Properties of the distribution function

If one applies the above definitions to an interval of the form $I =]a, b]$, one deduces that $\mathbb{P}\left(X \in I\right) = F_X(b) - F_X(a) \geq 0$ (a consequence of σ-additivity). One can therefore derive the following properties of F_X:

- F_X is monotonically increasing and its limit for x tending towards $-\infty$ and $+\infty$ are 0 and 1, respectively.
- F_X is right-continuous : $F_X(x^+) = F_X(x)$.
- F_X is left continuous (and thus continuous) at x if and only if $\mathbb{P}(X = x) = 0$ as $F_X(x^+) - F_X(x^-) = \mathbb{P}(X = x)$.

Thus, the distribution function may be discontinuous, which is the case for discrete random variables. However, we will only consider in the following the case of absolutely continuous distribution functions, associated with continuous random variables. Absolute continuity requires F_X to have a derivative f_X almost everywhere which is Lebesgue integrable and such as F_X is the indefinite integral of its derivative.

1.4 Probability Density Function (PDF)

1.4.1 Defintion

As mentioned above, for an absolutely continuous distribution function F_X one can define almost everywhere its derivative f_X which is Lebesgue integrable. Most importantly for every $(a,b) \in \mathbb{R}^2$, one has:

$$\mathbb{P}_X(]a,b]) = F_X(b) - F_X(a) = \int_a^b f_X(x)\mathrm{d}x = \int_{]a,b]} f_X \mathrm{d}\mu, \tag{1.5}$$

with μ the usual Lebesgue's measure. This function f_X is called probability density function (PDF) and allows one to map the probability measure $\mathbb{P}_X$, and hence $\mathbb{P}$, to Lebesgue's measure (the usual measure on $\mathbb{R}$).

A common interpretation of the PDF is the probability of having $X \in]x, x+\delta x]$ is equal to $\mathbb{P}(x < X \leq x + \delta x) = F_X(x+\delta x) - F_X(x) \simeq f_X(x)\delta x$, which justifies the name density. We note that some authors extend this definition to discrete random variables and use sums of Dirac's δ distribution.

1.4.2 Properties

As F_X is monotonically increasing, f_X is positive and the following normalisation constraint holds:

$$\int_{\mathbb{R}} f(x)\mathrm{d}x = 1. \tag{1.6}$$

It is usual in physics to add constraints on f_X that *do not follow* from the definitions and properties above. In addition of the properties derived earlier, it is often assumed that the PDF has limits when x tends to $-\infty$ and $+\infty$ which are then necessarily both 0, and we will do so.

1.5 Change of variables

The output of some experiment may not give directly access to the desired (random) quantity. In some cases, one can express this outcome as a function of the desired quantity and hence seek to specify the stochastic properties of random variable $Y = g(X)$ (which implies that $g(X)$ is measurable). One can show that the PDFs of Y and X are related by (Papoulis & Pillai, 1965):

$$f_Y(y) = \sum_k \frac{f_X(x_k)}{|g'(x_k)|}, \qquad \text{where the } x_k\text{'s are solutions of } g(x) = y. \tag{1.7}$$

1.6 Vector random variables

So far, we have studied the case of scalar random variables mapping the possibility set Ω onto $\mathbb{R}$. However, on the one hand some physical quantities are described by vectors and on the other hand one would like to be able to study the properties of a combination of scalar random variables. One therefore needs to generalize the previous result to the case of a n-dimensional *vector* random variables $\boldsymbol{X} = (X_1, ..., X_n)$. Such a random variable is a measurable function from $(\Omega, \mathcal{A}, \mathbb{P})$ to $(\mathbb{R}^n, \mathcal{B}_n, \mu)$ where $\mathcal{B}_n$ is Borel's σ-algebra and contains every cartesian products of intervals.

1.6.1 Distribution and density functions

This generalization is straightforward. As before, because $\boldsymbol{X}$ is measurable, one can define a probability measure on $\mathbb{R}^n$, $\mathbb{P}_{\boldsymbol{X}}$ and define for subsets $I_{x_1,...,x_n} =]-\infty, x_1] \times ... \times]-\infty, x_n]$ the function $F_{\boldsymbol{X}}(x_1,...,x_n) = \mathbb{P}_{\boldsymbol{X}}(I_{x_1,...,x_n})$ which is written by abuse of notation $F_{\boldsymbol{X}}(x_1,...,x_n) = \mathbb{P}(X_1 \leq x_1,...,X_n \leq x_n)$. This function is the (multidimensional) joint distribution function of the random variables $X_1,...,X_n$ and its values are in the $[0,1]$ interval. When it exists (i.e. when $\boldsymbol{X}$ is absolutely continuous) the (n-dimensional) joint probability density function $f_{\boldsymbol{X}}$ is defined by

$$f_{\boldsymbol{X}}(x_1,...,x_n) = \frac{\partial^n}{\partial x_1 ... \partial x_n} F_{\boldsymbol{X}}(x_1,...,x_n). \tag{1.8}$$

This function is positive and its integral over $\mathbb{R}^n$ is 1.

1.6.2 Marginal distributions and densities

Given the n-dimensional distribution function $F_{\boldsymbol{X}}$ (and hence $f_{\boldsymbol{X}}$), one can obtain the distribution and density functions of each of the random components X_i of the random vector $\boldsymbol{X}$. These distribution and density functions are termed marginal functions. The distribution function of X_k is indeed given by:

$$F_{X_k}(x_k) = F_{\boldsymbol{X}}(+\infty,...,x_k,...,+\infty), \tag{1.9}$$

and its probability density function by

$$f_{X_k}(x_k) = \int_{\mathbb{R}^{n-1}} f_{\boldsymbol{X}}(u_1,...,x_k,...,u_n) \prod_{i=1, i\neq k}^{n} \mathrm{d}u_i \tag{1.10}$$

1.6.3 Independent variables

If the variables $(X_1,...,X_n)$ are mutually independent then

$$F_{\boldsymbol{X}}(x_1,...,x_n) = F_{X_1}(x_1) ... F_{X_n}(x_n), \quad \text{and} \quad f_{\boldsymbol{X}}(x_1,...,x_n) = f_{X_1}(x_1) ... f_{X_n}(x_n). \tag{1.11}$$

1.7 Characteristic numbers

1.7.1 Mathematical expectation

The mathematical expectation, noted $\mathbb{E}(X)$, formalizes the notion of average of a random variable X. For random variable X on the probability space $(\Omega, \mathcal{A}, \mathbb{P})$, the function X being measurable, one defines $\mathbb{E}(X)$ as follows:

$$\mathbb{E}(X) = \int_{\Omega} X(\omega) \mathrm{d}\mathbb{P}. \tag{1.12}$$

If X is absolutly continuous then, as a corollary of Radon-Nikodym-Lebesgue theorem:

$$\mathbb{E}(X) = \int_{\mathbb{R}} x f_X(x)\, \mathrm{d}x. \tag{1.13}$$

In physics, one always assumes that this number is finite and frequently call it the statistical or ensemble average noted $\langle X \rangle$ or $\overline{X}$ when there is no ambiguity.

As it is defined in terms of Lebesgue integrals, the expectation is linear with respect to random variables and for a change of variables $Y = g(X)$, one has:

$$\mathbb{E}(Y) = \mathbb{E}(g(X)) = \int_{\mathbb{R}} g(x)\, f_X(x)\, \mathrm{d}x. \tag{1.14}$$

This implies that it is not necessary to know the law of Y or its PDF to compute its expectation. Knowledge of the law of X or its PDF is sufficient. In fact this illustrates that the statistics of X are entirely determined by the knowledge of f_X.

1.7.2 Moments

Moments are numbers characterizing the law followed by random variable X, in the absence of any knowledge of such a law. There are two types of moments, called centered or non centered moments.

The k-th non centered moment μ'_k of a random variable X, for $k \in \mathbb{N}$ is defined as follows:

$$\mu'_k = \mathbb{E}(X^k) = \int_{\mathbb{R}} x^k f_X(x)\,\mathrm{d}x, \tag{1.15}$$

whereas the k-th centered moment μ_k is such that:

$$\mu_k = \mathbb{E}\left([X - \mathbb{E}(X)]^k\right) = \int_{\mathbb{R}} (x - \mu'_1)^k f_X(x)\,\mathrm{d}x, \tag{1.16}$$

1.7.3 Variance and standard deviation

Among the different moments, two are of particular importance. Besides the expectation value μ'_1, also called average of X, the second centered moment μ_2, called variance, is of particular importance. It is often denoted σ^2, allowing the introduction of the standard deviation σ which is positive by definition. Knowledge of the average of X and its variance (or standard deviation) allows to characterize the range of values one expects for X (see Sec. 1.10).

1.7.4 Uncorrelated variables

Using the mathematical expectation, one can introduce the notion of uncorrelated variables. Two variables X_1 and X_2 are said to be uncorrelated if:

$$\mathbb{E}(X_1 \times X_2) = \int_{\mathbb{R}^2} x_1\,x_2 f_{X_1,X_2}(x_1,x_2)\mathrm{d}x_1\,\mathrm{d}x_2 = \mathbb{E}(X_1) \times \mathbb{E}(X_2). \tag{1.17}$$

Of course, independent variables are uncorrelated, but the reverse is not necessarily true. To be uncorrelated is a weaker condition than independence.

1.8 Gaussian random variables

The Normal (Gaussian) distribution is one of the most commonly used distributions due to its properties. X is a normal or Gaussian random variable with parameters μ and σ^2 if its density function is given by:

$$f_X(x) = \frac{1}{\sqrt{2\pi\sigma^2}}\exp\left(-\frac{(x-\mu)^2}{2\sigma^2}\right). \tag{1.18}$$

For such a random variable, all moments can be expressed in terms of the first two moments. One has indeed:

$$\mu_{2k} \;=\; \frac{(2k)!}{2^k\,k!}\sigma^{2k}, \quad \text{and} \quad \mu_{2k+1} = 0. \tag{1.19}$$

1.9 Conditional statistics

It may be of interest to consider the statistics of events A, knowing that some events B have occurred.

1.9.1 Conditional Distribution and density

For some random variable X, one can define the conditional distribution of X with the occurrence of B, $F_{X|B}(x)$, as the conditional probability $\mathbb{P}(X \leq x|B)$ such that, by definition (see above),

$$F_{X|B}(x) = \mathbb{P}(X \leq x|B) = \frac{\mathbb{P}([X \leq x] \cap B)}{\mathbb{P}(B)}. \tag{1.20}$$

One can then define the conditional PDF of X knowing B, $f_{X|B}(x)$ as the derivative of $F_{X|B}(x)$ with respect to x. For all the above definitions to be meaningful, $\mathbb{P}(B) \neq 0$. If one now considers two continuous random variables X_1, X_2 with joint density f_{X_1,X_2} and event $B = \{X_2 \in B_2\}$ with $B_2 \in \mathcal{B}$, the conditional PDF of X_1 knowing B is given by:

$$f_{X_1|B}(x_1) = \frac{\int_{B_2} f_{X_1,X_2}(x_1, u_2)\mathrm{d}u_2}{\int_{B_2} f_{X_2}(u_2)\mathrm{d}u_2}. \tag{1.21}$$

To generalize these results and describe the statistics of X_1 knowing that $X_2 = x_2$, one defines the conditional PDF of X_1 knowing that $X_2 = x_2$, $f_{X_1|x_2}$ as follows:

$$f_{X_1,X_2}(x_1, x_2) = f_{X_1|x_2}(x_1) f_{X_2}(x_2). \tag{1.22}$$

As before, permuting the roles of X_1 and X_2 yields the continuous Bayes' formula:

$$\boxed{f_{X_1|x_2}(x_1) = f_{X_2|x_1}(x_2)\frac{f_{X_1}(x_1)}{f_{X_2}(x_2)}} \tag{1.23}$$

1.9.2 Conditional expectations

The conditional expectation of X knowing B, $\mathbb{E}(X|B)$, is defined as

$$\mathbb{E}(X|B) = \int_{\mathbb{R}} x f_{X|B}(x)\mathrm{d}x, \tag{1.24}$$

For two random variables X_1, X_2, the conditional expectation of X_1 knowing that $X_2 = x_2$,$\langle X_1|x_2\rangle$ is:

$$\langle X_1|x_2\rangle = \int_{\mathbb{R}} u_1 f_{X_1|x_2}(u_1)\mathrm{d}u_1 = \frac{1}{f_{X_2}(x_2)}\int_{\mathbb{R}} u_1 f_{X_1,X_2}(u_1, x_2)\mathrm{d}u_1. \tag{1.25}$$

1.10 Practical application of the theory

1.10.1 Bienayme-Tchebychev's inequality

As mentioned above, knowledge of both $\mathbb{E}(X)$ and its variance σ^2 allows one to characterize the range of values one expects for the outcome $X(\omega)$ of a trial. Indeed a fundamental result is given by Bienayme-Tchebychev's inequality that states that, for any random variable X:

$$\boxed{\mathbb{P}(|X - \mathbb{E}(X)| \leq m\sigma) \geq 1 - \frac{1}{m^2},} \tag{1.26}$$

for any real number $m > 0$. Although the Bienayme-Tchebychev's inequality gives a lower bound for the probability, it allows one to obtain a confidence interval for X, *without having to know the (probability) law of* X. Its proof is quite simple. Let us start by noting that:

$$\sigma^2 = \int_{\mathbb{R}} (x - \mathbb{E}(X))^2 f_X(x)\mathrm{d}x \geq \int_{|x-\mathbb{E}(X)|>m\sigma} (x - \mathbb{E}(X))^2 f_X(x)\mathrm{d}x \geq (m\sigma)^2\mathbb{P}(|X - \mathbb{E}(X)| > m\sigma). \tag{1.27}$$

Hence

$$\mathbb{P}\left(|X-\mathbb{E}(X)|>m\sigma\right)\leq\frac{1}{m^2}, \tag{1.28}$$

which leads to Bienayme-Tchebychev's inequality. The usual value of $m = 10$ gives a confidence interval with probability greater than 99% for the outcome $X(\omega)$ of a trial. As mentioned at the beginning of this section, one cannot avoid some lack of precision as the 99% bound is arbitrary but this provides an accuracy estimate.

1.10.2 Accuracy of estimators and prediction theory

We are now ready to give some answer to the questions raised in Sec. 1.1 regarding the relative-frequency interpretation. As mentioned above, the relative-frequency interpretation of probabilities defines the probability of an event A as the ratio of the number of occurrence of event A, N_A over the number N of different trials, in the limit $N \to \infty$. Whereas it may be considered satisfactory in some regards because it is built on observations and specifies what is meant by "large number of trials", this definition does not provide an estimate of the accuracy of the prediction made by ratio N_A/N for a finite number of experiments N.

To provide some solution to this problem, we start by realizing that the probability of an event, or any other statistical quantity of interest, can be constructed as a function of a random variable. In the present case, let X be a random variable relevant to the problem. For the sake of simplicity, we assume that X is a scalar. The probability of event A is then:

$$\mathbb{P}(A)=\mathbb{E}\left(\mathbb{I}_{X(A)}\right) \tag{1.29}$$

where $\mathbb{I}_{X(A)}$ is the indicator function of the subset of $\mathbb{R}$, $X(A)$, which is equal to 1 when $x \in X(A)$ and 0 elsewhere. The proof of Eq. (1.29) is straightforward if one uses the PDF f_X to transport the measure $\mathbb{P}$ on the measure $f_X \mathrm{d}x$.

Then, building on the relative-frequency definition, we perform N independent trials (ω_i) and build the estimator of $\mathbb{P}(A)$, $\hat{p}_A$:

$$\hat{p}_A=\frac{1}{N}\sum_{i=1}^{N}\mathbb{I}_{X(A)}(X(\omega_i))=\frac{N_A}{N}. \tag{1.30}$$

The trick is then to regard the estimator $\hat{p}_A$ as a random variable. Thus, the average (expectation) of $\hat{p}_A$ is $\mathbb{E}\left(\hat{p}_A\right)=\mathbb{E}\left(\mathbb{I}_{X(A)}\right)=\mathbb{P}(A)$ due to the linearity of the expectation. We thus state that $\hat{p}_A$ is an *unbiased estimator* of $\mathbb{P}(A)$. Moreover the variance of $\hat{p}_A$ is

$$\mathrm{Var}\left(\hat{p}_A\right)=\frac{1}{N}\mathbb{E}\left(\mathbb{I}^2_{X(A)}\right)=\frac{1}{N}\mathbb{E}\left(\mathbb{I}_{X(A)}\right)=\frac{1}{N}\mathbb{P}(A). \tag{1.31}$$

Then, due to Bienayme-Tchebychev's inequality, one sees that:

$$\boxed{\mathbb{P}\left(|\hat{p}_A-\mathbb{P}(A)|\leq m\frac{\sqrt{\mathbb{P}(A)}}{\sqrt{N}}\right)\geq 1-\frac{1}{m^2}.} \tag{1.32}$$

Thus, for $N \to \infty$, $\hat{p}_A = \mathbb{P}(A)$ with probability 1, as expected from the relative frequency definition. Moreover, Eq. (1.32) allows an evaluation of the accuracy of the estimate $\hat{p}_A$.

2 Stochastic fields and analytical tools

Section 1 allowed us to introduce the notion of random variables X which associate a real number $X(\omega)$ with the outcome ω of an experiment (or trial). However, the fields of physical variables of interest here, such as the density field, themselves possess some random characteristics. We must therefore deal with not only random numbers but complete random functions that depend on a multi-dimensional space. A stochastic process or field is defined as a map of the possibility set Ω onto the space of functions on $\mathbb{R}^n$. Alternatively we can consider a stochastic field as a function giving a random variable at each point of $\mathbb{R}^n$. A stochastic process or field can thus be interpreted as either a random function (taken randomly in the space of functions on $\mathbb{R}^n$), or as a sequence of random variables indexed by position (Papoulis & Pillai, 1965). Another alternative is to define it as a map of $\Omega \times \mathbb{R}^n$ onto $\mathbb{R}^m$. An example is the density field $\rho(\omega, \boldsymbol{x}, t)$ where ω is a particular outcome (an element of Ω) and $(\boldsymbol{x}, t)$ are space-time positions. For simplicity, we will often drop the reference to Ω (and hence the ω) to write simply ρ as a function of space and time $(\boldsymbol{x}, t)$. In this manner, we equate the random field to its realization.

As the purpose of introducing stochastic fields is to deal with typical physical conditions in astrophysical flows for example, observations of a real physical field under specific physical conditions should be equivalent to a realization of a stochastic field. We thus have to determine the relevant statistical properties for such a description. If this approach is correct, the statistical tools developed should describe accurately any flows possessing the same physical properties and hence do not depend on any particular realization.

The aim of this section is to describe useful statistical tools to describe physical fields. We restrict ourselves to random scalar fields, but this can be generalized to random vector fields in a straightforward manner.

2.1 One point statistics

2.1.1 One point distributions and densities

For any random scalar field X and at any point in space $\boldsymbol{y}$ and time t, the map $X(\cdot, \boldsymbol{y}, t) : \Omega \to \mathbb{R}$ can be treated as a random variable. We can thus define its distribution function $F_{X,\boldsymbol{y},t}(x) = \mathbb{P}(X(\boldsymbol{y}, t) \leq x)$ as defined earlier. As this is true for every position in space-time, we drop the subscript $(\boldsymbol{y}, t)$ and introduce it as an argument of the distribution function $F_X(x; \boldsymbol{y}, t)$. This distribution function is called *first order* distribution function.

Moreover, if the stochastic field is absolutely continuous, as will always be assumed, we can define the *first order* probability function $f_X(x; \boldsymbol{y}, t)$ as follows:

$$f_X(x; \boldsymbol{y}, t) = \frac{\partial F_X(x; \boldsymbol{y}, t)}{\partial x}. \tag{1.33}$$

We note that f_X is also a function of space and time.

2.1.2 Moments

We can then construct all the moments defined in Sec. 1.7.2, that are also functions of space and time: $\mu_k(\boldsymbol{y}, t)$. In particular, the mathematical expectation $\mathbb{E}\left(X(\boldsymbol{y}, t)\right)$ is a function of space and time.

2.1.3 Commutation of the derivatives and the expectation

As the expectation is linear with respect to random variables, the derivatives of a stochastic field $X(\boldsymbol{y})$ and the expectation commute:

$$\boxed{\mathbb{E}\left(\frac{\partial X}{\partial y^\nu}\right) = \frac{\partial}{\partial y^\nu}\mathbb{E}\left(X\right),} \tag{1.34}$$

where $\nu = 1, ..., n$.

2.2 N-point statistics

2.2.1 N-point distributions and densities

One point statistics are useful to describe the statistics of a stochastic field at a precise point in space and time. However, they cannot, as one might expect, provide a complete description of the field. To improve the knowledge of the characteristics of a stochastic field, one has to study the joint statistics of the field at various locations in space and time. For the sake of simplicity, we will refer to the space-time position solely as $\boldsymbol{y}$. This introduces the n-th order joint distribution function $F_n(x_1,...,x_n;\boldsymbol{y}_1,...,\boldsymbol{y}_n)=\mathbb{P}\left(X_1(\boldsymbol{y}_1)\leq x_1,...,X_n(\boldsymbol{y}_n)\leq x_n\right)$ and the n-th order joint PDF as follows:

$$f_n(x_1,...,x_n;\boldsymbol{y}_1,...,\boldsymbol{y}_n)=\frac{\partial^n F_n(x_1,...,x_n;\boldsymbol{y}_1,...,\boldsymbol{y}_n)}{\partial x_1\,...\partial x_n} \tag{1.35}$$

2.2.2 Moments, correlation and covariance

As was the case for random variables, we define the moments of the n-th order joint PDF $f_n(x_1,...,x_n;\boldsymbol{y}_1,...,\boldsymbol{y}_n)$. The n-points auto-correlation function $R_{X,n}(\boldsymbol{y}_1,...,\boldsymbol{y}_n)$ is thendefined as

$$R_{X,n}(\boldsymbol{y}_1,...,\boldsymbol{y}_n)=\mathbb{E}\left(X_1(\boldsymbol{y}_1)...X_n(\boldsymbol{y}_n)\right)=\int_{\mathbb{R}^n}x_1\,...\,x_n\;f_n(x_1,...,x_n;\boldsymbol{y}_1,...,\boldsymbol{y}_n)\prod_{i=1}^{n}\mathrm{d}x_i, \tag{1.36}$$

while the n-points auto-covariance function $C_{X,n}(\boldsymbol{y}_1,...,\boldsymbol{y}_n)$ is defined as follows:

$$C_{X,n}(\boldsymbol{y}_1,...,\boldsymbol{y}_n)=\mathbb{E}\left([X_1(\boldsymbol{y}_1)-\mathbb{E}\left(X(\boldsymbol{y}_1)\right)]...[X_n(\boldsymbol{y}_n)-\mathbb{E}\left(X_n(\boldsymbol{y}_n)\right])\right). \tag{1.37}$$

The case of 2-points correlation is of particular importance, as will be seen in Sec. (3). The 2-points auto-correlation and auto-covariance functions $R_{X,2}(\boldsymbol{y}_1,\boldsymbol{y}_2)$ $C_{X,2}(\boldsymbol{y}_1,\boldsymbol{y}_2)$ are then simply called auto-correlation and auto-covariance functions (ACF). Without specifying that they are 2-point statistics, we shall write $R_{X,2}\equiv R_X$, $C_{X,2}\equiv C_X$. These two functions are, from their definitions, even functions :

$$R_X(\boldsymbol{y}_1,\boldsymbol{y}_2)=R_X(\boldsymbol{y}_2,\boldsymbol{y}_1), \tag{1.38}$$

$$C_X(\boldsymbol{y}_1,\boldsymbol{y}_2)=C_X(\boldsymbol{y}_2,\boldsymbol{y}_1), \tag{1.39}$$

2.3 Gaussian fields

There are many (equivalent) definitions of what is a gaussian field. In most instances, one states that $X(\omega,\boldsymbol{y})$ is a gaussian field if, for every test functions $g(\boldsymbol{y})$,

$$\int_{\mathbb{R}^n}X(\omega,\boldsymbol{y})\,g(\boldsymbol{y})\mathrm{d}\boldsymbol{y} \tag{1.40}$$

is a gaussian random variable. A consequence of such a definition yields another frequently used definition: a field $X(\omega,\boldsymbol{y})$ is gaussian, if for any n and any collection $(\boldsymbol{y}_1,...,\boldsymbol{y}_n)$, the random variables $(X(\boldsymbol{y}_1),...,X(\boldsymbol{y}_n))$ are jointly normal, which means that they can be treated as a gaussian random vector (Papoulis & Pillai, 1965). This time, for such a gaussian field, knowledge of the averages $\mathbb{E}\left(X\right)(\boldsymbol{y})$ and auto-covariance function $C_X(\boldsymbol{y}_1,\boldsymbol{y}_2)$ characterizes completely the statistical properties of the field.

2.4 Statistically stationary or homogeneous fields

In many situations, some additional assumptions are made to simplify the description of stochastic fields. As these fields are used to describe dynamical physical quantities governed by evolution equations, such as the density or velocity fields in turbulent flows, one is usually tempted to enforce the symmetries of the evolution equations on the statistics of the stochastic fields. For example, as physics is invariant under time or space translations (which corresponds to the freedom of setting an origin for time or space), a usual assumption is to require that the statistical properties of a given field are invariant under such translations. There are two possible definitions for such assumptions termed "strict sense" and "large sense" assumptions.

2.4.1 Stationarity

A stochastic field is "strict sense" *stationary* if all of its statistical properties are invariant under *time* translations. Thus, its distribution functions are such that:

$$F_n(x_1, ..., x_n; t_1, ..., t_n) = F_n(x_1, ..., x_n; t_1 + \tau, ..., t_n + \tau),\ \forall\tau. \tag{1.41}$$

As a consequence, the first order PDF does not depend on the *time* variable and so does the expectation $\mathbb{E}\left(X\right)(\boldsymbol{y}, t) \equiv \mathbb{E}\left(X\right)(\boldsymbol{y})$. The auto-correlation function and ACF $R_X(t_1, t_2)$, $C_X(t_1, t_2)$ then depend only on the time difference $t_1 - t_2$.

A looser definition, called "large sense" *stationarity*, requires only that the expectations, $\mathbb{E}\left(X\right)(\boldsymbol{y}, t)$, and the (2-point) and auto-correlation function $R_X(t_1, t_2)$ are invariant under *time* translations. As a consequence $C_X(t_1, t_2)$ is also invariant under time translations and so is the variance σ^2. One should note that, in both definitions, not only $\mathbb{E}\left(X\right)$ but also R_X (and C_X) are invariant by the time reversal symmetry ($t \rightarrow -t$), as R_X is an even function $R_X(t) = R_X(-t)$.

Evolution equation in physics are often not invariant by the time reversal symmetry ($t \rightarrow -t$), e.g. due to dissipation effects, these requirements imply either some separation of timescales or some source of randomness to keep at least the two first order moments constant.

2.4.2 Homogeneity

Another assumption is that of statistical homogeneity. One states that a stochastic field is "strict sense" *homogeneous* if all of its statistical properties are invariant under *space* translations. Thus, its distribution functions met the following conditions:

$$F_n(x_1, ..., x_n; \boldsymbol{y}_1, ..., \boldsymbol{y}_n) = F_n(x_1, ..., x_n; \boldsymbol{y}_1 + \boldsymbol{\delta}, ..., \boldsymbol{y}_n + \boldsymbol{\delta}),\ \forall\boldsymbol{\delta}. \tag{1.42}$$

As a consequence, the first order PDF does not depend on the *space* variable and so does the expectation $\mathbb{E}\left(X\right)(\boldsymbol{y}, t) \equiv \mathbb{E}\left(X\right)(t)$. The auto-correlation function and ACF $R_X(\boldsymbol{y}_1, \boldsymbol{y}_2)$, $C_X(\boldsymbol{y}_1, \boldsymbol{y}_2)$ then depend only on space coordinate differences $\boldsymbol{y}_1 - \boldsymbol{y}_2$.

A looser definition called "large sense" *homogeneity* can be introduced as before. This time $\mathbb{E}\left(X\right)$ but also R_X (and C_X) are invariant by the parity symmetry ($\boldsymbol{y} \rightarrow -\boldsymbol{y}$). The problem of time reversal invariance was raised when dealing with statistical stationarity and, in the same manner, the problem of parity invariance ($\boldsymbol{y} \rightarrow -\boldsymbol{y}$) arises for statistical homogeneity. Whereas dissipation effects usually break the invariance of the evolution equations under the time reversal symmetry, they do not break the invariance by parity, which is thus a usual symmetry of the evolution equations. The situation here is therefore quite different than that for stationarity.

We note however that boundary conditions or some special type of background forcing can be incompatible with the hypothesis of statistical homogeneity. However, as will be seen in Chapter **4**, these difficulties can be circumvented by linearizing background fields.

Finally, we note that stationarity has been used by some authors to describe invariance under space translations but we shall refrain from doing so in order to avoid confusion.

2.4.3 Isotropy

If a stochastic field is homogeneous, it is statistically isotropic if its properties are also invariant under any rotations (in space). In terms of the distribution functions, this yields,

$$F_n(x_1, ..., x_n; \mathcal{R}\boldsymbol{y}_1, ..., \mathcal{R}\boldsymbol{y}_n) = F_n(x_1, ..., x_n; \boldsymbol{y}_1, ..., \boldsymbol{y}_n), \ \forall \mathcal{R} \in \mathrm{SO}(3). \tag{1.43}$$

This implies that the ACF functions $C_X(\boldsymbol{r}_{1,2})$ are only functions of the norm of $\boldsymbol{r}_{1,2} = \boldsymbol{y}_2 - \boldsymbol{y}_1$.

2.4.4 Structure functions

It is possible to construct other measures of the behavior of 2-points statistics when the field is homogeneous. Commonly used in the study of turbulent flows, the structure function of order p, $S_X^{(p)}$ is defined as:

$$S_X^{(p)}(\boldsymbol{r}) = \mathbb{E}\left(|X(\boldsymbol{r} + \boldsymbol{y}) - X(\boldsymbol{y})|^p\right), \tag{1.44}$$

for any real number $p \geq 0$. In addition, structure functions of integer orders ($p \in \mathbb{N}$) obey Lyapunov's inequality (see Papoulis & Pillai 1965 for a demonstration):

$$\left[S_X^{(p-1)}(\boldsymbol{r})\right]^{1/(p-1)} \leq \left[S_X^{(p)}(\boldsymbol{r})\right]^{1/p}. \tag{1.45}$$

In particular, the second order structure function is related to the ACF of X by the following relation:

$$S_X^{(2)}(\boldsymbol{r}) = 2\left(\sigma(X)^2 - C_X(\boldsymbol{r})\right) \tag{1.46}$$

2.4.5 Properties of the ACF of homogeneous fields

For a statistically homogeneous field, the autocorrelation function (ACF) C_X is

$$C_X(\boldsymbol{y}_2 - \boldsymbol{y}_1) = C_X(\boldsymbol{r}_{1,2}) = \mathbb{E}\left(X(\boldsymbol{y}_1)X(\boldsymbol{y}_2)\right) - \mathbb{E}\left(X\right)^2. \tag{1.47}$$

Furthermore, the ACF is (as mentioned above) an even function of $\boldsymbol{r}$:

$$C_X(\boldsymbol{r}) = C_X(-\boldsymbol{r}), \tag{1.48}$$

and reaches a maximum at $\boldsymbol{r} = \boldsymbol{0}$: $C_X(\boldsymbol{r}) \leq C_X(\boldsymbol{0}) = \mathrm{Var}\left(X\right)$ (see Papoulis & Pillai 1965 for a demonstration). Furthermore, it is customary to assume that the larger the lag $\boldsymbol{r}$ the less correlated the variables $X(\boldsymbol{y} + \boldsymbol{r})$ and $X(\boldsymbol{y})$ are. It follows that it is customary to assume that $C_X(\boldsymbol{r}) \to 0$ for $|\boldsymbol{y}| \to \infty$ and we will come back to this point later.

For a homogeneous field, the ACF thus measures the mean degree of correlation between all pairs of points as a function of their spatial separation, or lag. In one sense, the ACF is a statistical sieve which sifts through all possible pairs of points in order to extract lags for which correlations occur more often than by chance. *Therefore length scales for which statistically significant correlations exist are encoded in the ACF.* This statistical procedure allows the extraction of characteristic length scales of physical processes from data (see also Sec. 3.3.4).

2.4.6 Correlation coefficients

To generate a measure of how correlated two values of the field X are, a common procedure is to introduce the correlation coefficient at lag $\boldsymbol{y}$, $\tilde{C}_X(\boldsymbol{y})$ such that:

$$\tilde{C}_X(\boldsymbol{y}) = \frac{C_X(\boldsymbol{y})}{\mathrm{Var}\left(X\right)}. \tag{1.49}$$

This coefficient is then maximum at $\boldsymbol{y} = \mathbf{0}$ where it is equal to 1. The correlation coefficients can then be used as measures of the correlation of structures characterized by a lag $\boldsymbol{y}$.

2.4.7 Power spectrum

If the stochastic field is homogeneous, and *providing* that its ACF $C_X(\boldsymbol{r})$ is integrable, one can define its Fourier transform which is called the power-spectrum of X, $\mathcal{P}_X$:

$$\mathcal{P}_X(\boldsymbol{k}) = \int_{\mathbb{R}^3} C_X(\boldsymbol{r}) e^{-i\boldsymbol{k}\cdot\boldsymbol{r}} \mathrm{d}\,\boldsymbol{r}. \tag{1.50}$$

The condition of integrability is related to the property of mean ergodicity to be described later.

3 Ergodic theory

3.1 Motivation

Observations of astrophysical flows show that their main properties (velocity, column-density) exhibit large fluctuations. When studying these random fields, be it with observations or numerical simulations of star forming clouds, usually one has only access to a small number of samples (only one most of the time). Therefore, one makes the basic assumption, sometimes called "fair-sample hypothesis", that this sample is large enough so that volumetric (or time) averages provide accurate estimations of the statistics. As volumetric averages are used to describe the statistics, for this procedure to be meaningful, the stochastic field *must* be *statistically homogeneous and ergodic* (Papoulis & Pillai, 1965). Ergodic theory provides a framework to circumvent the problem of dealing with a single sample, and leads to a robust *measure of the accuracy of the determination of the statistics of a stochastic field.*

We rederive here some ergodic theorems that lead to the definition of the correlation length. Let us consider a (scalar) stochastic field $X(\boldsymbol{y})$, which depends on a D-dimensional position vector $\boldsymbol{y}$ ($D = 1$, 2 or 3). For a specific and fixed $\boldsymbol{y}$, $X(\boldsymbol{y})$ is a random variable for which we seek to determine accurate statistics.

3.2 Frequency interpretation and repeated trials

The usual way to estimate the *statistical average* or *expectation* $\mathbb{E}\left(X(\boldsymbol{y})\right)$ of random variable $X(\boldsymbol{y})$ is to observe N samples $X(\boldsymbol{y}, \omega_i)$, $1 \leq i \leq N$, of $X(\boldsymbol{y})$ and to build the following *unbiased* estimator:

$$\hat{X}_{\boldsymbol{y},N} = \frac{1}{N}\sum_{i=1}^{N} X(\boldsymbol{y}, \omega_i), \tag{1.51}$$

with variance

$$\mathrm{Var}(\hat{X}_{\boldsymbol{y},N}) = \sigma(\hat{X}_{\boldsymbol{y},N})^2 = \frac{\mathrm{Var}(X(\boldsymbol{y}))}{N} = \frac{\sigma(X(\boldsymbol{y}))^2}{N}, \tag{1.52}$$

where σ is the standard deviation (std). From the Bienayme-Tchebychev *inequality* (see Sec. 1.10), we know that, for any real number $m > 0$,

$$\mathbb{P}\left(|\hat{X}_{\boldsymbol{y},N} - \mathbb{E}\left(X(\boldsymbol{y})\right)| \leq m\,\sigma(\hat{X}_{\boldsymbol{y},N})\right) \geq 1 - \frac{1}{m^2}, \tag{1.53}$$

where $\mathbb{P}$ denotes the probability of an event. We note that this inequality is valid for *any* random field, which may be gaussian or not, and that it can be turned into an equality if the statistics are gaussian (changing the bound). Although the Bienayme-Tchebychev inequality provides a lower bound for the probability, it leads to a confidence interval allowing one to estimate the accuracy of the estimator given by Eq. (1.51). The larger the number of samples N, the smaller the std $\sigma(\hat{X}_{\boldsymbol{y},N})$ and the more accurate the estimate in Eq. (1.51) is.

3.3 Ergodic theorems. Autocovariance function. Correlation length

3.3.1 Ergodic theorems and the autocovariance function

In practice, one usually deals with only a *single* sample of $X(\boldsymbol{y})$. As mentioned above, one assumes statistical homogeneity and builds the following estimator:

$$\hat{X}_L = \frac{1}{L^D} \int_{[-\frac{L}{2},\frac{L}{2}]^D} X(\boldsymbol{y})\,\mathrm{d}\boldsymbol{y}, \tag{1.54}$$

where $\Omega = [-\frac{L}{2},\frac{L}{2}]^D$ is a control volume of linear size L and volume L^D, which is sought to be as large as possible[1]. The ergodic estimator $\hat{X}_L$ has variance:

$$\mathrm{Var}(\hat{X}_L) = \frac{1}{(L)^D} \int_{[-L,L]^D} C_X(\boldsymbol{y}) \prod_{k=1}^{D} \left(1 - \frac{|y_k|}{L}\right) \mathrm{d}\boldsymbol{y}, \tag{1.55}$$

where $C_X(\boldsymbol{y}) = \mathbb{E}\left(X(\boldsymbol{y}' + \boldsymbol{y})\,X(\boldsymbol{y}')\right) - \mathbb{E}\left(X\right)^2$ is the *auto-covariance function* (ACF) of X at lag $\boldsymbol{y}$ (see 2.2). The stochastic field X is said to be mean ergodic if the estimator $\hat{X}_L$ converges toward $\mathbb{E}\left(X\right)$ as $L \to \infty$ either in the mean square (MS) sense, which is written as:

$$\mathbb{E}\left(|\hat{X}_L - \mathbb{E}\left(X\right)|^2\right) = \mathrm{Var}(\hat{X}_L) \xrightarrow[L\to\infty]{} 0, \tag{1.56}$$

or in probability terms $\mathbb{P}\left(|\hat{X}_L - \mathbb{E}\left(X\right))| > \epsilon)\right) \to 0$ for all $\epsilon > 0$. The Bienayme-Tchebychev inequality (Eq. (1.53)) not only shows that if X is MS mean ergodic $\hat{X}_L$ converges in probability, but also provides a confidence interval for the estimate $\hat{X}_L$. Slutsky's theorem allows to write an equivalence for the ergodicity of X in a more convenient form. Thus, X is MS mean ergodic if and only if

$$\boxed{\frac{1}{(L)^D} \int_{[-L,L]^D} C_X(\boldsymbol{y})\mathrm{d}\boldsymbol{y} \xrightarrow[L\to\infty]{} 0.} \tag{1.57}$$

From this, one derives two sufficient (physical) conditions for X to be mean ergodic. Either:

$$\int_{[-\infty,\infty]^D} C_X(\boldsymbol{y})\mathrm{d}\boldsymbol{y} < \infty, \tag{1.58}$$

or

$$C_X(\boldsymbol{y}) \xrightarrow[|\boldsymbol{y}|\to\infty]{} 0. \tag{1.59}$$

We will assume that both conditions hold.

3.3.2 Correlation length

The correlation length $l_c(X)$ of field X is defined in terms of its ACF. The common and proper *definition of the correlation length* is (Papoulis & Pillai, 1965):

$$\boxed{(l_c(X))^D = \frac{1}{2^D\,C_X(\mathbf{0})} \int_{[-\infty,\infty]^D} C_X(\boldsymbol{y})\mathrm{d}\boldsymbol{y} = \frac{1}{2^D} \int_{[-\infty,\infty]^D} \tilde{C}_X(\boldsymbol{y})\mathrm{d}\boldsymbol{y},} \tag{1.60}$$

---

[1] The following calculations are made with a cubic control volume for the sake of simplicity. Calculations for a control volume of any shape may be found in App. (D)

where $\tilde{C}_X$ are the correlation coefficients. This definition generalizes the usual definitions for 1D fields:

$$l_c(X) = \frac{1}{C_X(\mathbf{0})}\int_{[0,+\infty[} C_X(y)\mathrm{d}y = \frac{1}{2\,C_X(\mathbf{0})}\int_{\mathbb{R}} C_X(y)\mathrm{d}y. \tag{1.61}$$

Then, for $l_c(X) \ll L$, one deduces from Eq (3.4) that:

$$\mathrm{Var}(\hat{X}_L) \simeq \mathrm{Var}(X)\left(\frac{2\,l_c(X)}{L}\right)^D = \mathrm{Var}(X)\left(\frac{l_c(X)}{R}\right)^D, \tag{1.62}$$

where $R = L/2$. If we compare Eq. (3.11) with Eq. (1.52), we see that instead of involving the number of samples, N, we now deal with ratio $(R/l_c)^D$, where R (or L) is usually an observationally accessible quantity. We can thus interpret ratio $(R/l_c)^D$ as an *effective number of "independent" samples.*

Furthermore, the correlation length is linked to the value of the power spectrum $\mathcal{P}_X(\boldsymbol{k})$ of X at $\boldsymbol{k} = \mathbf{0}$. One has indeed:

$$(l_c(X))^D \;=\; \frac{1}{2^D\,C_X(\mathbf{0})}\int_{[-\infty,\infty]^D} C_X(\boldsymbol{y})\mathrm{d}\boldsymbol{y} = \frac{1}{2^D\,C_X(\mathbf{0})}\mathcal{P}_X(\mathbf{0}). \tag{1.63}$$

3.3.3 Integral scale

In homogeneous and isotropic turbulence, one introduces a quantity similar to the correlation length called the integral scale noted l_i. This integral scale (not to be confused with the injection scale of the turbulence) is defined in a different but similar manner as the correlation length (Batchelor 1953)

$$l_\mathrm{i}(X) = \frac{1}{C_X(\mathbf{0})}\int_0^\infty C_X(r)\mathrm{d}r = \int_0^\infty \tilde{C}_X(r)\mathrm{d}r\,. \tag{1.64}$$

One finds that $l_c \simeq l_\mathrm{i}$ in many cases. Indeed, for an exponential ACF with $C_X(\boldsymbol{y}) = \mathrm{Var}(X)e^{-|\boldsymbol{y}|/l_\mathrm{i}}$, one has $l_c = l_\mathrm{i}$, $l_c = (\pi/2)^{1/2}\,l_\mathrm{i}$ and $l_c = \pi^{1/3}\,l_\mathrm{i}$ for $D = 1,\,2,\,3$, respectively, whereas for a Gaussian ACF ($C_X(\boldsymbol{y}) = \mathrm{Var}(X)e^{-|\boldsymbol{y}|^2/\lambda}$) $l_c = l_i$ for $D = 1,\,2,\,3$. Moreover, for $D = 3$ and for an ACF of the form $C_X(r) = \mathrm{Var}(X)(1 - (r/l_0)^p)$ for $r < l_0$ and then decaying rapidly, relevant for the study of turbulent flows, where typically $p = 2/3$, $l_c = 1.9 - 0.8\,l_\mathrm{i}$ for $p \in [0.2, \infty[$.

This integral scale then serves as a proxy for the correlation length.

3.3.4 Average size of most correlated structures

We now consider the $D = 3$ case. If the ACF of the ergodic field X is isotropic, the above equation for the integral scale $l_\mathrm{i}(X)$ can be used to define a weight function $W_l(r)$ that measures the correlation of structures of size r

$$W_l(r) = \frac{1}{l_\mathrm{i}(X)}\frac{C_X(r)}{\mathrm{Var}\,(X)} = \frac{\tilde{C}_X(r)}{l_\mathrm{i}(X)}. \tag{1.65}$$

This weight function can in general have negative values, but its integral over all possible sizes r is 1 by construction. Furthermore, if the ACF of X is positive, $W_l(r)$ can be further identified as a PDF of the size r of correlated structures. We can then build the *weighted* average of the size of correlated structures, $\langle l_w\rangle$, as :

$$\langle l_w\rangle = \int_0^\infty rW_l(r)\mathrm{d}r = \frac{1}{l_\mathrm{i}(X)}\int_0^\infty \tilde{C}_X(r)\,r\,\mathrm{d}r. \tag{1.66}$$

Then, as was the case for the integral scale, $l_\mathrm{i}(X)$, in many situations

$$\int_0^\infty \tilde{C}_X(r)\,r\,\mathrm{d}r \simeq l_c(X)^2, \tag{1.67}$$

which yields:

$$\boxed{\langle l_w \rangle \simeq \frac{l_c(X)^2}{l_{\mathrm{i}}(X)} \simeq l_c(X).} \tag{1.68}$$

Thus, $l_c(X)$ measures the average size of correlated structures, weighted by the correlation coefficients $\tilde{C}_X(r)$. We then call this average size *the average size of the most correlated structures*, in order to indicate that it is a weighted average.

This construction, which relies on the assumption of isotropy, serves to illustrate the physical meaning of $l_c(X)$. In the absence of that assumption, $l_c(X)$ is the only quantity that can be defined, but it can still be interpreted as a measure of the average size of the most correlated structures. This is in agreement with the picture obtained from Eq. (3.11) and Eq. (1.52), where the ratio $(R/l_c)^D$ is interpreted as an effective number of "independent" samples in the volume $V = (2R)^D$.

3.4 Estimates of the autocovariance function and correlation length

As shown in the previous section, the knowledge of the ACF of X (or of the value of the power spectrum of X at $\boldsymbol{k} = \boldsymbol{0}$) is of crucial importance to measure the relevance of a statistical approach in studies of the properties of large (astrophysical) systems. In practice, however, the ACF of X must be evaluated from data.

3.4.1 Reliability of the estimators of the auto-covariance and the power spectrum.

In most cases, data are drawn from a finite size sample so that the ACF is not reliable at large lag (large scales). To simplify the notation, we now introduce the variable $X_\mu = X - \mathbb{E}(X) = X - \mu$ and define the estimate, for a sample of size L,

$$\hat{C}_X^L(\boldsymbol{y}) = \frac{1}{\prod_i (L - |y_i|)} \iiint_{-R+\frac{|y_i|}{2}}^{R-\frac{|y_i|}{2}} X_\mu\left(\boldsymbol{u} - \frac{\boldsymbol{y}}{2}\right) X_\mu\left(\boldsymbol{u} + \frac{\boldsymbol{y}}{2}\right) \mathrm{d}\boldsymbol{u} \tag{1.69}$$

$$= \frac{1}{\prod_i (L - |y_i|)} \iiint_{-L+|y_i|}^{L-|y_i|} X_\mu\left(\frac{\boldsymbol{u} - \boldsymbol{y}}{2}\right) X_\mu\left(\frac{\boldsymbol{u} + \boldsymbol{y}}{2}\right) \frac{\mathrm{d}\boldsymbol{u}}{2^D}. \tag{1.70}$$

This is an unbiased estimate of $C_X(\boldsymbol{y})$ but its variance is increasing as $|y_i| \to L$ and eventually becomes very large due to poor sampling. We thus introduce the biased estimate

$$\hat{C}_{X,L}(\boldsymbol{y}) = \frac{\prod_i (L - |y_i|)}{L^D} \hat{C}_X^L(\boldsymbol{y}), \tag{1.71}$$

which is still a good estimate at small scales compared to L and has a reduced variance. We note however that it is an unbiased estimator of the quantity entering the integral in Eq. (3.4). Finally, it is also the Fourier Transform of the periodogram S_L which is defined as:

$$S_L(\boldsymbol{k}) = \frac{1}{L^D} \left| \int_{[-\frac{L}{2},\frac{L}{2}]^D} X(\boldsymbol{y}) e^{i\boldsymbol{k}\cdot\boldsymbol{y}} \mathrm{d}\boldsymbol{y} \right|^2. \tag{1.72}$$

It is the usual estimate of the power spectrum of X, $\mathcal{P}_X$. It is, however, a *biased* estimator of the power spectrum $\mathcal{P}_X$ and is only unbiased asymptotically, in the limit $L \to \infty$. Moreover, the variance of the estimator S_L does not vanish as $L \to \infty$ (Papoulis & Pillai, 1965), which makes it quite unreliable.

We thus see that, because of the finite size of the sample, one cannot obtain a reliable estimate of the ACF (or of the power spectrum) for all lag values. Furthermore, in many cases, the mean value of X is not known and is replaced in Eq. (1.70) by its estimate $\hat{X}_L = \hat{\mu}$, which introduces further, but reasonable, bias (see Papoulis & Pillai 1965 for a more complete discussion).

3.4.2 Periodic estimators

To get rid of the effect of finite sampling, one may perform simulations in periodic calculation boxes or may artificially add some periodicity to the available data to obtain the following estimate :

$$\hat{C}_{X,\mathrm{per}}(\boldsymbol{y}) = \frac{1}{L^D} \int_{[-\frac{L}{2},\frac{L}{2}]^D} \left(X_{\hat{\mu}}(\boldsymbol{y}+\boldsymbol{u})\, X_{\hat{\mu}}(\boldsymbol{u})\right) \mathrm{d}\boldsymbol{u}, \tag{1.73}$$

where one makes the identification $X_{\hat{\mu}}(\boldsymbol{y}+\boldsymbol{n}L) = X_{\hat{\mu}}(\boldsymbol{y})$. However, in such cases, the spatial average of the estimated ACF is necessarily 0. Indeed

$$\int_{[-\frac{L}{2},\frac{L}{2}]^D} \frac{\hat{C}_{X,\mathrm{per}}(\boldsymbol{y})}{L^D} \mathrm{d}\,\boldsymbol{y} = \int_{([-\frac{L}{2},\frac{L}{2}]^D)^2} \frac{\left(X_{\hat{\mu}}(\boldsymbol{y}+\boldsymbol{u})\, X_{\hat{\mu}}(\boldsymbol{u})\right)}{L^{2D}} \mathrm{d}\boldsymbol{u}\, \mathrm{d}\boldsymbol{y} = \left(\int_{[-\frac{L}{2},\frac{L}{2}]^D} \frac{X_{\hat{\mu}}(\boldsymbol{u})}{L^D} \mathrm{d}\boldsymbol{u} \right)^2 = 0, \tag{1.74}$$

due to the assumption that $X_{\hat{\mu}}$ is periodic.

Therein lies a significant problem: as the correlation length is defined as an integral over all possible lags, it is not easy to evaluate the reliability of estimates that are obtained in this manner. We refer to Chapter **2** and **3** for methods used to obtain reliable estimates of $l_c(X)$ in astrophysical conditions.

3.5 Concluding remark

The results of ergodic theory derived above allows one to define under which conditions volumetric averages correspond to statistical averages and provide a confidence interval for the estimate $\hat{X}_L$ of the expectation of X. However, these results rely on the knowledge of the statistical properties of X and most precisely of its ACF, which is in general not known. To apply this theory to the study of a real field, such as the density field for example, one *must use ergodicity as an assumption.* The above results can then be used to test the validity of this assumption and the accuracy of the estimates that are derived from it.

Coupled to the results of the two previous Sec. 1 and 2, this section give a set of tools to describes and study the apparently disorganized structures of astrophysical flows. These results will be used extensively throughout this thesis.

4 Observations

In order to test theoretical models of natural phenomena and to determine constraints on them, one may use two types of data, which are associated with different difficulties and limitations: direct measurements and results of numerical simulations. In this section, we discuss properties of the interstellar medium that are revealed by the radiations received on Earth. We outline some of the information that can be inferred from measurements of *electromagnetic* radiations.

4.1 Elements of radiative transfer

4.1.1 Specific intensity

To characterize the (electromagnetic) radiation, one introduces the quantity I_ν called specific intensity (or spectral radiance). This intensity is defined from the energy flux $\mathrm{d}\phi_\nu$ through an elementary area $\mathrm{d}S$ and normal $\boldsymbol{n}$ at position $\boldsymbol{x}$, in the solid angle $\mathrm{d}\Omega$ about the direction $\boldsymbol{u}_\Omega$ in the frequency interval $[\nu, \nu + \mathrm{d}\nu[$ at time t, as:

$$\mathrm{d}\phi_\nu = I_\nu(\boldsymbol{x}, t, \boldsymbol{u})(\boldsymbol{u}_\Omega \cdot \boldsymbol{n})\,\mathrm{d}S\,\mathrm{d}\Omega\,\mathrm{d}\nu = I_\nu(\boldsymbol{x}, t, \boldsymbol{u}_\Omega)\cos(\theta)\,\mathrm{d}S\,\mathrm{d}\Omega\,\mathrm{d}\nu, \tag{1.75}$$

where $\cos(\theta) = (\boldsymbol{u}_\Omega \cdot \boldsymbol{n})$ is a term that accounts for the projection of the surface element in direction $\boldsymbol{u}_\Omega$. In the international system of units, the specific intensity has thus for units W m^{-2} sr^{-1} Hz^{-1}. If the radiation propagates freely, this quantity is conserved and the transport equation for I_ν is:

$$\frac{1}{c}\frac{\partial I_\nu}{\partial t} + (\boldsymbol{u}_\Omega \cdot \boldsymbol{\nabla})\, I_\nu = 0, \tag{1.76}$$

where c is the speed of light. However I_ν is not conserved when the radiation propagates through natural media due to interactions with the constituents of matter .

4.1.2 Equation for radiative transport

In material media, emission or absorption of radiation by the constituents of matter modify the transport equation of I_ν. In its more general form this is written as follows:

$$\frac{1}{c}\frac{\partial I_\nu}{\partial t} + (\boldsymbol{u}_\Omega \cdot \boldsymbol{\nabla})\, I_\nu = \Sigma_\nu - \Pi_\nu, \tag{1.77}$$

where Σ_ν and Π_ν are respectively source and destruction terms that need to be modeled from the physics of the light-matter interactions. The source term Σ_ν accounts for the emission of radiation by the matter constituents and the scattering of light on matter changing the propagation direction of of photons from some direction $\boldsymbol{u}'$ to $\boldsymbol{u}_\Omega$. The destruction term accounts for the absorption of light by matter constituents and again for the scattering of light on matter that modifies the propagation direction of photons, but this time from $\boldsymbol{u}_\Omega$ to some other $\boldsymbol{u}'$. Including all these terms leads to the following contracted equation:

$$\frac{1}{c}\frac{\partial I_\nu}{\partial t} + (\boldsymbol{u}_\Omega \cdot \boldsymbol{\nabla})\, I_\nu = \kappa_\nu\,(S_\nu - I_\nu)\,, \tag{1.78}$$

or, in terms of curvilinear coordinate s along the photon trajectory:

$$\frac{\mathrm{d}I_\nu}{\mathrm{d}s} = \kappa_\nu\,(S_\nu - I_\nu)\,, \tag{1.79}$$

where $\kappa_\nu = \rho_{\mathrm{matter}}(\kappa_\nu^{\mathrm{s}} + \kappa_\nu^{\mathrm{a}})$ is the total opacity coefficient per unit volume and where κ_ν^{s} and κ_ν^{a} are respectively the scattering and absorption cross sections per unit mass, also called opacities, and ρ_{matter}

is the density of matter.

An important property of Eq. (1.79) is that κ_ν is proportional to ρ_{matter}, a point to which we will come back later. Naturally, when $\rho_{\mathrm{matter}} \to 0$, Eq. (1.79) becomes the free transport equation Eq. (1.76).

4.1.3 Formal solution

A formal solution to Eq. (1.79) can be found by introducing the optical thickness at frequency ν, noted τ_ν, defined by :

$$\tau_\nu(\boldsymbol{x}, \boldsymbol{x_0}, \boldsymbol{u}_\Omega) = \int_{s_0(\boldsymbol{x_0}, \boldsymbol{u}_\Omega)}^{s(\boldsymbol{x}, \boldsymbol{u}_\Omega)} \kappa_\nu \mathrm{d}s, \tag{1.80}$$

where $s_0(\boldsymbol{x_0}, \boldsymbol{u}_\Omega)$ is some origin of the curvilinear coordinate s and $s(\boldsymbol{x}, \boldsymbol{u}_\Omega)$ this coordinate at point $\boldsymbol{x}$ (the term $\boldsymbol{u}_\Omega$ serves as a reminder of the direction in which the radiation propagates). A common choice is to choose $s_0 = 0$ at the far end of the medium considered. Eq. (1.79) can then be formally solved to give:

$$I_\nu(\boldsymbol{x}, \boldsymbol{u}_\Omega) = I_\nu(\boldsymbol{x}_0, \boldsymbol{u}_\Omega)\mathrm{exp}\left(-\tau_\nu(\boldsymbol{x}, \boldsymbol{x_0}, \boldsymbol{u}_\Omega)\right) + \int_0^s S_\nu(\boldsymbol{x'}, \boldsymbol{u}_\Omega) \exp\big(-\tau_\nu(\boldsymbol{x'}, \boldsymbol{x_0}, \boldsymbol{u}_\Omega)\big)\, \kappa_\nu(\boldsymbol{x'})\, \mathrm{d}s', \tag{1.81}$$

where $\boldsymbol{x_0}$ is the point of entry of the radiation into the medium.

4.1.4 Planck's law

At thermodynamic equilibrium (at temperature T), the specific intensity is given by Planck's function :

$$I_\nu = B_\nu(T) = \frac{2\,h\,\nu^3}{c^2}\frac{1}{\exp(h\nu/k_\mathrm{B}T) - 1}, \tag{1.82}$$

for all ν and where h is Planck's constant and k_B is Boltzmann's constant. There are two limiting forms of Planck's law at large and small values of the ratio $h\nu/k_\mathrm{B}T$. At large wavelengths λ (typically the case in radio astronomy, $\lambda \geq 1$ mm), i.e., at short frequencies $h\nu/k_\mathrm{B}T \ll 1$, Planck's law reduces to Rayleigh-Jeans law :

$$B_\nu(T) \simeq \frac{2\,h\,\nu^3}{c^2}\frac{k_\mathrm{B}T}{h\nu} = \frac{2k_\mathrm{B}T}{\lambda^2}. \tag{1.83}$$

Conversely, in the limit of high frequencies $h\nu/k_\mathrm{B}T \gg 1$, Planck's law reduces to Wien's law:

$$B_\nu(T) \simeq \frac{2\,h\,\nu^3}{c^2}\exp(-h\nu/k_\mathrm{B}T). \tag{1.84}$$

4.1.5 Various definitions of temperature

In general, out of thermodynamic equilibrium, $I_\nu \neq B_\nu(T)$ (depending on ν) for some T. However, one can define the *brightness temperature* $T_\mathrm{b}(\nu)$ as the temperature at which a black body in thermal equilibrium would have to be in order to produce the same specific intensity at frequency ν:

$$I_\nu = B_\nu(T_\mathrm{b}(\nu)). \tag{1.85}$$

The brightness temperature is thus, in general, a function of the frequency.

Likewise, one defines the *excitation temperature* $T_\mathrm{ex}(\nu)$ as the temperature to plug in Planck's function B_ν to make it equal to the source function of the medium:

$$S_\nu = B_\nu(T_\mathrm{ex}(\nu)). \tag{1.86}$$

In fact, the excitation temperature is the temperature characterizing the ratio of energy level populations of the various species studied.

At thermodynamic equilibrium, both temperatures are equivalent.

4.2 Spectral lines

A spectral line is a dark or bright narrow band in an otherwise uniform and continuous electromagnetic spectrum. Spectral lines are the result of the interaction between the atoms or molecules of a material medium and electromagnetic radiation. They are therefore the "fingerprints" of atoms and molecules and are used to identify the constituents of a medium.

Even though a spectral line corresponds to a specific frequency (ν_0) corresponding to the difference of quantified energy states of a molecule or atom, it is not infinitely thin. Indeed, if only from the point of view of quantum mechanics, the Heisenberg principle imposes that spectral lines have finite widths with lorentzian profiles. In the interstellar medium and in molecular clouds, the atoms and molecules constituting the medium have different velocities, due to either thermal agitation or turbulent motions. As a result of the Doppler effect, the frequencies at which photons are emitted or absorbed can vary slightly. In case of thermal agitation, the velocity are distributed with a centered gaussian distribution. In the non relativistic case, the Doppler shift is proportional to the velocity, implying that the observed spectral line also have a gaussian distribution, centered on the frequency at rest ν_0:

$$\phi(\nu) = \frac{1}{\sqrt{2\pi}\sigma_\mathrm{D}} \exp\left(-\frac{(\nu-\nu_0)^2}{2\sigma_\mathrm{D}^2}\right), \quad \text{with} \quad \sigma_\mathrm{D} = \frac{\nu_0}{c}\sqrt{\frac{k_\mathrm{B}T}{m}}, \tag{1.87}$$

where σ_D is the Doppler line-width. In the presence of turbulent motion, line-widths can be considerably larger than the thermal Doppler values. In these cases, the line profile may not necessarily be gaussian but one usually assumes that it is symmetric, as the gaussian and lorentzian profiles are.

4.3 Extinction

Extinction is a phenomenon that has long been known to astronomers and is linked to the absorption and scattering of electromagnetic radiation by dust and gas along the line of sight, between an emitting astronomical object and the observer. Its effects on measurements with visible light is to mask the stars behind the absorbing dust and gas so that the portion of sky observed appears dark and starless.

In many instances, background starlight is only extinct for visible wave-lengths and can be observed at higher wave-lengths. The spectra of background stars thus appear redder, a phenomenon referred to as interstellar reddening.This is a different phenomenon from the Doppler red-shift as it mostly affects low wave-lengths and leaves red wave-lengths almost unchanged.

4.3.1 Magnitude

To describe and quantify the luminosity of stellar objects, astronomers have introduced a quantity called apparent magnitude at frequency ν, m_ν^*, which is a logarithmic quantity. For a star emitting a *total* intensity L_ν (in 4π steradians), the *absolute* magnitude is $M_\nu^* = -2.5\log_{10}(L_\nu/L_0)$ for some reference intensity L_0 fixed by astronomers. This scale is defined so that the brighter objects are of smaller magnitudes. This is in keeping with the vocabulary of ancient Greek astronomers who called the brightest objects, objects of the first magnitude. The apparent magnitude m_ν^* is the portion of the *absolute* magnitude M_ν^* emitted in the solid angle about the direction of the observer and is thus related to the specific intensity: $m_\nu^* = -2.5\log_{10}(I_\nu/I_0)$.

4.3.2 The quantity extinction

In order to measure and quantify the extinction phenomenon, astronomers have defined the (physical) quantity extinction at frequency ν, A_ν, as follows:

$$A_\nu \equiv m_{\mathrm{obs},\nu} - m^*_\nu, \tag{1.88}$$

where $m_{\mathrm{obs},\nu}$ is the observed magnitude, which is supposedly higher (lower intensity) for larger extinctions. Thus, using Eq. (1.81) and assuming that the source term on the r.h.s can be neglected, one gets

$$\boxed{A_\nu \simeq \tau_\nu = \int_0^{L_{\mathrm{l.o.s}}} \kappa_\nu \mathrm{d}s = \int_0^{L_{\mathrm{l.o.s}}} \rho_{\mathrm{matter}}(\kappa^{\mathrm{s}}_\nu + \kappa^{\mathrm{a}}_\nu)\mathrm{d}s = (\kappa^{\mathrm{s}}_\nu + \kappa^{\mathrm{a}}_\nu) \int_0^{L_{\mathrm{l.o.s}}} \rho_{\mathrm{matter}}\mathrm{d}s,} \tag{1.89}$$

where $L_{\mathrm{l.o.s}}$ it the thickness of the material medium along the line of sight. The extinction A_ν is thus related to the integral of the density of matter that is scattering and absorbing light at frequency ν along the line of sight. This quantity is termed the column density Σ and is an important quantity because it is a tracer of the underlying density field.

4.4 Molecular lines

Another way of gathering information on a material medium is to look at specific spectral lines corresponding to some particular molecule. These are referred to as molecular lines. Two commonly used molecular lines correspond to the rotational transitions ($J : 1 \leftrightarrow 0$) of the ^{12}CO and ^{13}CO molecules. Laboratory measurements have established that these transitions occur at radio frequencies $\nu(^{12}\mathrm{CO}) = 115.27$ GHz and $\nu(^{13}\mathrm{CO}) = 110.20$ GHz.

An important feature of the ^{13}CO molecule is that its abundance in astrophysical clouds (mostly made of hydrogen) is very low. For example, compared to the ^{12}CO molecule, taking the ratio of natural abondance on Earth of carbon isotopes yields $X(^{12}\mathrm{CO})/X(^{13}\mathrm{CO}) \simeq 100$. Hence the ^{13}CO line has a great chance of being optically thin, implying that its optical depth $\tau_\nu \ll 1$, because of the relatively low $\rho(^{13}\mathrm{CO})$ value entering the definition of κ_ν and τ_ν.

Following the derivation of Dickman & Kleiner (1985), one can then compute, using the solution of the radiative transfer equation Eq. (1.81) in the optically thin limit and assuming uniform excitation, the brightness temperatures of the relevant molecular lines. From the first two moments of these brightness temperatures, one obtains estimates of the column density Σ and the centroid velocity v_c:

$$\boxed{\begin{aligned} \Sigma(x,y) &= \int_{\mathrm{los}(x,y)} \rho(x,y,z)\,\mathrm{d}z & (1.90)\\ v_c(x,y) &= \int_{\mathrm{los}(x,y)} \rho(x,y,z)v(x,y,z)\,\mathrm{d}z & (1.91)\end{aligned}}$$

which are integrals are calculated along the line of sight ($\mathrm{los}(x,y)$) of the density field $\rho(\boldsymbol{x})$ and velocity projected on the line of sight $v(\boldsymbol{x})$.

4.5 Dust emission

Recent observations of the Gould Belt, the nearest cloud complexes in the Galaxy, a giant (~ 700 pc $\times$ 1000 pc), flat structure inclined by $\sim 20°$ to the Galactic plane by the Herschel survey (André et al., 2010), yield determinations of dust emission and statistics with the best spatial resolution. The Herschel survey was designed to probe the densest portions of the Gould Belt with two instruments named SPIRE and PACS in the $250 - 500$ μm and $100 - 160$ μm wavelength bands.

Observed specific intensity values I_ν are fitted, assuming single-temperature dust emission T_d, by a grey-body function of the following form :

$$\boxed{I_\nu = B_\nu(T_d)(1 - e^{-\tau_\nu}),} \tag{1.92}$$

where $\tau_\nu = \Sigma\tilde{\kappa}_\nu$ is the dust optical depth, Σ the column density, and $\tilde{\kappa}_\nu$ is the dust opacity per unit (dust+gas) mass. Assuming that opacity values are known, the dust temperature T_d and column density Σ can be obtained from a grey body fit to the various frequencies measured by Herschel (Könyves et al., 2010).

5 Numerical simulations

Numerical solutions of the governing field equations generate results that can be analyzed using the same statistical tools but one must pay attention to resolution in both space and time as well as to the finite size of the computational domain. To understand how gravity affects the density ρ and column density Σ PDFs in star forming clouds and compare numerical results to the theoretical predictions of this thesis, we shall use a series of numerical simulations by Federrath & Klessen (2012, 2013), kindly provided by the authors. These numerical experiments are perfectly suited to the study of molecular clouds. They are presented in this section.

5.1 Numerical set up of Federrath & Klessen (2012)

The numerical simulations of Federrath & Klessen (2012, 2013) use an adaptive mesh refinement method (AMR; Berger & Colella 1989) code FLASH[2] (Fryxell et al. 2000) in version 2.5 to integrate the ideal, three-dimensional, MHD equations, including self-gravity. They deal with isothermal self-gravitating magneto-hydrodynamic turbulence on 3D periodic grids (topology $\mathbb{T}^3$) with resolution $N_{\mathrm{res}}^3 = 128^3$ to 1024^3. They are all uniform-grid simulations save for $N_{\mathrm{res}} = 1024$ cases. In the latter, a root grid with $N_{\mathrm{res}} = 512$ is used in addition of one level of the AMR method with a refinement criterion to ensure that there are at least 32 grid cells across the local Jeans length scale. This allows resolution of the turbulent vorticity and magnetic-field amplification at the Jeans scale.

In this study, we will mostly consider simulations with no magnetic field, keeping only two magnetic simulations. In each simulation, one starts with fully developed turbulent conditions at $t = 0$ and then adds gravity. The associated transport equations are as follows:

$$\frac{\partial \rho}{\partial t} + \boldsymbol{\nabla}\cdot(\rho \boldsymbol{v}) = 0, \tag{1.93}$$

$$\rho\left(\frac{\partial \boldsymbol{v}}{\partial t} + (\boldsymbol{v}\cdot\boldsymbol{\nabla})\,\boldsymbol{v}\right) = -\boldsymbol{\nabla}\left(P + \frac{1}{8\pi}\boldsymbol{\nabla}|\boldsymbol{B}|^2\right) + \rho\,\boldsymbol{\mathcal{G}}\Theta(t) + \frac{(\boldsymbol{B}\cdot\boldsymbol{\nabla})\,\boldsymbol{B}}{4\pi} + \rho\boldsymbol{F}_{\mathrm{stir}}, \tag{1.94}$$

$$\frac{\partial \boldsymbol{B}}{\partial t} = -\boldsymbol{\nabla}\times(\boldsymbol{v}\times\boldsymbol{B}), \tag{1.95}$$

$$\boldsymbol{\nabla}\cdot\boldsymbol{B} = 0, \tag{1.96}$$

$$\boldsymbol{\nabla}\times\boldsymbol{\mathcal{G}} = \boldsymbol{0}, \tag{1.97}$$

$$\boldsymbol{\nabla}\cdot\boldsymbol{\mathcal{G}} = -4\pi G(\rho - \rho_0), \tag{1.98}$$

$$P = c_s^2\rho \tag{1.99}$$

where ρ, P and $\boldsymbol{v}$ are the density, pressure and velocity of the gas, respectively, and $\boldsymbol{B}$ and $\boldsymbol{\mathcal{G}}$ denote the magnetic and gravitational fields. G is the universal gravitational constant. $\rho_0 \equiv \overline{\rho}$ is the constant averaged density of the computational domain, c_{s} is the sound speed (equal to 0.2 km.s^{-1}) and $\boldsymbol{F}_{\mathrm{stir}}$ is a turbulent forcing term. Finally, $\Theta(t)$ is the Heaviside step function ensuring that gravity kicks in at

---

[2] http://flash.uchicago.edu/site/flashcode/

$t = 0$. The last term in the parenthesis on the right hand side of Poisson's equation, Eq. (1.98), comes from the numerical Poisson solver that relies on periodic boundary conditions (Ricker, 2008; Guillet & Teyssier, 2011). This well known feature of statistical mechanics in Coulomb systems is due to the ill-posed problem of the standard Poisson formulation in $\mathbb{T}^3$. More details on the numerical methods used to solve the above equations can be found in Federrath & Klessen (2012).

Each simulation corresponds to a fixed initial Mach number $\mathcal{M} = \sigma_v / c_\mathrm{s}$, where σ_v is the root mean square (rms) velocity and B_0 is some fixed initial magnetic field. The Mach number and magnetic field strength are used to identify each simulation, as shown in Table 1.

5.2 Turbulent forcing

These simulations use "driven turbulence in a box" to draw statistical conclusions on the role of turbulence for star formation. They are not meant to account for potential astrophysical drivers of turbulence, whose statistical properties are poorly known. This turbulent forcing approach allows us to evaluate the role of the various velocity modes that get excited by a physical driver.

In practice, the turbulent forcing term $\boldsymbol{F}_\mathrm{stir}$ is applied as a source term. It only contains large-scale modes, $1 < k < 3$, and most of the power is injected at the $k = 2$ mode in Fourier space, which corresponds to half of the size of the computational domain in physical space, noted L. Without going into details on how this forcing is implemented, it is worth emphasizing that the key advantage of this forcing approach is that one can vary the proportions of solenoidal and compressive modes in $\boldsymbol{F}_\mathrm{stir}$. This is achieved through a decomposition of vector fields with random mixtures into its solenoidal and compressive components. In this manner, turbulence is driven by solenoidal ($\boldsymbol{\nabla}\cdot\boldsymbol{F}_\mathrm{stir} = 0$) or compressive ($\boldsymbol{\nabla}\times\boldsymbol{F}_\mathrm{stir} = \boldsymbol{0}$) forcing terms or by a combination of both (see Federrath et al. 2010; Federrath & Klessen 2012 for a more complete description). The ratio between compressive and solenoidal modes is usually described by prefactor b in front of the Mach number, $b\mathcal{M}$, in the density variance-velocity relation for isothermal turbulence: $\sigma_\rho^2 = \overline{\rho}^2 (b\mathcal{M})^2$ (Federrath et al., 2008).

5.3 Handling high density regions: sink particles

In order to properly describe cloud dynamics in high density regions, *without having to increase resolution* and/or *without having to reduce the integration time step by large amounts*, a subgrid contraption called "sink particles" is used. Sink particles account for the collapse and accretion of dense star-forming gas and are only allowed once gravity has been added, i.e. at $t > 0$. One important point is that sink particles are formed in the densest regions of a domain. As will be seen in the next section, the dynamics and statistics of the density field at such high densities are not well resolved (and hence the introduction of sink particles). Therefore, we only use these simulations to study the behavior of the density field at lower densities and do not pay attention to sink particles. For this reason, there is no need to describe in detail the algorithm behind the subgrid model and refer to Federrath & Klessen (2012).

5.4 List of models and general evolution of the simulations

The simulations start from initial turbulent conditions which display a density field ρ with a lognormal PDF (i.e the PDF of $s = \ln(\rho/\rho_0)$ is gaussian). Our aim is to follow changes of the density field statistics, as well as those of the column densities, and hence of their PDF. In order to be consistent with the authors, we describe the time evolution of the simulations by means of the reduced time $\tilde{t} = t/\tau_{\mathrm{ff},0}$, which is the time in units of the mean free fall time $\tau_{\mathrm{ff},0} \equiv \sqrt{\frac{3\pi}{32 G \rho_0}}$, and by means of the star formation efficiency (SFE), which is set at 0% at the formation of the first sink particle. The authors only determined the various PDFs of their results up to SFE= 20% which we will refer to as the "ong time" of the numerical runs.

TABLE 1 Parameters of the simulations of Federrath & Klessen (2012, 2013) used in this study

Model (GT) (1)	$N_{\rm res}$ (2)	Forcing (3)	ρ_0(g/cc) (4)	$L_{\rm b}$ (pc) (5)	$\mathcal{M}$ (6)	$\alpha_{\rm vir,0}$ (7)	b (8)	$\mathcal{M}_A$ (9)	B_0 (μG) (10)
256sM3	256	sol	$5.8\,10^{-19}$	0.33	$2-3$	0.07	1/3	∞	0
256mM3	256	mix	–	0.33	$2-3$	0.08	0.4	∞	0
512sM3	512	sol	–	0.33	$2-3$	0.07	1/3	∞	0
512cM3	512	comp	–	0.33	$2-3$	0.07	1	∞	0
256sM5	256	sol	$3.3\,10^{-21}$	2.0	5	1.0	1/3	∞	0
256mM5	256	mix	–	2.0	5	1.0	0.4	∞	0
256sM10	256	sol	$8.8\,10^{-22}$	8.0	10	1.1	1/3	∞	0
512mM10	512	mix	–	8.0	10	1.1	0.4	∞	0
512sM10	512	sol	–	8.0	10	1.1	1/3	∞	0
512mM10B1	512	mix	–	8.0	10	0.97	0.4	13	1
512mM10B3	512	mix	–	8.0	10	0.83	0.4	2.7	3
512cM50	512	comp	$3.3\,10^{-23}$	200	50	1	1	∞	0
1024cM50	1024	comp	–	200	50	1	1	∞	0

NOTE—Columns: (1) simulation name, (2) resolution $N_{\rm res}$, (3) forcing (solenoidal, mixed, compressive), (4-10) box size $L_{\rm b}$, Mach number $\mathcal{M}$, virial parameter $\alpha_{\rm vir,0}$, forcing parameter b, time averaged Alfvenic Mach number $\mathcal{M}_A$, initial magnetic field strength B_0.

In all cases, the Mach number $\mathcal{M}$ increases slightly with time due to regions that are collapsing. For most models, this only amounts to changes by a few percents, save for the $\mathcal{M}\simeq 3$ cases. The latter begin with $\mathcal{M}\simeq 2$ and end up with $\mathcal{M}\simeq 3-4$, due to the very small values of the virial parameter $\alpha_{\rm vir,0}=5\sigma_v^2/(6GL_{\rm b}^2\rho_0)$ (see Table 1). At late times, both the density and column density PDFs display large departures from gaussian statistics at high density values (see Fig. 1.1). More precisely, the PDFs display extended power-tails, a feature identified as being the signature of gravity.

Table 1 gives the subset of numerical models used in this study with their parameters. The Alfvenic Mach number $\mathcal{M}_A=\sigma_v/v_A$, where $v_A=|B|/\sqrt{4\pi\rho}$ and $|B|$ is the average strength of the magnetic field, is used to characterize the amplitude of the magnetic field in the simulations. v_A is the Alfven velocity (Alfvén, 1942).

5.5 Resolution and limits for resolving the PDFs

Truelove et al. (1997) have shown that the resolution Δx in a domain with density ρ must be at least 4 times smaller than the Jeans length to avoid artificial fragmentation. Thus:

$$\Delta x \leq \frac{1}{4}\sqrt{\frac{\pi c_{\rm s}^2}{G\rho}}. \tag{1.100}$$

In turn, this gives the density $\rho_{\rm max}$ above which collapse is not resolved and simulations do not properly describe cloud statistics:

$$\rho_{\rm max}=\rho_0\, e^{s_{\rm max}}=\frac{\pi c_{\rm s}^2}{16G\Delta x_{\rm min}^2}, \tag{1.101}$$

where $\Delta x_{\rm min}$ is the size of the best resolved cell. Thus, the effects of gravity on density PDFs can only

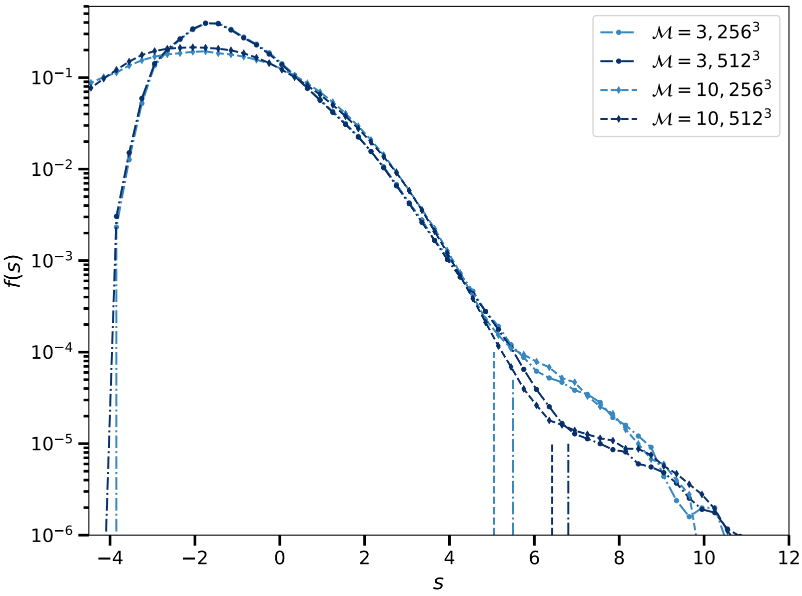

FIGURE 1.1 s-PDF for solenoidal simulations with $\mathcal{M} \sim 3$ (dash-dotted lines with circles) and $\mathcal{M} = 10$ (dashed lines with diamonds) for resolutions increasing from 256^3 to 512^3 (from light to dark blue lines). Shallow power-laws develop for $s \geq s_{\max}$ according to the Truelove criterion, corresponding to the vertical lines with the same color and line coding).

be properly studied for densities $s < s_{\max}$. We can recast Eq. (1.101) as follows:

$$\boxed{s_{\max} = \ln\left(\alpha_{\mathrm{vir},0}\right) + 2\ln\left(\frac{N_{res}}{\mathcal{M}}\right) + \ln\left(\frac{6\pi}{80}\right),}$$

Therefore, at fixed $\alpha_{\mathrm{vir},0}$, resolution must be increased as a function of the Mach number $\mathcal{M}$ to properly capture the effects of gravity on high density regions.

Regions denser than $s_{\max}$ will fragment artificially, and hence one expects to observe an excess of regions with density $s \sim s_{\max}$. Fig. 1.1 illustrates such behaviour for solenoidal simulations at $\mathcal{M} \sim 3$ and $\mathcal{M} = 10$ with resolution increasing from 256^3 to 512^3. Above $s_{\max}$, we observe the development of shallow power-laws corresponding to the artificial fragmentation of regions with $s > s_{\max}$. These power-laws develop for increasing density values with increasing numerical resolution, according to Eq. (1.101). In contrast, for densities $s < s_{\max}$, PDF calculations seem to have converged satisfactorily. Note that the resolution-dependent transition to these shallow power-laws has already been discussed by Federrath & Klessen (2013).

5.6 Concluding summary

In Sec. 4 and 5 we gave an outline of the two different types of tools useful to test theoretical models of natural phenomena and to determine constraints on them. Properties and limitation of the obtained data from either direct measurements or results of numerical simulations were presented.

From observations of specified spectral lines, observational data yield the measure of either the r.m.s thermal or turbulent velocity. Moreover from the measure of either absorption or emission of dust particles, observations measure of the column density and centroid velocity maps which are the integral of the density and velocity field along the line of sight.

Numerical experiments allow to draw statistical conclusions on the role of turbulence for star formation and to evaluate the role of the various velocity modes that get excited by physical drivers of turbulence. They however are limited due to the resolution in both space and time as well as to the finite size of the computational domain.

The present overview was made because these two types of data will be used throughout this thesis to test our theoretical models.

Appendix

A Ergodic estimate for a general control volume Ω.

We described in Sec. (2) some known ergodic results, but they are derived for a cubic control volume $\Omega = [-\frac{L}{2}, \frac{L}{2}]^D$. These results obviously do not depend on the shape of the control volume. We give here the general formulation for any control volume Ω possessing a center of symmetry (such that $\forall \boldsymbol{y} \in \Omega$, $-\boldsymbol{y} \in \Omega$). We again denote by $|\Omega|$ the volume of Ω and define the linear size of Ω as $L^D = |\Omega|$. The ergodic estimate Eq. (3.3) is then

$$\hat{X}_\Omega = \frac{1}{|\Omega|} \int_\Omega X(\boldsymbol{y})\, \mathrm{d}\boldsymbol{y}. \tag{1.102}$$

To obtain its variance, one has to compute the double integral

$$\begin{aligned} \mathrm{Var}\left(\hat{X}_\Omega\right) &= \frac{1}{|\Omega|^2} \iint_{\Omega^2} \mathbb{E}\left(X(\boldsymbol{y})\, X(\boldsymbol{z}) - \mathbb{E}\left(X\right)^2\right) \mathrm{d}\boldsymbol{y}\, \mathrm{d}\boldsymbol{z} \\ &= \frac{1}{|\Omega|^2} \iint_{\Omega^2} C_X(\boldsymbol{y}-\boldsymbol{z})\, \mathrm{d}\boldsymbol{y}\, \mathrm{d}\boldsymbol{z}. \end{aligned} \tag{1.103}$$

Using the change of variables $(\boldsymbol{u}, \boldsymbol{v}) = \varphi(\boldsymbol{y}, \boldsymbol{z}) = (\boldsymbol{y}-\boldsymbol{z}, \boldsymbol{y}+\boldsymbol{z})$, one obtain

$$\mathrm{Var}\left(\hat{X}_\Omega\right) = \frac{1}{|\Omega|^2} \int_{2\,\Omega} C_X(\boldsymbol{u}) \int_{\varphi_2^{\boldsymbol{u}}(\Omega)} \frac{\mathrm{d}\boldsymbol{u}\, \mathrm{d}\boldsymbol{v}}{2^D} \tag{1.104}$$

where

$$\varphi_2^{\boldsymbol{u}}(\Omega) = 2\left((\Omega - \boldsymbol{u}) \cap \Omega\right) + \boldsymbol{u} \tag{1.105}$$

to obtain

$$\mathrm{Var}\left(\hat{X}_\Omega\right) = \frac{1}{|\Omega|} \int_{2\,\Omega} C_X(\boldsymbol{u}) \frac{|(\Omega - \boldsymbol{u}) \cap \Omega|}{|\Omega|}\, \mathrm{d}\boldsymbol{u}. \tag{1.106}$$

We then obtain the general Slutsky's theorem, X is mean ergodic if and only if

$$\frac{1}{L^D} \int_{2\,\Omega} C_X(\boldsymbol{u})\, \mathrm{d}\boldsymbol{u} \xrightarrow[L\to\infty]{} 0. \tag{1.107}$$

Chapter

2 Column densities as tracers of the underlying density field: the link with observation

Contents

1 Motivation

We now turn to observations of star-forming molecular clouds. Measurements provide values of the column-density $\Sigma(x, y)$, which is the integral of density along the line of sight ($\mathrm{los}(x, y)$):

$$\begin{aligned}\Sigma(x,y) &= \int_{\mathrm{los}(x,y)} \rho(x,y,z)\,\mathrm{d}z \\ &= \mathbb{E}\left(\rho\right) l(x,y) + \int_{\mathrm{los}(x,y)} \delta\rho(x,y,z)\,\mathrm{d}z, \qquad (2.1)\end{aligned}$$

where $l(x, y)$ is the thickness of the cloud along the line of sight at (x, y) and $\delta\rho = \rho - \mathbb{E}(\rho)$ is the density fluctuation. Column densities are the only data that depend directly on the density field and one must determine how to retrieve reliable information from them.

This chapter is organized as follows. In Sec. 2, we study potential statistical biases introduced by integration along the line of sight and the relation between the auto covariance functions (ACF) and the correlation lengths of Σ and ρ (see Chap. **1**). In Sec. 3, we focus mainly on methods to reconstruct density PDFs from measurements of column-density PDFs.

2 One and two point statistics.

In this section, we study the statistical properties of the column-density field Σ using the assumption that the underlying density field ρ is statistically homogeneous. We focus on the statistical bias introduced by integration along the line of sight and on the relationship between the ACFs of the two fields Σ and ρ.

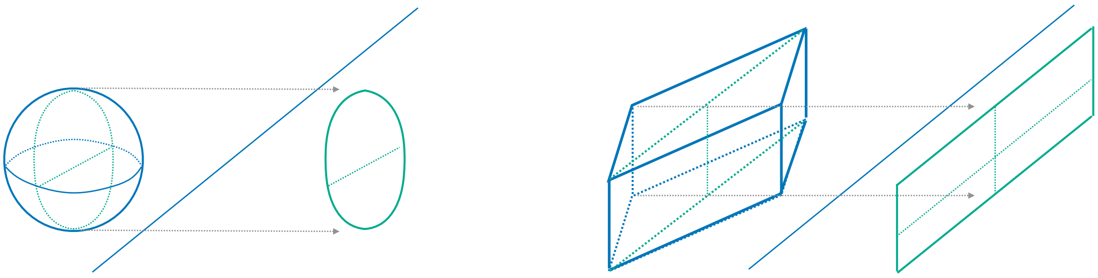

FIGURE 2.1 Projection of the two idealized situation Left panel: Case of a sphere. Right panel: Case of a cuboid mis-aligned with the line of sight.

2.1 Inhomogeneity and anisotropy due to integration along the line-of-sight

Star forming clouds are shaped by turbulent motions conferring statistical properties to their geometrical characteristics, and hence to the area projected in a plane perpendicular to the line of sight and to the thickness projected along the line of sight. This is responsible for difficulties in evaluating exactly the *statistical average* of $\Sigma(x, y)$. However, provided that the cloud thickness is much larger than the correlation length, *i.e.* if $l(x, y) \gg l_c(\rho)$, we can reasonably assume that (see Eq. (2.1)):

$$\boxed{\mathbb{E}\left(\Sigma(x,y)\right) \simeq \mathbb{E}\left(\rho\right)\mathbb{E}\left(l(x,y)\right).} \tag{2.2}$$

One must note here that we are dealing with the *statistical average* and not with the spatial average. This equation shows that $\Sigma(x, y)$ may not be statistically homogeneous even if the density field ρ is, just because of integration effects. To illustrate this important point, let us imagine two idealized situations. In one of them, the cloud is a sphere of radius R. In the other one, the cloud is a "cube" of side L mis-aligned with the line of sight and seen from one of its edges such that the projected surface is of size $\sqrt{2}L \times L$ (see Fig. (2.1)). For the sphere, the thickness along the line of sight is:

$$\mathbb{E}\left(l_{\mathrm{S(R)}}\right)(x,y) = 2R\left(1 - \frac{x^2+y^2}{R^2}\right)^{1/2}, \quad x^2+y^2 < R^2, \tag{2.3}$$

whereas it is :

$$\mathbb{E}\left(l_{\mathrm{C(L)}}\right)(x,y) = L\left(1 - \frac{\sqrt{2}|x|}{L}\right), \quad |x| \leq \frac{L}{\sqrt{2}},\ |y| \leq \frac{L}{2}. \tag{2.4}$$

for the cubic cloud. Even though they are very simple, these two examples demonstrate that the column-density field may exhibit large scale gradients and hence may not be statistically homogeneous, even if the density field is. Furthermore, as seen with the example of the cube, integration effects can also generate some anisotropy in the column-density field.

2.2 Column-density field in a numerical simulation box

2.2.1 Statistical homogeneity

For a cubic simulation domain of size L, projecting the density field along one of the 3 principal directions of the cube leads to a statistically homogeneous column density field such that :

$$\mathbb{E}\left(\Sigma(x,y)\right) = \mathbb{E}\left(\rho\right) \times L. \tag{2.5}$$

2.2.2 Auto-covariance function and variance.

In a cubic simulation box, the ACF of Σ is

$$\begin{aligned} C_\Sigma(\boldsymbol{r}) &= \mathbb{E}\left((\Sigma(\boldsymbol{u}+\boldsymbol{r}) - \mathbb{E}(\rho)\, L)\,(\Sigma(\boldsymbol{u}) - \mathbb{E}(\rho)\, L)\right) \\ &= \int_{[-L/2,L/2]^2} C_\rho(\boldsymbol{r}, z-z')\,\mathrm{d}z\,\mathrm{d}z' \\ &= \int_{[-L,L]} C_\rho(\boldsymbol{r}, u)\mathrm{d}u \int_{-L+|u|}^{L-|u|} \frac{\mathrm{d}v}{2} \\ &= L \int_{[-L,L]} C_\rho(\boldsymbol{r}, u)\left(1-\frac{|u|}{L}\right)\mathrm{d}u, \end{aligned} \tag{2.6}$$

while the variance is

$$\mathrm{Var}(\Sigma) = C_\Sigma(\boldsymbol{0}) = L \int_{[-L,L]} C_\rho(\boldsymbol{0}, u)\left(1-\frac{|u|}{L}\right)\mathrm{d}u. \tag{2.7}$$

Thus, assuming that the density field is statistically isotropic at small scales (i.e. the ACF is isotropic at short lags), one obtains:

$$\mathrm{Var}(\Sigma) \simeq L \int_{[-L,L]} C_\rho(|u|)\left(1-\frac{|u|}{L}\right)\mathrm{d}u. \tag{2.8}$$

Provided that the correlation length of the density field, is much smaller than the size of the box L (*i.e.* $l_c(\rho) \ll L$), one can approximate the integral on the r.h.s of Eq. (2.8) by the following expression:

$$\int_{[-L,L]} C_\rho(|u|)\left(1-\frac{|u|}{L}\right)\mathrm{d}u \simeq 2 l_{\mathrm{i}}(\rho)\mathrm{Var}(\rho) \simeq 2 l_c(\rho)\mathrm{Var}(\rho), \tag{2.9}$$

where $l_{\mathrm{i}}(\rho)$ is the integral scale of the density field (see Chap. **1**). Thus,

$$\mathrm{Var}(\Sigma) \simeq 2\, L\, l_c(\rho)\, \mathrm{Var}(\rho). \tag{2.10}$$

A similar equation for the centroid velocities was given by Scalo (1984) but was not written expressed in terms of the correlation length. Then Eq. (2.10) yields:

$$\boxed{\mathrm{Var}\left(\frac{\Sigma}{\mathbb{E}(\Sigma)}\right) \simeq \mathrm{Var}\left(\frac{\rho}{\mathbb{E}(\rho)}\right)\frac{2\, l_c(\rho)}{L} = \mathrm{Var}\left(\frac{\rho}{\mathbb{E}(\rho)}\right)\frac{l_c(\rho)}{R},} \tag{2.11}$$

where $R = L/2$. This is an important result because it provides a *measure of* $l_c(\rho)/R$ *independently of the ACF.* In their calculations, Brunt et al. (2010a); Federrath et al. (2010) found that ratio $\mathrm{Var}\left(\Sigma/\mathbb{E}(\Sigma)\right)/\mathrm{Var}\left(\rho/\mathbb{E}(\rho)\right)$ lies between 0.03 and 0.15. Eq. (2.11) is essentially similar to the relation derived by Brunt et al. (2010a) but it involves the correlation length instead of the power-spectrum (see next section).

Vazquez-Semadeni & Garcia (2001) were the first to study the impact of the $l_c(\rho)/R$ ratio on the statistics of column-density fields. Based on a crude interpretation of the central limit theorem (CLT), they proposed that, for $l_c(\rho)/R \to 0$, the column-density PDF should appear to be gaussian instead of lognormal. This is not consistent with the apparent lognormality of the observed column-density PDFs, which led these authors to conclude that $l_c(\rho)/R$ cannot be vanishingly small and that it must be of the order of 10^{-1}. However, the CLT only applies to independent variables and can hardly be valid for the sum of correlated variables, even if correlations decay. This casts doubt on the conclusions of

Vazquez-Semadeni & Garcia (2001). More recently, Szyszkowicz & Yanikomeroglu (2009) and Beaulieu (2011) have shown that, for some special types of correlations, the sum of a large number N of lognormal variables tends to a lognormal distribution as $N \to \infty$. We conclude that knowledge of the $l_c(\rho)/R$ value does not allow robust conclusions on the shape of the column-density PDF. However, as shown by Eq. (2.11), the variance $\mathrm{Var}\left(\frac{\Sigma}{\mathbb{E}(\Sigma)}\right)$ does become vanishingly small as $l_c(\rho)/R$ tends to zero. In that case, one can show with high probability that:

$$\ln\left(\frac{\Sigma}{\mathbb{E}\left(\Sigma\right)}\right) \simeq \frac{\Sigma - \mathbb{E}\left(\Sigma\right)}{\mathbb{E}\left(\Sigma\right)}. \tag{2.12}$$

Thus, in the limit of vanishing values of $l_c(\rho)/R$, the distributions of $\Sigma/\mathbb{E}\left(\Sigma\right)$ and its logarithm are both gaussian if one of them is.

2.3 Decay length of correlations

We now examine how the decay of correlations of ρ impacts the decay of correlations of Σ. For the sake of simplicity, we again consider the case of a cubic box in order to avoid unncessary complications. For the 2D field Σ, the correlation length is given by :

$$\begin{aligned} l_c(\Sigma)^2 &= \frac{1}{4}\frac{1}{\mathrm{Var}\left(\Sigma\right)}\iint C_\Sigma(\boldsymbol{r})\,\mathrm{d}\boldsymbol{r}, \\ &= \frac{1}{4}\frac{1}{\mathrm{Var}\left(\Sigma\right)}\iint L\int_{[-L,L]} C_\rho(\boldsymbol{r},u)\left(1-\frac{|u|}{L}\right)\mathrm{d}u\,\mathrm{d}\boldsymbol{r}, \\ &\simeq 2\frac{L\mathrm{Var}\left(\rho\right)}{\mathrm{Var}\left(\Sigma\right)}l_c(\rho)^3, \end{aligned} \tag{2.13}$$

Using Eq. (2.10), this implies that:

$$\boxed{l_c(\Sigma)^2 \simeq l_c(\rho)^2.} \tag{2.14}$$

This shows that *correlations of the column-density fields are decaying over a characteristic length close to $l_c(\rho)$, the correlation length of the underlying density field.* In general, we thus expect that $l_c(\Sigma) \sim l_c(\rho)$, so that information gathered from the column-density yield an estimate of the characteristic decay length of correlations of the underlying density field ρ.

3 Column density PDFs as tracers of the underlying density PDFs

Observations of MCs show that regions where stars have not begun to appear exhibit lognormal column-density PDFs and that these PDFs have power-law tails at high column densities in regions with numerous prestellar cores (Kainulainen et al., 2009; Schneider et al., 2013). Similarly, numerical simulations of star formation in turbulent clouds lead to density PDFs that develop power-law tails as time increases (Klessen, 2000; Federrath & Klessen, 2013). There is now a sizable body of data on the PDF of the density ρ and column density Σ, and on that of their logarithmic deviations $s = \ln(\rho/\overline{\rho})$ and $\eta = \ln(\Sigma/\overline{\Sigma})$, noted respectively s and η-PDF. This has motivated many authors to formally relate the observed η-PDF to properties of the underlying s-PDF (Vazquez-Semadeni & Garcia, 2001; Brunt et al., 2010a,b; Burkhart & Lazarian, 2012; Federrath & Klessen, 2013; Jaupart & Chabrier, 2020).

3.1 Current status of research

3.1.1 Variance in column density and density PDFs.

In their numerical simulations, Brunt et al. (2010a) and Burkhart & Lazarian (2012) have studied how the variances of the s-PDF and η-PDF, noted σ_s^2 and σ_η^2, respectively, are related to one another. Using their results for σ_ρ^2 and σ_Σ^2 in a cubic box of size L, Brunt et al. (2010a) proposed the following relation in terms of the power spectrum of the 2D column density P_2:

$$\mathrm{Var}\,(e^\eta) = \frac{\sigma_\Sigma^2}{\overline{\Sigma}^2} = R\,\frac{\sigma_\rho^2}{\overline{\rho}^2} = R\,\mathrm{Var}\,(e^s) \tag{2.15}$$

$$\text{where}\, R = \frac{\sum_{\boldsymbol{k}\in\mathbb{Z}^2} P_2(|\boldsymbol{k}|) - P_2(0)}{\sum_{\boldsymbol{k}\in\mathbb{Z}^3} P_2(|\boldsymbol{k}|) - P_2(0)}. \tag{2.16}$$

This result relies on two assumptions. One is that the density field is isotropic, so that P_2 is only a function of $|\boldsymbol{k}|$ and is proportional to the power spectrum of the 3D density field P_3. The other assumption is that the cloud is roughly of the same dimension L in the three directions. The above relation is useful but it requires knowlege of power spectra of either P_2 or P_3 in order to retrieve the variance σ_ρ^2 from the observed column density PDF. We have shown Chapter **1**, however, that this is affected by important systematic biases. In fact, Eq. (2.15) essentially reduces to Eq. (2.11) if it is written in terms of the correlation length instead of the power-spectra.

Burkhart & Lazarian (2012) have investigated the relation between σ_s and σ_η for *lognormal* PDFs. They have proposed and tested the following relation:

$$\sigma_\eta^2 = A_{\eta s} \times \sigma_s^2, \tag{2.17}$$

where $A_{\eta s}$ may depend on the forcing parameter b in the governing equations (see section above). In simulations of compressible turbulence without gravity and with a solenoidal driving term ($b = 1/3$), they found from a best fit analysis that $A_{\eta s} \simeq 0.11$. For a forcing parameter $b = 0.5$, corresponding to a combination of solenoidal and compressive driving terms, $A_{\eta s} \simeq 0.12 - 0.16$. We note that a consistency check for this procedure consists in estimating the average velocity dispersion to obtain the average Mach number in the cloud which can then be fed into the $\mathcal{M}$-variance relation ($\sigma_s^2 = \ln(1 + (b\mathcal{M})^2)$, see below). This consistency check require the computation of neither the power spectrum nor the ACF and hence only requires the determination of *one point* statistics. This procedure is thus easier to implement from available data.

3.1.2 Exponents in power-law PDFs.

For PDFs that exhibit power-law tails, Federrath & Klessen (2013) have proposed and tested numerically that the exponent of the η-PDF, noted α_η, is linked to that of s-PDF, noted α_s, through the following relationship:

$$\alpha_\eta = -\frac{2}{1 - \frac{3}{\alpha_s}}, \tag{2.18}$$

This result is linked to the isotropic character of the density fields. For s-PDF with power-law tails with $\alpha_s = 2$ or $\alpha_s = 3/2$, in particular, we expect that $\alpha_\eta = 2$ and $\alpha_\eta = 4$, respectively.

3.1.3 Shape of the PDFs

Building on the relationship between σ_ρ^2 and σ_Σ^2 from Brunt et al. (2010a), Brunt et al. (2010b) have proposed a method to reconstruct the s-PDF from the observed η-PDF. Because they can only constrain the two first moments of the ρ distribution, they have suggested the following relation:

$$\frac{\rho}{\overline{\rho}} = e^s = a \left(\frac{\Sigma}{\overline{\overline{\Sigma}}} \right)^{\xi} = a \, (e^{\eta})^{\xi} \tag{2.19}$$

where constants a and ξ are deduced from values of the average (which is 1) and of the variance of e^{η} determined from Eq. (2.15). In terms of s and η, this yields:

$$s = \xi \, \eta + \ln(a), \qquad \text{implying that} \qquad \sigma_s^2 = \xi \times \sigma_{\eta}^2, \tag{2.20}$$

which is similar to an earlier suggestion by Burkhart & Lazarian (2012). For a lognormal PDF, one can use Eq. (2.20) to obtain ξ. In other cases, however, one has to use Eq. (2.19) and trial values of ξ until the variance values match. Brunt et al. (2010b) were quite successful with their numerical tests and were able to reproduce the general characteristics of the PDFs, but their method suffers from the same limitations as the previous one (Eq. (2.17)).

3.2 Aim of this section

We have summarized attempts by Burkhart & Lazarian (2012) and Federrath & Klessen (2013) to obtain either the variance in the lognormal part of the s-PDF or the exponent of its power-law tail from data on the column density PDF. In order to reconstruct the s-PDF solely from data on the η-PDF, one final step is missing, however. Indeed, one must still determine the relationship between the critical density values for the onset of power-law tails in the s-PDFs and η-PDFs. This is the purpose of this section. The extra step would allow a complementary way of reconstructing the s-PDF from column density data. It would also enable us to use either Eq. (2.11) or Eq. (2.15) as proxies to obtain *an estimation of the correlation length.*

3.3 Critical densities for the onset of power-law tails

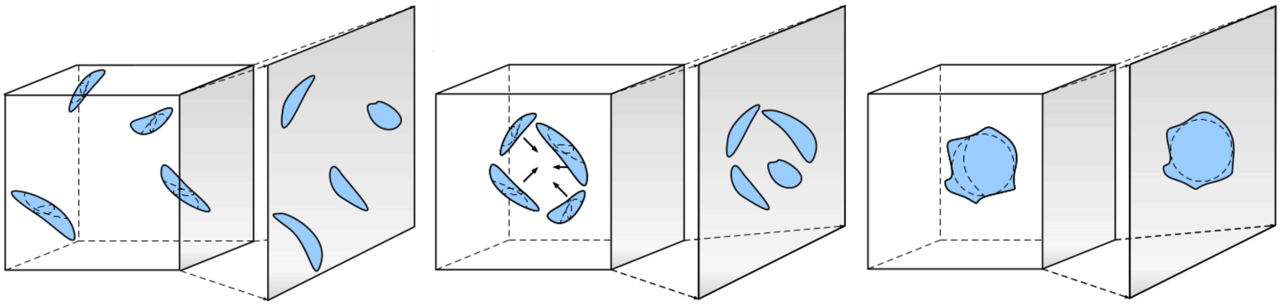

FIGURE 2.2 Left panel: Regions with volume density exceeding $s_{\rm crit}$ and their projected surface corresponding to regions with surface density exceeding $\eta_{\rm crit}$. Middle and right panels: packing the blue regions together and keeping their orientations and shapes results in a volume expected to be approximately spherical because there are no preferential directions (the constraint of isotropy). Pieced together, the projected surfaces are expected to outline a roughly circular object, allowing us to write down Eq. 2.22.

In this section, we derive a relationship between the threshold values of the *volume density* and *column density* for which $f(s)$, the s-PDF, and $p(\eta)$, the η-PDF, develop power-law tails. One step in the derivation is not a rigourous demonstration and we shall establish the validity of the final result through a comparison with numerical results.

We denote by $s_{\rm crit}$ the critical density value for the beginning of a power-law tail in the s-PDF. Assuming ergodicity, one can relate the volume fraction of regions with densities larger than $s_{\rm crit}$ to the probability of finding densities exceeding $s_{\rm crit}$:

$$\frac{V\left(s \geq s_{\rm crit}\right)}{V(\text{cloud})} = \int_{s_{\rm crit}}^{\infty} f(s)\mathrm{d}s. \tag{2.21}$$

We now need to evaluate the projected area of this volume onto the plane perpendicular to the line of sight $S(s \geq s_{\rm crit})$. Assuming statistical isotropy (at short scales), we get :

$$\frac{S(s \geq s_{\rm crit})}{S(\text{cloud})} \simeq \left(\frac{V\left(s \geq s_{\rm crit}\right)}{V(\text{cloud})}\right)^{2/3}. \tag{2.22}$$

which is illustrated in Fig. 2.2. We then equate regions in the cloud which contribute to the power-law tail in the η-PDF with regions that are included in the projected area $S(s \geq s_{\rm crit})$. This yields the critical surface density $\eta_{\rm crit}$ such that the η-PDF transitions to a power-law:

$$\boxed{\int_{\eta_{\rm crit}}^{\infty} p(\eta)\mathrm{d}\eta = \frac{S(s \geq s_{\rm crit})}{S(\text{cloud})} \simeq \left(\int_{s_{\rm crit}}^{\infty} f(s)\mathrm{d}s\right)^{2/3}.} \tag{2.23}$$

We note that this relationship is only valid because the s-PDF no longer possesses an axis of symmetry and develops a long tail at high density (produced by gravity in the present context). In particular, this result would not hold for a purely lognormal PDF. The procedure is tested against numerical simulations in the next section.

In cases where there are more than one power-law tail, for example 2, say, starting at s_1 and s_2, Eq. (2.23) remains a good approximation as long as $s_2 - s_1 \gtrsim 1$. so that the upper bound in the integrals does not affect the results significantly.

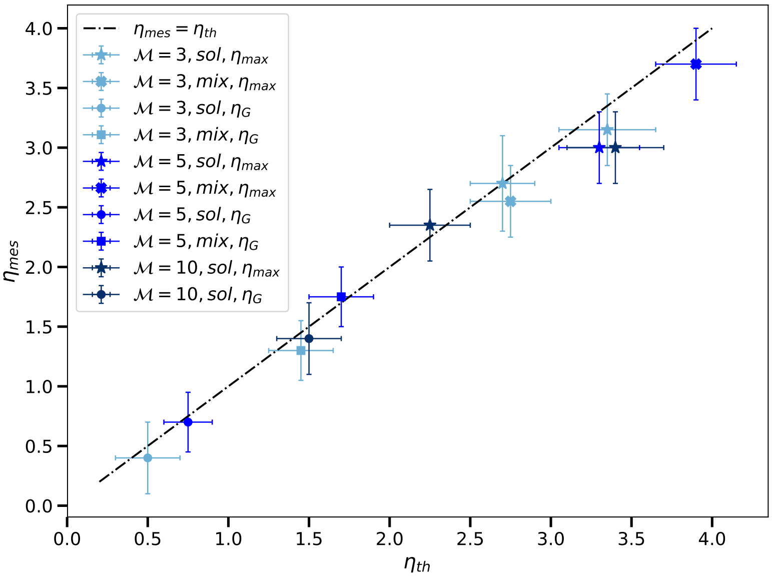

FIGURE 2.3 Theoretical values of the threshold density values for the onset of power-law tails in the η-PDF, $\eta_{\rm th}$, deduced from the s-PDF using Eq. (2.22) as a function of measured values, $\eta_{\rm mes}$, obtained from the η-PDFs, for numerical calculations for Mach numbers $\mathcal{M} = 3$, 5, 10 (light to dark blue). Each distribution has two power-law tails, with one that is due to resolution issues at very large density values (see text for a more detailed explanation). For $\mathcal{M} \sim 3$ and $\mathcal{M} = 10$, calculations with different resolutions ($N_{\rm res} = 256$ and $N_{\rm res} = 512$) lead to two different values of this second threshold density value. There is excellent agreement between the theoretical and observed threshold density values.

3.4 Numerical test

We now use the simulations of Federrath & Klessen (2012, 2013), presented in Chapter **1**, to test Eq. (2.23).

In each simulation, $f(s)$, the s-PDF, and $p(\eta)$, the η-PDF, are initially lognormal and eventually grow power-law tails with exponents $\alpha_s = 3/2$ and $\alpha_\eta = 2$, respectively. In addition, shallow power-law tails develop at high logarithmic column densities, for $\eta > \eta_{\rm max}$, due to the artificial fragmentation of regions where density s exceeds critical value $s_{\rm max}$, as explained in Chapter **1**. Thus, we can use two threshold density values for each distribution, even though one of them corresponds to a resolution problem and hence is not representative of a true situation. The smaller one is such that the PDF develops the expected power-law tail and the larger one corresponds to the onset of numerical resolution problems. We compare the (logarithmic) threshold column density values determined from the η-PDFs to those that are deduced from the s-PDFs through Eq. (2.23) in Fig. 2.3. The agreement between the theoretical and measured values is excellent.

3.5 Model with one or two power-law tails.

In this section, we develop a simple model to infer the global s-PDFs of molecular clouds from the observed η-PDFs. We assume that the PDFs are continuous and have one power-law tail at high densities and a lognormal cutoff at low densities:

$$\begin{aligned} f(s) &= A_1\, e^{-\frac{(s-\mu)^2}{2\sigma_s^2}}, \; s \le s_{\rm crit} \\ &= A_2\, e^{-\alpha_s (s - s_{\rm crit})}, \; s \ge s_{\rm crit}. \end{aligned} \tag{2.24}$$

where A_1 and A_2 are two coefficients to be determined. Normalizing f and enforcing continuity as well as the necessary condition $\overline{e^s} = 1$ (from the definition of s), we obtain:

$$A_1 = A_2\, e^{\frac{(s_{\rm crit}-\mu)^2}{2\sigma_s^2}} \tag{2.25}$$

$$1 = \frac{1}{2} A_1 \sqrt{2\pi\sigma_s^2}\left[1 + {\rm erf}\left(\frac{s_{\rm crit}-\mu}{\sqrt{2}\sigma_s}\right)\right] + \frac{A_2}{\alpha_s} \tag{2.26}$$

$$\begin{aligned} 1 = {}& A_1 \sqrt{\frac{\pi}{2}\sigma_s^2}\, e^{\mu + \frac{\sigma_s^2}{2}}\left[1 + {\rm erf}\left(\frac{s_{\rm crit}-\mu-\sigma_s^2}{\sqrt{2}\sigma_s}\right)\right] \\ &+ \frac{A_2\, e^{s_{\rm crit}}}{\alpha_s - 1}. \end{aligned} \tag{2.27}$$

We next assume that the variance σ_s in the lognormal part and the exponent α_s of the power-law tail are inferred from the observed η-PDFs following §3.1.1 and §3.1.2. More precisely, we use the formula of Burkhart & Lazarian (2012), $\sigma_\eta^2 = A_{\eta s} \times \sigma_s^2$, where $A_{\eta s}$ depends on the turbulence forcing parameter b, which provides one equation. From §3.3, A_2/α_s, and hence A_2, are obtained from the observations. We are now left with a system of 3 equations for 3 unknown quantities, namely $s_{\rm crit}$, μ and A_1. We note that, in this procedure, parameter μ, which determines the peak of the lognormal part of the distribution, is shifted to lower density values to ensure that $\overline{e^s} = 1$. Injecting Eq. (2.25) into Eq. (2.26), we obtain an implicit equation with variable $x = \frac{s_{\rm crit}-\mu}{\sqrt{2}\sigma_s}$:

$$1 = A_2\, e^{x^2} \sqrt{2\pi\sigma_s^2}\, \Phi(x) + \frac{A_2}{\alpha_s}, \tag{2.28}$$

where $\Phi(x) = \frac{1}{2}\left[1 + {\rm erf}(x)\right]$ is the cumulative distribution function for the normal distribution. Eq. (2.27) is used to obtain μ and then $s_{\rm crit}$.

In cases such that the η-PDF exhibits two power-law tails with exponents $\alpha_\eta = 4$ and $\alpha_\eta = 2$, we assume the following functional form for the density distribution:

$$
\begin{aligned}
f(s) &= A_1\, e^{-\frac{(s-\mu)^2}{2\sigma_s^2}}, \; s \leq s_1 \\
&= A_2\, e^{-\alpha_1 (s-s_1)}, \; s_1 \leq s \leq s_2 \\
&= A_2\, e^{-\alpha_1 (s_2-s_1)}\, e^{-\alpha_2 (s-s_2)}, \; s_2 \leq s,
\end{aligned} \tag{2.29}
$$

where $\alpha_1 = 2$ and $\alpha_2 = 3/2$. We adapt the previous procedure to this case as follows. First, we build the s-PDF as if there was only one power-law with exponent $\alpha_\eta = 4$ in the η-PDF with the above procedure and obtain values for A_1, A_2, μ and s_1. We then use Eq. (2.23) to obtain s_2:

$$
\frac{A_2\, e^{-\alpha_1 (s_2-s_1)}}{\alpha_2} = \left(\int_{\eta_2}^{\infty} p(\eta) \mathrm{d}\eta \right)^{3/2}, \tag{2.30}
$$

where η_2 is the column density at the beginning of the second power-law tail with exponent $\alpha_\eta = 2$. This modified procedure, while simple to implement, is sufficiently accurate for our purposes because s_2 is large, so that molecular cloud regions where $s > s_2$ only account for a very small fraction of the total volume ($\lesssim 10^{-5}$).

We confront this procedure to observations in Chapter **4**. Errors arising from the determinations of η_{crit} and σ_s from the observations yield an error $\Delta s_{\mathrm{crit}} = \pm 0.3$ on s_{crit}, which is reasonable.

4 Conclusion

In this chapter, we have studied the statistics of the observed column-density fields and the information on the underlying density field that can be obtained from such observations.

In this section, we first noted that the statistics of the column-density field are affected by systematic biases due to integration effects along the line of sight. Specifically, these effects are likely to generate large scale gradients in the column density field which may therefore appear to be statistically heterogeneous. They are also responsible for anisotropy in the ACFs. In Chapter **3**, we discuss methods that are able to reduce these artefacts. For example, one may use appropriate filters to smooth out large scale gradients and focus on high column density contrasts.

We have shown that, provided that these biases are avoided, the correlation length of the column density field which is calculated from its ACF allows the determination of the correlation length of the underlying density field. In a next step, we have developed a method to derive the correlation length, or more exactly the ratio of the correlation length over the size of the cloud (or the box for numerical simulations), from the variances of the density and column-density fields (Sec.2.2). Finally, we have proposed a strategy to derive the (volume) density PDF from the column density PDF in Sec. 3. We are now equipped with a set of statistical tools to study the statistics of star forming clouds and to assess whether a statistical approach based on ergodicity is relevant.

Chapter

3 Relevance of a statistical approach

Contents

Appendices

1 Introduction

1.1 Motivation

Observations of molecular clouds (MC) show that their main properties (velocity, column-density) exhibit large fluctuations. These fluctuations are at the heart of the star formation process (Padoan & Nordlund 2002; Mac Low & Klessen 2004; Hennebelle & Chabrier 2008; Hopkins 2012b), implying that knowledge of their statistical characteristics is of prime importance. The accurate determination of the statistics of any quantity must rely on either a large enough number of samples or a large enough sample, so that a natural question arises: can we derive accurate statistical properties of MCs from observations, and if so how can we evaluate the level of accuracy ? The relevance of a general statistical analysis of the global properties of MCs (e.g mass, density PDF, temperature, velocity dispersion) deduced from observations and numerical simulations for studies of star formation processes must be assessed properly. For example, all the theories that are built for the mass spectrum, i.e. the initial mass function (IMF), or the star formation rate (SFR) in a molecular cloud, for instance, rely on the assumption that a restricted number of observations or numerical simulations are representative of any MCs with similar properties. This key assumption must be tested.

1.2 Fair-sample hypothesis

In studies of star formation based on observations or numerical simulations, one has only access to a small number of samples (and in reality only one most of the time). Therefore, in order to evaluate the statistics of the various stochastic fields of interest, one makes the basic assumption, sometimes called the "fair-sample hypothesis", that the available sample is large enough for volumetric (or time) averages to be meaningful (see e.g. Peebles 1973 for a discussion in the context of cosmology). This assumption is only valid for stochastic fields that are *statistically homogeneous and ergodic* (Papoulis & Pillai, 1965). Here, one should note that *statistical* homogeneity must not be confused with *spatial* homogeneity (we will come back to this point below). The assumption of statistical homogeneity is adopted by many authors, for example in studies of turbulent flows with or without self gravity (Chandrasekhar, 1951b,a; Batchelor, 1953; Pope, 1985; Frisch, 1995; Pan et al., 2018, 2019a,b; Jaupart & Chabrier, 2020) and in cosmology for studies of the dynamics of structures in the universe (Peebles, 1973; Heinesen, 2020). This assumption, however, provides no information on the magnitude of fluctuations around the average.

Ergodic theory (see Chap. **1**) allows one to circumvent the problem of dealing with a single sample and to derive a robust *measure of the accuracy of field statistics derived from the available data.* In the present context, it enables us to assess and quantify the relevance of a statistical approach on the evolution of star forming MCs. The key quantity is the *correlation length*, which is defined in terms of the integral of the auto-covariance function (see e.g. Papoulis & Pillai 1965). The fundamental result is that ergodic estimates are accurate if the dimensions of the sample, *i.e.* a whole cloud or part of it, are large enough compared to the correlation length. A proper determination of the correlation length in MCs is therefore of prime importance.

1.3 Informations available from observations

Observations cannot directly provide information on the stochastic fields of a MC and, by definition, are limited to a single sample, the cloud under investigation. Using optically thin molecular lines in the electromagnetic radiation spectrum and the first two moments of the associated brightness temperatures, for example, one can generate maps of the column density Σ and the centroid velocity v_c, which are defined as follows:

$$\Sigma(x,y) \quad = \quad \int_{\mathrm{los}(x,y)} \rho(x,y,z)\,\mathrm{d}z \tag{3.1}$$

$$v_c(x,y) \;=\; \int_{\mathrm{los}(x,y)} \rho(x,y,z)v(x,y,z)\,\mathrm{d}z \tag{3.2}$$

where $\rho(\boldsymbol{x})$ is density along the line of sight ($\mathrm{los}(x,y)$) and $v(\boldsymbol{x})$ is the velocity projected on the line of sight. The integrals are carried out along the line of sight (see Chap. **1**).

In their pioneering works, Scalo (1984) and Kleiner & Dickman (1985) studied the correlations of centroid velocities in the ρ-Oph and Taurus complex and only found evidence for weak correlations at short scales close to the spatial resolution of their data. Previously, Kleiner & Dickman (1984) had used correlations of the column density field of the Taurus complex to search for a statistically significant length scale characterizing the separation distance between condensations but had made no attempt to determine the correlation length.

1.4 Objectives of this chapter

The objectives of this chapter are twofold. First, we aim at examining the relevance and validity of a statistical approach based on ergodic theory to studies of the stochastic fields of star-forming MCs. Second, we seek to identify which statistical properties of the density field can be inferred from column density data.

The plan of this chapter is as follows. In Sec. 2, we outline the mathematical framework for the auto-covariance function and correlation length of a statistical sample. In Sec. 3, we examine the density field that is generated by turbulence in a compressible fluid and how to determine the auto-covariance function (ACF) and correlation length in astrophysical systems. In Sec. 4, we apply our calculations to Polaris, a typical star-forming cloud. We identify artefacts that are generated when one uses the statistical properties of the column-density field to infer those of the real density field and show how to reduce them. In Sec.5, we examine another star-forming cloud, Orion B. Then, in Sec. 6 we apply the same formalism to a different problem, which is to determine the total gravitational (binding) energy of a cloud and its virial parameter from estimates of its total mass and size. We end with a conclusion summarizing our key results.

2 Mathematical framework for a statistical approach

As mentioned in the Introduction, a statistical approach of any given property of a cloud or part of a cloud is only valid if the target is large enough compared to the associated correlation length. Is this condition is met, statistical quantities that are deduced from the data can be regarded as representative of the genuine quantities with a high degree of confidence. Establishing the degree of confidence and the relevance of a statistical approach may be achieved within the framework of the ergodic theory, a common staple of statistical physics and studies of dynamical systems. Ergodicity implies by definition that different observations/realizations of a statistical quantity yield results that are all representative of the true distribution.

2.1 Ergodic theory

We have already described the theorem behind ergodic theory in Chap. **1** and restrict ourselves to a short summary. Let us consider a (scalar) stochastic field $X(\boldsymbol{y})$, which depends on a D-dimensional position vector $\boldsymbol{y}$ ($D = 1$, 2 or 3). In the context of MCs, one is usually dealing with only a *single* sample of $X(\boldsymbol{y})$. As mentioned in the introduction, we assume statistical homogeneity and build the following ergodic estimator:

$$\hat{X}_L = \frac{1}{L^D}\int_{[-\frac{L}{2},\frac{L}{2}]^D} X(\boldsymbol{y})\,\mathrm{d}\boldsymbol{y}, \tag{3.3}$$

where $\Omega = [-\frac{L}{2}, \frac{L}{2}]^D$ is a control volume of linear size L and volume L^D, which is sought to be as large as possible. The ergodic estimator $\hat{X}_L$ has the following variance:

$$\mathrm{Var}(\hat{X}_L) = \frac{1}{(L)^D} \int_{[-L,L]^D} C_X(\boldsymbol{y}) \prod_{k=1}^{D} \left(1 - \frac{|y_k|}{L}\right) \mathrm{d}\boldsymbol{y}, \tag{3.4}$$

where $C_X(\boldsymbol{y}) = \mathbb{E}\left(X(\boldsymbol{y}' + \boldsymbol{y})\, X(\boldsymbol{y}')\right) - \mathbb{E}\left(X\right)^2$ is the *auto-covariance function* (ACF) of X at a lag $\boldsymbol{y}$. The stochastic field X is said to be mean ergodic if the estimator $\hat{X}_L$ converges toward $\mathbb{E}(X)$ as $L \to \infty$. This can be framed in a mean square (MS) sense as follows:

$$\mathbb{E}\left(|\hat{X}_L - \mathbb{E}\left(X\right)|^2\right) = \mathrm{Var}(\hat{X}_L) \xrightarrow[L\to\infty]{} 0. \tag{3.5}$$

Alternatively, this may be framed in probabilistic terms:

$$\mathbb{P}\left(|\hat{X}_L - \mathbb{E}\left(X\right)| > \epsilon)\right) \to 0\, \forall \epsilon > 0. \tag{3.6}$$

Using the Bienayme-Tchebychev inequality,

$$\mathbb{P}\left(|\hat{X}_L - \mathbb{E}\left(X\right)| \leq m\, \sigma(\hat{X}_L)\right) \geq 1 - \frac{1}{m^2}, \tag{3.7}$$

one shows that, if X is MS mean ergodic, $\hat{X}_L$ converges in a probabilistic sense. In addition, one obtains a confidence interval for the estimate $\hat{X}_L$. Slutsky's theorem leads to two sufficient (physical) conditions for X to be mean ergodic. Either:

$$\int_{\mathbb{R}^D} C_X(\boldsymbol{y}) \mathrm{d}\boldsymbol{y} < \infty, \tag{3.8}$$

or

$$C_X(\boldsymbol{y}) \xrightarrow[|\boldsymbol{y}|\to\infty]{} 0. \tag{3.9}$$

One usually assumes that both conditions hold. It follows that the proper *definition of the correlation length* $l_c(X)$ of field X as a function of the autocorrelation function (ACF) (Papoulis & Pillai, 1965) is:

$$(l_c(X))^D = \frac{1}{2^D\, C_X(\mathbf{0})} \int_{\mathbb{R}^D} C_X(\boldsymbol{y}) \mathrm{d}\boldsymbol{y}. \tag{3.10}$$

For $l_c(X) \ll L$, we then have from Eq (3.4) :

$$\mathrm{Var}(\hat{X}_L) \simeq \mathrm{Var}(X) \left(\frac{2\, l_c(X)}{L}\right)^D = \mathrm{Var}(X) \left(\frac{l_c(X)}{R}\right)^D, \tag{3.11}$$

where $R = L/2$.

2.2 Expected fluctuations in repeated trials

We consider here that one can repeat the same experiment several times, as can be done for instance with numerical simulations or with clouds that are supposed to be in similar conditions. We wish to determine the amplitudes of variations of averaged quantities between samples. We expect these to depend on ratio (l_c/R), and hence we must be able to estimate the value of this ratio, *without having to calculate the ACF*.

For each experiment in N trials, indexed by i, one obtains a value of the estimate $\hat{X}_{L,i}$ defined by

Eq. (3.3). Using the Tchebychev inequality, we know that

$$\mathbb{P}\left(|\hat{X}_{L,i}-\mathbb{E}\left(X\right)|\leq m\,\sigma(X)\left(\frac{l_c(X)}{R}\right)^{D/2}\right)\geq 1-\frac{1}{m^2}. \tag{3.12}$$

The average over the N trials (the sample average) is:

$$\hat{X}_{L,N}=\frac{1}{N}\sum_{i=1}^{N}\hat{X}_{L,i} \tag{3.13}$$

which is obviously a better estimate of $\mathbb{E}\left(X\right)$ as:

$$\mathbb{P}\left(|\hat{X}_{L,N}-\mathbb{E}\left(X\right)|\leq m\,\frac{\sigma(X)}{\sqrt{N}}\left(\frac{l_c(X)}{R}\right)^{D/2}\right)\geq 1-\frac{1}{m^2}. \tag{3.14}$$

We then expect $\hat{X}_{L,i}$ to fluctuate around the sample average $\hat{X}_{L,N}$, such that:

$$\mathbb{P}\left(|\hat{X}_{L,i}-\hat{X}_{L,N}|\leq m\,\sigma(X)\left(\frac{l_c(X)}{R}\right)^{D/2}\left(1-\frac{1}{N}\right)^{1/2}\right)\geq 1-\frac{1}{m^2}. \tag{3.15}$$

If $l_c(X)$ is known, Eqs. (3.12) and (3.15) provide statistical error bars. Alternatively, if $l_c(X)$ is not known, these equations give information on the product $\sigma(X)(l_c(X)/R)^{D/2}$ when one repeats the same statistical experiment several times. For N trials, one first builds the sample average $\hat{X}_{L,N}$ from Eq. (3.13). One then determines the half length $l_{50\%}$ of the segment centered on $\hat{X}_{L,N}$ where 50% of the various estimates $\hat{X}_{L,i}$ lie. This allows to obtain the estimate

$$\sqrt{2}\sigma(X)\left(\frac{l_c(X)}{R}\right)^{D/2}\left(1-\frac{1}{N}\right)^{1/2}\lesssim l_{50\%}. \tag{3.16}$$

We note that, if the statistics are gaussian, the prefactor in this equation is 0.67 instead of $\sqrt{2}$. Thus, an order of magnitude estimate of $\sigma(X)(l_c(X)/R)^{D/2}$ is:

$$\boxed{\sigma(X)\left(\frac{l_c(X)}{R}\right)^{D/2}\sim\frac{l_{50\%}}{\sqrt{2}}\left(1-\frac{1}{N}\right)^{-1/2}\sim\frac{l_{50\%}}{\sqrt{2}}.} \tag{3.17}$$

We now have an easy and rigorous method to determine correct error bars for statistical experiments.

3

3 Application to astrophysical density fields

The general results derived in §2 can be applied to many physical and astrophysical systems. They have been used extensively in cosmology but have somehow been overlooked in studies of star formation. Today, it is generally accepted that star formation is triggered by density fluctuations generated by large scale compressible turbulence in MCs (see e.g. McKee & Ostriker 2007 and reference therein). In this context, the density field ρ (or the logarithmic density field $s=\ln(\rho/\mathbb{E}\left(\rho\right))$) is of prime interest and its cumulative distribution function (CMF) and probability density function (PDF) must be determined accurately. Each of these statistical quantities is associated with a stochastic field X to which the results of §2 can be applied. For instance, the CMF $F_\rho(\rho_0)$ at ρ_0 is linked to the stochastic field $h_{\rho_0}(\boldsymbol{y})=\Theta\left(\rho_0-\rho(\boldsymbol{y})\right)$ (where Θ is the Heavyside function), because $F_\rho(\rho_0)=\mathbb{E}\left(h_{\rho_0}(\boldsymbol{y})\right)=\mathbb{E}\left(h_{\rho_0}\right)$. In principle, knowledge of the ACF of *all* these fields is required to establish the accuracy of the estimations. Fortunately, it may be shown that, with a few simplifying assumptions, one can make do with the ACF of ρ only in many situations. This is explained in detail in App. (B).

3.1 Exact results regarding the properties of the auto-covariance function (ACF) of the density field $\boldsymbol{\rho}$

For homogeneous turbulence, the ACF of ρ, the density field, can be expressed in term of the second order structure function :

$$S_\rho^{(2)}(\boldsymbol{y}) = \mathbb{E}\left(\{\rho(\boldsymbol{u}+\boldsymbol{y}) - \rho(\boldsymbol{u})\}^2\right), \tag{3.18}$$

as $S_\rho^{(2)}(\boldsymbol{y}) = 2\,(C_\rho(\mathbf{0}) - C_\rho(\boldsymbol{y})$. A similar statement can be made for the logarithmic density field $s = \ln(\rho/\mathbb{E}\,(\rho))$. This helps us to grasp some key features of the ACF. At *very short scale* (below the viscous scale), the density field is supposed to be differentiable and hence C_ρ must possess second-derivatives at $\boldsymbol{y} = \mathbf{0}$. Then, due to the parity of the ACF, its gradient must exist and be equal to $\mathbf{0}$ at $\boldsymbol{y} = \mathbf{0}$.

3.2 Phenomenology of (compressible) turbulence

The phenomenology of compressible turbulence (Kritsuk et al., 2007) can be derived, with some adjustments, from that of incompressible turbulence (Frisch, 1995). Thus, we will use the latter to derive some expected features of the density ACF in star-forming MCs.

In *isotropic* turbulence, the second order structure function is observed to be a monotonic increasing function of separation distance, at least in the inertial range, and to converge rapidly towards $2\mathrm{Var}\,(\rho)$ at scales that are larger than the integral scale l_i. This integral scale (not to be confused with the injection scale of turbulence) is defined in the same manner as the correlation length (Batchelor 1953)

$$l_\mathrm{i} = \frac{1}{C(\mathbf{0})}\int_0^\infty C(r)\mathrm{d}r. \tag{3.19}$$

In many situations, $l_c \sim l_\mathrm{i}$, as shown in Chap. **1**. Thus, at small scales (short lags) and in the inertial range, the ACF must be a *monotonically decreasing function.* Above the inertial range, it is often assumed that the structure function and the ACF are still monotonic and the ACF is usually approximated by a decaying exponential, even though density fluctuations are likely to generate oscillations of the *observed and estimated* ACF as it tends to zero (Batchelor 1953; Reinke et al. 2016, 2018).

In compressible isothermal turbulence, the density field ρ is found to be approximately lognormal (Kritsuk et al., 2007; Federrath et al., 2010), implying that the logarithmic density field $s = \ln(\rho/\mathbb{E}\,(\rho))$ is gaussian with variance $\sigma(s)^2 = \ln(1 + (b\mathcal{M})^2)$. In such *gaussian* conditions, the ACFs of ρ and s are linked by the following equation:

$$C_\rho(\boldsymbol{y}) = \mathbb{E}\,(\rho)^2\left(e^{C_s(\boldsymbol{y})} - 1\right). \tag{3.20}$$

As a consequence, if C_ρ (or C_s) is monotonically decaying towards 0, we deduce that:

$$\left(\frac{\sigma(s)^2}{e^{\sigma(s)^2} - 1}\right)^{1/3} l_c(s) \le l_c(\rho) \le l_c(s)\,, \tag{3.21}$$

where we have used the following inequalities: $e^{ax} - 1 \le x(e^a - 1)$ for $0 \le x \le 1$ and $ax \le e^{ax} - 1\ \forall x$. For typical star forming conditions, $\sigma(s)^2 \lesssim 4$, implying that:

$$0.4\,l_c(s) \lesssim l_c(\rho) \le l_c(s), \tag{3.22}$$

or,

$$\boxed{l_c(s) \sim l_c(\rho).} \tag{3.23}$$

This shows that under *gaussian conditions*, for the two lengths $l_c(s)$ and $l_c(\rho)$, knowledge of one of them is sufficient to characterize the other one within an order of magnitude.

3.3 Autocovariance function and correlation length in astrophysical situations

3.3.1 ACF from data

As seen in the previous sections, knowledge of the ACF of X is of crucial importance when one seeks to assess the relevance of a statistical approach in studies of large astrophysical systems. In practice, however, this ACF must be evaluated from data. In Chap. **1**, we have discussed various estimators and have shown that they are unreliable at large lags. Thus, estimates of $l_c(X)$ that are deduced from the ACF may well be unreliable.

3.3.2 Usual estimates

There are two traditional methods to obtain an estimate for l_c (or l_i). The first one relies on the reduced ACF of $\hat{C}_X/\mathrm{Var}\,(X)$. With an exponential envelope for this ACF, one searches for the separation distance for which the ACF is equal to e^{-1} and this is taken as an estimate of the correlation length (see e.g. Kleiner & Dickman 1984, 1985). The other method is only applicable to ACFs that decay sufficiently rapidly at scales larger than $l_c(X)$, as in turbulent flows (see previous section). In this case, the ACF is extrapolated with a decaying exponential in regions where it becomes non monotonic (see e.g. Batchelor 1953; Reinke et al. 2016, 2018), so that one can calculate the above integral and obtain a reliable estimate of $l_c(X)$ provided that $l_c(X) \ll L$.

3.4 Practical assumptions regarding the ACF

On the basis of the above results, we assume that the ACF decays rapidly at scales larger than the correlation length l_c ($l_c \sim l_\mathrm{i}$). Thus, the integral Eq. (3.10) need be calculated only up to a few l_c. Moreover, we assume that the ACF can be bounded by a decaying exponential $\exp(-|\boldsymbol{y}|/\lambda)$, where $\lambda \sim l_c$ in the inertial range and above, so that we can calculate the correlation length (note that such an exponential behaviour is prohibited at *very* small scales due to the differentiability of ρ).

3.5 Homogeneity and correlation scales in cosmology

As mentioned earlier, the concept of correlation length is often used in cosmology. In this branch of astrophysics, a statistical approach is used to describe the evolution of the cosmological fluid under the influence of its own gravity. This framework is therefore complementary to that of turbulence.

In this section, we show that the statistical formalism and the concept of statistical homogeneity derived in the previous sections can be applied to cosmological density fields in a straightforward manner. In this branch of astrophysics, one introduces the homogeneity scale λ_H, such that a smoothed Universe appears to be fairly homogeneous at larger scales. At these large scales, density deviations from the mean value are vanishingly small and the standard conjecture is that the dynamics of the Universe are governed by the Friedman equations (see Heinesen 2020 and reference therein for a more complete description). The homogeneity scale is thus somewhat analogous to the correlation length. We show here that λ_H is indeed a disguised version of the correlation length $l_c(n)$ of the galaxy number density $n(\boldsymbol{x})$ (see Peebles 1973 for a more general discussion).

One can define λ_H with a general metric but here we use a euclidian flat metric ($\mathbb{R}^3$ or $\mathbb{T}^3$). The homogeneity scale λ_H is defined as follows. Starting from the number density $n(\boldsymbol{x})$, one defines the number-count in a ball of radius r, noted $N(< r, \boldsymbol{x})$, as follows:

$$N(< r, \boldsymbol{x}) = \int_\Omega n(\boldsymbol{y})\, \Theta(r - |\boldsymbol{x} - \boldsymbol{y}|)\, \mathrm{d}\boldsymbol{y}, \tag{3.24}$$

where Θ is the Heaviside step function and Ω is some control volume that may be the whole universe. For the sake of simplicity, we will take $\Omega = [-L/2, L/2]^3$, as in Newtonian cosmology. One then defines the normalised number count $\mathcal{N}(< r, \boldsymbol{x})$ as follows:

$$\mathcal{N}(< r, \boldsymbol{x}) = \frac{3\, N(< r, \boldsymbol{x})}{\eta\, 4\pi\, r^3} \tag{3.25}$$

where η is the expectation value (statistical average) of the *statistically homogeneous* number density field. Then, one defines the weighted average number count $\mathcal{N}(< r)$:

$$\mathcal{N}(< r) = \frac{3\, N(< r)}{\eta\, 4\pi\, r^3} = \frac{1}{N} \int_\Omega n(\boldsymbol{x})\, \mathcal{N}(< r, \boldsymbol{x})\, \mathrm{d}\boldsymbol{x} \tag{3.26}$$

where $N = \int_\Omega n(\boldsymbol{x})\, \mathrm{d}\boldsymbol{x} \simeq \eta V_\Sigma = \eta L^3$ and where the last two equalities hold if $L \gg l_\mathrm{c}$ (see the previous section). As $\mathcal{N}(< r) \xrightarrow{r \gg 1} 1$, cosmologists define

$$D(< r) = 3 + \frac{\mathrm{d}\ln\mathcal{N}(< r)}{\mathrm{d}\ln r}. \tag{3.27}$$

λ_H is such that $|D(< r) - 3| \leq 10^{-2}, \forall r \geq \lambda_\mathrm{H}$. In the Λ-CDM model, this estimate gives $\lambda_H \simeq 100$ Mpc/h which, with $L > 10$ Gpc/h, gives $\lambda_H / L < 10^{-2}$. After a few manipulations that are detailed in App. (A) and assuming that $l_c(n) \lesssim \lambda_H \ll L$, we obtain:

$$|D(< r) - 3| \simeq \frac{\mathrm{Var}(n)}{\eta^2} \frac{9}{4\pi} \left(\frac{2\, l_c(n)}{r} \right)^3, \tag{3.28}$$

which yields:

$$\boxed{\lambda_H \simeq 2\, l_c(n) \times \left(100\, \mathrm{Var}\left(\frac{n}{\eta} \right) \right)^{1/3}.} \tag{3.29}$$

Therefore, the variance of the number density field n_{λ_H} smoothed at a scale λ_H is $\mathrm{Var}\,(n_{\lambda_H}) \simeq 1.7\, 10^{-3} \eta^2$. Using Tchebychev inequality Eq. (3.12), we obtain:

$$\mathbb{P}\left(\left| \frac{n_{\lambda_H} - \eta}{\eta} \right| \leq 0.1 \right) \geq 90\%, \tag{3.30}$$

or, if the statistics are Gaussian,

$$\mathbb{P}\left(\left| \frac{n_{\lambda_H} - \eta}{\eta} \right| \leq 0.1 \right) \simeq 99.7\%. \tag{3.31}$$

4 Application to observations of the Polaris cloud

As mentioned in Chapter **2**, one can determine the column-density field of molecular clouds from measurements (Kleiner & Dickman, 1984). One observes that their distributions depend on the evolutionary stage of a cloud or a cloud region. The column-density field exhibit a lognormal PDF where star formation has not started yet and a PDF with a power-law tail (PLT) at high density where abundant prestellar cores exist (Kainulainen et al., 2009; Schneider et al., 2013). Unfortunately, these observations are affected by several artefacts. We have shown in a previous chapter that integration

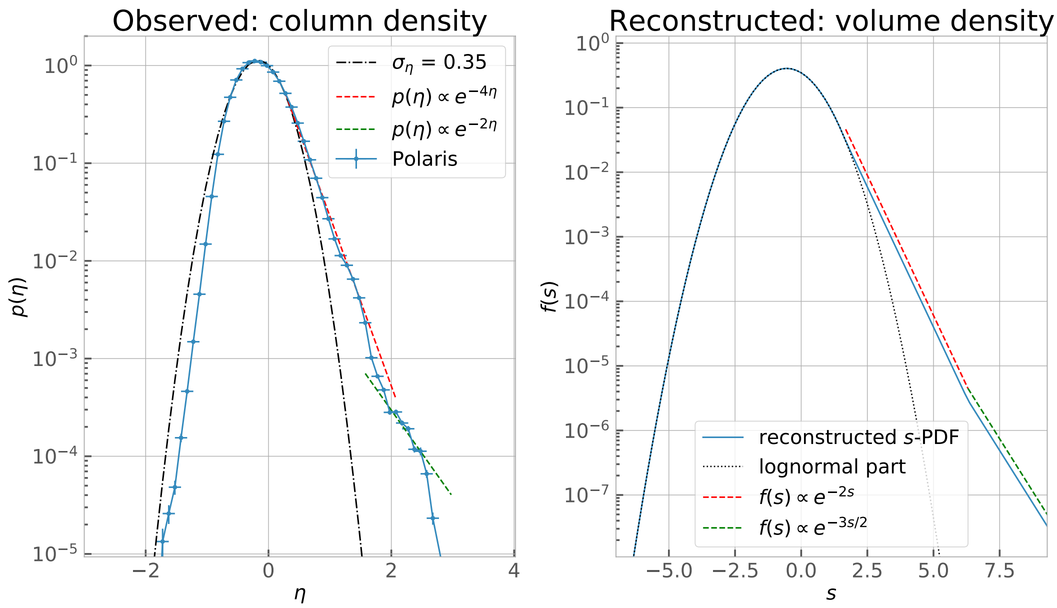

FIGURE 3.1 Left: Observed logarithmic column-density ($\eta = \ln(\Sigma/\langle\Sigma\rangle)$-PDF of the Polaris cloud (Schneider et al., 2013; Jaupart & Chabrier, 2020). Right: Estimated and reconstructed underlying logarithmic density ($s = \ln(\rho/\mathbb{E}(\rho))$)-PDF with the procedure from Jaupart & Chabrier (2020).

along the line of sight (l.o.s.) is likely to confer some heterogeneity and anisotropy to the data. Further, one must account for l.o.s. contamination and noise (Schneider et al., 2015; Ossenkopf-Okada et al., 2016). For regions with prestellar cores, contamination acts to steepen the power-law tail of the column-density PDF and to decrease the variance in the lognormal part of the PDF (Schneider et al. (2013)). Overall, l.o.s. contamination leads to an underestimation of the *total* column-density variance.

As a typical example of initial conditions of star formation in MCs, we focus on the Polaris flare, where line of sight contamination appears to be negligible (André et al., 2010; Miville-Deschênes et al., 2010; Schneider et al., 2013). Furthermore, most of the stellar cores in this cloud are still unbound (André et al., 2010), showing that star formation activity is very recent. Polaris is therefore a good candidate to probe the statistics of *initial phases of star formation* in MCs. Data from Herschel Gould Belt survey extend across part of this cloud over approximately a 10 square degrees region with a linear size $L \sim 10$ parsecs (pc) (André et al. 2010, see also Chap. **1**). The cloud total mass and area above an extinction $A_v \geq 1$ are $M_{c,A_v\geq 1} = 1.21 \times 10^3 M_\odot$ and $A_{c,A_v\geq 1} = 3.9\,\mathrm{pc}^2$, respectively. Dust temperatures are in a narrow $T_{\mathrm{dust}} = 13 \pm 1\mathrm{K}$ interval, indicating fairly isothermal conditions with an average Mach-number $\mathcal{M} \simeq 3$ (Schneider et al., 2013).

The Polaris logarithmic column-density field η, where $\eta = \ln(\Sigma/\langle\Sigma\rangle)$, has an extended lognormal PDF with two emerging power-law tails, a first one with exponent $\alpha_{\eta,1} \simeq -4$ followed by a shallower one with exponent $\alpha_{\eta,2} \simeq -2$ (Fig. 3.1). Jaupart & Chabrier (2020) (see Chapter **4**) have shown that the first steep PLT may be due to gravity beginning to affect turbulence in parts of the cloud and hence records an early stage of (local) collapse. We have outlined in Chapter **2** a procedure to reconstruct the underlying logarithmic volume density PDF, noted$s$-PDF, where $s = \ln(\rho/\mathbb{E}(\rho))$, from data on the η-PDF. The underlying s-PDF displays a lognormal part and two PLTs with exponents $\alpha_{s,1} = -2$ and $\alpha_{s,2} = -3/2$ (see Fig. 3.1).

4.1 Filtering out large scale gradients

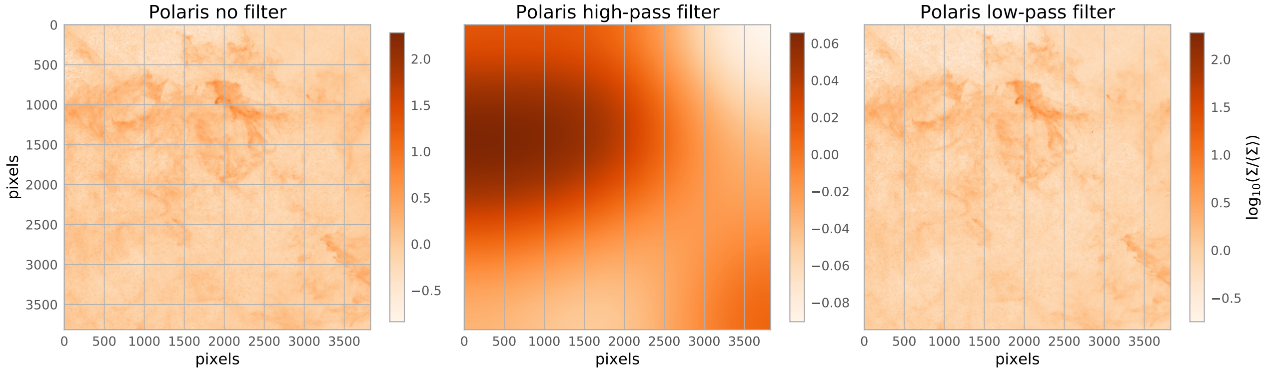

Figure 3.2 Column-density maps of the Polaris cloud. Left panel: raw data. Middle panel: with a high-pass filter, scales that are smaller than $L/2$ are effectively screened out. Right panel: a low pass filter removes data at scales larger than $L/2$. The low pass filter does not alter qualitatively the richness of structures found in the Polaris flare, whereas the high-pass filter puts emphasis on a large scale gradient likely due to integration along the line of sight.

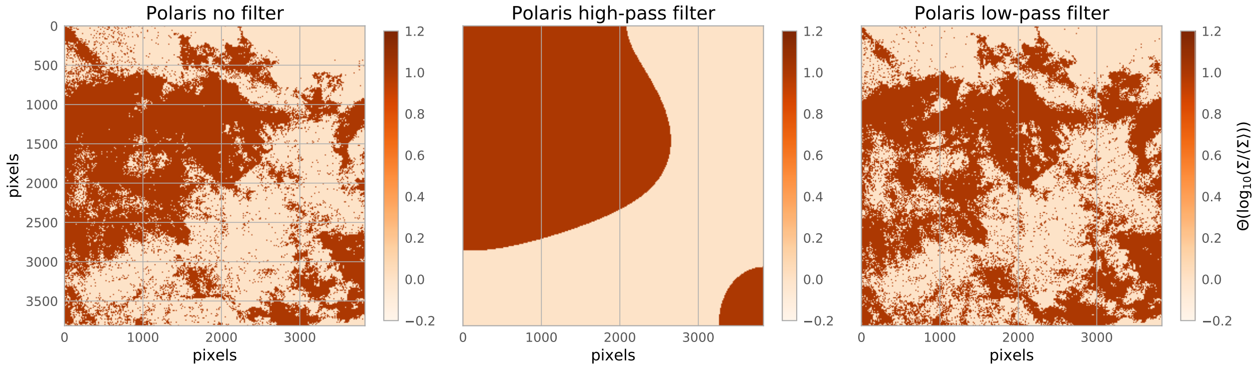

Figure 3.3 Same as Fig. (3.2) but for the binary map $\Theta(\log(\Sigma/\langle\Sigma\rangle))$ where Θ is Heaviside's step function. Regions where $\Sigma > \langle\Sigma\rangle$ appear darker than regions where $\Sigma < \langle\Sigma\rangle$.

We have shown in Chapter **2** that l.o.s. integration can generate large scale gradients and break statistical homogeneity as well as isotropy in the column density field. Filtered and unfiltered column-density maps of the Polaris flare are displayed in Figs. 3.2 and 3.3. The low pass filter does not alter qualitatively the intricate structures that exist, while the high-pass filter reveals a large scale gradient likely due to integration effects. In order to partially reduce measurement artefacts, we use a low pass filter that screens out structures larger than $L/2$ in the column-density contrast $(\Sigma - \langle\Sigma\rangle)$, and where L is the size of the observed region. We can then treat the column-density field as if it was homogeneous.

The low pass filter slightly diminishes the variance $\mathrm{Var}\,(\Sigma/\langle\Sigma\rangle)$ which is $\simeq 0.20$ and $\simeq 0.17$ for the unfiltered and low pass filtered data, respectively. It barely affects structures with a positive column-density contrasts but increases the occurrence of highly negative column-density contrasts. This is seen in Fig. 3.4, which portrays the η-PDFs of the unfiltered and low pass filtered column-density maps.

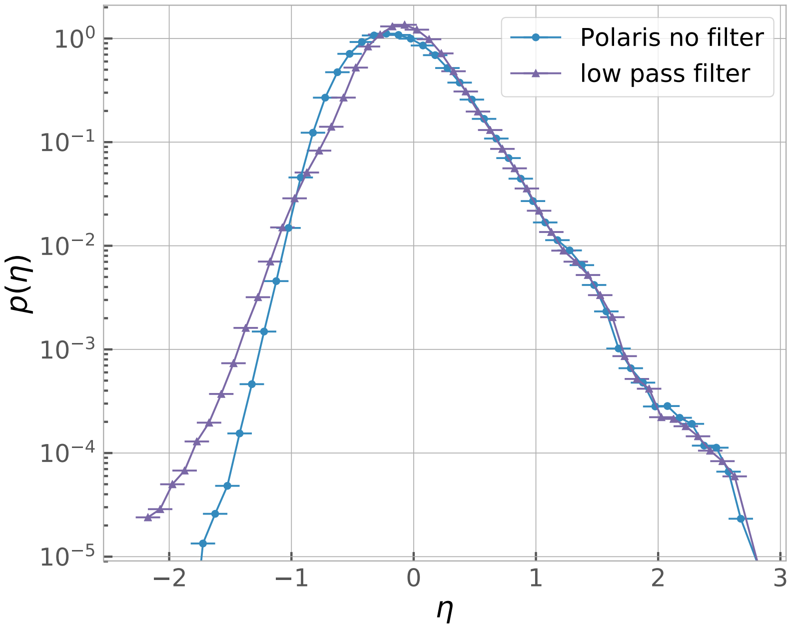

FIGURE 3.4 $\eta = \ln(\Sigma / \langle\Sigma\rangle)$-PDFs. Blue circular and purple triangular symbols represent the PDFs of the unfiltered and low pass filtered maps, respectively. The filter does not alter regions with $\eta > 0$ but increases the occurrence of regions with $\eta < -1$. Horizontal error bars represent bin spacing.

4.2 Estimated ACF and correlation length

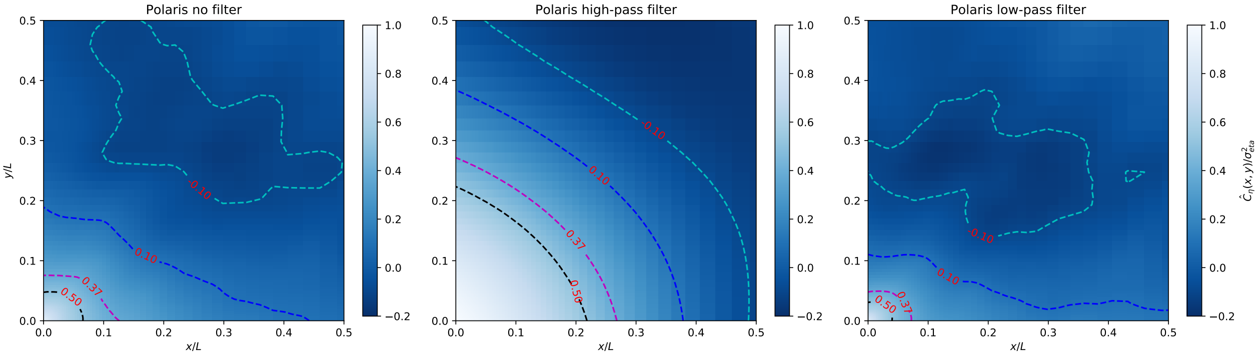

FIGURE 3.5 Reduced ACF function of η ($\hat{C}_\eta / \mathrm{Var}(\eta)$) for the Polaris flare. Left panel: without filter. Middle panel: with a high pass filter screening out scales smaller than $L/2$. Right panel: with a low pass filter screening out scales larger than $L/2$. Contours from black to purple to blue to light blue give the value of the reduced ACF at 0.5, $e^{-1} \simeq 0.37$, 0.1, −0.1.

4.2.1 Correlation length from the ACF

We now estimate the ACFs of the logarithmic column-density field $\eta = \ln(\Sigma / \langle\Sigma\rangle)$ for the three data sets (unfiltered, low and high pass filtered), using Eq. (1.71). The 2D heat-maps of the reduced ACFs $\hat{C}_\eta / \mathrm{Var}(\eta)$ are given in Fig. 3.5. The high pass filtered ACF illustrates the bias that can be introduced by integration effects. The three ACFs all seem to be anisotropic at large lags (scales) while the low pass filtered ACF seems to decay more rapidly at short lags than the unfiltered one. Fig. 3.6 displays the reduced ACF of the low pass filtered map in 3 different directions, x ($\theta = 0$), $x = y$ ($\theta = \pi/4$) and

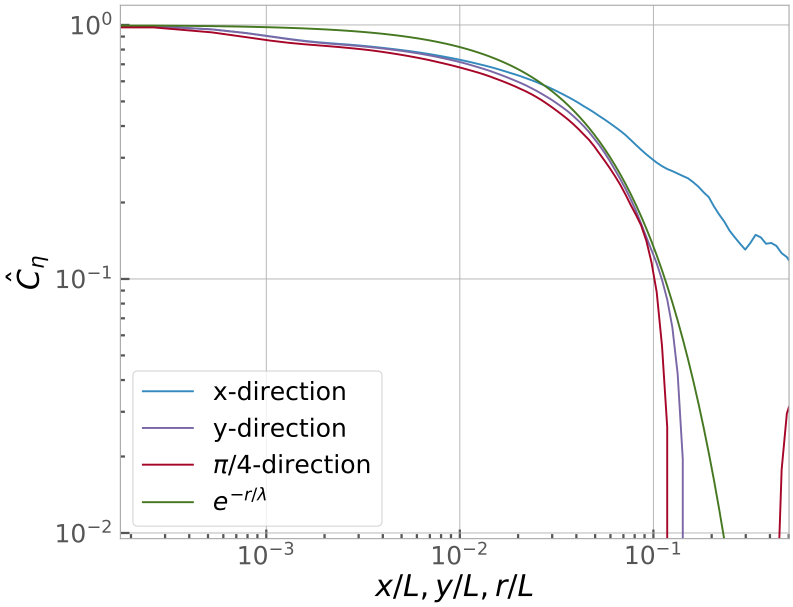

FIGURE 3.6 Reduced ACF of the low pass filtered map in three different directions. Blue line: x-direction ($y = 0$). Purple line: y-direction ($x = 0$). Red line: $\pi/4$ or $x = y$-direction. Green line: exponential fit to the tail of the ACF allowing an estimate of the decay rate (here $\lambda/L \simeq 5 10^{-2}$). A strong anisotropy is present in the x direction at large scales ($x/L \geq 2\,10^{-2}$).

y ($\theta = \pi/2$). As can be seen from the heat maps but also from Fig. 3.6, a strong anisotropy is detected at large scales in the x direction ($x/L \geq 2\,10^{-2}$). From the y-direction to the $\pi/4$-direction, the data seem to be fairly isotropic and bounded by an exponential with $\lambda/L \simeq 5 \times 10^{-2}$. Anisotropy is most pronounced along the x-direction and the resulting estimated correlation length $\hat{l}_c(\eta)$ is :

$$\boxed{\hat{l}_c(\eta) \simeq 6 \times 10^{-2}\, L \simeq \frac{1}{2}(2\pi)^{1/2}\lambda,} \tag{3.32}$$

or $\hat{l}_c(\eta)/R \simeq 1.2 \times 10^{-1}$, thus $\hat{l}_c(\eta)/R \sim 10^{-1}$. In fact, we expect Eq. (3.32) to provide upper bounds for ratios $l_c(\eta)/R$ and $l_c(\rho)/R$, because integration artefacts are partially cancelled by the low pass filter.

4.2.2 Correlation length from the variance of Σ

As discussed in Chapter **2** and Eq. (2.11), one can also estimate of value of ratio $l_c(\rho)/R$ by (1) computing the variance $\mathrm{Var}\left(\Sigma/\mathbb{E}\left(\Sigma\right)\right)$, (2) giving an estimate of $\mathrm{Var}\left(\rho/\mathbb{E}\left(\rho\right)\right)$ and (3) giving an estimate of the average thickness of the cloud (the length of the line of sight), for example by assuming that the cloud has roughly the same dimension in the three directions.

In pure compressible turbulence, $\mathrm{Var}\left(\rho/\mathbb{E}\left(\rho\right)\right) \simeq (b\mathcal{M})^2$, which is $\simeq 1$ for the Polaris case. However, when gravity starts generating power-law tails in the density PDF, the variance becomes larger than $(b\mathcal{M})^2$ (Jaupart & Chabrier, 2020). For Polaris, the column-density PDF displays a power-law tail with exponent $\alpha_\eta \simeq -4$, which is linked to an underlying density PDF with a power law tail exponent $\alpha_s \simeq -2$ (Federrath & Klessen 2013; Jaupart & Chabrier 2020 and Chap. **2**). Using the reconstructed s-PDF of Fig. (3.1) from the procedure described in Chapter **2**, we can derive an estimate of $\mathrm{Var}\left(\rho/\mathbb{E}\left(\rho\right)\right)$. In principle, for such a model PDF, the variance is infinitely large due to the power-law tails exponents $\alpha_{s,1} = -2$ and $\alpha_{s,2} = -3/2$. However, we expect a cut-off at high (column)-density, which is indeed visible in the data. This cutoff may be due to a change of thermodynamic conditions of the cloud, e.g. from isothermal to adiabatic conditions. For a typical cut-off number-density $n_{\rm ad} = 10^{10}$ cm^{-3} (Masunaga & Inutsuka, 2000; Machida et al., 2006; Vaytet et al., 2013, 2018) and for a cloud of average density $\overline{n} = 10^3$ cm^{-3}, the cutoff occurs at $s_{\rm ad} \simeq 16$. However, there may be other causes for a high density cut-off. In order to assess this possibility, we thus determine three different estimates of the variance $\mathrm{Var}\left(\rho/\mathbb{E}\left(\rho\right)\right)$ from the reconstructed s-PDF of Fig. 3.1: one densities up to 6.3 ($s \leq 6.3$), which corresponds to the onset of the 2nd PLT, a second one for $s \leq 8$ in order to include contributions from the 2nd PLT, and a third one for $s \leq 16 \simeq s_{\rm ad}$ in order to include all the data up to the adiabatic limit. We obtain $\mathrm{Var}\left(\rho/\mathbb{E}\left(\rho\right)\right) \simeq 5,\ 7,\ 227$, respectively, such that:

$$\boxed{l_c(\rho)/R \simeq 0.04,\ 0.03,\ 0.001.} \tag{3.33}$$

This provides us with the conservative estimate $l_c(\rho)/R \sim 10^{-2}$, which is an order of magnitude smaller than the value estimated from the ACF (Eq. (3.32)).

4.3 Ergodic estimate and real error bars for the observed PDF

As mentioned earlier, column-density PDFs serve as tracers of the statistics of the underlying density field. The various forms of these PDFs can be attributed to the various processes that are operating in MCs, from a fully lognormal distribution when purely turbulent motions dominate to a lognormal distribution with high density PLTs when gravitational effects become significant (Vazquez-Semadeni, 1994; Passot & Vázquez-Semadeni, 1998; Kainulainen et al., 2009; Schneider et al., 2013). This calls for a precise determination of the statistical uncertainty on the observed PDF, especially at high-density values.

The empirical PDF $\hat{f}_X(\xi_0)$ of stochastic field X (here X will be the column density η) is deduced from histograms with some bin size $\Delta\xi$. Error bars are usually estimated from Poisson statistics (using the number of points per bin) and can therefore be very small (Schneider et al., 2013). It is worth delving deeper into this issue. A histogram yields the following estimate:

$$\hat{f}_{X;L}(\xi_0)\Delta\xi \simeq \hat{F}_{X;L}(\xi_0+\Delta\xi) - \hat{F}_{X;L}(\xi_0), \tag{3.34}$$

where $\hat{F}_{X;L}$ is the empirical cumulative distribution function. Formally, this amounts to the *ergodic estimate* of the average of the following field, noted $g_{\xi_0}(\boldsymbol{y})$:

$$\begin{aligned} g_{\xi_0}(\boldsymbol{y}) &= h_{\xi_0+\Delta\xi}(X(\boldsymbol{y})) - h_{\xi_0}(X(\boldsymbol{y})), && (3.35)\\ \text{where } h_{\xi_0}(X(\boldsymbol{y})) &= \Theta(\xi_0 - X(\boldsymbol{y})) && (3.36) \end{aligned}$$

(see Chapter **2** and Sec. 3). Thus, proper statistical error levels must be calculated using the results of Sec. (2) and *in general* are *not given by Poisson statistics.* In App. B.2, we study in detail ergodic estimates of average quantities. In general, the correlation length of g_{ξ_0} is a function of ξ_0 itself. For gaussian (or lognormal) distributions, an important result is that the confidence interval becomes quite large for values $|\xi_0 - \mathbb{E}\left(X\right)| \geq \sigma(X)$, resulting in large errors if the sample size is too small. Thus, a reliable evaluation of the statistics of rare events (away from the average) requires very large sample sizes.

4.3.1 Reduced integration effects at high density contrasts

In this study, we focus on the column-density field $X = \eta$ and its PDF, noted $p(\eta)$. Using $g_{\eta_0}(\boldsymbol{y})$ and its ACF for various values η_0, we are able to determine the appropriate statistical error bars and to get rid of some of the artefacts that are due to integration along the line of sight. In practice, we expect that such artefacts are not significant in high column-density regions (see §4.1). For example, anisotropy

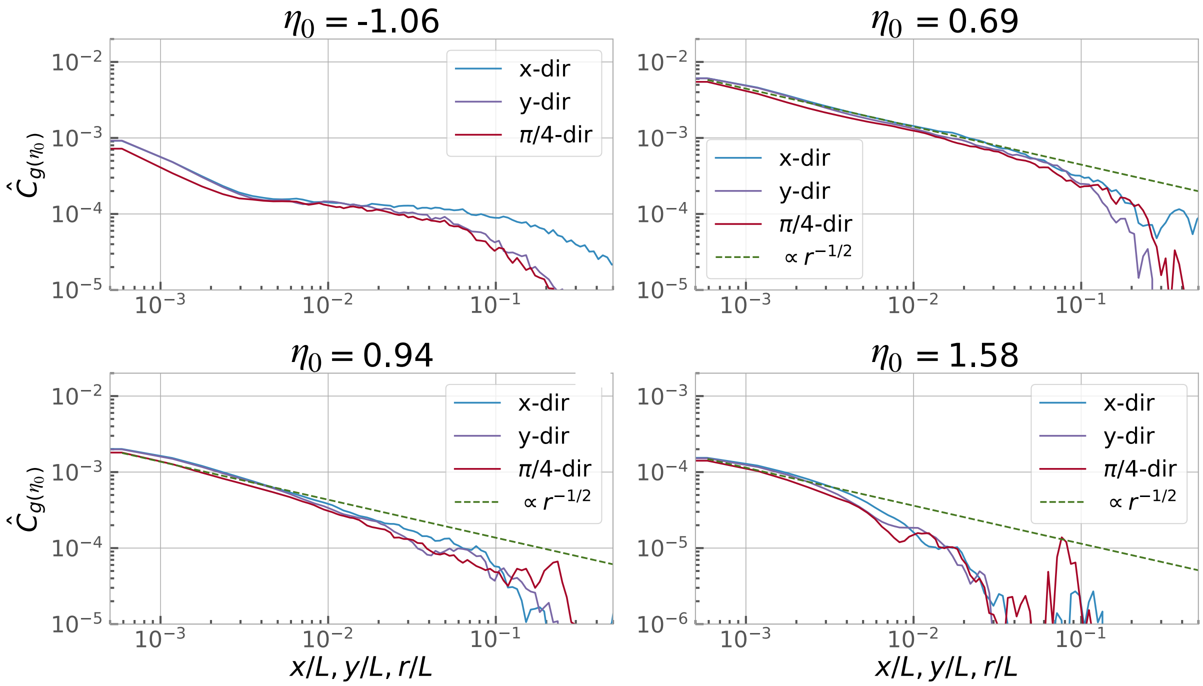

FIGURE 3.7 Estimated ACF of the field $g_{\eta_0}(\boldsymbol{y})$ for different values of $\eta_0 = \eta$ in 3 different directions. Blue, purple and red lines represent respectively the x, y and $\pi/4$ $(x = y)$ directions. The two top panels are for $\eta_0 = -1.06$ and 0.69, whereas the two bottom panels are for $\eta_0 = 0.94$ and 1.58. At low column-densities ($\eta_0 = -1.06$), a strong anisotropy is detected in the x-direction and becomes noticeable at $x/L \geq 2\,10^{-2}$ as was the case for the column-density ACF (see Fig. (3.6)). For high column-densities ($\eta_0 > 0$), however, the anisotropy is subdued and the ACFs are fairly isotropic at small scales up to x/L, $r/L \sim 10^{-1}$ where the data become quite noisy. Green dashed lines show the profile of an isotropic ACF proportional to $r^{-1/2}$ that matches the data at short scales fairly well, at least over a decade.

of the Polaris column density ACF in the x-direction is likely due to integration effects (see Sec. 4.2). We expect, however, that the ACF of field g_{η_0} for $\eta_0 > 0$ is expected to show a reduced anisotropy at short scales. We thus obtain an empirical ACF of g_{η_0} using Eq. (1.71). Fig. 3.7 displays the estimated PDF of g_{η_0} for the low pass filtered column-density map. At low column-density ($\eta_0 = -1.06$), a strong anisotropy is observed in the x-direction starting at $x/L \geq 2 \times 10^{-2}$, as for the ACF of η (see Fig. 3.6). For positive column density contrasts ($\eta_0 > 0$), this anisotropy is reduced and the ACFs are fairly isotropic at small scales in both the x and $\theta = \pi/4$ directions, up to $x/L \sim 10^{-1}$ and $r/L \sim 10^{-1}$, respectively, where r denotes separation distance in the $\theta = \pi/4$ direction. At larger separation distances, the data become quite noisy. This is consistent with the fact that the low path filtering procedure does not modify the PDF significantly in regions where $\eta > 0$ (see Fig 3.4). This suggests that most of the η ACF anisotropy in the x-direction at scales in the $10^{-2} - 10^{-1}$ range is due to integration effects.

The peak of the correlation in the $\pi/4$-direction at high column-densities ($\eta_0 = 1.58$) is probably due to the presence of the "Saxophone"-shaped filamentary structure that may be seen at the top of Fig. 3.2, which hosts most of the Polaris high density regions (Schneider et al., 2013).

4.3.2 Statistical Errorbars

Using the statistics of $g_{\eta_0}(\boldsymbol{y})$ has several advantages. One is that it reduces the impact of l.o.s. integration artefacts. In addition, it leads to proper error estimates for the empirical PDF. Introducing some function of η_0 noted $\varphi(\eta_0)$ which is expected to increase for increasing values of $|\eta_0|$, the confidence interval above $(1-1/m^2)$ can be written as follows (see Bienayme-Tchebychev inequality, Eq. (3.7)):

$$\boxed{p(\eta_0) \equiv f_\eta(\eta_0) = \hat{f}_L(\eta_0)\left(1 \pm m\left(\varphi(\eta_0)\right)^{1/2}\left(\frac{l_c(X)}{R}\right)^{D/2}\right),} \tag{3.37}$$

From the empirical ACF $C_{g_{\eta_0}}$, one can then estimate the correlation length of g_{η_0} and thus that of $\varphi(\eta_0)$ for every η_0. Unfortunately, this procedure is hampered by the fact that the ACF becomes increasingly noisy at high contrasts $|\eta_0| > 1$, due to sample sizes that are too small.

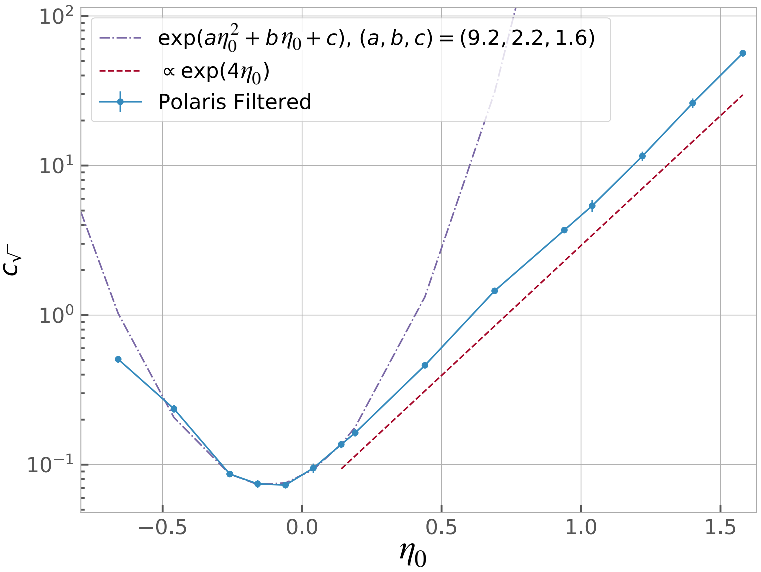

FIGURE 3.8 Constant of proportionality $c_{\sqrt{}}$ such that $C_{g_{\eta_0}}(\boldsymbol{y}) = (f_\eta(\eta_0)\Delta x)^2 \times c_{\sqrt{}}/\sqrt{|\boldsymbol{y}|/L}$ at short scales.

In principle, one must calculate the complete integral that defines $l_c(g_{\eta_0})$ in order to determine $\varphi(\eta_0)$. This may be avoided as follows. The growth of $\varphi(\eta_0)$ may be obtained by looking at the short scale behaviour of the ACFs of g_{η_0}. In Fig. 3.7, it appears that the values of $\hat{C}_{g_{\eta_0}}$ for positive column density contrasts ($\eta > 0$) are isotropic and close to being $\propto |\boldsymbol{y}|^{-1/2}$ at short scales. We thus write that:

$$\hat{C}_{g_{\eta_0}}(\boldsymbol{y}) = (f_\eta(\eta_0)\Delta x)^2 \times c_{\sqrt{}}\,|\boldsymbol{y}/L|^{-1/2} \tag{3.38}$$

where $c_{\sqrt{}}$ is a constant of proportionality that depends on η_0. Values of $c_{\sqrt{}}$ as a function of η_0 are given in Fig. 3.8. We have only studied g_{η_0} for $-0.7 \leq \eta_0 \leq 1.58$, because the ACFs are extremely noisy at high positive density contrasts ($\eta \geq 1.58$) due to poor sampling. At negative density contrasts ($\eta \leq -0.7$), where integration artefacts are the largest (see §4.3.1), the ACFs are no longer sufficiently isotropic and do not conform to a scaling in $|\boldsymbol{y}|^{-1/2}$. Fig. 3.8 shows that $c_{\sqrt{}}(\eta_0)$ is an increasing function of $|\eta_0|$ for large $|\eta_0|$, illustrating that $\varphi(\eta_0)$ is expected to be large compared to $f_\eta(\eta_0)$ for large contrasts $|\eta_0| > 1$.

4.3.3 Gaussian approximation; effective error bars on the observed PDF

To emphasize the behaviour of $\varphi(\eta_0)$ and to circumvent difficulties in estimating it, *we assume* that $X = \eta$ is either gaussian (usual lognormal description) or, more generally, is a deterministic function of a Gaussian field $X = \psi(S)$, where ψ is a diffeomorphism and S a Gaussian field (see App. B.4).

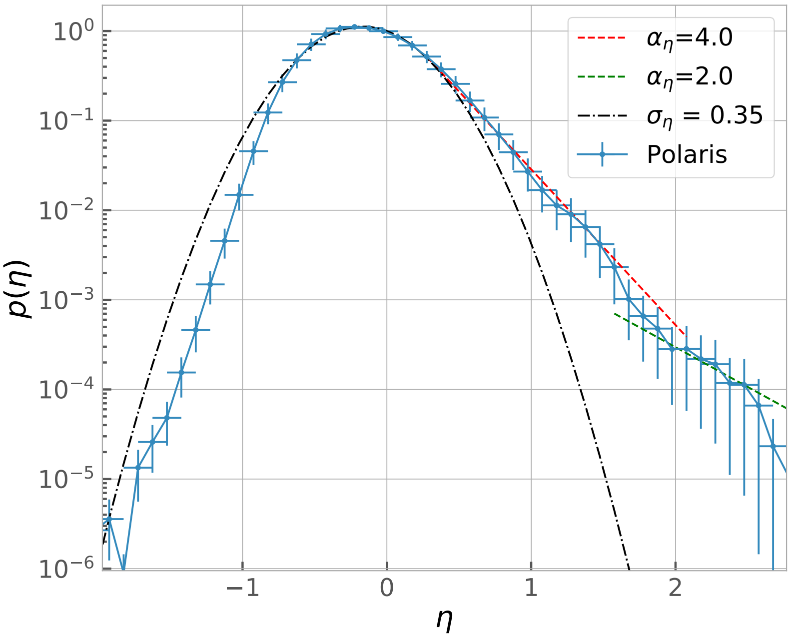

FIGURE 3.9 PDF of the logarithmic column-density η with statistical errorbars; $m = \sqrt{2}$, $l_c(\eta)/R = 10^{-2}$. In all likelihood, these error bars are underestimated at high column densities for $|\eta| \geq 1$. This emphasizes that error bars should not be derived from Poisson statistics and that the accuracy of the high end part of the PDF gets degraded by the small sample size.

Assuming further C_S is a monotonically decreasing function, one has:

$$\varphi(\eta_0) \geq \left(\frac{l_c(S)}{l_c(\eta)}\right)^D \left(c_0 + c_1\, \psi^{-1}(\eta_0)^2\right), \tag{3.39}$$

where $c_0 \gtrsim 0.1$, $c_1 \geq 0.77$ and $\psi^{-1}(\eta_0) = (\eta_0 - \langle\eta\rangle)/\sigma(\eta)$ if η is already gaussian. Provided that the variance of $X = \eta$ is not too large, we further expect that $l_c(S) \sim l_c(\eta)$ (as is the case for a lognormal distribution where $\psi = \exp$ (see §3 and App. B.4).

Fig. (3.9) displays the empirical Polaris PDF, with error bars computed from Eqs. (3.37) and (3.39) using:

$$\boxed{\varphi(\eta_0) = 0.17 + 0.88(\eta_0^r)^2,} \tag{3.40}$$

where values of (c_0, c_1) are calculated for an exponential ACF and where $\eta_0^r = (\eta_0 - \langle\eta\rangle)/\sigma(\eta)$. We have taken $l_c(\eta)/R = 10^{-2}$ and $m = \sqrt{2}$ to obtain a confidence interval larger than 50%. With this parameterization, one may determine appropriate error bars for cloud PDFs. These error bars are likely underestimated for $|\eta| \geq 1$. However, they serve to emphasize that error bars should not be derived from Poisson statistics and that the accuracy of the high end part of the PDF is severely degraded by sample sizes that are too small.

Furthermore, under the assumption that η is either gaussian (i.e. Σ is lognormal, as common usage) or, more generally, a deterministic function of a Gaussian field, the $|\boldsymbol{y}|^{-1/2}$ scaling indicates that the resolution of the data remains larger than the "viscous scale", which is such that $\left[\tilde{C}_\eta(\boldsymbol{y}) - 1\right] \propto |\boldsymbol{y}|^2$. (which corresponds to a scaling $\propto |\boldsymbol{y}|^{-1}$). Thus, the short scale behavior of $\hat{C}_{g_{\eta_0}}$ is given by:

$$\frac{1}{\left(1 - \tilde{C}_S(\boldsymbol{y})^2\right)^{1/2}} \exp\left(-\frac{1}{2}(\psi^{-1}(\eta_0))^2\right) \times f_X(\eta_0)^2\,(\Delta x)^2. \tag{3.41}$$

If $\hat{C}_{g_{\eta_0}}(\boldsymbol{y}) \propto |\boldsymbol{y}|^{-1/2}$, this implies that $\tilde{C}_S(\boldsymbol{y}) \simeq 1 - |\boldsymbol{y}|/\lambda$ at short scale, and that:

$$c_{\surd}(\eta_0) = \exp\left(-\frac{1}{2}(\psi^{-1}(\eta_0))^2\right)\sqrt{\frac{\lambda}{2L}}. \tag{3.42}$$

We then determine the minimum of $c_{\surd}(\eta_0)$ and find that $\lambda/L \simeq 1.2 \times 10^{-2}$. Assuming that, due to the fact that η is almost gaussian, $\lambda/L \sim l_c(\eta)/L$, we obtain $l_c(\eta)/R \sim 10^{-2}$, in agreement with Eq. (3.33).

5 Applications to the Orion B cloud

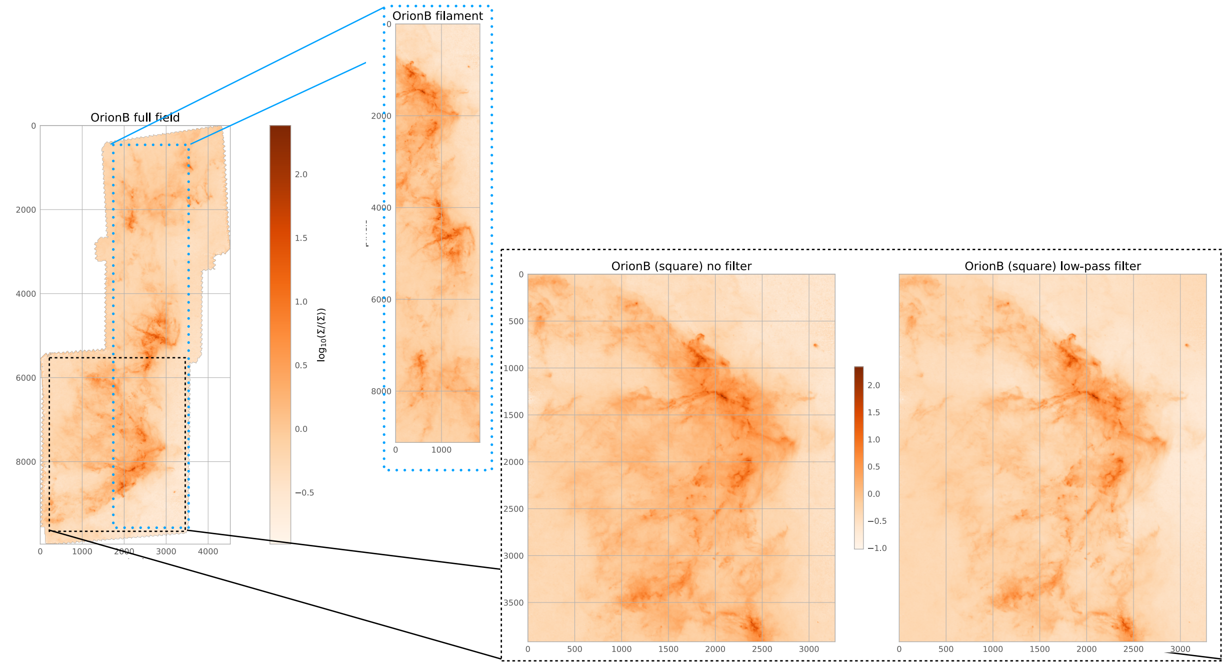

FIGURE 3.10 Column-density maps of the Orion B cloud. Left panel: Full observed field. Middle panel: extracted filament region. Right panel: extracted "square" region, unfiltered and low pass filtered (see §4).

In this section, we apply the results of §2 to the Orion B cloud (Schneider et al., 2013; Orkisz et al., 2017), another well studied star-forming MC. In this case, one encounters additional difficulties because the observed field is markedly elongated in the "vertical" direction (y) with data over a region whose geometrical shape is not suited to a straightforward data analysis (see Fig. 3.10). For this reason, we have extracted 2 parts of the cloud with rectangular shapes. One is elongated with a length that is close to the vertical dimension (L_y) of the total field of observation, which we shall refer to as a "filament". A second part is rectangular one with an aspect ratio close to 1 with a length close to the maximum horizontal length of the full cloud (L_x), which we shall refer to as a "square" region (see Fig. 3.10). We determine the ACF of these two subregions and the associated correlation lengths in App. C .

Using the ACF, we find that $l_c(\eta)/L_x \sim 10^{-1}$. From use the variances $\mathrm{Var}\,(\rho)$ and $\mathrm{Var}\,(\Sigma)$, we obtain a lower value : $l_c(\eta)/L_z \sim 10^{-2}$, where L_z is the characteristic thickness of the cloud (along the line of sight).

6 Consequences for the estimation of the total gravitational energy of a cloud.

Previously, we have built a general framework aimed to assess the relevance and validity of a statistical approach to studies of star-forming molecular clouds (MCs) relying on a limited number of observations or simulations. We have calculated the auto-covariance function (ACF) and correlation length in molecular cloud density fields and shown how to determine proper statistical error bars on the observed probability density functions (PDF). Applying these results to two typical star-forming clouds, Polaris and Orion B, which display two different types of column-density PDFs, we have shown that the ratio of the correlation length of density fluctuations over the cloud size is typically $l_c/L \lesssim 0.1$, which justifies the assumption of statistical homogeneity.

6.1 Motivation

In this section, we apply the same formalism to other characteristics (observational or numerical) of MCs. Observations cannot unravel the entire complexity of the internal structure of star forming clouds. Thus, it is important to know whether *global* characteristics, such as the total mass and size of the cloud, can be used to obtain accurate estimates of other global physical quantities of importance for cloud dynamics, such as the total gravitational (binding) energy and its virial parameter.

6.2 Correlation length and gravitational binding energy

In Sec. 2, we have relied on the correlation length to determine confidence intervals for the measured statistical quantities. Here, we follow similar lines of argument to assess the accuracy of estimates of cloud characteristics deduced from *global* properties without any knowledge of the cloud internal structure. We focus on the cloud potential energy, noted $|e_G|$, and virial parameter, noted $\alpha_{\rm vir}$, which can be deduced the total mass M and size L. This key issue was raised in particular by Federrath & Klessen (2012, 2013) (see Chapter **1**). In their numerical simulations of turbulent star-forming MCs, these authors found a large discrepancy between values of the virial parameter deduced from the cloud's global (average) characteristics and measured directly in the numerical results. These authors concluded that *"this shows that comparing simple theoretical estimates of the virial parameter, solely based on the total mass, as a measure for $|e_G|$ [...], should be considered with great caution because such an estimate ignores the internal structure of the clouds."* We show below that the dependence of the total potential energy and virial parameter on the "internal structure" can be assessed from the knowledge of the correlation length of density fluctuations within the cloud, $l_c(\rho)$. We further show that the problem raised by Federrath & Klessen (2012) is due primarily to artificial effects stemming from the resolution of the Poisson equation in a periodic box.

We first start by deriving the total potential energy, noted ${e_G}$[3], of a *statistically* homogeneous cloud in a domain Ω in any geometry, and isolate the contribution of the "internal structure" from the rest. For the sake of simplicity, we assume that the cloud possesses a center of symmetry which we take as the origin, such that $\forall \boldsymbol{y} \in \Omega$, $-\boldsymbol{y} \in \Omega$:

$$
\begin{aligned}
\langle e_G \rangle &= \langle e_G(\rho) \rangle = \frac{1}{|\Omega|} \int_\Omega \rho(\boldsymbol{x})\, \Phi_G(\boldsymbol{x}) \mathrm{d}\boldsymbol{x} && (3.43) \\
&= \frac{1}{|\Omega|} \int_\Omega \rho(\boldsymbol{x}) \int_\Omega \rho(\boldsymbol{x'})\, \Phi_{\rm Green}(\boldsymbol{x}-\boldsymbol{x'})\, \mathrm{d}\boldsymbol{x'}\, \mathrm{d}\boldsymbol{x} && (3.44) \\
&= \langle e_G(\langle \rho \rangle) \rangle + \int_{\Omega^2} \frac{\delta\rho(\boldsymbol{x})\delta\rho(\boldsymbol{x'})}{|\Omega|} \Phi_{\rm Green}(\boldsymbol{x}-\boldsymbol{x'})\, \mathrm{d}\boldsymbol{x'}\, \mathrm{d}\boldsymbol{x}
\end{aligned}
$$

---

[3] The usual definition of the binding energy involves a 1/2 multiplying factor in order to account for summations on interacting pairs, which we omit here for the sake of clarity.

$$
\begin{aligned}
& +2\left\langle\rho\right\rangle \int_{\Omega^2} \frac{\delta\rho(\boldsymbol{x})}{|\Omega|}\Phi_{\text{Green}}(\boldsymbol{x}-\boldsymbol{x'})\,\mathrm{d}\boldsymbol{x'}\,\mathrm{d}\boldsymbol{x} && (3.45)\\
= \; & \left\langle e_G(\left\langle\rho\right\rangle)\right\rangle + I_C(\rho) + 2\left\langle\rho\right\rangle I_\delta(\rho), && (3.46)
\end{aligned}
$$

where $|\Omega| = L^3$ is the volume of the Ω domain, Φ_{Green} is the Green's function of the gravitation potential which is parity invariant, $\langle\rho\rangle$ is the (volumetric) average density of the cloud

$$
\left\langle\rho\right\rangle = \frac{1}{|\Omega|}\int_\Omega \rho(\boldsymbol{x})\mathrm{d}\boldsymbol{x} = M/|\Omega|, \tag{3.47}
$$

$\delta\rho = \rho - \langle\rho\rangle$, and $\langle e_G(\langle\rho\rangle)\rangle$ is the potential energy of the cloud if it was strictly homogeneous:

$$
\left\langle e_G(\left\langle\rho\right\rangle)\right\rangle = \frac{1}{|\Omega|}\int_\Omega \left\langle\rho\right\rangle \Phi_G(\boldsymbol{x})\mathrm{d}\boldsymbol{x}. \tag{3.48}
$$

Using the change of fields $(\boldsymbol{u},\boldsymbol{v}) = \varphi(\boldsymbol{x},\boldsymbol{x'}) = (\boldsymbol{x}-\boldsymbol{x'},\boldsymbol{x}+\boldsymbol{x'})$ and denoting by $\hat{C}_{\rho,L}$ the biased ergodic estimator of the ρ ACF (see Chapter **1**), we obtain:

$$
\begin{aligned}
I_C(\rho) &= \int_{\varphi_1(\Omega)} \mathrm{d}\boldsymbol{u}\Phi_{\text{Green}}(\boldsymbol{u}) \int_{\varphi_2^{\boldsymbol{u}}(\Omega)} \frac{\mathrm{d}\boldsymbol{v}}{8|\Omega|}\delta\rho(\frac{\boldsymbol{u}+\boldsymbol{v}}{2})\delta\rho(\frac{\boldsymbol{u}-\boldsymbol{v}}{2})\\
&= \int_{\varphi_1(\Omega)} \mathrm{d}\boldsymbol{u}\Phi_{\text{Green}}(\boldsymbol{u})\,\hat{C}_{\rho,L}(\boldsymbol{u}), && (3.49)
\end{aligned}
$$

$$
\begin{aligned}
I_\delta(\rho) &= \int_{\varphi_1(\Omega)} \mathrm{d}\boldsymbol{u}\Phi_{\text{Green}}(\boldsymbol{u}) \int_{\varphi_2^{\boldsymbol{u}}(\Omega)} \frac{\mathrm{d}\boldsymbol{v}}{8|\Omega|}\delta\rho(\frac{\boldsymbol{u}+\boldsymbol{v}}{2})\\
&\ll \frac{\left\langle e_G(\left\langle\rho\right\rangle)\right\rangle}{2\left\langle\rho\right\rangle}, && (3.50)
\end{aligned}
$$

where $(\varphi_1(\Omega), \varphi_2^{\boldsymbol{u}}(\Omega))$ is a parameterisation of $\varphi(\Omega^2)$ (see App. D). For example,

$$
\begin{aligned}
\text{if } \Omega &= \left[-\frac{L}{2},\frac{L}{2}\right]^3, && (3.51)\\
\varphi_1(\Omega) &= [-L, L]^3 && (3.52)\\
\text{and } \varphi_2^{\boldsymbol{u}}(\Omega)) &= [-L+|u_i|, L-|u_i|]]\,. && (3.53)
\end{aligned}
$$

We then write $\hat{C}_\rho = \mathrm{Var}(\rho)\times\tilde{C}_\rho$, such that $\tilde{C}_\rho(0) = 1$ to finally obtain:

$$
\boxed{\left\langle e_G\right\rangle \simeq \left\langle e_G(\left\langle\rho\right\rangle)\right\rangle + \mathrm{Var}\left(\rho\right)\int_{\varphi_1(\Omega)} \mathrm{d}\boldsymbol{u}\Phi_{\text{Green}}(\boldsymbol{u})\,\tilde{C}_{\rho,L}(\boldsymbol{u}).} \tag{3.54}
$$

In this expression, the contributions from the global (average) observables and the 'internal structure' are separated explicitly. We now compare the case of two geometrical configurations, the 'real' space $\mathbb{R}^3$, relevant to observations, and the periodic simulation box $\mathbb{T}^3$.

6.2.1 Isolated cloud

In $\mathbb{R}^3$, $\Phi_{\text{Green}}(\boldsymbol{x}) = -G/|\boldsymbol{x}|$. Thus:

$$
\left\langle e_G\right\rangle_{\mathbb{R}^3} = \left\langle e_G(\left\langle\rho\right\rangle)\right\rangle_{\mathbb{R}^3} - G\mathrm{Var}\left(\rho\right)\int_{\varphi_1(\Omega)} \mathrm{d}\boldsymbol{u}\,\frac{\tilde{C}_{\rho,L}(\boldsymbol{u})}{|\boldsymbol{u}|}, \tag{3.55}
$$

where

$$\langle e_G(\langle\rho\rangle)\rangle_{\mathbb{R}^3} = -2\,G\,Mc_g\frac{\langle\rho\rangle}{L}, \tag{3.56}$$

where c_g is a geometric factor of order unity *if the cloud is roughly of the same dimension L in the three directions*. For example, if $\Omega = B(R)$ is a ball[4] of radius $R = L/2$, $c_g = 1.2$. On the other hand, if $\Omega = \left[-\frac{L}{2}, \frac{L}{2}\right]^3$ is a cuboid of size L, $c_g \simeq 1.9/2 \simeq 0.95$. We then write:

$$\int_{\varphi_1(\Omega)} \mathrm{d}\boldsymbol{u}\,\frac{\tilde{C}_{\rho,L}(\boldsymbol{u})}{|\boldsymbol{u}|} = 8\,\tilde{c_g}\,l_c(\rho)^2 f\left(R/l_c(\rho)\right), \tag{3.57}$$

where $\tilde{c_g}$ is another geometric factor of order unity and f is some function which converges rapidly towards 1. For an exponential ACF, $\tilde{c_g} = \pi^{1/3}/2 \simeq 0.73$ and $f(x) \simeq 1-(1+x)\mathrm{e}^{-x}$. Taking advantage of the fact that $l_c/R \lesssim 0.1$ (see Sec. 4 and 5), we obtain $f\left(R/l_c(\rho)\right) \simeq 1$ and:

$$\langle e_G\rangle_{\mathbb{R}^3} \simeq -2\,G\,Mc_g\frac{\langle\rho\rangle}{L}\left(1+\frac{4\mathrm{Var}\left(\rho\right)L}{\langle\rho\rangle\,M}\frac{\tilde{c_g}}{c_g}l_c(\rho)^2\right) \tag{3.58}$$

$$\simeq -2\,G\,Mc_g\frac{\langle\rho\rangle}{L}\left(1+2\frac{\tilde{c_g}}{c_g\,\xi_g}\mathrm{Var}\left(\frac{\rho}{\langle\rho\rangle}\right)\left(\frac{l_c(\rho)}{R}\right)^2\right), \tag{3.59}$$

where, ξ_g is of order unity (for a ball $\xi_g = \pi/3$ and for a cube $\xi_g = 2$). In Chapter **2**, we have derived a useful relation relating the variance of the density field ρ to that of the column density Σ and the correlation length $l_c(\rho)$:

$$\mathrm{Var}\left(\frac{\Sigma}{\langle\Sigma\rangle}\right) \simeq \mathrm{Var}\left(\frac{\rho}{\langle\rho\rangle}\right)\frac{l_c(\rho)}{R}, \tag{3.60}$$

provided that $l_c/R \ll 1$ (see Eq. (2.11)). Thus, we have

$$\langle e_G\rangle_{\mathbb{R}^3} \simeq -2\,G\,Mc_g\frac{\langle\rho\rangle}{L}\left(1+2\frac{\tilde{c_g}}{c_g\,\xi_g}\mathrm{Var}\left(\frac{\Sigma}{\langle\Sigma\rangle}\right)\left(\frac{l_c(\rho)}{R}\right)\right). \tag{3.61}$$

This equation enables us to evaluate the influence of the internal structure of the cloud from observations of column-densities. We thus see that the contribution of the cloud internal structure to the average gravitational energy is negligible if, for volume densities, the product $\mathrm{Var}\left(\rho/\left\langle\rho\right\rangle\right) \times \left(l_c(\rho)/R\right)^2 \ll 1$, or if, for column densities, the product $\mathrm{Var}\left(\Sigma/\left\langle\Sigma\right\rangle\right) \times \left(l_c(\rho)/R\right) \ll 1$.

For isothermal turbulent conditions, $\mathrm{Var}(\rho) \simeq (b\mathcal{M})^2\mathbb{E}\left(\rho\right)^2 \simeq (b\mathcal{M})^2\left\langle\rho\right\rangle^2$ and we get :

$$\mathrm{Var}\left(\frac{\rho}{\langle\rho\rangle}\right)\left(\frac{l_c(\rho)}{R}\right)^2 \simeq \left(\frac{(b\mathcal{M})l_c(\rho)}{R}\right)^2, \tag{3.62}$$

where b is a coefficient that depends on the type of forcing on turbulence (Federrath et al. 2008 and previous chapters). For typical MC conditions in the Milky Way, $(b\mathcal{M}) \lesssim 5$ ($\mathcal{M} \sim 10$ and $b \simeq 0.5$). As shown in Sec. 4 and 5, $l_c(\rho)/R \lesssim 0.1$ (and even probably $l_c(\rho)/R \sim 10^{-2}$) in these clouds, and hence we conclude that :

$$\boxed{\langle e_G\rangle_{\mathbb{R}^3} \simeq -2\,G\,Mc_g\frac{\langle\rho\rangle}{L}\left(1+\tilde{\xi_g}\right),} \tag{3.63}$$

where $\tilde{\xi_g} \equiv \tilde{\xi_g}\left(b\mathcal{M}, l_c(\rho)/R\right)$ is again *at most* of order unity for large values of $b\mathcal{M} \sim 10$ and $l_c/R \simeq 0.1$, but is of the order of a few percents in most cases.

---

[4] Remember that we have omitted the usual factor 1/2 in the definition of the binding energy.

When gravity starts to affect the cloud dynamics and the density PDF develops an extended power-law tail, the variance of ρ can become very large. In that case, the product $\mathrm{Var}\left(\rho/\left<\rho\right>\right) \times (l_c(\rho)/R)^2$ may become large enough to affect the e_G estimate significantly. Physically speaking, this occurs when gravity has started to break up the cloud in small condensed regions. Even so, we still expect that $\mathrm{Var}\left(\Sigma/\left<\Sigma\right>\right) \times (l_c(\rho)/R) \ll 1$ for typical star forming initial conditions, as found in Sec. 4 and 5 for Polaris and Orion B, where $\mathrm{Var}\left(\Sigma/\left<\Sigma\right>\right) \times (l_c(\rho)/R) \lesssim 10^{-1}$.

Therefore, we conclude that for typical star forming conditions, the gravitational potential energy can be obtained from the total mass and size of the cloud with a good accuracy. Uncertainties come mostly from geometrical factors in Eq. (3.56) and the (observationally undertermined) internal structure of the cloud only contributes a small correction. We now show that this is no longer true for numerical simulations in a periodic box of Volume $V_{Box} = L^3$.

6.2.2 Simulations in a periodic box

In a periodic box (topology $\mathbb{T}^3$) of volume $V_{Box} = L^3$, the gravitation potential Φ_G satisfies the modified Poisson equation:

$$\Delta\Phi_{\mathrm{G}}^L(x) = 4\pi G\left(\rho(x) - \frac{M}{V_{box}}\right), \tag{3.64}$$

where M is the total mass in the box (Ricker, 2008; Guillet & Teyssier, 2011). This is due to the ill-posed problem of the standard Poisson equation in $\mathbb{T}^3$ and is a well known feature of statistical mechanics of Coulomb systems. Then, the Green function of the gravitational potential satisfies:

$$\Delta\Phi_{\mathrm{Green}}^L(x) = 4\pi G\left(\delta(x) - \frac{1}{V_{box}}\right). \tag{3.65}$$

Rescaling the various fields, $y = x/L$, $\Phi_{\mathrm{Green}}^L(x) = \Phi_{\mathrm{Green}}(Ly)$, one ends up with:

$$\Delta\Phi_{\mathrm{Green}}(y) = 4\pi G(\delta(y) - 1). \tag{3.66}$$

We note that Φ_{Green} is periodic and defined up to a constant which is usually chosen to be such that the average of Φ_{Green}, or the zero mode of its Fourier transform, is 0. Then

$$\left<e_G(\left<\rho\right>)\right>_{\mathbb{T}^3} = 0, \tag{3.67}$$

and

$$\begin{aligned}
\left<e_G\right>_{\mathbb{T}^3} &= \int_{[-\frac{1}{2},\frac{1}{2}]^3} \hat{C}_{\rho,L}(L\boldsymbol{y})\,\Phi_{Green}(y)\mathrm{d}y && (3.68)\\
&= 8\int_{[0,\frac{1}{2}]^3} \hat{C}_{\rho,L}(L\boldsymbol{y})\,\Phi_{Green}(y)\mathrm{d}y, && (3.69)
\end{aligned}$$

where we have used the periodicity of ρ and Φ_{Green} and the symmetry properties of the box. Then:

$$\boxed{\left<e_G\right>_{\mathbb{T}^3} = 8\,\mathrm{Var}(\rho)\int_{[0,\frac{1}{2}]^3} \tilde{C}_{\rho,L}(Ly)\,\Phi_{Green}(y)\mathrm{d}y.} \tag{3.70}$$

In this case, therefore, the gravitational potential is *only a measure of the internal, fluctuating density structure within the box.*

In the following, we examine the case of pure turbulent (initial) conditions, as in Federrath &

Klessen (2012, 2013). We thus write

$$\langle e_G \rangle_{\mathbb{T}^3} \;=\; 2\,G\,\mathrm{Var}(\rho)\,l_\mathrm{c}^2\,g_{b,\mathcal{M}}\,(L/l_\mathrm{c})\,, \tag{3.71}$$

where $g_{b,\mathcal{M}}$ is some bounded function which may depend on the Mach number $\mathcal{M}$ and the type of turbulence forcing, as measured by coefficient b. Noting that $\mathrm{Var}(\rho) \simeq (b\mathcal{M})^2\,\langle\rho\rangle^2$, we obtain:

$$\begin{aligned} \langle e_G \rangle_{\mathbb{T}^3} &= 2\,G\,(b\mathcal{M})^2\,\langle\rho\rangle^2\,l_\mathrm{c}^2\,g_{b,\mathcal{M}}\,(L/l_\mathrm{c}) & (3.72)\\ &= 2\,G\,M\frac{\langle\rho\rangle}{L}\left(\frac{(b\mathcal{M})l_c}{L}\right)^2 g_{b,\mathcal{M}}\,(L/l_\mathrm{c})\,. & (3.73) \end{aligned}$$

6.3 Virial parameter

An important quantity in the study of MCs is the virial parameter, which is defined as the ratio of twice the kinetic energy over the gravitational energy, $\alpha_\mathrm{vir} = 2\,\langle e_K\rangle/|\,\langle e_G\rangle\,|$ (see e.g. McKee & Zweibel 1992 for a more complete discussion). For clarity purposes, we shall use again the simulations of Federrath & Klessen (2012) for comparisons in $\mathbb{T}^3$ and restrict ourselves to isothermal turbulence conditions. In these conditions, the following conditional expectation holds (Kritsuk et al., 2007; Federrath et al., 2010):

$$\mathbb{E}\,(\mathcal{M}\,|\,\rho) \simeq \mathbb{E}\,(\mathcal{M})\,, \tag{3.74}$$

and we get :

$$\langle e_K\rangle \simeq \langle\rho\rangle\,\sigma_V^2 \simeq \mathbb{E}\,(\rho)\,\sigma_V^2, \tag{3.75}$$

where σ_V is the 3D velocity dispersion. This yields the virial parameters

$$\alpha_{\mathrm{vir},\mathbb{R}^3} = \frac{\sigma_V^2\,L}{2\,G\,M\,(1+\tilde{\xi}_g)\,c_g} = \frac{\sigma_V^2\,L}{2\,G\,M}\frac{1}{(1+\tilde{\xi}_g)\,c_g}, \tag{3.76}$$

where $2\,\tilde{\xi}_g\,c_g$ is usually taken to be equal to 1 in order to match the virial parameter with that of a homogeneous sphere, and

$$\alpha_{\mathrm{vir},\mathbb{T}^3} = \frac{\sigma_V^2\,L}{2\,G\,M g_{b,\mathcal{M}}\,(L/l_\mathrm{c})}\left(\frac{L}{(b\mathcal{M})\,l_\mathrm{c}}\right)^2. \tag{3.77}$$

The ratio of the two virial parameters is therefore:

$$\boxed{\frac{\alpha_{\mathrm{vir},\mathbb{T}^3}}{\alpha_{\mathrm{vir},\mathbb{R}^3}} \simeq \frac{1}{g_{b,\mathcal{M}}\,(L/l_c)}\left(\frac{L}{(b\mathcal{M})\,l_\mathrm{c}}\right)^2.} \tag{3.78}$$

We can test the validity of this equation. Assuming that the type of turbulence forcing has only a moderate influence on $\tilde{C}_{\rho,L}$ and thus on $g_{b,\mathcal{M}}\,(L/l_c)\,l_\mathrm{c}^2$ (see Eq. (3.71)), we have, for a given large scale Mach number $\mathcal{M}$ and size L:

$$\alpha_{\mathrm{vir},\mathbb{T}^3}/\alpha_{\mathrm{vir},\mathbb{R}^3} \propto b^{-2}. \tag{3.79}$$

Even though forcing parameter b may have some small influence on $g_{b,\mathcal{M}}\,(L/l_c)\,l_\mathrm{c}^2$, we still expect the ratio Eq. (3.78) to decrease when b increases, with a scaling close to b^{-2}. Indeed, we find a good agreement, within one order of magnitude, between this scaling and the results obtained in (Federrath & Klessen, 2012, 2013), even when we consider variations in the Mach number and virial parameters (Fig. 3.11).

These calculations demonstrate the origin of the large differences between values of the gravitational potential and virial parameter that are calculated in a periodic simulation domain($\mathbb{T}^3$) and those that

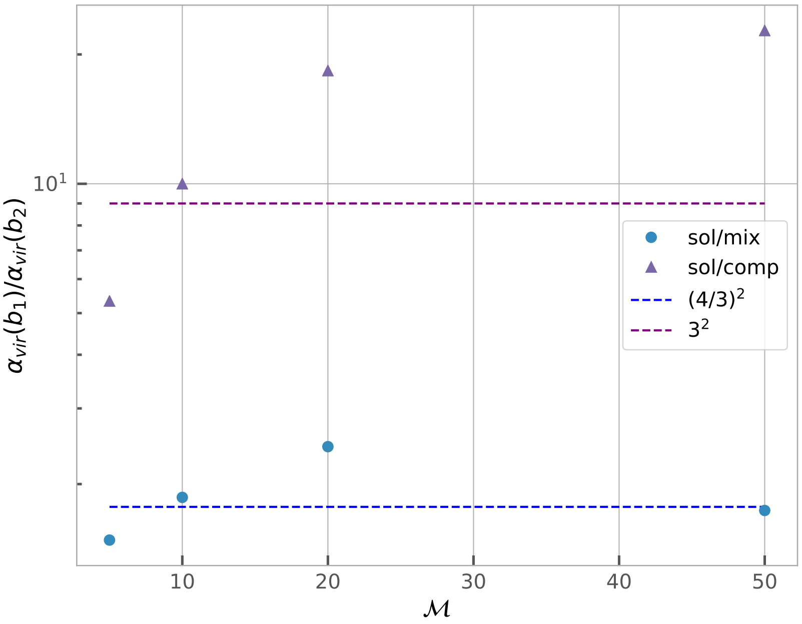

FIGURE 3.11 Ratio of virial parameters from the simulations of Federrath & Klessen (2012, 2013) for three different types of forcing. Each point corresponds to a Mach number $\mathcal{M}$ and size L. Triangles (sol/comp): ratio between virial parameters for solenoidal ($b \simeq 0.3$) and compressive forcing ($b \simeq 1$): circles (sol/mix): ratio between solenoidal and mixed forcing ($b \simeq 0.4$). The horizontal dashed lines give the expected value of the ratios for a scaling in b^{-2}.

are derived from observations in space ($\mathbb{R}^3$) from the size and mass of the cloud. This mismatch is a numerical artefact due to the numerical resolution of the Poisson equation in a tore geometry. It should be emphasized, however, that this does not imply that the numerical results of Federrath & Klessen (2012, 2013) are erroneous, but this does call for a reexamination of interpretations involving the estimation of α_{vir} from the gravitational potential returned by the simulations.

7 Conclusion

In this chapter, we have examined the validity of statistical homogeneity and ergodicity when deriving general properties of star-forming molecular clouds from observations or numerical results of some of their properties. Notably we focused on the field of density fluctuations and its PDF. This is a fundamental question since these fluctuations are believed to be at the root of the star formation process. It is thus essential to examine the validity of a statistical approach in order to assess the accuracy of the determination of the statistical properties of the cloud from the observations or simulations of a limited number of samples. To fulfill this goal, we first use the ergodic theory for any random field X to derive some rigorous statistical results. We explain how to calculate the correlation length of fluctuations in this field, $l_c(X)$, from the autocovariance function (ACF) (Eq. (3.10)). We show that the estimation of the correlation length allows one to define an effective number of samples, N, such that a space (or time) average of a single realisation is formally equivalent to averaging over N independent samples (see e.g. Papoulis & Pillai 1965). When it is difficult to determine the correlation length, we have shown how it can still be estimated by performing several identical trials in Sec. (2.2).

We then apply this statistical approach and the results of ergodic theory to astrophysical systems characterized by a field of density fluctuations, which may be used in cosmology for the formation of structures (Peebles, 1973; Heinesen, 2020) and in star-forming clouds for star formation. Focussing on the latter, we apply our results to the observed column-density field, which is related to the (volume) density field in the cloud. In Chapter **2**, we have devised a method to determine the correlation length, or more exactly the ratio of the correlation length over the size of the cloud (or the box of numerical simulations), from the variances of both the density and column-density fields We have also shown that the statistics of the column-density field are affected by artefacts due to integration along the line of sight. These artefacts tend to generate an artificial anistropy in the empirical ACF, resulting in an overestimation of the correlation length of density fluctuations within the cloud. Estimating the variance of the underlying density field, $\mathrm{Var}\left(\rho/\left\langle\rho\right\rangle\right)$, and computing the variance of the column-density field, $\mathrm{Var}\left(\Sigma/\left\langle\Sigma\right\rangle\right)$, we are able to derive a more accurate estimate of the correlation length l_c (Eq. (2.11)), which can be an order of magnitude smaller than the one obtained from the empirical ACF (§4.2). The statistics of the PDF ergodic estimator for positive column-density contrasts enables us to get rid of most of the integration anisotropy bias (§4.3.1). It also allows a proper evaluation of statistical error bars and shows that these (i) can *not* be derived from simple Poisson statistics and (ii) become increasingly large for increasing density contrasts ($|\eta| \geq 1$), severely reducing the accuracy of the high end part of the PDF because of the small sample size (see Sec. 4.3.2). We provide a method that can be used by observers and numerical simulation specialists to determine approximate, but robust, error bars in Sec. 4.3.3.

We have examined in detail the Polaris cloud, which serves as a template for initial stages of star formation in MCs. Using the data available, we have calculated the density ACF and correlation length in this cloud and shown that the latter is of about ∼1% of the size of the cloud ($l_c(\rho)/R \sim 10^{-2}$). We have also examined the more complex Orion B cloud to confirm results obtained on Polaris.

In a next section, we have applied the same statistical formalism to the determination of the total gravitational energy and virial parameter of the cloud. We have demonstrated that the contribution of the (undetermined) internal structure of the clouds has only a small impact on these determinations. The cloud's gravitational energy and virial parameter can thus be safely estimated from the observed total mass and size, with no knowledge of its internal structure. This is an important result becaude the virial parameter determines the dynamics of a cloud, equilibrium, expansion or gravitational contraction.

Examining the same problem in a tore geometrical configuration, which is characteristic of numerical simulations in a periodic box, we have shown that, in contrast to the real space, only the inner structure of the density fluctuations in the box contributes to the determination of the gravitational potential and the virial parameter. In that case, the (dominant) average contribution is indeed absent, a consequence of the ill-posed problem of solving the Poisson equation in $\mathbb{T}^3$. We have demonstrated that the ratio of the viral parameter values in the box over the ones in 'real' geometry is proportional to $\left((l_c/L) \times (b\mathcal{M})\right)^{-2}$ (Eq. (3.78)). Thus, for a given large-scale Mach number and size of the simulation box, this decreases approximately as $\sim b^{-2}$, where $b \in [1/3, 1]$ denotes the (solenoidal vs compressive) turbulence forcing parameter. This explains the puzzling large discrepancy found in Federrath & Klessen (2012, 2013) between the gravitational potential and virial parameter values inferred from the global characteristics of the simulation box and those that are inferred from the numerical results. We note that this does not affect the validity of the simulations of Federrath & Klessen (2012, 2013). However this does call for a reexamination of the interpretations involving the estimation of α_{vir} from the gravitation potential returned by the simulations.

These calculations provide a rigorous framework for analyses of the global properties of star-forming clouds from limited statistical observations of their density and surface properties. Moreover this framework is a powerful tool to explore the general statistical properties of star-forming molecular clouds from a limited number of data. In particular, this may be applied to determinations of the global gravitational energy and virial parameter, thus the magnitude of binding in the cloud. Finally these calculations show that *for typical star-forming clouds at the onset of the star formation process, the correlation length of density fluctuations is much smaller than the size of the cloud.* This justifies the relevance of a statistical approach based on the assumption of statistical homogeneity when studying the statistics of the cloud (Jaupart & Chabrier 2020), as done e.g. in cosmology or in the study of turbulence.

We will therefore use a statistical approach based on statistical homogeneity and ergodicity to study the evolution of the statistics of stochastic fields in star forming clouds in the next chapter.

Appendices

A Homogeneity scale

We develop here the equation introduced in Sec. (3.5). Starting from the definition of $N(< r)$, we have

$$N(< r) = \frac{1}{N}\int_{\Omega^2} n(\boldsymbol{x})\, n(\boldsymbol{y})\, \Theta(r-|\boldsymbol{x}-\boldsymbol{y}|)\, \mathrm{d}\boldsymbol{y}\mathrm{d}\boldsymbol{x} \tag{3.80}$$

$$\begin{aligned} &= \frac{\eta^2}{N}\int_{\Omega^2} \Theta(r-|\boldsymbol{x}-\boldsymbol{y}|)\, \mathrm{d}\boldsymbol{y}\mathrm{d}\boldsymbol{x} \\ &\quad +2\frac{\eta}{N}\int_{\Omega^2} \Theta(r-|\boldsymbol{x}-\boldsymbol{y}|)\, \delta n(\boldsymbol{x})\, \mathrm{d}\boldsymbol{y}\mathrm{d}\boldsymbol{x} \\ &\quad +\frac{1}{N}\int_{\Omega^2} \Theta(r-|\boldsymbol{x}-\boldsymbol{y}|)\, \delta n(\boldsymbol{x})\, \delta n(\boldsymbol{y})\, \mathrm{d}\boldsymbol{y}\mathrm{d}\boldsymbol{x} \end{aligned} \tag{3.81}$$

$$= \eta \int_{B(<r)} \prod_{k=1}^{3}\left(1-\frac{|u_k|}{L}\right)\mathrm{d}\boldsymbol{u} + 2\frac{\eta}{N} I_\delta + \frac{1}{N} I_{\delta,\delta} \tag{3.82}$$

with, $\delta n = n - \eta$. Changing fields, $(\boldsymbol{u},\boldsymbol{v}) = \varphi(\boldsymbol{x},\boldsymbol{y}) = (\boldsymbol{x}-\boldsymbol{y}, \boldsymbol{x}+\boldsymbol{y})$, and one obtains

$$I_\delta = \int_{[-L,L]^3} \mathrm{d}\boldsymbol{u}\, \Theta(r-|\boldsymbol{u}|) \iiint_{-L+|u_i|}^{L-|u_i|} \frac{\mathrm{d}\boldsymbol{v}}{8}\delta n\left(\frac{\boldsymbol{u}+\boldsymbol{v}}{2}\right) \tag{3.83}$$

$$\begin{aligned} I_{\delta,\delta} &= L^3 \int_{[-L,L]^3} \mathrm{d}\boldsymbol{u}\, \Theta(r-|\boldsymbol{u}|) \times \\ &\qquad \iiint_{-L+|u_i|}^{L-|u_i|} \frac{\mathrm{d}\boldsymbol{v}}{8} \frac{\delta n\left(\frac{\boldsymbol{u}+\boldsymbol{v}}{2}\right)\, \delta n\left(\frac{\boldsymbol{u}-\boldsymbol{v}}{2}\right)}{L^3} \end{aligned} \tag{3.84}$$

$$= L^3 \int_{[-L,L]^3} \mathrm{d}\boldsymbol{u}\, \Theta(r-|\boldsymbol{u}|)\, \hat{C}_{n,L}(\boldsymbol{u}), \tag{3.85}$$

where $\hat{C}_{n,L}(\boldsymbol{u})$ is the ergodic estimator Eq. (1.71). Furthermore, as

$$I(\boldsymbol{u}) = \iiint_{-L+|u_i|}^{L-|u_i|} \frac{\mathrm{d}\boldsymbol{v}}{8}\delta n\left(\frac{\boldsymbol{u}+\boldsymbol{v}}{2}\right) = \iiint_{\frac{-L+|u_i|+u_i}{2}}^{\frac{L-|u_i|+u_i}{2}} \delta n\left(\boldsymbol{x}\right)\, \mathrm{d}\boldsymbol{x}, \tag{3.86}$$

if $(L-2r) \gg l_c(n)$, then $I(\boldsymbol{u}) \simeq L^3 \langle \delta n \rangle$ and

$$\eta \int_{B(<r)} \prod_{k=1}^{3}\left(1-\frac{|u_k|}{L}\right)\mathrm{d}\boldsymbol{u} \gg 2\frac{\eta}{N} I_\delta. \tag{3.87}$$

Thus,

$$N(< r) = \eta \int_{B(<r)} \prod_{k=1}^{3}\left(1-\frac{|u_k|}{L}\right)\mathrm{d}\boldsymbol{u} + \int_{B(<r)} \frac{\hat{C}_{n,L}(\boldsymbol{u})}{\eta}\,\mathrm{d}\boldsymbol{u} \tag{3.88}$$

$$= \frac{\eta\, 4\pi\, r^3}{3}\left(1 + f(\frac{r}{L}) + \frac{\mathrm{Var}(n)}{\eta^2}\frac{3}{4\pi}\left(\frac{2\, l_c(n)}{r}\right)^3 + R_r\right), \tag{3.89}$$

where $f(r/L)$ is a geometrical factor such that $-3r/L \leq f(r/L) \leq 0$ for $r \ll L$ and R_r is a rest such that $R_r \propto r^{-3}\int_{|\boldsymbol{u}|>r} C_n(\boldsymbol{u})\mathrm{d}\boldsymbol{u} = \underset{r\to\infty}{\mathrm{o}}(r^{-3})$. If $r \gtrsim l_c(n)$. Keeping only the dominant terms, we have

$$\mathcal{N}(< r) \simeq 1 + \frac{\mathrm{Var}(n)}{\eta^2}\frac{3}{4\pi}\left(\frac{2\, l_c(n)}{r}\right)^3 \tag{3.90}$$

which yields

$$D(< r) \simeq 3 - \frac{\mathrm{Var}(n)}{\eta^2}\frac{9}{4\pi}\left(\frac{2\, l_c(n)}{r}\right)^3 \times \frac{1}{1 + \frac{\mathrm{Var}(n)}{\eta^2}\frac{3}{4\pi}\left(\frac{2\, l_c(n)}{r}\right)^3}. \tag{3.91}$$

Hence, when $D(< r) - 3 \ll 1$:

$$D(< r) - 3 \simeq -\frac{\mathrm{Var}(n)}{\eta^2}\frac{9}{4\pi}\left(\frac{2\, l_c(n)}{r}\right)^3, \tag{3.92}$$

giving

$$\lambda_H \simeq 2\, l_c(n) \times \left(\frac{100\,\mathrm{Var}(n)}{\eta^2}\right)^{1/3}. \tag{3.93}$$

For this results to be self consistent, the condition that $l_c(n) \lesssim \lambda_H \ll L$ must be met.

B Ergodic estimators of the CMF and PDF

B.1 Cumulative Distribution Function (CMF)

The CMF of the stochastic field X can be constructed as the average of a particular function of the field X. Indeed, by definition, $F_X(\xi_0) = \mathbb{P}\left(X(\boldsymbol{y}) \leq \xi_0\right)$ and a simple calculation shows that :

$$\mathbb{P}\left(X(\boldsymbol{y}) \leq \xi_0\right) = \mathbb{E}\left(h_{\xi_0}\left(X(\boldsymbol{y})\right)\right) \tag{3.94}$$

where $h_{\xi_0}(z) = \Theta(\xi_0 - z)$ and Θ is the Heaviside step function. We are then ready to determine the confidence interval for the estimated CMF F_X of X. To do so, we apply the results of Sec. (2) to the field $h_{\xi_0}(X(\boldsymbol{y}))$. The "natural" ergodic estimator of $F_X(\xi_0)$ is thus:

$$\hat{F}_L(\xi_0) = \frac{1}{L^D}\int_{[-\frac{L}{2},\frac{L}{2}]^D} h_{\xi_0}\left(X(\boldsymbol{y})\right)\mathrm{d}\boldsymbol{y}. \tag{3.95}$$

Then, to obtain the variance of $\hat{F}_L(\xi_0)$ we need to derive the ACF of $h_{\xi_0}\left(X(\boldsymbol{y})\right)$. We have

$$C_{h_{\xi_0}}(\boldsymbol{y}) = F_X^{(2)}(\xi_0, \xi_0, \boldsymbol{y}) - F_X(\xi_0)^2 \tag{3.96}$$

where $F_X^{(2)}(\xi_0, \xi_0, \boldsymbol{y}) = \mathbb{P}\left(X(\boldsymbol{u}+\boldsymbol{y})) \leq \xi_0;\ \&;\ X(\boldsymbol{u}) \leq \xi_0\right)$ is the second-order distribution function and is the probability that $X(\boldsymbol{u}+\boldsymbol{y}) \leq \xi_0$ and $X(\boldsymbol{u}) \leq \xi_0$. The variance of $\hat{F}_L(\xi_0)$ is then

$$\begin{aligned}
\mathrm{Var}\left(\hat{F}_L(\xi_0)\right) &= \frac{1}{(L)^D}\int_{[-L,L]^D} C_{h_{\xi_0}}(\boldsymbol{y})\prod_{k=1}^{D}\left(1 - \frac{|y_k|}{L}\right)\mathrm{d}\boldsymbol{y} \qquad (3.97)\\
&\simeq C_{h_{\xi_0}}(\boldsymbol{0})\left(\frac{l_c(h_{\xi_0})}{R}\right)^D
\end{aligned}$$

$$= F_X(\xi_0)\,(1-F_X(\xi_0))\left(\frac{l_c(h_{\xi_0})}{R}\right)^D, \tag{3.98}$$

provided that $C_{h_{\xi_0}}$ is integrable so one can define $l_c(h_{\xi_0})$. Again, comparing with the result for a repeated trial experiment where N samples of $X(\boldsymbol{y})$ are drawn (for the same point $\boldsymbol{y}$) shows that the ratio $(R/l_c(h_{\xi_0}))^D$ serves as an *effective number* N of trials (see e.g. Papoulis & Pillai 1965).

In practice and in order to determine an interval of confidence when F_X is not known, one can use the estimate $\hat{F}_L$ in Eq. (3.98) (Papoulis & Pillai, 1965). Furthermore, here, $l_c(h_{\xi_0})$ is a function of ξ_0 and cannot in general be estimated from $l_c(X)$. The length $l_c(h_{\xi_0})$ can, however, be estimated by repeating the experiment several times and using the results of Sec. (2.2).

B.2 Probability Density Function (PDF)

To build an estimator of the PDF $f_X(\xi_0)$ of X, we do not use the definition $f_X(\xi_0) = \mathbb{E}\left(\delta(X(\boldsymbol{y})-\xi_0)\right)$ but the following common approximation, which is suitable for data analysis:

$$f_X(\xi_0)\Delta x \simeq F_X(\xi_0+\Delta x) - F_X(\xi_0) = \mathbb{E}\left(h_{\xi_0+\Delta x}(X(\boldsymbol{y})) - h_{\xi_0}(X(\boldsymbol{y}))\right) \tag{3.99}$$

which is valid for a sufficiently small bin spacing Δx. Noting $g_{\xi_0}(X(\boldsymbol{y}) = h_{\xi_0+\Delta x}(X(\boldsymbol{y})) - h_{\xi_0}(X(\boldsymbol{y}))$, we build the following estimator :

$$\hat{f}_L(\xi_0)\Delta x = \frac{1}{L^D}\int_{[-\frac{L}{2},\frac{L}{2}]^D} g_{\xi_0}\left(X(\boldsymbol{y})\right)\,\mathrm{d}\boldsymbol{y}. \tag{3.100}$$

The ACF of $g_{\xi_0}(X)$ is

$$\begin{aligned} C_{g_{\xi_0}}(\boldsymbol{y}) &= F_X^{(2)}(\xi_0+\Delta x,\xi_0+\Delta x,\boldsymbol{y}) + F_X^{(2)}(\xi_0,\xi_0,\boldsymbol{y}) \\ &\quad -F_X^{(2)}(\xi_0+\Delta x,\xi_0,\boldsymbol{y}) - F_X^{(2)}(\xi_0,\xi_0+\Delta x,\boldsymbol{y}) \\ &\quad -\left(F_X(\xi_0+\Delta x) - F_X(\xi_0)\right)^2 \end{aligned} \tag{3.101}$$

with

$$\begin{aligned} C_{g_{\xi_0}}(\mathbf{0}) &= F_X(\xi_0+\Delta x) - F_X(\xi_0) - \left(F_X(\xi_0+\Delta x) - F_X(\xi_0)\right)^2 \\ &\simeq f_X(\xi_0)\Delta x\,(1-f_X(\xi_0)\Delta x) + \mathrm{O}(\Delta x^2) \qquad (3.102) \\ &\simeq f_X(\xi_0)\Delta x + \mathrm{O}(\Delta x^2). \qquad (3.103) \end{aligned}$$

We then know that a sufficient condition for X to be density ergodic is either that $C_{g_{\xi_0}}(\boldsymbol{y}) \xrightarrow[|\boldsymbol{y}|\to\infty]{} 0$ or that $C_{g_{\xi_0}}(\boldsymbol{y})$ is integrable.

To find out how rapidly $C_{g_{\xi_0}}(\boldsymbol{y})$ decays to zero, we note that

$$\begin{aligned} C_{g_{\xi_0}}(\boldsymbol{y}) &\simeq \left(\frac{\partial^2 F_X^{(2)}}{\partial x_1 \partial x_2}(\xi_0,\xi_0,\boldsymbol{y}) - f_X(\xi_0)^2\right)\Delta x^2 + \mathrm{O}(\Delta x^3) \qquad (3.104) \\ &= \left(f_X^{(2)}(\xi_0,\xi_0,\boldsymbol{y}) - f_X(\xi_0)^2\right)\Delta x^2 + \mathrm{O}(\Delta x^3), \qquad (3.105) \end{aligned}$$

where $f_X^{(2)}$ is the second-order density function. Eqs. 3.104 and 3.105 are only valid for $\boldsymbol{y} \neq \mathbf{0}$ because $f_X^{(2)}$ is degenerate for $\boldsymbol{y} = \mathbf{0}$ as $F_X^{(2)}(x_1,x_2,\mathbf{0}) = F_X(\min(x_1,x_2))$, where $\min(x_1,x_2)$ is not differentiable.

The variance of the ergodic estimator $\hat{f}_{L,\xi_0}$ is, then,

$$\mathrm{Var}\left(\hat{f}_{L,\xi_0}\right) = (f_X(\xi_0)\Delta x)\left(\frac{l_c(g_{\xi_0})}{R}\right)^D , \tag{3.106}$$

where $l_c(g_{\xi_0})^D \propto \Delta x$ (see Eq. (3.105)).

B.3 Gaussian process

If the field $X(\boldsymbol{y})$ is Gaussian:

$$f^{(2)}_{X,G}(\xi_1, \xi_2, \boldsymbol{y}) = \frac{1}{2\pi\left|\underline{\boldsymbol{\Sigma}}(\boldsymbol{y})\right|^{1/2}} \exp\left(-\frac{1}{2}(\boldsymbol{\xi}_\mu)^T \underline{\boldsymbol{\Sigma}}(\boldsymbol{y})^{-1}(\boldsymbol{\xi}_\mu)\right) \tag{3.107}$$

where $\boldsymbol{\xi}_\mu = (\xi_1 - \mu, \xi_2 - \mu)$, with $\mu = \mathbb{E}\,(X)$, $|\underline{\boldsymbol{\Sigma}}(\boldsymbol{y})|$ is the determinant of the matrix $\underline{\boldsymbol{\Sigma}}(\boldsymbol{y})$ and

$$\underline{\boldsymbol{\Sigma}}(\boldsymbol{y}) = \begin{pmatrix} \sigma(X)^2 & C_X(\boldsymbol{y}) \\ C_X(\boldsymbol{y}) & \sigma(X)^2 \end{pmatrix} , \tag{3.108}$$

We see that, as $|\underline{\boldsymbol{\Sigma}}(\boldsymbol{y})| = \sigma(X)^4 - C_X(\boldsymbol{y})^2 = \left(\sigma(X)^2 - C_X(\boldsymbol{y})\right)\left(\sigma(X)^2 + C_X(\boldsymbol{y})\right)$, $f^{(2)}$ is degenerate for $\boldsymbol{y} = \boldsymbol{0}$. However, for $\boldsymbol{y} \neq \boldsymbol{0}$, we have

$$\begin{aligned} f^{(2)}_{X,G}(\xi_0, \xi_0, \boldsymbol{y}) &= \frac{1}{2\pi\left|\underline{\boldsymbol{\Sigma}}(\boldsymbol{y})\right|^{1/2}} \exp\left(-\xi^2_{0,\mu}\,\frac{\sigma(X)^2 - C_X(\boldsymbol{y})}{\sigma(X)^4 - C_X(\boldsymbol{y})^2}\right) \\ &= \frac{1}{2\pi\left|\underline{\boldsymbol{\Sigma}}(\boldsymbol{y})\right|^{1/2}} \exp\left(-\frac{(\xi_0 - \mu)^2}{\sigma(X)^2 + C_X(\boldsymbol{y})}\right) \end{aligned} \tag{3.109}$$

Hence

$$\begin{aligned} C_{g_{\xi_0}}(\boldsymbol{y}) \simeq\ & \left(\frac{1}{\left(\left(1 + \frac{C_X(\boldsymbol{y})}{\sigma(X)^2}\right)\left(1 - \frac{C_X(\boldsymbol{y})}{\sigma(X)^2}\right)\right)^{1/2}} \exp\left(\frac{C_X(\boldsymbol{y})(\xi_0 - \mu)^2}{\sigma(X)^4\left(1 + \frac{C_X(\boldsymbol{y})}{\sigma(X)^2}\right)}\right) - 1\right) \\ & \times \frac{\Delta x^2}{2\pi\sigma(X)^2} \exp\left(-\frac{(\xi_0 - \mu)^2}{\sigma(X)^2}\right) + \mathrm{O}(\Delta x^3). \end{aligned} \tag{3.110}$$

Noting the normalized ACF $\tilde{C}_X = C_X / C_X(\boldsymbol{0}) = C_X / \sigma(X)^2$ and the reduced field $\xi^r_0 = (\xi_0 - \mu)/\sigma(X)$ we have

$$\begin{aligned} C_{g_{\xi_0}}(\boldsymbol{y}) \simeq\ & \left(\frac{1}{\left(1 - \tilde{C}_X(\boldsymbol{y})^2\right)^{1/2}} \exp\left(\frac{\tilde{C}_X(\boldsymbol{y})(\xi^r_0)^2}{1 + \tilde{C}_X(\boldsymbol{y})}\right) - 1\right) \\ & \times \frac{\Delta x^2}{2\pi\sigma(X)^2} \exp\left(-(\xi^r_0)^2\right) + \mathrm{O}(\Delta x^3) \end{aligned} \tag{3.111}$$

$$\begin{aligned} \simeq\ & \left(\frac{1}{\left(1 - \tilde{C}_X(\boldsymbol{y})^2\right)^{1/2}} \exp\left(\frac{\tilde{C}_X(\boldsymbol{y})(\xi^r_0)^2}{1 + \tilde{C}_X(\boldsymbol{y})}\right) - 1\right) \\ & \times f_X(\xi_0)^2\,(\Delta x)^2 + \mathrm{O}(\Delta x^3). \end{aligned} \tag{3.112}$$

B.3.1 Integrability of the ACF and short scale analysis

If C_X decays to zero (as assumed) then for $|\boldsymbol{y}| \to \infty$, we have $C_{g_{\xi_0}}(\boldsymbol{y}) \sim \tilde{C}_X(\boldsymbol{y})\,(\xi_0^r)^2\, f_X(\xi_0)^2\,(\Delta x)^2$. Thus, if C_X is integrable, then so is $C_{g_{\xi_0}}$ at $|\boldsymbol{y}| \to \infty$.

As mentioned above, Eq. (3.112) is only valid for $|\boldsymbol{y}| > 0$, so the divergence at $\boldsymbol{y} = \boldsymbol{0}$ is artificial as $C_{g_{\xi_0}}(\boldsymbol{0}) = f_X(\xi_0)\Delta x$ is finite. However, if Eq. (3.112) is integrable at $\boldsymbol{y} = \boldsymbol{0}$, this ensures that the errors of approximation of $C_{g_{\xi_0}}$ near $\boldsymbol{y} = \boldsymbol{0}$ have a small effect on the estimation of $l_c(g_{\xi_0})$ (which is an integral). The divergence of Eq. (3.112) at $\boldsymbol{y} = \boldsymbol{0}$ is given by

$$\frac{1}{\left(1 - \tilde{C}_X(\boldsymbol{y})^2\right)^{1/2}} \exp\left(-\frac{1}{2}(\xi_0^r)^2\right) \times f_X(\xi_0)^2\,(\Delta x)^2. \tag{3.113}$$

For an exponential isotropic ACF, this yields a divergence that is $\propto r^{-1/2}$; For a differentiable field X with an ACF which is isotropic at short scales, the divergence is $\propto r^{-1}$. Thus, in most cases for $D \geq 2$ Eq. (3.112) is integrable at $|\boldsymbol{y}| \to 0$.

Computing the integral of $C_{g_{\xi_0}}(\boldsymbol{y})$ is not straightforward for any decaying and integrable ACF $C_X(\boldsymbol{y})$. Expanding the exponential in Eq. (3.112), we have

$$\exp\left(\frac{\tilde{C}_X(\boldsymbol{y})(\xi_0^r)^2}{1 + \tilde{C}_X(\boldsymbol{y})}\right) \quad = \quad 1 + \sum_{n \geq 1} \frac{(\xi_0^r)^{2n}}{n!}\left(\frac{\tilde{C}_X(\boldsymbol{y})}{1 + \tilde{C}_X(\boldsymbol{y})}\right)^n. \tag{3.114}$$

We then have to specify or bound the integrals

$$\int_{[0,+\infty]^D} \left(\frac{\tilde{C}_X(\boldsymbol{y})}{1 + \tilde{C}_X(\boldsymbol{y})}\right)^n \frac{\mathrm{d}\boldsymbol{y}}{\left(1 - \tilde{C}_X(\boldsymbol{y})^2\right)^{1/2}} \quad = \quad l_c(X)^D\, c_n, \tag{3.115}$$

$$\int_{[0,+\infty]^D} \left(\frac{1}{\left(1 - \tilde{C}_X(\boldsymbol{y})^2\right)^{1/2}} - 1\right) \mathrm{d}\boldsymbol{y} \quad = \quad l_c(X)^D\, c_0, \tag{3.116}$$

to obtain

$$\int_{[0,+\infty]^D} C_{g_{\xi_0}}(\boldsymbol{y})\,\mathrm{d}\boldsymbol{y} = l_c(X)^D \varphi(\xi_0^r) \times f_X(\xi_0)^2\,(\Delta x)^2 + \mathrm{O}(\Delta x^3), \tag{3.117}$$

where $\varphi(\xi_0^r)$ is a function of ξ_0 for which we need to provide bounds in order to determine a confidence interval. A lower bound of $\varphi(\xi_0^r)$ can be obtained due to the convexity of the exponential:

$$\varphi(\xi_0^r) \geq c_0 + c_1(\xi_0^r)^2 \tag{3.118}$$

For general monotonic decreasing (and hence positive) ACFs, the study of the functions $\frac{x}{1+x}\frac{1}{(1-x^2)^{1/2}}$ and $\frac{1}{(1-x^2)^{1/2}} - 1$ shows that $c_0 \gtrsim 0.1$ and $c_1 \geq 0.77$.

B.3.2 Exponential ACF

To go a little further and obtain a formula that will help us grasp some expected features of the ergodic estimate of g_{ξ_0}, we study the special case of an exponential ACF. For the present study we limit ourselves to the case $D \leq 2$. Then if $\tilde{C}_X$ is an (isotropic) exponential, $\tilde{C}_X(y) = \exp(-|y|/\lambda)$, we can bound the integral of Eq. (3.112). Indeed, for $n \geq 1$,

$$\frac{l_c(X)}{2^{n-1}} \geq \int_{[0,+\infty]^D} \left(\frac{\tilde{C}_X(\boldsymbol{y})}{1+\tilde{C}_X(y)} \right)^n \times \frac{\mathrm{d}\boldsymbol{y}}{\left(1-\tilde{C}_X(\boldsymbol{y})^2\right)^{1/2}}. \tag{3.119}$$

We then have

$$\begin{aligned} \int_{[0,+\infty]^D} C_{g_{\xi_0}}(\boldsymbol{y})\,\mathrm{d}\boldsymbol{y} \;\leq\; & l_c(X)^D \left(2\exp\left(\frac{(\xi_0^r)^2}{2}\right) + \tilde{c}_0^D - 2 \right) \\ & \times (f_X(\xi_0)\Delta x)^2 + \mathrm{O}(\Delta x^3) \end{aligned} \tag{3.120}$$

where $\tilde{c}_0^D = \ln(2)$ and 0.17 for $D = 1$ and $D = 2$, respectively. This gives an upper bound to the correlation length of g_{ξ_0} but overestimates its value for $|\xi_0^r| \gg 1$. However, near the average ($|\xi_0^r| \ll 1$), a good approximation is:

$$\begin{aligned} \int_{[0,+\infty]^D} C_{g_{\xi_0}}(\boldsymbol{y})\,\mathrm{d}\boldsymbol{y} \;\simeq\; & l_c(X)^D \left(\tilde{c}_1^D\,(\xi_0^r)^2 + \tilde{c}_0^D\right) \\ & \times (f_X(\xi_0)\Delta x)^2 + \mathrm{O}(\Delta x^3), \end{aligned} \tag{3.121}$$

where $\tilde{c}_1^D = 1$ and 0.88 for $D = 1$ and $D = 2$, respectively. We note that, due to the convexity of the exponential, the right hand side of Eq. (3.121) is actually a lower bound of the integral $\forall \xi_0$.

We can then construct a confidence interval with more than $1 - 1/m^2$ of confidence such that the *true* $f_X(\xi_0)$ lies in

$$f_X(\xi_0) = \hat{f}_L(\xi_0) \left(1 \pm m\,(\varphi(\xi_0^r))^{1/2} \left(\frac{l_c(X)}{R}\right)^{D/2} \right),$$

where

$$\tilde{c}_1^D\,(\xi_0^r)^2 + \tilde{c}_0^D \leq \varphi(\xi_0^r) \leq 2\exp\left(\frac{(\xi_0^r)^2}{2}\right) + \tilde{c}_0^D - 2. \tag{3.122}$$

Using the lower bound to approximate $\varphi(\xi_0^r)$, $\varphi(\xi_0^r) \simeq \tilde{c}_1^D\,(\xi_0^r)^2 + \tilde{c}_0^D$, while accurate for $|\xi_0^r| \ll 1$, is most probably an underestimation for $|\xi_0^r| \gg 1$. However, it allows to show that the statistics of events that deviate largely from the mean needs an increasingly large sample size to have a high degree of confidence.

B.4 Deterministic function of a Gaussian field.

The results derived in App. B.3 can be extended to the case where $X(\boldsymbol{y}) = \psi(S(\boldsymbol{y}))$ with ψ a diffeomorphism and S a Gaussian field. One particular example is that of a lognormal field where $\psi = \exp$. We call this function ψ a deterministic function because statistical properties of the field X can be obtained from those of S. Indeed, for such a field X, the first and second order distribution functions are:

$$f_X(\xi_0) = \frac{f_S(s_0)}{|(\psi^{-1})'(\xi_0)|} \tag{3.123}$$

$$f_X^{(2)}(\xi_1, \xi_2; \boldsymbol{y}) = \frac{f_S^{(2)}(s_1, s_2; \boldsymbol{y})}{|(\psi^{-1})'(\xi_1)||(\psi^{-1})'(\xi_2)|}, \tag{3.124}$$

where $s_j = \psi^{-1}(\xi_j)$ (Papoulis & Pillai, 1965). With no loss of generality, we can further assume that the field S is centered with unit variance. We note that the ψ function can be obtained by inverting Eq. (3.123). Indeed, if only f_X and f_S are known, we can obtain ψ by taking into account the fact that

ψ^{-1} verifies the differential equation:

$$|(\psi^{-1})'(\xi_0)| = \frac{f_S((\psi^{-1})(\xi_0))}{f_X(\xi_0)}. \tag{3.125}$$

If one further assumes that ψ is an increasing diffeomorphism $(\psi^{-1})' \geq 0$, one obtains

$$s_0 = \psi^{-1}(\xi_0) = \sqrt{2}\,\mathrm{erf}^{-1}\left(-1 + 2\int_{\xi_{\min}}^{\xi_0} f_X(x)\,\mathrm{d}x\right), \tag{3.126}$$

where $\xi_{\min}$ is the minimum value that can be taken by field X and erf^{-1} is the inverse of the error function. The use of this equation requires a high precision on f_X due to the large variation of erf^{-1}, which complicates matters.

Then the ACF of X can be obtained by performing the integral:

$$C_X(\boldsymbol{y}) = \int \psi(s_1)\psi(s_2)\left(f_S^{(2)}(s_1, s_2; \boldsymbol{y}) - f_S(s_1)\, f_S(s_2)\right) \mathrm{d}s_1\, \mathrm{d}s_2.$$

Then Eq. (3.112) becomes

$$\begin{aligned} C_{g_{\xi_0}}(\boldsymbol{y}) \quad \simeq \quad & \left(\frac{1}{\left(1 - \tilde{C}_S(\boldsymbol{y})^2\right)^{1/2}} \exp\left(\frac{\tilde{C}_S(\boldsymbol{y})(s_0)^2}{1 + \tilde{C}_S(\boldsymbol{y})}\right) - 1\right) \\ & \times f_X(\xi_0)^2\, (\Delta x)^2 + \mathrm{O}(\Delta x^3). \end{aligned} \tag{3.127}$$

B.4.1 Log-normal fields

For a log-normal field $\rho = \exp(s)$, $\psi = \exp$, $\psi^{-1} = \ln$ and s is not centered ($\mathbb{E}\,(s) \neq 0$) and does not have unit variance ($\sigma(s) \neq 1$), in general. Then the calculation of the ACF yields:

$$C_\rho(\boldsymbol{y}) = \mathbb{E}\,(\rho)^2 \left(e^{C_s(\boldsymbol{y})} - 1\right). \tag{3.128}$$

As a consequence, because $e^{ax} - 1 \leq x(e^a - 1)$ for $0 \leq x \leq 1$ and $ax \leq e^{ax} - 1\ \forall x$, if C_ρ (or C_s) is monotonically decaying to 0 then

$$\left(\frac{\sigma(s)^2}{e^{\sigma(s)^2} - 1}\right)^{1/3} l_c(s) \leq l_c(\rho) \leq l_c(s). \tag{3.129}$$

In typical star forming conditions $\sigma(s)^2 \lesssim 4$ giving

$$0.4\, l_c(s) \lesssim l_c(\rho) \leq l_c(s), \tag{3.130}$$

or,

$$l_c(s) \sim l_c(\rho). \tag{3.131}$$

This suggests that as long as $\mathrm{Var}\,(X) = \mathrm{Var}\,(\psi(S))$ is not too large, one can expect that $l_c(X) \sim l_c(S)$.

C Orion B cloud

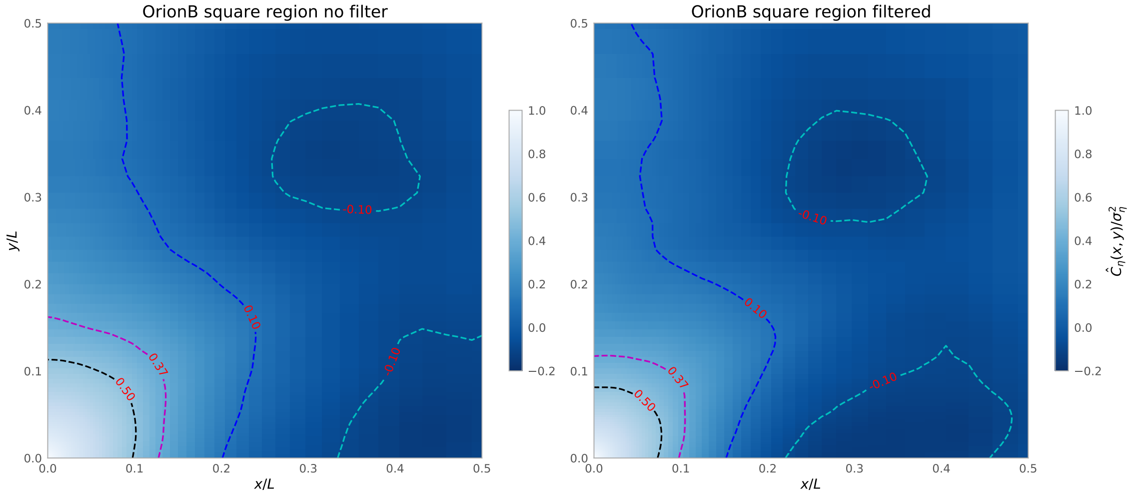

FIGURE 3.12 ACF of the “square region". Left panel: unfiltered. Right panel: low pass filtered up to scale $L/2$. Again, filtering large scale gradients reduces the anisotropy at short scales and reduces the estimated correlation length.

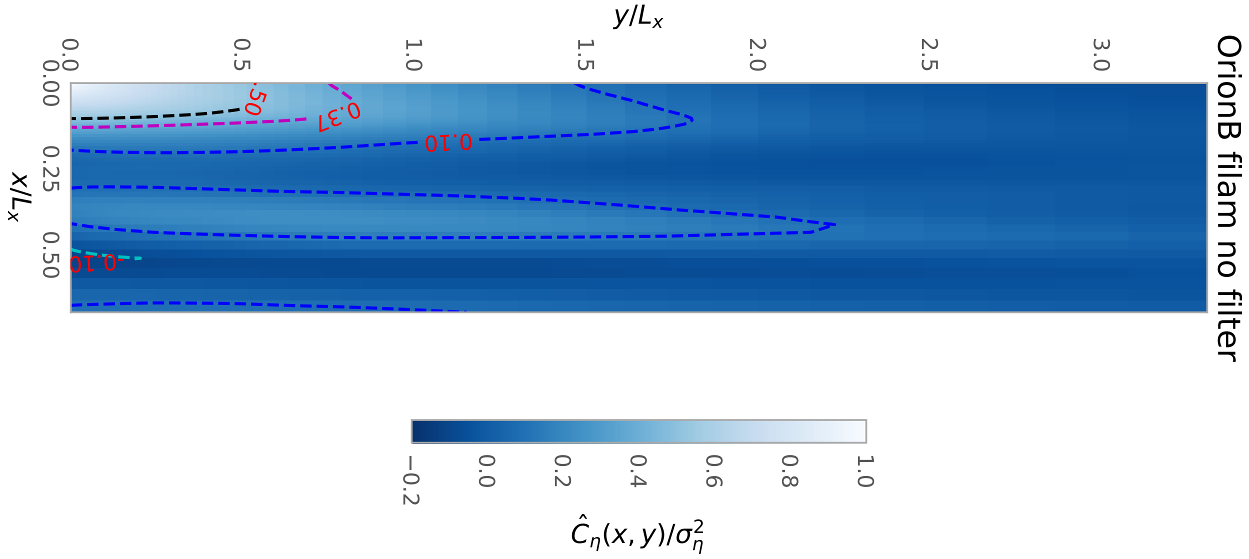

FIGURE 3.13 ACF of the unfiltered “filament region". A strong anisotropy is present in the y-direction.

C.1 ACF of the square and filament region

We computed the ACF of the unfiltered and low pass filtered square region (up to scale $L/2$, see §4), as well as the (unfiltered) "filament" region. The results are presented on Figs. (3.12) and (3.13). Filtering large scale gradients reduces again the anisotropy at short scales and reduces the estimated correlation length.

To get a closer look at the behavior of the ACF of Orion B, we display in Fig. (3.14) the reduced ACF of the low pass filtered map in 3 different directions, x ($\theta = 0$), $x = y$ ($\theta = \pi/4$) and y ($\theta = \pi/2$). As seen from the heat maps but also from fig. (3.14), a strong anisotropy is present in the y direction at large scales ($y/L \geq 10^{-1}$). The resulting estimated correlation length $\hat{l}_c(\eta)$ is of the order $l_c(\eta)/L_x \simeq 10^{-1}$.

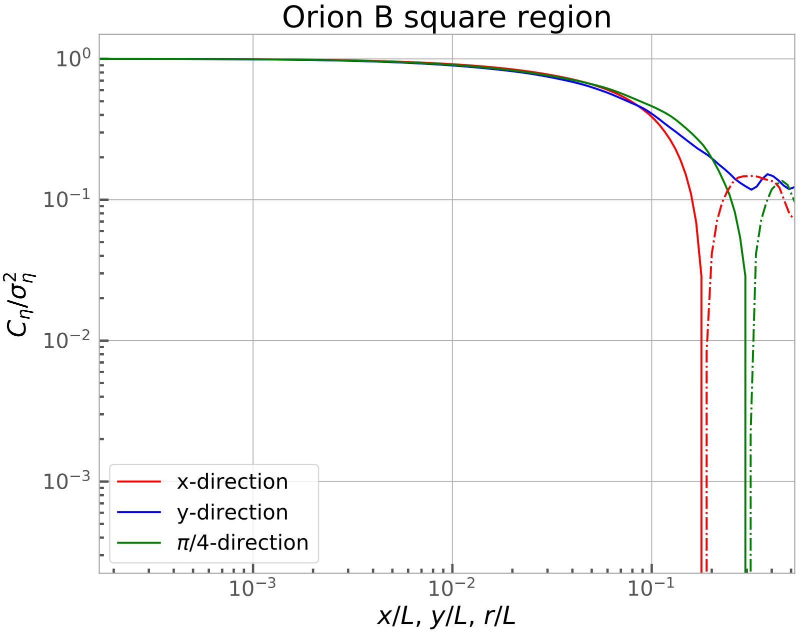

FIGURE 3.14 Reduced ACF of the low pass filtered map in three different directions. Red line: x-direction ($y = 0$). Blue line: y-direction ($x = 0$). Green line: $\pi/4$ or $x = y$-direction. Dash dotted lines represent the values of the ACF when it is negative. A strong anisotropy is present in the y direction at large scales ($y/L \geq 10^{-1}$).

C.2 Correlation length from the variance of the column densities.

As seen in Sec. (2.2) and Eq. (2.11), one can also give an estimate of the $l_c(\rho)/R$ ratio by (1) computing the variance $\mathrm{Var}\left(\Sigma/\mathbb{E}\left(\Sigma\right)\right)$, (2) giving an estimate of $\mathrm{Var}\left(\rho/\mathbb{E}\left(\rho\right)\right)$ and (3) giving an estimate of the average thickness of the cloud (along the line of sight) L_z. Here Orion B appears to be a very elongated structure, and we will therefore only assume that $L_y \geq L_z \gtrsim L_x$ (with $L_y \simeq 3-4\,L_x$).

From the observed column densities, we obtain $\mathrm{Var}\left(\Sigma/\left\langle\Sigma\right\rangle\right) \simeq 1.1$. The PDF of column densities exhibits a power-law tail of exponent $\alpha_\eta = -2$ (Schneider et al., 2013; Jaupart & Chabrier, 2020), indicating that the underlying volume density PDF has a power-law tail of exponent $-3/2$, which implies that the variance is large. As for Polaris, running the power-law tail from $s = 8$ to $s = s_{\mathrm{ad}} \simeq 16$ yields a variance $\mathrm{Var}\left(\rho/\mathbb{E}\left(\rho\right)\right) = 40$ and $\mathrm{Var}\left(\rho/\mathbb{E}\left(\rho\right)\right) \simeq 2300$, respectively (see Jaupart & Chabrier 2020). This yields a ratio $l_c(\rho)/L_z \lesssim 10^{-2}$.

D Computation of the total potential energy on a control volume Ω.

We derived in Sec. (6.2) the gravitational binding energy of a cloud covering a domain Ω, and divided it into three contributions to isolate the effects of the "internal structure" (which stands for deviations from the average):

$$\left\langle e_G(\left\langle\rho\right\rangle)\right\rangle = \int_{\Omega^2} \frac{\left\langle\rho\right\rangle^2}{|\Omega|} \Phi_{\mathrm{Green}}(\boldsymbol{x}-\boldsymbol{x}')\,\mathrm{d}\boldsymbol{x}'\,\mathrm{d}\boldsymbol{x}, \tag{3.132}$$

$$I_C(\rho) = \int_{\Omega^2} \frac{\delta\rho(\boldsymbol{x})\delta\rho(\boldsymbol{x}')}{|\Omega|} \Phi_{\mathrm{Green}}(\boldsymbol{x}-\boldsymbol{x}')\,\mathrm{d}\boldsymbol{x}'\,\mathrm{d}\boldsymbol{x}, \tag{3.133}$$

$$2\left\langle\rho\right\rangle I_\delta(\rho) = 2\left\langle\rho\right\rangle \int_{\Omega^2} \frac{\delta\rho(\boldsymbol{x})}{|\Omega|} \Phi_{\mathrm{Green}}(\boldsymbol{x}-\boldsymbol{x}')\,\mathrm{d}\boldsymbol{x}'\,\mathrm{d}\boldsymbol{x}. \tag{3.134}$$

Then, using the change of fields $(\boldsymbol{u},\boldsymbol{v}) = \varphi(\boldsymbol{x},\boldsymbol{x'}) = (\boldsymbol{x}-\boldsymbol{x'},\boldsymbol{x}+\boldsymbol{x'})$, we obtain

$$
\begin{aligned}
\langle e_G(\langle\rho\rangle)\rangle &= \langle\rho\rangle \int_{\varphi_1(\Omega)} \mathrm{d}\boldsymbol{u}\Phi_{\text{Green}}(\boldsymbol{u}) \int_{\varphi_2^{\boldsymbol{u}}(\Omega)} \langle\rho\rangle \frac{\mathrm{d}\boldsymbol{v}}{8|\Omega|}, && (3.135)\\
I_C(\rho) &= \int_{\varphi_1(\Omega)} \mathrm{d}\boldsymbol{u}\Phi_{\text{Green}}(\boldsymbol{u}) \int_{\varphi_2^{\boldsymbol{u}}(\Omega)} \frac{\mathrm{d}\boldsymbol{v}}{8|\Omega|}\delta\rho(\frac{\boldsymbol{u}+\boldsymbol{v}}{2})\delta\rho(\frac{\boldsymbol{u}-\boldsymbol{v}}{2}) &&\\
&= \int_{\varphi_1(\Omega)} \mathrm{d}\boldsymbol{u}\Phi_{\text{Green}}(\boldsymbol{u})\, \hat{C}_{\rho,L}(\boldsymbol{u}), && (3.136)\\
I_\delta(\rho) &= \int_{\varphi_1(\Omega)} \mathrm{d}\boldsymbol{u}\Phi_{\text{Green}}(\boldsymbol{u}) \int_{\varphi_2^{\boldsymbol{u}}(\Omega)} \frac{\mathrm{d}\boldsymbol{v}}{8|\Omega|}\delta\rho(\frac{\boldsymbol{u}+\boldsymbol{v}}{2}) && (3.137)
\end{aligned}
$$

where we have used the fact that Ω possess a center of symmetry, $\hat{C}_{\rho,L}$ is the biased ergodic estimator of the ACF of ρ (see Chapter **1**), and where:

$$
\varphi_2^{\boldsymbol{u}}(\Omega) = 2\left((\Omega-\boldsymbol{u})\cap\Omega\right)+\boldsymbol{u}, \tag{3.138}
$$

For example, if $\Omega = [-\frac{L}{2},\frac{L}{2}]^3$, $\varphi_2^{\boldsymbol{u}}(\Omega) = [-L+|u_i|, L-|u_i|]]$.

Furthermore, introducing

$$
I(\boldsymbol{u}) = \int_{\varphi_2^{\boldsymbol{u}}(\Omega)} \frac{\mathrm{d}\boldsymbol{v}}{8|\Omega|}\delta\rho(\frac{\boldsymbol{u}+\boldsymbol{v}}{2}), \tag{3.139}
$$

we see that $I(\boldsymbol{u})$ is, modulo the factor $1/|\Omega|$, the average of the density deviations $\delta\rho$ in the subvolume $((\Omega-\boldsymbol{u})\cap\Omega)+\boldsymbol{u}/2$. This is easier to see in the pedagogical case such that $\Omega = [-\frac{L}{2},\frac{L}{2}]^3$, because, in this case:

$$
\begin{aligned}
I(\boldsymbol{u}) &= \iiint_{-L+|u_i|}^{L-|u_i|} \frac{\mathrm{d}\boldsymbol{v}}{8|\Omega|}\delta\rho\left(\frac{\boldsymbol{u}+\boldsymbol{v}}{2}\right)\\
&= \frac{1}{|\Omega|}\iiint_{\frac{-L+|u_i|+u_i}{2}}^{\frac{L-|u_i|+u_i}{2}} \delta\rho\left(\boldsymbol{x}\right)\,\mathrm{d}\boldsymbol{x}. && (3.140)
\end{aligned}
$$

Then, if the volume of $((\Omega-\boldsymbol{u})\cap\Omega)$ is sufficiently large, e.g. $|\left((\Omega-\boldsymbol{u})\cap\Omega\right)| \gg l_c(\rho)^3$, $I(\boldsymbol{u}) \simeq |\left((\Omega-\boldsymbol{u})\cap\Omega\right)|\,\langle\delta\rho\rangle = 0$ and

$$
I(\boldsymbol{u}) \ll \int_{\varphi_2^{\boldsymbol{u}}(\Omega)} \langle\rho\rangle\frac{\mathrm{d}\boldsymbol{v}}{8|\Omega|} = \langle\rho\rangle\,|\left((\Omega-\boldsymbol{u})\cap\Omega\right)|. \tag{3.141}
$$

The integral $I(\boldsymbol{u})$ thus only give non negligible contributions for $\boldsymbol{u}$ in a small volume of order $l_c(\rho)^3$ near the border $\partial(2\Omega)$ such as $|\left((\Omega-\boldsymbol{u})\cap\Omega\right)| \lesssim l_c(\rho)^3$.

Therefore, providing that $L = |\Omega|^{1/3} \gg l_c(\rho)$ we can neglect $2\,\langle\rho\rangle\,I_\delta(\rho)$ with respect to $\langle e_G(\langle\rho\rangle)\rangle$. This leaves

$$
\langle e_G\rangle \simeq \langle e_G(\langle\rho\rangle)\rangle + \int_{\varphi_1(\Omega)} \mathrm{d}\boldsymbol{u}\Phi_{\text{Green}}(\boldsymbol{u})\,\hat{C}_{\rho,L}(\boldsymbol{u}). \tag{3.142}
$$

Chapter

4 Evolution of the statistics of the density field in star forming clouds

Contents

1 Introduction

1.1 Context

As mentioned in the Introduction, supersonic turbulence pervades the entire interstellar medium (ISM) and determines the dynamics and evolution of structures at all scales, from galaxies to molecular clouds (MCs) and prestellar cores. Molecular clouds, notably, are characterized by very large Reynolds numbers, pointing to highly turbulent media (e.g. Elmegreen & Scalo 2004; Hennebelle & Falgarone 2012). In these systems, the spectral line widths that are observed (e.g. Larson 1981; Heyer & Brunt 2004; Kritsuk et al. 2013, 2017) reveal the existence of random supersonic motions in MCs, which source have been attributed, for example, to the shearing that accompanies galactic differential rotation (Fleck Jr, 1981). Turbulence generates shock-compressed density structures over a wide range of scales, from the injection scale, which is the galactic scale height for giant molecular clouds or the cloud size itself for smaller clouds, to the dissipation scale, which is about $\sim$0.1 pc, the sonic length, or the ambipolar dissipation scale for typical Milky Way conditions (see e.g. Hennebelle & Inutsuka 2019). This is the mechanism that triggers star formation (McKee & Ostriker, 2007). In spite of the strong shock cascade that affects it, the cold cloud gas remains approximately isothermal due to the competing effects of collisional heating and radiative cooling until it becomes opaque to its own radiation, which acts to stop the fragmentation process (Klessen & Glover, 2016). Supersonic turbulence sets the initial conditions of star formation in MCs, so that one aims to acquire a precise understanding of the dynamics and statistics of the induced density fluctuations. The probability density function (PDF) of these fluctuations deserves special attention because it may be compared to the PDF of the *observed* column density field of MCs. This is a powerful statistical tool to get an insight into the dynamics of turbulence and self-gravity in MCs.

Many studies have established that the volume-weighted density distribution of supersonic isothermal "inertial" turbulence is nearly lognormal for solenoidally driven turbulence, at least for Mach numbers $\mathcal{M} \lesssim 30$ (Vazquez-Semadeni 1994; Passot & Vázquez-Semadeni 1998; Kritsuk et al. 2007; Federrath et al. 2008, 2010; Pan et al. 2019b) even in the presence of a magnetic field (Lemaster & Stone 2008; Collins et al. 2012). In dense star-forming regions, however, the line-of-sight extinction and inferred column density PDFs have been observed to develop a power-law tail at high densities, for extinctions $A_V \gtrsim$ 2-5 (e.g. Kainulainen et al. 2006, 2009; Schneider et al. 2012, 2013 and references therein), a feature which has been identified as the signature of gravity. This is Indeed a feature of PDFs that are obtained in numerical simulations of turbulence that include self-gravity (e.g.Kritsuk et al. 2010; Ballesteros-Paredes et al. 2011; Cho & Kim 2011; Collins et al. 2012; Federrath & Klessen 2013; Lee et al. 2015; Burkhart et al. 2016).

1.2 Current status of research

As mentioned above, the statistical properties of supersonic turbulence are at the core of analytical theories of star formation and we aim to determine the shape of the density PDF and how it evolves with time. It is now clear that the two different forms of molecular cloud density PDFs, lognormal without and with a power-law tail, are characteristic of isothermal "inertial" turbulence and cloud collapse, respectively. But we do not understand precisely yet when and how gravity starts to affect the dynamics of turbulence and to modify the density PDF.

1.2.1 Is gravity the only cause of these observed departures from lognormal like statistics ?

To develop a better understanding of the dynamics of density fluctuations in turbulent clouds, it is important to identify the physical mechanism that is responsible for departures from lognormal statistics. Cloud regions where star formation is occurring are associated with density PDFs that exhibit power-law tails and are dense, which is consistent with the influence of gravity, but other mechanisms have been proposed. Brunt (2015) has argued that cold and warm phases coexist, so that the resulting density distribution is the superposition of two (or more) lognormal ones. Passot & Vázquez-Semadeni (1998); Audit & Hennebelle (2010) have shown that departures from an isothermal equation of state (e.o.s.)

lead to PDF power-law tails for both low and high densities depending on the effective polytropic index γ entering the e.o.s. Departures from lognormal statistics occur at high densities when the e.o.s. is sub-isothermal, *i.e.* when $\gamma < 1$, and at low densities when the e.o.s. is over-isothermal, *i.e.* when $\gamma > 1$. In order to generate PLTs at high densities the gas thermodynamic path should therefore be that of an effective sub-isothermal polytrope ($\gamma < 1$). For $\gamma = 0.7$, which is the characteristic polytropic index of cold interstellar gas, one obtains a high density PLT with exponent $\alpha_s = 3/2$ (Audit & Hennebelle, 2010). This also yields $\alpha_s = 1.2$ for $\gamma = 0.5$ (Passot & Vázquez-Semadeni, 1998). Lastly, Tremblin et al. (2014) have invoked the impact of an ionisation compression front at high density.

Amongst these three alternative models, the first two are hard to reconcile with current knowledge on heating and cooling conditions in high density cloud regions ($n > 10^2$ /cc) at low temperatures ($T \sim 10$ K). They are more appropriate for other phases of interstellar medium (ISM) evolution which they were originally developed for. The last model could well explain departures from isothermal lognormal statistics in regions with feedback from massive (O) stars in late stages of cloud evolution, but there can be no doubt that gravity plays a dominant role in regions were star formation and gravitational collapse occur. Thus, we focus on the impact of gravity on the dynamics of turbulent flows and investigate departures from lognormal statistics at high density.

1.2.2 Gravitational infall as a mechanism producing PLTs.

The most common explanation for the development of power-law tails in cloud density PDFs and the associated exponents is based on the observed dynamics of collapsed prestellar cores at the very smallest scales and highest densities of star formation. In these small core regions, one observes that the exponent of the PLTs is linked to the exponent of the *radial* density profiles (Kritsuk et al., 2010; Federrath & Klessen, 2013) through what could be called a deterministic geometric counting process. For *radial* power law density profiles $\rho \propto r^{-n}$, $\mathrm{d}V_n(\rho')$, the volume of shells with density $\rho \in [\rho', \rho' + \mathrm{d}\rho'[$, is:

$$\mathrm{d}V_n(\rho') = \left(\frac{\mathrm{d}V_n}{\mathrm{d}r}\right)_{r(\rho')} \mathrm{d}r(\rho') \ \propto \ \rho'^{-(\frac{3}{n}+1)}\, \mathrm{d}\rho', \tag{4.1}$$

which behaves as a power law in ρ. Then one assumes that, in *of the whole cloud*, the total volume of regions where the density field is such that $\rho \in [\rho', \rho' + \mathrm{d}\rho'[$, noted $\Omega(\rho')$, is the sum of volumes of small shells in *radial* density profiles :

$$\Omega\left(\rho'\right) \simeq \sum \mathrm{d}V_n(\rho'). \tag{4.2}$$

One then uses the ergodicity assumption:

$$\mathbb{P}\left(\rho \in [\rho', \rho' + \mathrm{d}\rho'[\right) \propto \Omega\left(\rho'\right), \tag{4.3}$$

where $\mathbb{P}$ denotes the probability of having $\rho \in [\rho', \rho' + \mathrm{d}\rho'[$. The end result is a PDF with a power-law tail. What is puzzling, however, is that the exponent of the PLT that is inferred from the dynamics at short scales and high densities appears to be the same as that of larger scale structures with lower density which are the largest contributors to the PLT. Kritsuk et al. (2010) commented that "when the contributions from individual cores combine to form the density PDF for the whole computational domain, *by some magic* the resulting slope appears to be the same as that from the collapsing larger-scale structures characterized by a lower density".

A few other attempts have been made to explain the development of power law tails in the density PDF of molecular clouds and to determine the value of their exponent (Girichidis et al., 2014; Guszejnov et al., 2018b; Donkov & Stefanov, 2018). These approaches were focussed on the gravitationally unstable parts of a cloud and were based on analytical models of scale-free gravitational collapse and/or *geometrical* arguments. They do derive asymptotic exponents of power-law tails but lack a complete statistical description of the density fluctuations, both in the gravitationally stable and unstable parts of a cloud. In addition, with the exception of the numerical simulations of Girichidis et al. (2014), they treat the PDF as a static property and do not follow its evolution through time.

1.2.3 Statistical approach of turbulence based on first principles

The statistical approach of turbulence in *compressible media* dates back to the first famous formulation for incompressible flows (Batchelor, 1953). Chandrasekhar (1951b,a) studied the dynamics of the auto-covariance function (ACF) of the density field for homogeneous and isotropic turbulence. Through an analysis of linearized dynamics, he showed that (1) in the absence of gravity, density disturbances propagate at a *modified* sound speed $c_{\mathrm{s,eff}}^2 = c_{\mathrm{s}}^2 + \overline{\boldsymbol{u}^2}/3$, where c_{s} is the actual sound speed and $\overline{\boldsymbol{u}^2}$ is the r.m.s velocity, (2) in the presence of self gravity, the Jeans criterion for the collapse of a molecular cloud is modified. Progress on the PDF of density fluctuations in turbulent flows has been slower. A large number of efforts have dealt with incompressible fluids and it is only recently that a robust theoretical framework has been established for compressible fluids by Pan et al. (2018, 2019a,b). This framework relies on the formalism developed by Pope (1981, 1985) and Pope & Ching (1993) in which the PDF of any quantity is expressed as the conditional expectations of its time derivatives. Pan et al. (2019b) was able to derive a theoretical formulation of the density fluctuation PDF at steady state *from first principles*, but without gravity.

1.3 Objectives of this chapter

In this chapter, we study the dynamics and physics of density fluctuation statistics and their probability density function (PDF) in turbulent clouds *including the effects of self gravity*. As seen in the previous chapter, such a statistical approach is relevant to the study of MCs. We extend the *first principles* framework of Pope (1981) and Pan et al. (2019b) to turbulence in the presence of self gravity and develop an analytical theory for the dynamics of dense MC regions. In addition to the impact of gravity on turbulence, we also study how the density PDF evolves with time. Thus, we do not rely on the governing equations for a static system and in particular allow for the conditional expectation of the flow velocity divergence to be time-dependent as well as non zero. We couple this approach to that of Chandrasekhar (1951b) for the auto-covariance function and obtain a consistent physical picture of the evolution of density fluctuation statistics. This work has resulted in the publication of two articles (Jaupart & Chabrier 2020, Jaupart & Chabrier 2021 in prep.). It leads to an exact relation between the statistics of the flow velocity divergence and the shape of the density PDF, and determines the density thresholds above which gravity strongly affects and eventually dominates the dynamics of the flow.

This chapter is organized as follows. The general mathematical framework of the theory, as well as the derivation of transport equations for the density PDF and ACF may be found in Sec. 2. Application of these results to astrophysical flows in star forming clouds is given in Sec. 3. The velocity-divergence density PDF relation is derived in 3.1. The impact of flow dynamics on the PDF and the density threshold for which gravity acts to modify the lognormal "inertial" statistics are presented in Sec. 3.2. The time evolution of the density PDF and correlation length are presented in Sec. 3.3 and 3.4, respectively. Theoretical results are compared to the results of numerical simulations and observations in Sec. 4 and 5, respectively. We then discuss consequences for the evolution of molecular clouds and for star formation in a wider context in section 6. Section 7 concludes the chapter.

2 Mathematical Framework

2.1 Description of a molecular cloud

We consider an isolated, turbulent, self-gravitating molecular cloud. The cloud evolution is then governed by the standard Navier-Stokes and Poisson equations:

$$\begin{aligned}
\frac{\partial \rho}{\partial t}+\boldsymbol{\nabla}\cdot(\rho\boldsymbol{v}) &= 0, && (4.4)\\
\frac{\partial \boldsymbol{v}}{\partial t}+(\boldsymbol{v}\cdot\boldsymbol{\nabla})\,\boldsymbol{v} &= -\frac{1}{\rho}\boldsymbol{\nabla}P+\boldsymbol{\mathcal{G}}+\frac{\boldsymbol{F}_{\mathrm{m}}}{\rho}+\frac{1}{\rho}\boldsymbol{\nabla}\cdot\underline{\underline{\boldsymbol{\sigma}_{\nu}}}, && (4.5)\\
\boldsymbol{F}_{\mathrm{m}} &= \frac{(\boldsymbol{B}\cdot\boldsymbol{\nabla})\,\boldsymbol{B}}{4\pi}-\frac{1}{8\pi}\boldsymbol{\nabla}|\boldsymbol{B}|^2, && (4.6)\\
\boldsymbol{\nabla}\cdot\boldsymbol{B} &= 0, && (4.7)\\
\boldsymbol{\nabla}\times\boldsymbol{\mathcal{G}} &= \boldsymbol{0} && (4.8)\\
\boldsymbol{\nabla}\cdot\boldsymbol{\mathcal{G}} &= -4\pi G\rho-\Lambda, && (4.9)
\end{aligned}$$

where ρ and P stand for the gas density and pressure in the cloud, respectively, $\boldsymbol{v}$ is the velocity field, $\boldsymbol{\mathcal{G}}$ and $\boldsymbol{B}$ are the gravity and magnetic field, $\boldsymbol{F}_{\mathrm{m}}$ is the magnetic force and $\underline{\underline{\boldsymbol{\sigma}_{\nu}}}$ is the viscous stress tensor. The two first equations correspond to the conservation of mass and momentum, respectively, and the last ones specify the role of gravity in the cloud. Constant Λ is in fact zero in molecular clouds, but we introduce this term in order to allow comparisons with numerical simulations. Calculations that rely on a Poisson solver for periodic boundary conditions involve a non-zero $\Lambda = 4\pi G M_{\mathrm{box}}/V_{\mathrm{box}}$, where V_{box} is the volume of the simulation box and M_{box} is the total mass inside it (Ricker, 2008; Guillet & Teyssier, 2011). Eq. (4.9) is thus a generalized Newton-Gauss equation which enables us to handle both cases with the same formalism.

We close this system of equations with a barotropic equation of state $P = P(\rho)$ for the gas and restrict our study to the case of ideal magneto-hydrodynamics (MHD), such that:

$$\frac{\partial \boldsymbol{B}}{\partial t} = -\boldsymbol{\nabla}\times(\boldsymbol{v}\times\boldsymbol{B}). \tag{4.10}$$

This ideal description is found to be sufficiently accurate for the description of gas evolution in *early stages* of star formation, before the formation of first Larson cores (Vaytet et al., 2018), even though non ideal corrections, notably ambipolar diffusion, are believed to be of importance at small scales or high densities, notably to set the size of filamentary structure (see e.g. Hennebelle 2013; Hennebelle & Inutsuka 2019 for a more complete discussion).

Combining Eqs. (4.4–4.5) gives the conservative form of Eq. 4.5:

$$\frac{\partial\,(\rho\,\boldsymbol{v})}{\partial t}+\boldsymbol{\nabla}\cdot\left(\rho\boldsymbol{v}\otimes\boldsymbol{v}-\underline{\underline{\boldsymbol{\sigma}_{\nu}}}\right) = -\boldsymbol{\nabla}P+\rho\,\boldsymbol{\mathcal{G}}+\boldsymbol{F}_{\mathrm{m}}. \tag{4.11}$$

We are interested in clouds that might eventually condense locally to form stars, and hence separate the evolution of the background from that of local density deviations. The velocity field $\boldsymbol{v}$ is written as the sum of the mean velocity $\boldsymbol{V}$ and the (turbulent) velocity $\boldsymbol{u}$ (Ledoux & Walraven 1958). Introducing the logarithmic excess of density, s, we get, by definition:

$$\begin{aligned}
\boldsymbol{V} &\equiv \frac{1}{\overline{\rho}}\overline{\rho\boldsymbol{v}}, && (4.12)\\
\boldsymbol{u} &\equiv \boldsymbol{v}-\boldsymbol{V}, && (4.13)\\
\rho &\equiv \overline{\rho}(\boldsymbol{x},t)\,e^{s}, && (4.14)
\end{aligned}$$

where $\overline{\Phi}(\boldsymbol{x},t)$ is the mathematical expectation, also called statistical average or mean, of random field Φ (e.g. Pope 1985; Frisch 1995). We note that $\overline{\boldsymbol{u}} \neq 0$ *a priori* but $\overline{\rho\boldsymbol{u}} \equiv 0$. This ensures that *on average* there is no transfer of mass due to turbulence and the equation of continuity (4.4) remains valid for the mean field,

$$\frac{\partial\overline{\rho}}{\partial t} + \boldsymbol{\nabla}\cdot\left(\overline{\rho}\,\boldsymbol{V}\right) \;=\; 0. \tag{4.15}$$

In similar fashion, the magnetic field $\boldsymbol{B}$ is split it into a regular (averaged) part and a stochastic (turbulent) part:

$$\begin{aligned} \boldsymbol{B} &= \boldsymbol{B}_{\mathrm{reg}} + \boldsymbol{B}_{\mathrm{st}}, && (4.16)\\ \boldsymbol{B}_{\mathrm{reg}} &= \overline{\boldsymbol{B}}. && (4.17) \end{aligned}$$

Averaging Eq. (4.11) yields an evolution equation for the mean flow,

$$\frac{\partial\left(\overline{\rho}\,\boldsymbol{V}\right)}{\partial t} + \boldsymbol{\nabla}\cdot\left(\overline{\rho}\boldsymbol{V}\otimes\boldsymbol{V}\right) \;=\; -\boldsymbol{\nabla}\overline{P} + \overline{\rho\boldsymbol{\mathcal{G}}} + \overline{\boldsymbol{F}_{\mathrm{m}}} + \boldsymbol{\nabla}\cdot\left(\overline{\underline{\underline{\boldsymbol{\sigma}_{\nu}}}} - \overline{\rho\boldsymbol{u}\otimes\boldsymbol{u}}\right), \tag{4.18}$$

which has a similar form as Eq. (4.11), with all quantities replaced by their mean values, save for an additional stress called the turbulent Reynolds stress tensor, $-\overline{\rho\boldsymbol{u}\otimes\boldsymbol{u}}$. The trace of this tensor corresponds to the turbulent pressure, to be added to the gas mean thermal pressure, while the deviatoric component is related to the *turbulent* viscous tensor. The evolution of the bulk flow thus requires the evaluation of this stress, a well known closure problem (Ledoux & Walraven, 1958). In molecular clouds where the Reynolds number is very large, *molecular* viscous effects can be neglected and hence we drop the viscous tensor $\underline{\underline{\boldsymbol{\sigma}_{\nu}}}$ in the momentum conservation equation.

Subtracting the equations for the averaged variables from the original equations, we can tackle the evolution of density deviations. Using Eqs. (4.4) and (4.15), we obtain a transport equation for the logarithmic density fluctuations s, written in Lagrangian form:

$$\frac{\mathrm{D}s}{\mathrm{D}t} = -\boldsymbol{\nabla}\cdot\boldsymbol{u} - \left(\boldsymbol{u}\cdot\boldsymbol{\nabla}\right)\ln(\overline{\rho}), \tag{4.19}$$

where $\frac{\mathrm{D}}{\mathrm{D}t} = \frac{\partial}{\partial t} + (\boldsymbol{v}\cdot\boldsymbol{\nabla})$ is the Lagrangian (material) derivative.

2.2 Probability distribution functions (PDF)

Probability distribution functions (PDF) are useful tools to characterize the statistics of turbulent field $\boldsymbol{u}$ and especially those of the density field s. We define two probability distribution functions. One is the joint probability distribution function of $(\boldsymbol{\nabla}\cdot\boldsymbol{u})$ and s, noted $P_2(\upsilon,\xi,\boldsymbol{x},t)$ (see Chap. **1**) :

$$P_2(\upsilon,\xi,\boldsymbol{x},t)\mathrm{d}\upsilon\,\mathrm{d}\xi = \mathbb{P}\left((\boldsymbol{\nabla}\cdot\boldsymbol{u})(\boldsymbol{x},t)\in[\upsilon,\upsilon+\mathrm{d}\upsilon[\,\mathrm{and}\,s(\boldsymbol{x},t)\in[\xi,\xi+\mathrm{d}\xi[\right). \tag{4.20}$$

The other is the probability distribution function of s, noted $f(\xi,\boldsymbol{x},t)$:

$$f(\xi,\boldsymbol{x},t)\mathrm{d}\xi = \mathbb{P}\left(s(\boldsymbol{x},t)\in[\xi,\xi+\mathrm{d}\xi[\right). \tag{4.21}$$

Pope (1981, 1985) has shown that:

$$\begin{aligned} P_2(\upsilon,\xi,\boldsymbol{x},t) &= \overline{\delta\left(\boldsymbol{\nabla}\cdot\boldsymbol{u}(\boldsymbol{x},t)-\upsilon\right)\,\delta\left(s(\boldsymbol{x},t)-\xi\right)} \equiv \overline{g_2(\upsilon,\xi,t,\boldsymbol{x})}, && (4.22)\\ f(\xi,\boldsymbol{x},t) &= \overline{\delta\left(s(\boldsymbol{x},t)-\xi\right)} \equiv \overline{g_1(\xi,t,\boldsymbol{x})}, && (4.23) \end{aligned}$$

where δ denotes the Dirac distribution. Without any hypothesis on the stochastic fields, P_2 and f are functions of time t and position $\boldsymbol{x}$. One has:

$$f(\xi,\boldsymbol{x},t)=\int_{\mathbb{R}} P_2(\upsilon,\xi,\boldsymbol{x},t)\mathrm{d}\upsilon. \tag{4.24}$$

Noting that

$$\frac{\partial g_2}{\partial x^\mu}=-\frac{\partial g_2}{\partial \xi}\times\frac{\partial s}{\partial x^\mu}-\frac{\partial g_2}{\partial \upsilon}\times\frac{\partial \boldsymbol{\nabla}\cdot\boldsymbol{u}}{\partial x^\mu}, \tag{4.25}$$

where $x^\mu=(x^0,x^1,x^2,x^3)=(t,\boldsymbol{x})$, we obtain:

$$\frac{\mathrm{D}g_2}{\mathrm{D}t} \;=\; -\frac{\partial g_2}{\partial \xi}\times\frac{\mathrm{D}s}{\mathrm{D}t}-\frac{\partial g_2}{\partial \upsilon}\times\frac{\mathrm{D}\left(\boldsymbol{\nabla}\cdot\boldsymbol{u}\right)}{\mathrm{D}t}. \tag{4.26}$$

Taking the average of Eq. (4.26) and using Eq. (4.19), we obtain the transport equation for P_2:

$$\boxed{\begin{aligned}\frac{\partial P_2}{\partial t}+(\boldsymbol{V}\cdot\boldsymbol{\nabla})P_2=P_2\upsilon-\overline{\boldsymbol{\nabla}\cdot(\boldsymbol{u}g_2)}+\frac{\partial}{\partial\xi}\left(P_2\left[\nu+\langle\boldsymbol{u}\cdot\boldsymbol{\nabla}\ln(\overline{\rho})|\xi,\upsilon\rangle\right]\right)\\ -\frac{\partial}{\partial\upsilon}\left(P_2\left\langle\frac{\mathrm{D}\boldsymbol{\nabla}\cdot\boldsymbol{u}}{\mathrm{D}t}|\xi,\upsilon\right\rangle\right),\end{aligned}} \tag{4.27}$$

where terms of the form $\langle\Phi|\xi,\upsilon\rangle\equiv\langle\Phi|s=\xi,\boldsymbol{\nabla}\cdot\boldsymbol{u}=\upsilon\rangle$ denote the conditional expectations of the random field Φ knowing that $s=\xi$ and $\boldsymbol{\nabla}\cdot\boldsymbol{u}=\upsilon$ (see Chap. **1**). These terms can be computed as the average of the field Φ in all regions where $(\boldsymbol{\nabla}\cdot\boldsymbol{u})(\boldsymbol{x},t)\in[\upsilon,\upsilon+\mathrm{d}\upsilon[$ and $s(\boldsymbol{x},t)\in[\xi,\xi+\mathrm{d}\xi[$. The $\langle\Phi|\xi,\upsilon\rangle$ form was adopted for simplicity. The derivation of this transport equation is generic to the study of turbulent flows (Pope, 1981, 1985; Pan et al., 2019b). In order to solve Eq. (4.27), terms involving g_2 must be prescribed.

2.3 Model for the statistics of a turbulent cloud

2.3.1 Homogeneous clouds

In studies of star formation, be the observations of some particular cloud or time consuming numerical simulations, one has usually access to only a small number of samples (and in fact only one in most cases). Thus, one has to make the basic assumption, sometimes called the "fair-sample hypothesis", that the observed sample is large enough for volumetric (or time) averages over this single sample provide accurate statistical estimates. For this procedure to be statistically meaningful, the stochastic field *must* be *statistically* homogeneous and ergodic (Papoulis & Pillai, 1965). Note that *statistical* homogeneity must not to be confused with *spatial* homogeneity. This statistical assumption is frequently made in studies of turbulent flows with or without self gravity (Chandrasekhar, 1951b,a; Batchelor, 1953; Pope, 1985; Frisch, 1995; Pan et al., 2018, 2019a,b; Jaupart & Chabrier, 2020) or in studies of the dynamical evolution of structures in the Universe in cosmology (Peebles, 1973; Heinesen, 2020). This assumption does not constrain fluctuations around the average to be small. Statistical homogeneity implies that, for *any* turbulent field Φ, $\overline{\Phi(\boldsymbol{x},t)}=\overline{\Phi}(t)$. In particular, one has $\overline{\rho}(\boldsymbol{x},t)=\overline{\rho}(t)$.

With these assumptions, the dynamics of the cloud density field and its logarithmic fluctuations are governed by the following equations:

$$-\frac{\mathrm{d}\ln(\overline{\rho})}{\mathrm{d}t} \;=\; -\frac{1}{\overline{\rho}}\frac{\mathrm{d}\overline{\rho}}{\mathrm{d}t}=\boldsymbol{\nabla}\cdot\boldsymbol{V}, \tag{4.28}$$

$$\frac{\mathrm{d}}{\mathrm{d}t}(\boldsymbol{\nabla}\cdot\boldsymbol{V}) \;=\; -\boldsymbol{\nabla}\boldsymbol{V}:\boldsymbol{\nabla}\boldsymbol{V}-4\pi G\left(\overline{\rho}-\Lambda\right)+\boldsymbol{\nabla}\cdot\overline{\left(\frac{\boldsymbol{F}_m}{\rho}\right)} \tag{4.29}$$

$$\begin{aligned}
\frac{\mathrm{D}s}{\mathrm{D}t} &= -\boldsymbol{\nabla}\cdot\boldsymbol{u}, && (4.30)\\
\frac{\mathrm{D}\boldsymbol{\nabla}\cdot\boldsymbol{u}}{\mathrm{D}t} &= -\boldsymbol{\nabla}\boldsymbol{u}:\boldsymbol{\nabla}\boldsymbol{u} - 4\pi G\overline{\rho}\left(e^{s}-1\right) - 2\boldsymbol{\nabla}\boldsymbol{V}:\boldsymbol{\nabla}\boldsymbol{u} - \boldsymbol{\nabla}\cdot\left(\frac{1}{\rho}\boldsymbol{\nabla}P\right)\\
&\quad +\boldsymbol{\nabla}\cdot\left(\frac{\boldsymbol{F}_m}{\rho} - \overline{\left(\frac{\boldsymbol{F}_m}{\rho}\right)}\right), && (4.31)
\end{aligned}$$

where $\frac{\mathrm{d}}{\mathrm{d}t}$ denotes the derivative of a variable that is only a function of time t, $\boldsymbol{\nabla}\boldsymbol{u}:\boldsymbol{\nabla}\boldsymbol{u} = \left(\partial_i u_j\right)\left(\partial_j u_i\right)$ and $\boldsymbol{\nabla}\boldsymbol{V}:\boldsymbol{\nabla}\boldsymbol{u} = \left(\partial_i V_j\right)\left(\partial_j u_i\right)$ using Einstein's summation convention. The transport equation for the joint PDF P_2 hence reduces to:

$$\boxed{\frac{\partial P_2}{\partial t} = P_2\upsilon + \frac{\partial}{\partial \xi}\left(P_2\upsilon\right) - \frac{\partial}{\partial \upsilon}\left(P_2\left\langle\frac{\mathrm{D}\boldsymbol{\nabla}\cdot\boldsymbol{u}}{\mathrm{D}t}|\xi,\upsilon\right\rangle\right).} \qquad (4.32)$$

We note that Eq. (4.32) has the same functional form with or without a magnetic field because the difference is hidden in the expression of $\left\langle\frac{\mathrm{D}\boldsymbol{\nabla}\cdot\boldsymbol{u}}{\mathrm{D}t}|\xi,\upsilon\right\rangle$. Furthermore Eqs. (4.28)–(4.29) show that the homogeneity hypothesis constrains the flow to belong to a particular class of flows. Indeed, to be consistent with the statistical homogeneity of ρ and Eq. (4.28), the right hand side of Eq.(4.29) must be a function of time t only. For this to hold, it suffices that :

$$\boxed{\begin{aligned}
\boldsymbol{V}(\boldsymbol{x},t) &= \underline{\underline{\mathrm{L}_V}}(t)\cdot\boldsymbol{x} + \boldsymbol{c}_V(t) && (4.33)\\
\boldsymbol{B}_{\mathrm{reg}}(\boldsymbol{x},t) &= \underline{\underline{\mathrm{L}_B}}(t)\cdot\boldsymbol{x} + \boldsymbol{c}_B(t), && (4.34)
\end{aligned}}$$

where $\underline{\underline{\mathrm{L}_V}}(t)$, $\underline{\underline{\mathrm{L}_B}}(t)$ are 3×3 matrices and $\boldsymbol{c}_V(t)$, $\boldsymbol{c}_B(t)$ spatially constant vectors.

We note, that Eqs. (4.30)–(4.32) with $\boldsymbol{V} = 0$, $\boldsymbol{B}_{\mathrm{reg}} = \boldsymbol{c}_B(t)$ are exactly the equations governing the evolution of a periodic simulation box (Federrath & Klessen, 2012; Pan et al., 2019b). For those cases, the *whole derivation can be repeated with a volumetric average over the whole box instead of a statistical average.*

2.3.2 Accepted class of flows

In our homogeneous model, the bulk flow $\boldsymbol{V}$ is restricted to a certain class of flows. This class, however, contains many kinds of flows relevant to the present study, such as linearized shears, notably galactic shears, homogeneous rotations, and in particular solid rotations, and global homogeneous contractions or expansions, which need not be isotropic. Moreover, the regular magnetic field $\boldsymbol{B}_{\mathrm{reg}}$ (if it is present) can account for the presence of a linearized background magnetic field. We note that this construction is similar to that used in Newtonian cosmology, where $\boldsymbol{V} = H(t)\,\boldsymbol{x}$ is the Hubble flow and $H(t)$ is Hubble's rate of expansion, and which allows for a statistically homogeneous density field *and* a non-trivial global evolution (Buchert & Ehlers, 1997; Vigneron, 2021). Therefore, these models can properly describe the evolution of the density field statistics and PDF in star-forming clouds.

2.4 Transport equations for the density PDF

Once we have obtained the transport equation for the joint PDF, P_2, we can obtain transport equations for the density PDF f.

2.4.1 Transport equations

Eq. (4.32) has the same functional form with or without magnetic field and hence we obtain the same transport equation as in JC20. Starting from Eq. (4.32) and writing:

$$\langle (\boldsymbol{\nabla}\cdot\boldsymbol{u})^n \,|\xi\rangle \, f(\xi,t) = \int_{\mathbb{R}} P_2(v,\xi,t) v^n \mathrm{d}v, \tag{4.35}$$

for all integers n, we readily obtain:

$$\boxed{\frac{\partial}{\partial t}\left[\langle (\boldsymbol{\nabla}\cdot\boldsymbol{u})^n \,|\xi\rangle \, f\right] = \left\{1+\frac{\partial}{\partial \xi}\right\}\left[\left\langle (\boldsymbol{\nabla}\cdot\boldsymbol{u})^{n+1} \,|\xi\right\rangle f\right] + f\left\langle \frac{\mathrm{D}\,(\boldsymbol{\nabla}\cdot\boldsymbol{u})^n}{\mathrm{D}t}|\xi\right\rangle.} \tag{4.36}$$

We highlight the results for $n=0$ and $n=1$:

$$\frac{\partial}{\partial t} f(\xi,t) \;=\; \left\{1+\frac{\partial}{\partial \xi}\right\}\left[\langle (\boldsymbol{\nabla}\cdot\boldsymbol{u}) \,|\xi\rangle \, f\right], \tag{4.37}$$

$$\frac{\partial}{\partial t}\left[\langle (\boldsymbol{\nabla}\cdot\boldsymbol{u}) \,|\xi\rangle \, f\right] \;=\; \left\{1+\frac{\partial}{\partial \xi}\right\}\left[\left\langle (\boldsymbol{\nabla}\cdot\boldsymbol{u})^2 \,|\xi\right\rangle f\right] + f\left\langle \frac{\mathrm{D}\boldsymbol{\nabla}\cdot\boldsymbol{u}}{\mathrm{D}t}|\xi\right\rangle. \tag{4.38}$$

Eqs. (4.37)-(4.38) are exactly those that were obtained by Pan et al. (2018, 2019a,b), JC20, whereas Eq. (4.36) for $n>2$ constrains high order moments. For simplicity, we will write the sampling variable ξ as s in order to have the s-PDF (f) expressed as a function of s.

2.4.2 Velocity divergence - density PDF relationship

A first important relation is given by Eq. (4.37), which is a straightforward consequence of mass conservation and statistical homogeneity. It allows to relate the statistics of the velocity divergence $\langle (\boldsymbol{\nabla}\cdot\boldsymbol{u}) \,|s\rangle$ to the behavior of the s-PDF.

- Steady state equivalence:

For the *continuous* logarithmic density field s, Pan et al. (2018) showed that f is stationary (i.e. at steady state) if and only if $\langle \boldsymbol{\nabla}\cdot\boldsymbol{u}|s\rangle = 0$, $\forall s$.

Indeed if $\langle \boldsymbol{\nabla}\cdot\boldsymbol{u}|s\rangle = 0 \;\forall s$, then from Eq. (4.37) $\partial_t f = 0 \;\forall s$. Reciprocally, at steady state, i.e. $\partial_t f = 0 \;\forall s$, we integrate Eq. (4.37) to obtain $f(s)\,\langle \boldsymbol{\nabla}\cdot\boldsymbol{u}|s\rangle = Ce^{-s}$. Then, due to the assumption of statistical homogeneity,

$$\overline{\boldsymbol{\nabla}\cdot\boldsymbol{u}} = 0 = \int f(s)\,\langle \boldsymbol{\nabla}\cdot\boldsymbol{u}|s\rangle \,\mathrm{d}s, \tag{4.39}$$

which implies that $C=0$ and $\langle \boldsymbol{\nabla}\cdot\boldsymbol{u}|s\rangle = 0 \;\forall s$.

- Non-stationary behaviour relationship:

In the case of a non-stationary PDF, then $\langle \boldsymbol{\nabla}\cdot\boldsymbol{u}|s\rangle \neq 0$. From that realization, an *exact* relation can be derived from Eq. (4.37) without any additional assumptions on either f or $\langle \boldsymbol{\nabla}\cdot\boldsymbol{u}|s\rangle$.

Indeed, let us write

$$f(s,t) = A(s,t)\, e^{-(a+1)s}, \tag{4.40}$$

for some $a>0$ and some (strictly positive) function $A(s,t)$. This functional form is completely general (since we do not specify anything on $A(s,t)$) but is useful as one will see. Re-writing Eq. 4.37 as follows:

$$\left\{\frac{\partial}{\partial s} + \frac{\partial \mathrm{ln} A}{\partial s} - a\right\}\langle \boldsymbol{\nabla}\cdot\boldsymbol{u}|s,t\rangle = \frac{\partial \mathrm{ln} A}{\partial t}, \tag{4.41}$$

one obtains

$$\langle \boldsymbol{\nabla}\cdot\boldsymbol{u}|s,t\rangle = C(t)\times A(s,t)^{-1}\times e^{a\,s} + A(s,t)^{-1}\,e^{as}\int_{s_i}^{s} e^{-as'}\frac{\partial A}{\partial t}(s',t)\,\mathrm{d}s', \tag{4.42}$$

where $C(t)$ is a function of time only and s_i is some fixed density. As f is not stationary, $\langle \boldsymbol{\nabla}\cdot\boldsymbol{u}|s,t\rangle$ is not zero everywhere. At any time t, however, there exists $s_0(t)$ such as $\langle \boldsymbol{\nabla}\cdot\boldsymbol{u}|s_0(t),t\rangle = 0$ to ensure that $\overline{\boldsymbol{\nabla}\cdot\boldsymbol{u}} = 0$. We can then write without any loss of generality:

$$\boxed{\langle \boldsymbol{\nabla}\cdot\boldsymbol{u}|s,t\rangle = e^{as}\,A(s,t)^{-1}\int_{s_0(t)}^{s} e^{-as'}\frac{\partial A}{\partial t}(s',t)\,\mathrm{d}s',} \tag{4.43}$$

where the function of time $C(t)$ has been "absorbed" in the lower boundary of the integral $s_0(t)$. This gives an *exact* relation between the (non-stationary) behaviour of the s-PDF and the behaviour of $\langle \boldsymbol{\nabla}\cdot\boldsymbol{u}|s,t\rangle$. We note that, for a stationary s-PDF, $\partial_t A = 0$, so that $\langle \boldsymbol{\nabla}\cdot\boldsymbol{u}|s\rangle = 0\ \forall s$.

A formal inversion of Eq. (4.43) to obtain $A(s,t)$ as a function of $\langle \boldsymbol{\nabla}\cdot\boldsymbol{u}|s,t\rangle$ in general is not straightforward. A fairly general solution can be obtained by assuming that the time and density variables are separable. In this case, $\langle \boldsymbol{\nabla}\cdot\boldsymbol{u}|s,t\rangle = h(t)\times g(s)e^{as}$, and we use the method of characteristics to obtain :

$$f(s,t) = \Phi\left(\int h\mathrm{d}t' + \int \frac{e^{-as'}}{g}\mathrm{d}s'\right)\frac{e^{-(a+1)s}}{g(s)}, \tag{4.44}$$

where Φ is some differentiable function. This relation only holds when $g(s)\neq 0$ and is therefore only appropriate for the behaviour of the s-PDF at high densities (see next).

2.5 Transport equations for the auto-covariance function of the density field

Now that we have derived the transport equation for the s-PDF and obtained a relation between the statistics of the velocity divergence and the density PDF, which are one point statistics, we aim to determine the auto-covariance function of the density field. To this end, we generalize the results of Chandrasekhar (1951b) for the auto-covariance function to our class of statistical *homogeneous* flows where $\overline{\rho}(t)$, $\overline{\boldsymbol{v}}\neq\boldsymbol{0}$ and $\overline{\boldsymbol{B}}\neq\boldsymbol{0}$. From **the previous chapter**, the correlation and auto-covariance (ACF) functions of the density field, noted R_ρ and C_ρ, respectively, are defined as:

$$R_\rho(\boldsymbol{x}-\boldsymbol{x'},t) = R_\rho(\boldsymbol{x'}-\boldsymbol{x},t) = \overline{\rho(\boldsymbol{x})\rho(\boldsymbol{x'})}, \tag{4.45}$$

$$C_\rho(\boldsymbol{x}-\boldsymbol{x'},t) = C_\rho(\boldsymbol{x'}-\boldsymbol{x},t) = \overline{\rho(\boldsymbol{x})\rho(\boldsymbol{x'})} - \overline{\rho}(t)^2. \tag{4.46}$$

2.5.1 Transport equation

Starting from the mass conservation equation (Eq. (4.4)) and multiplying it by $\rho'\equiv\rho(\boldsymbol{x'})$, we obtain:

$$\rho'\frac{\partial\rho}{\partial t} + \frac{\partial}{\partial x_i}\left(\rho'\rho\,v_i\right) = 0. \tag{4.47}$$

Interchanging the primed and the unprimed quantities in the above equation yields

$$\rho\frac{\partial\rho'}{\partial t} + \frac{\partial}{\partial x_i'}\left(\rho\,\rho'\,v_i'\right) = 0. \tag{4.48}$$

Adding the two equations and taking the average, one obtains (Chandrasekhar, 1951b):

$$\frac{\partial}{\partial t}R_\rho(\boldsymbol{x}-\boldsymbol{x'},t) + \frac{\partial}{\partial x_i}\left(\overline{\rho'\rho\,v_i}\right) + \frac{\partial}{\partial x_i'}\left(\overline{\rho\,\rho'\,v_i'}\right) = 0. \tag{4.49}$$

Decomposing $\boldsymbol{v}$ into the mean velocity $\boldsymbol{V}$ and turbulent component $\boldsymbol{u}$ ($\boldsymbol{v} = \boldsymbol{V} + \boldsymbol{u}$) and using the relation $R_\rho = C_\rho + \overline{\rho}(t)^2$, we obtain:

$$\begin{aligned}
0 \;&=\; \frac{\partial}{\partial t} C_\rho(\boldsymbol{\xi}, t) + 2\,\overline{\rho}\frac{\partial}{\partial t}\overline{\rho} + 2\,\overline{\rho}^2(\boldsymbol{\nabla}\cdot\boldsymbol{V}) + 2\,C_\rho(\boldsymbol{\xi})(\boldsymbol{\nabla}\cdot\boldsymbol{V}) + V_i\frac{\partial}{\partial x_i}C_\rho(\boldsymbol{\xi}) + V_i'\frac{\partial}{\partial x_i'}C_\rho(\boldsymbol{\xi}) \\
&\quad + \frac{\partial}{\partial x_i}\left(\overline{\rho' \rho\, u_i}\right) + \frac{\partial}{\partial x_i'}\left(\overline{\rho\,\rho'\, u_i'}\right) \qquad (4.50) \\
&=\; \frac{\partial}{\partial t} C_\rho(\boldsymbol{\xi}, t) - 2\,C_\rho(\boldsymbol{\xi})\frac{1}{\overline{\rho}}\frac{\partial}{\partial t}\overline{\rho} + (V_i - V_i')\frac{\partial}{\partial \xi_i}C_\rho(\boldsymbol{\xi}) + \frac{\partial}{\partial x_i}\left(\overline{\rho' \rho\, u_i}\right) + \frac{\partial}{\partial x_i'}\left(\overline{\rho\,\rho'\, u_i'}\right) \qquad (4.51)
\end{aligned}$$

where $\xi = \boldsymbol{x} - \boldsymbol{x'}$ and where we have used Eq. (4.28). Then, dividing both sides by $\overline{\rho}(t)^2$ and using Eq. (4.33), we obtain:

$$0 = \frac{\partial}{\partial t}\left(\frac{C_\rho(\boldsymbol{\xi})}{\overline{\rho}^2}\right) + \left(\underline{\underline{\mathrm{L}_V}}(t)\cdot\boldsymbol{\xi}\right)^i \frac{\partial}{\partial \xi_i}\left(\frac{C_\rho(\boldsymbol{\xi})}{\overline{\rho}^2}\right) + \frac{\partial}{\partial x_i}\left(\overline{\frac{\rho'\rho}{\overline{\rho}^2}\, u_i}\right) + \frac{\partial}{\partial x_i'}\left(\overline{\frac{\rho\,\rho'}{\overline{\rho}^2}\, u_i'}\right). \qquad (4.52)$$

Expressing everything in terms of the logarithmic density s (see Eq. (4.14)), we find:

$$\boxed{\begin{aligned}
0 &= \frac{\partial}{\partial t}\left(C_{e^s}(\boldsymbol{\xi})\right) + \left(\underline{\underline{\mathrm{L}_V}}(t)\cdot\boldsymbol{\xi}\right)^i \frac{\partial}{\partial \xi_i}\left(C_{e^s}(\boldsymbol{\xi})\right) + \frac{\partial}{\partial x_i}\left(\overline{e^{s'}\, e^{s}\, u_i}\right) + \frac{\partial}{\partial x_i'}\left(\overline{e^{s}\, e^{s'}\, u_i'}\right), \\
&= \frac{\partial}{\partial t}\left(C_{e^s}(\boldsymbol{\xi})\right) + \left(\underline{\underline{\mathrm{L}_V}}(t)\cdot\boldsymbol{\xi}\right)^i \frac{\partial}{\partial \xi_i}\left(C_{e^s}(\boldsymbol{\xi})\right) + \frac{\partial}{\partial \xi_i}\left(R^i_{e^s, e^s\boldsymbol{u}}\right)_{\boldsymbol{\xi}} + \frac{\partial}{\partial \xi_i}\left(R^i_{e^s, e^s\boldsymbol{u}}\right)_{-\boldsymbol{\xi}}
\end{aligned}} \qquad \begin{aligned}(4.53)\\(4.54)\end{aligned}$$

where $R^i_{e^s, e^s\boldsymbol{u}}$ is the cross correlation function of the two fields e^s and $e^s u^i$, which depends only on the lag $\boldsymbol{\xi} = \boldsymbol{x} - \boldsymbol{x'}$ under the assumption of statistical homogeneity . In fact, from the definition of $\boldsymbol{u}$, $\overline{e^s u_i} = 0$, so that $R^i_{e^s, e^s\boldsymbol{u}}$ is also the cross covariance function of e^s and $e^s u^i$. Furthermore, assuming statistical isotropy,

$$R^i_{e^s, e^s\boldsymbol{u}}(\boldsymbol{\xi}) = L_{e^s, e^s u}(|\boldsymbol{\xi}|)\,\xi^i, \qquad (4.55)$$

and the last two terms on the right-hand side of Eq. (4.54) can be combined to give $2\partial_{\xi_i}\left(R^i_{e^s, e^s\boldsymbol{u}}\right)_{\boldsymbol{\xi}}$. Eq. (4.54) thus generalizes the transport equation for the ACF of ρ derived by Chandrasekhar (1951b) with the addition of the advection term for velocity $\left(\underline{\underline{\mathrm{L}_V}}(t)\cdot\boldsymbol{\xi}\right)^i$. We discuss this new term later.

As in Chap. **1**, **2** and **3** we use the two common *physical* assumptions that enforce ergodicity. The covariance and cross covariance functions C_ρ (or C_{e^s}) and $R^i_{e^s, e^s\boldsymbol{u}}$ are both taken to decay rapidly to 0 as $|\xi| \to \infty$ and to be integrable.

2.5.2 Correlation length and conserved quantity

An important quantity characterizing the statistics of the stochastic field ρ (or e^s) is the correlation length $l_c(\rho)$ (or $l_c(e^s)$), defined as follows (Papoulis & Pillai, 1965):

$$l_c(\rho)^3 = \frac{1}{8\mathrm{Var}\,(\rho)}\iiint_{\mathbb{R}^3} C_\rho(\boldsymbol{\xi})\,\mathrm{d}\boldsymbol{\xi} = \frac{1}{8\mathrm{Var}\,(e^s)}\iiint_{\mathbb{R}^3} C_{e^s}(\boldsymbol{\xi})\,\mathrm{d}\boldsymbol{\xi} = l_c(e^s)^3. \qquad (4.56)$$

Then

$$\begin{aligned}
\frac{\mathrm{d}}{\mathrm{d}t}\left(\iiint_{\mathbb{R}^3} C_{e^s}(\boldsymbol{\xi})\,\mathrm{d}\boldsymbol{\xi}\right) \;&=\; \iiint_{\mathbb{R}^3} \partial_t C_{e^s}(\boldsymbol{\xi}, t)\,\mathrm{d}\boldsymbol{\xi} \\
&=\; -\iiint_{\mathbb{R}^3}\left(\underline{\underline{\mathrm{L}_V}}(t)\cdot\boldsymbol{\xi}\right)^i \frac{\partial}{\partial \xi_i}\left(C_{e^s}(\boldsymbol{\xi})\right)\,\mathrm{d}\boldsymbol{\xi} - 2\iint_{\text{"}\partial\mathbb{R}^3\text{"}} R^i_{e^s, e^s\boldsymbol{u}}(\boldsymbol{\xi})\,\mathrm{d}S^i \qquad (4.57) \\
&\qquad (4.58)
\end{aligned}$$

where the surface integral (the second term on the right hand side of the equation) vanishes due to the assumption on $R^i_{e^s,e^s\boldsymbol{u}}$. The first term on the right hand side may be rewritten so that:

$$\frac{\mathrm{d}}{\mathrm{d}t}\left(\iiint_{\mathbb{R}^3} C_{e^s}(\boldsymbol{\xi})\,\mathrm{d}\boldsymbol{\xi}\right) = -\iiint_{\mathbb{R}^3} \boldsymbol{\nabla}\cdot\left(C_{e^s}(\boldsymbol{\xi})\,\underline{\underline{\mathrm{L}_V}}(t)\cdot\boldsymbol{\xi}\right)\,\mathrm{d}\boldsymbol{\xi} + \iiint_{\mathbb{R}^3} (\boldsymbol{\nabla}\cdot\boldsymbol{V})C_{e^s}(\boldsymbol{\xi})\,\mathrm{d}\boldsymbol{\xi}. \tag{4.59}$$

The first term on the right hand side can be turned into a surface integral, which also vanishes due to the assumption on C_{e^s}. We are thus left with:

$$\frac{\mathrm{d}}{\mathrm{d}t}\left(\iiint_{\mathbb{R}^3} C_{e^s}(\boldsymbol{\xi})\,\mathrm{d}\boldsymbol{\xi}\right) = -\frac{\mathrm{d}\ln(\overline{\rho})}{\mathrm{d}t} \times \left(8\mathrm{Var}\,(e^s)\,l_c(e^s)^3\right), \tag{4.60}$$

which yields:

$$\frac{\mathrm{d}}{\mathrm{d}t}\left(\mathrm{Var}\,(e^s)\,l_c(e^s)^3\right) = -\left(\mathrm{Var}\,(e^s)\,l_c(e^s)^3\right) \times \frac{\mathrm{d}\ln(\overline{\rho})}{\mathrm{d}t}, \tag{4.61}$$

and

$$\boxed{\left(\mathrm{Var}\,(e^s)\,l_c(e^s)^3\right)_t\overline{\rho}(t) = cst.} \tag{4.62}$$

or, in terms of the density field ρ:

$$\frac{\left(\mathrm{Var}\,(\rho)\,l_c(\rho)^3\right)_t}{\overline{\rho}(t)} = cst. \tag{4.63}$$

These two equations are modified versions of the conservation equation derived by Chandrasekhar (1951b). They account for variations of the averaged (background) density field and depend explicitly on the correlation length.

In principle, the integral in Eq. (4.56) is to be carried out over all possible lags $\boldsymbol{\xi}$ and hence over the whole space $\mathbb{R}^3$, which may seem conceptually problematic as we are dealing with a cloud of finite size. As regards the bulk flow, however, we rely on the same line of reasoning as in statistical mechanics: if the actual subspace of permitted lags is large enough, it can be assimilated to the whole space $\mathbb{R}^3$. The argument is the following. If Ω, the subspace of permitted lags, is such that its volume $|\Omega|$ is $\gg l_c(e^s)^3$, i.e. contains a large number of correlation volumes, and if C_ρ (or C_{e^s}) tends to 0 as $|\xi| \to \infty$ and is integrable, the integral over Ω can be seen as an integral over $\mathbb{R}^3$.

To understand the meaning of the conserved quantity in Eqs. (4.61) and (4.62) and the approximation made, we now consider a finite subspace of permitted lags. Let Ω_t be the "average" volume of space describing the cloud under study, evolving with the average velocity field $\overline{\boldsymbol{v}} = \boldsymbol{V}(\boldsymbol{x},t) + \overline{\boldsymbol{u}}(t) = \underline{\underline{\mathrm{L}_V}}(t)\cdot\boldsymbol{x} + \boldsymbol{c}_V(t) + \overline{\boldsymbol{u}}(t)$. Ω_t is hence a mass conserving domain and, like $\overline{\rho}(t)$, is allowed to evolve with time. If Ω_t possesses point symmetry, then the subspace of permitted lags is simply $\Omega_{t,\xi} = 2\,\Omega_t$. This subspace is evolving with the *relative* velocity field $\Delta\overline{\boldsymbol{v}} = \overline{\boldsymbol{v}}(\boldsymbol{x},t) - \overline{\boldsymbol{v}}(\boldsymbol{x'},t) = \underline{\underline{\mathrm{L}_V}}(t)\cdot\boldsymbol{\xi}$, because distorsion can only be generated by the relative motion (Kolmogorov, 1941; Frisch, 1995). Due to Reynolds' transport theorem, one has:

$$\begin{aligned}\frac{\mathrm{d}}{\mathrm{d}t}\left(\frac{1}{|\Omega_t|}\iiint_{\Omega_{t,\boldsymbol{\xi}}} C_{e^s}(\boldsymbol{\xi})\,\mathrm{d}\boldsymbol{\xi}\right) &= -\frac{1}{|\Omega_t|^2}\frac{\mathrm{d}|\Omega_t|}{\mathrm{d}t}\iiint_{\Omega_{t,\boldsymbol{\xi}}} C_{e^s}(\boldsymbol{\xi})\,\mathrm{d}\boldsymbol{\xi} + \frac{1}{|\Omega_t|}\iiint_{\Omega_{t,\boldsymbol{\xi}}} C_{e^s}(\boldsymbol{\xi}) \times (\boldsymbol{\nabla}\cdot\,\Delta\overline{\boldsymbol{v}})\,\mathrm{d}\boldsymbol{\xi} \\ &\quad + \frac{1}{|\Omega_t|}\iiint_{\Omega_{t,\boldsymbol{\xi}}}\left(\partial_t + (\underline{\underline{\mathrm{L}_V}}(t)\cdot\boldsymbol{\xi})\cdot\boldsymbol{\nabla}\right)C_{e^s}(\boldsymbol{\xi})\,\mathrm{d}\boldsymbol{\xi},\end{aligned} \tag{4.64}$$

where:

$$\boldsymbol{\nabla}\cdot\,\Delta\overline{\boldsymbol{v}} = \boldsymbol{\nabla}\cdot\,\left(\underline{\underline{\mathrm{L}_V}}(t)\cdot\boldsymbol{\xi}\right) = \boldsymbol{\nabla}\cdot\,\boldsymbol{V} = -\frac{\mathrm{d}\ln(\overline{\rho})}{\mathrm{d}t}, \tag{4.65}$$

$$\frac{1}{|\Omega_t|}\frac{\mathrm{d}|\Omega_t|}{\mathrm{d}t} = -\frac{\mathrm{d}\ln(\overline{\rho})}{\mathrm{d}t} = \boldsymbol{\nabla}\cdot\,\boldsymbol{V}. \tag{4.66}$$

This leads to:

$$\begin{aligned}\frac{\mathrm{d}}{\mathrm{d}t}\left(\frac{1}{|\Omega_t|}\iiint_{\Omega_{t,\boldsymbol{\xi}}} C_{e^s}(\boldsymbol{\xi})\,\mathrm{d}\boldsymbol{\xi}\right) &= \frac{1}{|\Omega_t|}\iiint_{\Omega_{t,\boldsymbol{\xi}}}\Big(\partial_t + (\underline{\underline{\mathrm{L}_V}}(t)\cdot\boldsymbol{\xi})\cdot\boldsymbol{\nabla}\Big)C_{e^s}(\boldsymbol{\xi})\,\mathrm{d}\boldsymbol{\xi},\\ &= -2\frac{1}{|\Omega_t|}\iint_{\partial\Omega_{t,\boldsymbol{\xi}}} R^i_{e^s,e^s\boldsymbol{u}}(\boldsymbol{\xi})\,\mathrm{d}S^i.\end{aligned} \tag{4.67}$$

Assuming now that the contribution from the surface integral at the r.h.s of Eq. (4.67) is negligible, *i.e.* assuming that $R^i_{e^s,e^s\boldsymbol{u}}$ decays rapidly to 0 at large lags $\boldsymbol{\xi}$ and that Ω_t (and hence $\Omega_{t,\boldsymbol{\xi}}$) is large enough (for example such that $|\Omega_t| \gg l_c(e^s)^3$), we are left with:

$$\frac{1}{|\Omega_t|}\iiint_{\Omega_{t,\boldsymbol{\xi}}} C_{e^s}(\boldsymbol{\xi})\,\mathrm{d}\boldsymbol{\xi} \simeq 8\,\mathrm{Var}\,(e^s)\,\frac{l_c(e^s)^3}{|\Omega_t|} = \mathrm{cst}. \tag{4.68}$$

Using the fact that $\overline{\rho}(t)|\Omega_t| = M(\Omega_t) = \mathrm{cst}$, we obtain:

$$\boxed{\mathrm{Var}\,(e^s)\;l_c(e^s)^3\,\overline{\rho}(t) = \mathrm{cst},} \tag{4.69}$$

which is Eq. (4.62). These calculations are valid for any (mass conserving) sub-domain Ω_t that is large enough for the surface integral at the r.h.s of Eq. (4.67) to be negligible. Eq. (4.69) (and hence Eq. (4.61)) therefore yields that the fundamental quantity $\mathrm{Var}\,(e^s)\;l_c(e^s)^3\,\overline{\rho}(t)$ is conserved. We note that this conserved quantity has the dimension of mass and we will come back to this point later.

3 Implications for astrophysical flows in star forming clouds

We now apply the above results to astrophysical flows in star forming clouds.

3.1 Velocity divergence - density PDF relationship

A first important relation is given by Eq. (4.37) which is a straightforward consequence of mass conservation and statistical homogeneity only (see Sec. 2.4.2). Observations of column-density PDFs in MCs lead to lognormal distributions in regions where star formation has not occurred yet and lognormal distributions with power-law tails at high densities in regions with numerous prestellar cores (Kainulainen et al., 2009; Schneider et al., 2013). Similarly, numerical simulations of star formation show that density PDFs develop power-law tails as time increases (Klessen, 2000; Federrath & Klessen, 2013). This indicates that the density PDF is not stationary but evolves with time, implying that $\langle\boldsymbol{\nabla}\cdot\boldsymbol{u}|s\rangle \neq 0$. From Eq. (4.43), we know that, for a general PDF of the form $f(s,t) = A(s,t)\,e^{-(a+1)s}$,

$$\langle\boldsymbol{\nabla}\cdot\boldsymbol{u}|s,t\rangle = e^{as}\,A(s,t)^{-1}\int_{s_0(t)}^{s} e^{-as'}\frac{\partial A}{\partial t}(s',t)\,\mathrm{d}s'. \tag{4.70}$$

We now add a few assumptions that are relevant to astrophysical conditions. As mentioned above, observations and simulations indicate that the density PDF develops power-law tails at high density, *i.e.* that $f_\rho(\rho) \propto \rho^{-n}$. In terms of the PDF of the logarithmic density field s, this yields $f(s) \propto e^{-(n-1)s}$. For the sake of simplicity, we shall say from now on that the s-PDF develops a power law tail at high density in order to imply that $f(s) \propto e^{-(n-1)s}$ for some value of n. In the present case, we say that the s-PDF at high s is close to a power-law tail of exponent $\alpha_s = a+1$ only if we can write

$f(s,t) = A(s,t)e^{-\alpha_s s}$ with $\ln(A(s,t))/s \underset{s\to\infty}{\to} 0$. This is written as [5] $f(s,t) \underset{s\to\infty}{\asymp} e^{-\alpha_s s}$. This allows for more general situations.

3.1.1 Physical class of flows

We further restrict ourselves to the physical class of flows where the PDF $f(s,t)$ is continuous and such that $f(s,t)$, $e^s f(s,t)$ and $e^s\,\partial_t f(s,t) \underset{s\to\infty}{\to} 0$. The two last conditions are sufficient (physical) conditions for $\overline{e^s} = \overline{\rho}/\overline{\rho} = 1$.

For such flows, if $f(s,t) \underset{s\to\infty}{\asymp} e^{-\alpha_s s}$ with $\alpha_s = a{+}1$ and $a > 0$, this implies that $|\,\langle \boldsymbol{\nabla}\cdot\boldsymbol{u}|s,t\rangle\,| \underset{s\to\infty}{\asymp} e^{as}$. Indeed, from Eq. (4.70), we get:

$$\ln\left(|\,\langle \boldsymbol{\nabla}\cdot\boldsymbol{u}|s,t\rangle\,|\right) = a\,s - \ln(A(s,t)) + \ln\left(\left|\int_{s_0(t)}^{s} e^{-as'}\frac{\partial A}{\partial t}(s',t)\,\mathrm{d}s'.\right|\right), \tag{4.71}$$

Using the condition that $e^{-as}\partial_t A \underset{s\to\infty}{\to} 0$ by assumption:

$$\left|\int_{s_0(t)}^{s} e^{-as'}\frac{\partial A}{\partial t}(s',t)\,\mathrm{d}s'.\right| = \underset{s\to\infty}{\mathcal{O}}(s) \tag{4.72}$$

implying that:

$$|\,\langle \boldsymbol{\nabla}\cdot\boldsymbol{u}|s,t\rangle\,| = h(s,t)e^{as},\ \text{ with } \ln(h(s,t))/s \underset{s\to\infty}{\to} 0. \tag{4.73}$$

This is to say that $|\,\langle \boldsymbol{\nabla}\cdot\boldsymbol{u}|s,t\rangle\,| \underset{s\to\infty}{\asymp} e^{as}$.

It may be shown that this sequence of equations can be turned around. To work our way through the reciprocal demonstration, we start from the velocity divergence of a flow belonging to the class described above, which is such that $f(s,t)$, $e^s f(s,t)$ and $e^s\,\partial_t f(s,t) \underset{s\to\infty}{\to} 0$. Let us assume further that $|\,\langle \boldsymbol{\nabla}\cdot\boldsymbol{u}|s,t\rangle\,| \underset{s\to\infty}{\asymp} e^{as}$ and more precisely that :

$$\langle \boldsymbol{\nabla}\cdot\boldsymbol{u}|s,t\rangle = h(s,t)e^{as},\ \text{ with } \ln(|h(s,t)|)/s \underset{s\to\infty}{\to} 0. \tag{4.74}$$

We write further that $f(s,t) = A(s,t)e^{-(a+1)s}$. Inserting this in Eq. (4.70) yields:

$$h(s,t) = A(s,t)^{-1}\int_{s_0(t)}^{s} e^{-as'}\frac{\partial A}{\partial t}(s',t)\,\mathrm{d}s', \tag{4.75}$$

which yields:

$$\ln A(s,t) = -\ln(|h(s,t)|) + \ln\left(\left|\int_{s_0(t)}^{s} e^{-as'}\frac{\partial A}{\partial t}(s',t)\,\mathrm{d}s'\right|\right). \tag{4.76}$$

Then again, by assumption, $\int_{s_0(t)}^{s} e^{-as'}\frac{\partial A}{\partial t}(s',t)\,\mathrm{d}s' = \mathcal{O}(s)$. It thus remains that $\ln A(s,t)/s \underset{s\to\infty}{\to} 0$ holds because this is also true for $|h(s,t)|$. Hence $f(s,t) \underset{s\to\infty}{\asymp} e^{-\alpha_s s}$ with $\alpha_s = a+1$.

3.1.2 Separation of variables

In JC20, we have derived these results for cases such that the time and density variables are separable at high density, e.g. $\langle \boldsymbol{\nabla}\cdot\boldsymbol{u}|s,t\rangle = h(t)\times g(s)e^{as}$, $a > 0$ for $s \geq s_c$ for some s_c. In this situation, we can

---

[5] This notation is frequently used for the notion of logarithm equivalence.

use Eq. (4.44) to obtain

$$f(s,t) = \Phi\left(\int h\mathrm{d}t' + \int \frac{e^{-as'}}{g}\mathrm{d}s'\right)\frac{e^{-(a+1)s}}{g(s)}. \tag{4.77}$$

Then, if $g(s)$ is such that $\ln(g(s))/s \underset{s\to\infty}{\to} 0$, then f verifies $f(s,t)$, $e^s f(s,t)$ and $e^s\,\partial_t f(s,t) \underset{s\to\infty}{\to} 0$, which corresponds to the class of flow described above. Moreover $f(s,t) \underset{s\to\infty}{\asymp} e^{-\alpha_s s}$ with $\alpha_s = a+1$. The reciprocal argument can be developed from Eq. (4.70).

3.1.3 Summary

Thus, observed power-law tails, $f(s,t) \underset{s\to\infty}{\asymp} e^{-\alpha_s s}$, corresponds to an underlying expectation of the velocity divergence $\langle\boldsymbol{\nabla}\cdot\boldsymbol{u}|s,t\rangle \underset{s\to\infty}{\asymp} e^{(\alpha_s-1)s}$ (we will come back to the actual expected values of exponent α_s later). This result allows us to attribute the development of PLTs and their exponents to the impact of gravity on turbulence.

3.2 Dynamical effects on the s-PDF shape

Eq. (4.38) give insights on the interplay between values of dynamical quantities (the $\left\langle\frac{\mathrm{D}\boldsymbol{\nabla}\cdot\boldsymbol{u}}{\mathrm{D}t}|s\right\rangle$ term) and the shape of the density PDF f

3.2.1 Stationary solutions

Pan et al. (2018, 2019a,b) have already shown and tested numerically that, at steady state, the density PDF f can formally be calculated as follows:

$$f(s) = \frac{Ce^{-s}}{\left\langle(\boldsymbol{\nabla}\cdot\boldsymbol{u})^2|s\right\rangle}\exp\left(-\int_0^s \frac{\left\langle\frac{\mathrm{D}\boldsymbol{\nabla}\cdot\boldsymbol{u}}{\mathrm{D}t}|s'\right\rangle}{\left\langle(\boldsymbol{\nabla}\cdot\boldsymbol{u})^2|s'\right\rangle}\mathrm{d}s'\right), \tag{4.78}$$

which enables one to discuss the impact of dynamical effects on the shape of f.

3.2.2 Density threshold for a gravity induced transitions of regime.

Observations and numerical simulations have shown that the growing impact of gravity induces changes of the s-PDF with two characteristic regimes. At low density, the PDF is close to being log-normal, much a regime governed by the statistics of (isothermal) "inertial" turbulence. At high density the s-PDF develops power-law tails heralding a regime governed by gravitationally induced motions (infall). The transition between these two regimes, "inertial" turbulence versus gravity dominated, has yet to be determined. JC20 have obtained an order of magnitude estimate of such a threshold in the case of non magnetized hydrodynamics. To do so, they realized that the effect of gravity on the density PDF *without assuming a steady state* can be inferred by recasting Eq. (4.38) as an equation for $\ln f$:

$$\langle\boldsymbol{\nabla}\cdot\boldsymbol{u}|s\rangle\frac{\partial}{\partial t}\ln f - \langle(\boldsymbol{\nabla}\cdot\boldsymbol{u})^2|s\rangle\frac{\partial}{\partial s}\ln f + \frac{\partial}{\partial t}\langle\boldsymbol{\nabla}\cdot\boldsymbol{u}|s\rangle = \left\{1+\frac{\partial}{\partial s}\right\}\left\langle(\boldsymbol{\nabla}\cdot\boldsymbol{u})^2|s\right\rangle + \left\langle\frac{\mathrm{D}\boldsymbol{\nabla}\cdot\boldsymbol{u}}{\mathrm{D}t}|s\right\rangle, \tag{4.79}$$

where the terms on the r.h.s. are treated as source terms. We note that, due to Eq. (4.37), the term $\partial t\,\langle\boldsymbol{\nabla}\cdot\boldsymbol{u}|s\rangle$ on the l.h.s. of Eq. (4.79) is in fact seen as an operator acting on f. This is analogous to treating the pressure gradient as a non local operator acting on the velocity field in standard studies of incompressible hydrodynamics with periodic boundary conditions (see e.g. Frisch 1995). We then decompose $\left\langle\frac{\mathrm{D}\boldsymbol{\nabla}\cdot\boldsymbol{u}}{\mathrm{D}t}|s\right\rangle$ as follows:

$$\left\langle\frac{\mathrm{D}\boldsymbol{\nabla}\cdot\boldsymbol{u}}{\mathrm{D}t}|s\right\rangle = S_{\mathrm{turb}}(s,t)+S_{\mathrm{grav}}(s,t)+S_{\mathrm{th}}(s,t)+S_{\mathrm{mag}}(s,t) \tag{4.80}$$

where

$$S_{\mathrm{grav}}(s,t) \equiv -4\pi G\overline{\rho}\,(e^{s}-1)\,, \tag{4.81}$$

$$S_{\mathrm{th}}(s,t) \equiv -\left\langle\boldsymbol{\nabla}\cdot\left(\frac{1}{\rho}\boldsymbol{\nabla}P\right)|s\right\rangle, \tag{4.82}$$

(see Eq. 4.31) and, in our so-called “homogeneous" cloud,

$$S_{\mathrm{turb}}(s,t) \equiv -\left\langle\boldsymbol{\nabla}\boldsymbol{u}:\boldsymbol{\nabla}\boldsymbol{u}|s\right\rangle-2\left\langle\boldsymbol{\nabla}\boldsymbol{V}:\boldsymbol{\nabla}\boldsymbol{u}|s\right\rangle, \tag{4.83}$$

$$S_{\mathrm{mag}}(s,t) \equiv \left\langle\boldsymbol{\nabla}\cdot\left(\frac{\boldsymbol{F}_m}{\rho}-\overline{\left(\frac{\boldsymbol{F}_m}{\rho}\right)}\right)|s\right\rangle. \tag{4.84}$$

We note that S_{grav} does not need to be solved for or calculated numerically because it has already been written explicitly in terms of a known function of s. Then, using Eq. (4.79), *we expect the statistics of the flow in the cloud to be dominated by gravity whenever*:

$$|S_{\mathrm{grav}}(s)| \gtrsim \max\Big(|S_{turb}|,\,|S_{\mathrm{th}}|,\,|S_{\mathrm{mag}}|,\,\left|\{1+\partial_s\}\left\langle(\boldsymbol{\nabla}\cdot\boldsymbol{u})^2|s\right\rangle\right|\Big). \tag{4.85}$$

Note that if the dynamics is dominated by gravity, we expect that $\langle(\boldsymbol{\nabla}\cdot\boldsymbol{u})|s\rangle$ to be amplified in collapsing regions such that $|S_{\mathrm{grav}}(s)|\sim\left\langle(\boldsymbol{\nabla}\cdot\boldsymbol{u})^2|s\right\rangle$ (see § 3.3.2). Physically, Eq. (4.85) expresses the fact that gravity dominates whenever either one of the two following conditions is fullfilled. (1) Gravity effects overcome thermal (pressure), "inertial" turbulent and magnetic contributions to the cloud dynamics ($|S_{\mathrm{grav}}(s)|\gtrsim\max\left(|S_{turb}|,\,|S_{\mathrm{th}}|,\,|S_{\mathrm{mag}}|\right)$). (2) Either (i) convergent flows are produced by gravitational collapse ($|S_{\mathrm{grav}}(s)|\sim\left\langle(\boldsymbol{\nabla}\cdot\boldsymbol{u})^2|s\right\rangle$), or (ii) divergent flows are forced to collapse, independently of their initial expansion ($S_{\mathrm{grav}}(s)|>\left\langle(\boldsymbol{\nabla}\cdot\boldsymbol{u})^2|s\right\rangle$).

The aim of our study is to determine the transition to a regime when gravity begins to impact pure (gravitationless) "inertial" turbulence significantly. By definition, this transition is such that the statistics begin to deviate from those of (isothermal) "inertial" turbulent motions, so that we can evaluate the terms on the r.h.s. of Eq. (4.85) from standard steady-state turbulence theory without gravity (we denote with the subscript $\not{G}$):

$$|S_{\mathrm{grav}}(s)| \gtrsim \max\Big(|S_{turb}|,\,|S_{\mathrm{th}}|,\,|S_{\mathrm{mag}}|,\,\left|\{1+\partial_s\}\left\langle(\boldsymbol{\nabla}\cdot\boldsymbol{u})^2|s\right\rangle\right|\Big)_{\not{G}}. \tag{4.86}$$

Pan et al. (2019b) did carry out this analysis for non magnetized isothermal turbulence and found that $\left\langle(\boldsymbol{\nabla}\cdot\boldsymbol{u})^2|s\right\rangle_{\not{G}}\sim\overline{(\boldsymbol{\nabla}\cdot\boldsymbol{u}^2)}_{\not{G}}$, but the other terms have no straightforward functional forms. To further simplify Eq. (4.86), we start from Eq. (4.79) for turbulence without gravity:

$$-\left(\left\langle(\boldsymbol{\nabla}\cdot\boldsymbol{u})^2|s\right\rangle\frac{\partial}{\partial s}\mathrm{ln}f\right)_{\not{G}} = (S_{turb})_{\not{G}}+(S_{\mathrm{th}})_{\not{G}}+(S_{\mathrm{mag}})_{\not{G}}+\left(\{1+\partial_s\}\left\langle(\boldsymbol{\nabla}\cdot\boldsymbol{u})^2|s\right\rangle\right)_{\not{G}}, \tag{4.87}$$

then, using the triangle inequality,

$$\left|\left\langle(\boldsymbol{\nabla}\cdot\boldsymbol{u})^2|s\right\rangle\frac{\partial}{\partial s}\mathrm{ln}f\right|_{\not{G}} \leq |S_{turb}|_{\not{G}}+|S_{\mathrm{th}}|_{\not{G}}+|S_{\mathrm{mag}}|_{\not{G}}+\left|\left(\{1+\partial_s\}\left\langle(\boldsymbol{\nabla}\cdot\boldsymbol{u})^2|s\right\rangle\right)_{\not{G}}\right|,$$

(4.88)

which yields for the condition given by Eq. (4.86):

$$\boxed{|S_{\rm grav}(s)| \gtrsim \left|\left\langle (\boldsymbol{\nabla}\cdot\boldsymbol{u})^2|s\right\rangle \frac{\partial}{\partial s}\ln f\right|_{\not{G}}.} \tag{4.89}$$

This equation has already been derived in JC20 (on Eq. (21)). It equation holds whether or not magnetic effects are taken into account (ideal and non ideal effects). We now distinguish between two cases.

3.2.3 Non-magnetized supersonic hydrodynamics

Neglecting the impact of the magnetic field (as in JC20) and making the standard approximation in supersonic turbulence that $f_{\not{G}}$ has a lognormal distribution with variance σ_s, we obtain the following simplified condition:

$$\boxed{|S_{\rm grav}(s)| \gtrsim \overline{(\boldsymbol{\nabla}\cdot\boldsymbol{u})^2}_{\not{G}} \times \left|\frac{s+\frac{1}{2}\sigma_s^2}{\sigma_s^2}\right\|,} \tag{4.90}$$

where σ_s depends on the r.m.s. Mach number $\mathcal{M}$ and turbulence forcing parameter b as (e.g. Federrath et al. 2008) as follows:

$$\sigma_s^2 = \ln(1+(b\mathcal{M})^2). \tag{4.91}$$

We then approximate $\overline{(\boldsymbol{\nabla}\cdot\boldsymbol{u})^2}_{\not{G}}$ to within one order of magnitude:

$$\overline{(\boldsymbol{\nabla}\cdot\boldsymbol{u})^2}_{\not{G}} = \frac{1}{\overline{\rho}^2}\frac{\overline{(\Delta\rho)^2}}{\tau_{\rm turb}^2}, \tag{4.92}$$

where $\overline{(\Delta\rho)^2} = \overline{(\rho-\overline{\rho})^2} \simeq (b\mathcal{M}\overline{\rho})^2$. $\tau_{\rm turb}$ is a typical turbulent timescale, of the order of the crossing time $\tau_{\rm c} = L_{\rm c}/(2\sigma_v)$, where σ_v the 3D velocity dispersion and $L_{\rm c}$ is the diameter of the cloud. Eq. (4.90) can be reduced to:

$$\boxed{\begin{aligned} |e^s-1| &\gtrsim (b\mathcal{M})^2 \times \left(\frac{\tau_{\rm G,0}}{\tau_{\rm turb}}\right)^2 \times \left|\frac{s+\frac{1}{2}\sigma_s^2}{\sigma_s^2}\right| \\ &\gtrsim (b\mathcal{M})^2 \times \alpha_{\rm vir}(t) \times \left|\frac{s+\frac{1}{2}\sigma_s^2}{\sigma_s^2}\right|, \end{aligned}} \tag{4.93}$$

where $\tau_{\rm G,0} = 1/\sqrt{4\pi G\overline{\rho}}$ and $\alpha_{\rm vir}(t) = 5\sigma_v^2/(\pi G L_{\rm c}^2\overline{\rho}(t))$ is the virial parameter, equal to $= 2E_{\rm kin}/E_{\rm grav}$ for a homogeneous spherical cloud. This Eq. (4.93) is given in JC20.

3.2.4 Magnetized supersonic hydrodynamics

In supersonic MHD case, the s-PDF is also close to being log-normal (Lemaster & Stone 2008; Collins et al. 2012; Molina et al. 2012). We then obtain the simplified condition:

$$|S_{\rm grav}(s)| \gtrsim \left\langle (\boldsymbol{\nabla}\cdot\boldsymbol{u})^2|s\right\rangle_{\not{G}} \times \left|\frac{s+\frac{1}{2}\sigma_s^2}{\sigma_s^2}\right|, \tag{4.94}$$

where σ_s is no longer given by Eq. (4.91). Molina et al. (2012) suggested that, in most instances,

$$\sigma_s^2 = \ln\left(1+(b\mathcal{M})^2\frac{\beta}{1+\beta}\right). \tag{4.95}$$

where $\beta = P_{\rm th}/P_{\rm mag} = 2c_s^2/v_A^2 = 2\mathcal{M}_A^2/\mathcal{M}^2$, with v_A the Alfven velocity (Alfvén, 1942) and $\mathcal{M}_A = \sigma_v/v_A$ the Alfvenic Mach number. Eq. (4.95) is found to be valid for $\mathcal{M}_A \gtrsim 2$. To go further, one needs to estimate the term $\left\langle(\boldsymbol{\nabla}\cdot\boldsymbol{u})^2|s\right\rangle_{\not{\mathcal{G}}}$. Pan et al. (2019b) found that $\left\langle(\boldsymbol{\nabla}\cdot\boldsymbol{u})^2|s\right\rangle_{\not{\mathcal{G}}} \sim \overline{(\boldsymbol{\nabla}\cdot\boldsymbol{u}^2)}_{\not{\mathcal{G}}}$ for non magnetized supersonic hydrodynamics, but, to our knowledge, there has been no study of this relation for supersonic MHD flows. In the absence of such an analysis, we will assume that this relation still holds and obtain again

$$|S_{\rm grav}(s)| \gtrsim \overline{(\boldsymbol{\nabla}\cdot\boldsymbol{u})^2}_{\not{\mathcal{G}}} \times \left|\frac{s+\frac{1}{2}\sigma_s^2}{\sigma_s^2}\right| . \tag{4.96}$$

To within one order of magnitude, $\overline{(\boldsymbol{\nabla}\cdot\boldsymbol{u})^2}_{\not{\mathcal{G}}}$ may be approximated as follows:

$$\overline{(\boldsymbol{\nabla}\cdot\boldsymbol{u})^2}_{\not{\mathcal{G}}} = \frac{1}{\overline{\rho}^2}\frac{\overline{(\Delta\rho)^2}}{\tau_{\rm dyn}^2}, \tag{4.97}$$

where this time $\overline{(\Delta\rho)^2} \simeq \frac{\beta}{1+\beta}(b\mathcal{M}\overline{\rho})^2$ and $\tau_{\rm dyn}$ is a typical magneto-turbulent timescale, of the order of $L_{\rm c}/(2(\sigma_v^2+v_A^2)^{1/2})$. Eq. (4.96) reduces to:

$$\boxed{\begin{aligned} |e^s-1| &\gtrsim (b\mathcal{M})^2\frac{\beta}{1+\beta}\times\left(\frac{\tau_{\rm G,0}}{\tau_{\rm dyn}}\right)^2\times\left|\frac{s+\frac{1}{2}\sigma_s^2}{\sigma_s^2}\right|, \\ &\gtrsim (b\mathcal{M})^2\frac{\beta}{1+\beta}(1+\mathcal{M}_A^{-2})\alpha_{\rm vir}(t)\left|\frac{s+\frac{1}{2}\sigma_s^2}{\sigma_s^2}\right|, \\ &\gtrsim (b\mathcal{M})^2\frac{\beta}{1+\beta}\times\alpha_{\rm vir,m}(t)\times\left|\frac{s+\frac{1}{2}\sigma_s^2}{\sigma_s^2}\right|, \end{aligned}} \tag{4.98}$$

where $\alpha_{\rm vir,m}(t) = 5(\sigma_v^2+v_A^2)/(\pi G L_{\rm c}^2\overline{\rho}(t))$ is a magnetic virial parameter. We note that the magnetic modifications given by Eq. (4.98) only account for magnetic pressure, *i.e.*, the isotropic pressure induced by the small-scale magnetic field. Including magnetic tension would require a (so far uncertain) correction for magnetic field anisotropies. However, as long as the turbulence remains super- to trans-Alfvenic, we expect that the dominant contribution is in the form of magnetic pressure.

- Eqns (4.93) and (4.98) introduce a new characteristic timescale, $\tau_{\rm G,0} \equiv 1/\sqrt{4\pi G\overline{\rho}}$, which stems from the Poisson equation (4.9). This timescale characterizes the impact of gravity on the PDF evolution of a turbulent cloud. It it is roughly half the mean free-fall time of the cloud, $\tau_{\rm ff,0} \equiv \sqrt{\frac{3\pi}{32G\overline{\rho}}}$.

We finally note that at high Mach numbers, the PDF $f_{\not{\mathcal{G}}}$ may depart from and decrease faster than a lognormal form at large s due to intermittency effects (Federrath et al., 2010; Hopkins, 2013). *Equations (4.93) and (4.98) then allow a determination, within a factor of a few, of the density above which gravity is expected to change significantly the statistics of the flow* and enables us to derive the physical quantities governing this transition.

3.2.5 Modified Jeans criteria

To improve our understanding of the physics behind Eqs. (4.93) and (4.98), we recast these equations as follows:

$$|e^s-1| \quad \gtrsim \quad \alpha_{\rm Jeans}\times\left|\frac{s+\frac{1}{2}\sigma_s^2}{\sigma_s^2}\right|, \tag{4.99}$$

where, in the non magnetized case,

$$\alpha_{\mathrm{Jeans}} = c\frac{\lambda_{\mathrm{J},0}^2}{L_c^2} \times b^2\mathcal{M}^4 = c\,b^2\,\frac{\lambda_{\mathrm{J},0}^2}{\lambda_{\mathrm{s}}^2}, \tag{4.100}$$

or, in the magnetized case,

$$\begin{aligned}\alpha_{\mathrm{Jeans}} &= c\frac{\lambda_{\mathrm{J},0}^2}{L_c^2} \times b^2\mathcal{M}^4\frac{\beta}{1+\beta}(1+\mathcal{M}_A^{-2}) = c\,b^2\,(1+\mathcal{M}_A^{-2})\frac{\lambda_{\mathrm{J},0}^2}{\lambda_{\mathrm{s,mag}}^2} \\ &\simeq c\,b^2\frac{\beta}{1+\beta}(1+\mathcal{M}_A^{-2})\frac{\lambda_{\mathrm{J,0,mag}}^2}{\lambda_{\mathrm{s,mag}}^2},\end{aligned} \tag{4.101}$$

where $\lambda_{\mathrm{J},0} \propto c_s/\sqrt{G\bar{\rho}}$ is the thermal Jeans length and $\lambda_{\mathrm{J,0,mag}} = \lambda_{\mathrm{J},0} \times (1+\beta^{-1})^{1/2}$ is a magnetothermal Jeans length. λ_{s} and $\lambda_{\mathrm{s,mag}}$ are the sonic and magneto sonic lengths (see e.g. Federrath & Klessen 2012; Federrath 2016a) and c is some constant of proportionality of order of a few.

The following ratios

$$\frac{\lambda_{\mathrm{s}}}{b} = \frac{L_c}{b\,\mathcal{M}^2}, \tag{4.102}$$

$$\frac{\lambda_{\mathrm{s,mag}}}{b}\sqrt{\frac{1+\beta}{\beta(1+\mathcal{M}_A^{-2})}} = \frac{\lambda_{\mathrm{s}}}{b}\frac{1+\beta}{\beta}\frac{1}{(1+\mathcal{M}_A^{-2})^{1/2}} = \frac{\lambda_{\mathrm{s}}}{b}\frac{\mathcal{M}^2+2\mathcal{M}_A^2}{2\mathcal{M}_A\,(\mathcal{M}_A^2+1)^{1/2}} \tag{4.103}$$

can be interpreted as the average size of a shock layer. The dependence on the b parameter then shows that the more compressive the forcing is, the thinner the shock layers are. In the magnetized case, the dependence on $\mathcal{M}_A$ shows that a magnetic field acts like a buffer and produces thicker shock layers than in the non magnetized case.

Eqs. (4.93) and (4.98) can be interpreted as stating that the transition to a gravity dominated regime occurs for densities produced by shock layers with Jeans lengths that are smaller than their size. They can therefore be interpreted as modified Jeans criteria. We note that these scalings and interpretations are only valid for supersonic turbulence ($\mathcal{M} \gtrsim 1$).

3.2.6 Overall effects of gravity

As mentioned above, observations and numerical simulations have shown that the growing impact of gravity induces a s-PDF with two characteristic regime. In § (3.2.3) and (3.2.4), we found an order of magnitude estimate of the density threshold governing for the transition from an (isothermal) "inertial" turbulent regime to a regime dominated by gravity. Furthermore, following Pan et al. (2019b) and using Eq. (4.78), we see that because $S_{\mathrm{grav}}(s) < 0$ when $s > 0$ and $S_{\mathrm{grav}}(s) > 0$ when $s < 0$, respectively, gravity tends to broaden the PDF at both small and large densities, *resulting in a larger variance compared to the gravity-less regime.* This can be understood by considering that gravity acts as an extra compressive forcing. From a numerical point of view, this is equivalent to increasing the b parameter or potentially the Mach number itself, because $(b\mathcal{M})$ enters the variance-Mach relation $\sigma_s(\mathcal{M})$ in simulations of compressible turbulence (Eq. (4.91)).

Therefore, we expect 2 regimes (in terms of density) with different contributions governing the statistics of turbulence:

- a *first regime*, corresponding to densities $s < s_{\mathrm{G}}$, where s_{G} is given by Eqs. (4.93) and (4.98), where the statistics are similar to those of gravitationless "inertial" turbulence but with a gravity-induced variance increase. The magnitude of this increase depends on the quantities entering Eqs. (4.93) and (4.98)) The s-PDF in this regime is thus lognormal-like,

- and a *second regime*, corresponding to densities $s > s_{\rm G}$, where gravity has a dominant impact on the flow statistics, where the PDF will depart from (gaussian) lognormal statistics.

The transition density $s_{\rm G}$ between the two regimes *evolves with time* on the same timescale $\bar{\tau}$ as the *global or average* properties of the cloud ($\overline{\rho}(t)$, $\alpha_{\rm vir}(t)$, $\overline{(\boldsymbol{\nabla}\cdot\boldsymbol{u})^2}(t)$)[6], according to Eqs. (4.93) and (4.98). As will be shown in detail in Sec. 3.3 below, at densities $s > s_{\rm G}$, the PDF will start to deviate from a lognormal form and to develop a power law on *shorter timescales*, of the order of a typical *local* free-fall time, $\tau_{\rm ff}(s) < \bar{\tau}$. Note that for large thermal or turbulent supports, which impliy $s_{\rm G} \gg 1$, we do not expect a significant increase of the variance due to gravity.

Finally, it is worth remembering that the criteria Eq. (4.93) and (4.98) have been obtained assuming an isothermal equation of state, i.e. $P \propto \rho^\gamma$ with $\gamma = 1$. In regions with high enough densities ($\rho > \rho_{\rm ad}$, i.e. $s > s_{\rm ad}$), this assumption is no longer valid and the thermodynamics of the cloud gas is better approximated by a nearly adiabatic equation of state, i.e. $\gamma > 1$. As long as the transition density $s_{\rm G}$ calculated in the isothermal regime is smaller than $s_{\rm ad}$ ($\rho_{\rm G} \ll \rho_{\rm ad}$), which is the necessary condition for clump fragmentation, the above study remains valid. We note that for a transition density value $\rho_{\rm ad}$ that corresponds to a typical number density $n_{\rm ad} = 10^{10}$ cm^{-3} (Masunaga & Inutsuka, 2000; Machida et al., 2006; Vaytet et al., 2013, 2018) and for a cloud of average density $\overline{n} = 10^3$ cm^{-3}, $s_{\rm ad} \simeq 16$. For typical conditions with $(b\mathcal{M}) \sim 3$ and $\alpha_{\rm vir} \sim 1$, $s_{\rm G} \simeq 3$.

3.3 Time evolution of the density PDF in star forming clouds

At any time in a cloud, we can compute the threshold value $s_{\rm G}$ above which gravity starts to affect the statistics of fully developed "inertial" turbulence significantly. For diffuse, hot and/or turbulent clouds ($\alpha_{\rm vir} \gg 1$). This value, however, can be so large that the probability $\mathbb{P}(s > s_{\rm G})$ of finding regions $s > s_{\rm G}$, becomes very small. In this case, one can completely neglect the effect of gravity. To be more quantitative, let us assume that gravity can be neglected if $\mathbb{P}(s > s_{\rm G}) \leq 10^{-9}$. Assuming a lognormal density PDF, this yields $s_{\rm G} \geq 6\sigma_s - 0.5\,\sigma_s^2$ (where σ_s is the variance in Eq. (4.91)). In hot and turbulent clouds, where $T \sim 8000$ K, $(b\mathcal{M}) \sim 1$ (e.g. Draco, Miville-Deschênes et al. 2017), this corresponds to a virial parameter $\alpha_{\rm vir} \gtrsim 5.5$ (see Eq. 4.93). As the cloud cools down and contracts, $\alpha_{\rm vir}$ decreases, resulting in a value of $s_{\rm G}$ that is small enough to detect significant departures from a lognormal PDF. We can thus define time t_0 in the lifetime of the cloud that is such that the volume fraction of the cloud corresponding to (dense) regions with $s > s_{\rm G}$, where the gas PDF starts to deviate from the statistics of pure "inertial" turbulence, $\langle \boldsymbol{\nabla}\cdot\boldsymbol{u}|s\rangle \simeq 0$ due to the inceasing influence of gravity, becomes *noticeable*, i.e. statistically significant. This fixes the "zero of time" in star forming clouds, whatever the (undefinable) initial time of cloud formation is. Time t_0 thus corresponds to the time at which some dense regions start to collapse and depart from the *global* evolution (contraction or expansion) of the cloud, which is described by the time variation of $\overline{\rho}(t)$.

3.3.1 Transient regime and short time evolution

For regions with $s > s_{\rm G}$, we expect from Eqs. (4.79-4.80) that, at short times $t = t_0 + t_{\rm coll}$ after t_0, *i.e.* in the linear regime, to have :

$$\langle \boldsymbol{\nabla}\cdot\boldsymbol{u}|s\rangle \simeq -4\pi G\overline{\rho}e^s(t-t_0) = -4\pi G\overline{\rho}e^s t_{\rm coll}, \tag{4.104}$$

---

[6]. The timescale $\bar{\tau}$ of $\overline{\rho}$ variations is not necessarily equal to $\tau_{\rm ff,0}$. For example, it may well be larger if there is enough turbulent support. This depends on what drives the *global* evolution of the cloud.

(i.e. $a = 1$ in Eq. (4.44)), which yields for the PDF f:

$$f(s,t) = \tilde{\Phi}\left(\tau_{\mathrm{G},0}^{-2}\int t'\mathrm{d}t' + e^{-s}\right)e^{-2s}, \tag{4.105}$$

where $\tilde{\Phi}$ is some differentiable function. Time t_0 then enables us to determine a *physically motivated* value to fix the indefinite integral in Eq. 4.105, as that which is equal to 0 at $t = t_0$, yielding

$$\boxed{f(s,t) \simeq \tilde{\Phi}\left(\tau_{\mathrm{G},0}^{-2}\,\frac{t_{\mathrm{coll}}^2}{2} + e^{-s}\right)e^{-2s}.} \tag{4.106}$$

Therefore, for densities $s > s_{\mathrm{G}}$, it is expected that, in this transient and short phase, the PDF will change form and develop a *first power law tail* with a steep exponent $\alpha_s \simeq 2$. Eq. (4.106) show that convergence toward this short time attractor PLT occurs over a typical timescale $\tau_{\mathrm{G}}(s) = \tau_{\mathrm{G},0}\,e^{-s/2}$ (such as $\tilde{\Phi}\left(\tau_{\mathrm{G},0}^{-2}\,\frac{t_{\mathrm{coll}}^2}{2} + e^{-s}\right) \simeq \tilde{\Phi}\left(\tau_{\mathrm{G},0}^{-2}\,\frac{t_{\mathrm{coll}}^2}{2}\right)$). Conversely, the onset of this first power-law tail is expected to occur, for given time t, at a density $s_t = \rho_t(t_{\mathrm{coll}})/\overline{\rho} \simeq (\tau_{\mathrm{G},0}/t_{\mathrm{coll}})^2 \simeq 0.25(\tau_{\mathrm{ff},0}/t_{\mathrm{coll}})^2$, in agreement with numerical calculations (Girichidis et al., 2014). At later times (a few $\tau_{\mathrm{ff}}(s)$, see Sec. 3.3.2) for a given density or at higher densities for a given time, a *second power-law* develops with $\alpha_s = 3/2$, which is the signature of regions where gravitational effects are fully developed (which we call, perhaps abusively, regions of "free-fall" collapse), as seen in §3.3.2.

3.3.2 Asymptotic case: evolution in regions of "free-fall" collapse (fully developed gravity induced dynamics)

The densest regions in star forming clouds are expected to collapse under their own gravity on a timescale of the order of the *local free-fall time* $\tau_{\mathrm{ff}}(\rho) \propto (G\rho)^{-1/2}$. In these regions, where gravitational effects are fully developed, we thus expect the asymptotic scaling:

$$-\left\langle \tau_{\mathrm{ff}}^{-1}(\rho)|s\right\rangle \propto \langle \boldsymbol{\nabla}\cdot\boldsymbol{u}|s\rangle = -c\sqrt{4\pi G\overline{\rho}}\,e^{s/2}, \tag{4.107}$$

i.e. $a = 1/2$ in Eq. (4.44), and where c is a constant of proportionality of order unity, yielding

$$f(s,t) = \Phi\left(\frac{c}{2}\sqrt{4\pi G}\int_{t_0}^{t}\sqrt{\overline{\rho}(t')}\,\mathrm{d}t' + \mathrm{e}^{-s/2}\right)\mathrm{e}^{-\frac{3}{2}s}, \tag{4.108}$$

where $t = t_0 + t_{\mathrm{coll}}$. Then, if the time at which a dense region of the cloud starts to collapse, t_{coll}, is short compared to the characteristic time of variation of $\overline{\rho}$, $t_{\mathrm{coll}} \ll \overline{\tau}$, the global properties of the cloud have not had time to evolve significantly, we can write:

$$\boxed{f(s,t) \simeq \Phi\left(\frac{c}{2}\sqrt{4\pi G\,\overline{\rho}(t)}\,t_{\mathrm{coll}} + \mathrm{e}^{-s/2}\right)\mathrm{e}^{-\frac{3}{2}s}.} \tag{4.109}$$

Therefore, the s-PDF is expected to develop a power-law tail with *a specific exponent* $-3/2$, for $s \geq s_{\mathrm{G}}$, over a typical time $t(s) \equiv 2\,c^{-1}\,\tau_{\mathrm{G},0}\,e^{-s/2} \simeq c^{-1}\tau_{\mathrm{ff},0}\,e^{-s/2} \simeq c^{-1}\tau_{\mathrm{ff}}(s)$.

This analysis shows that the onset of power-law tails, $f(s) \propto e^{-\alpha_s s}$, in the PDF reflects the growing impact of gravity on the turbulent flow, with an initial power-law attractor of exponent $\alpha_s \lesssim 2$ and an asymptotic value $\alpha_s = 3/2$ in regions of "free fall" collapse.

We call here and in JC20 these regions, perhaps abusively, regions of "free-fall" collapse *simply* due to the scaling Eq. (4.107), which is a signature of fully developed gravity induced dynamics. *This does not mean that there is no pressure support, for example, but rather that the dynamics are mostly induced by gravitational infall.* For example, one expects that this scaling ($\langle \boldsymbol{\nabla}\cdot\boldsymbol{u}|s\rangle \asymp e^{s/2}$) is found at small scales, in the isothermal phase of collapsing clumps, even if pressure gradients are not negligible (Larson, 1969). In his pioneering work, Larson (1969) derived an asymptotic similarity solution for the isothermal collapse of a sphere and found that, as collapse proceeds, velocity $u(r)$ is nearly constant and density $\rho(r) \propto r^{-2}$, giving $\boldsymbol{\nabla} \cdot \boldsymbol{u} \simeq 2u/r \propto \sqrt{\rho}$ (his App. C).

A physical interpretation of the results of this Sec. 3 may be found in Sec. 6.2.

3.4 Evolution of the correlation length of the density field in star forming clouds

As seen from the previous sections (3.2) and (3.3), gravity enhances the variance of the density field both in the "inertial" turbulence regime and the gravity dominated one. In the second, high density regime, the onsets of power-law tails on a short local timescale $\tau_{\mathrm{ff}}(s) \ll \overline{\tau}$ induce a drastic increase of variance due to the exponents of the PLT, $\alpha_s = 2$ and $\alpha_s = 3/2$ as $\mathrm{Var}\,(e^s) = \overline{e^{2s}} - 1$. In principle, for such PDFs, the variance is even infinitely large. However, we expect a cut-off at high density due to a change in the thermodynamics of the cloud, e.g. from isothermal to adiabatic conditions at density s_{ad} (see Sec. 3.2.6). In any case, the variance is expected to grow drastically on a time scale which is short compared to that of the averaged global evolution $\overline{\tau}$. Then, as seen from Sec. (2.5), this increase of the variance results in a decrease of the product $\overline{\rho}(t) l_c(e^s)^3$ in order to meet the constraint of the conservation equation:

$$\mathrm{Var}\,(e^s)\;l_c(e^s)^3\,\overline{\rho}(t) = cst \tag{4.110}$$

(Eqs. (4.61) or (4.69)). Due to the difference of timescales, we can assume, that, during this phase of variance increase, the (background) average density $\overline{\rho}$ is almost constant and the conservation equation essentially holds

$$\boxed{\frac{(l_c(e^s))_t^3}{(l_c(e^s))_{t=t_0}^3} \simeq \frac{(\mathrm{Var}\,(e^s))_{t=t_0}}{(\mathrm{Var}\,(e^s))_t} \ll 1.} \tag{4.111}$$

Thus, the growing impact of gravity on the turbulent flow is accompanied by a drastic decrease of the correlation length of the density field $l_c(e^s) = l_c(\rho)$.

Physically if the correlation length represents the average size of the most correlated substructures (see **Chapter 2**), Eq. 4.111 implies that the distribution of matter in the cloud evolves from being concentrated in correlated structures of average size $(l_c(e^s))_{t=t_0}$ to being concentrated in smaller and denser correlated volumes of average size $(l_c(e^s))_t$. We discuss and interpret this result in Sec. 6.2.

4 Comparison with numerical simulations

To understand how gravity affects the statistics of the density field and thus the s and η PDFs in star forming clouds and to test our theoretical formulation, we use results of a series of numerical simulations due to Federrath & Klessen (2012, 2013), kindly provided by the authors and already described in Chap. **1**.

4.1 Numerical set up

4.1.1 Methods

For clarity purposes, we briefly outline again the essential features of these simulations presented in Chap. **1**, which deal with isothermal self-gravitating magneto-hydrodynamic turbulence on 3D periodic grids with resolution $N_{\mathrm{res}}^3 = 128^3$ to 1024^3. We will mostly consider results with no magnetic field present, keeping only two magnetic cases. In the simulations, turbulence is driven by solenoidal or compressive forcing or by a mixture of both. Sink particles are used to account for fragmentation. In each simulation, gravity is added and sink particles are allowed to form after a fully developed turbulent state is reached, which determines the initial conditions at $t = 0$. The associated transport equations are:

$$
\begin{aligned}
\boldsymbol{V} &= 0, && (4.112)\\
\overline{\rho} &= \rho_0, && (4.113)\\
s &= \ln\left(\rho/\rho_0\right), && (4.114)\\
\frac{\mathrm{D}\boldsymbol{\nabla}\cdot\boldsymbol{u}}{\mathrm{D}t} &= -\boldsymbol{\nabla}\boldsymbol{u} : \boldsymbol{\nabla}\boldsymbol{u} - 4\pi G\rho_0\left(e^s - 1\right)\Theta(t) - c_{\mathrm{s}}^2\,\boldsymbol{\nabla}^2 s + \boldsymbol{S}_{\mathrm{mag}} + \boldsymbol{\nabla}\cdot\boldsymbol{F}_{\mathrm{stir}}, && (4.115)\\
\frac{\partial}{\partial t}\left[\left\langle\left(\boldsymbol{\nabla}\cdot\boldsymbol{u}\right)^n|s\right\rangle f\right] &= \left\{1+\frac{\partial}{\partial s}\right\}\left[\left\langle\left(\boldsymbol{\nabla}\cdot\boldsymbol{u}\right)^{n+1}|s\right\rangle f\right] + f\left\langle\frac{\mathrm{D}\left(\boldsymbol{\nabla}\cdot\boldsymbol{u}\right)^n}{\mathrm{D}t}|s\right\rangle, && (4.116)
\end{aligned}
$$

where ρ_0 is constant, $c_{\mathrm{s}} = 0.2$ km.s^{-1} is the sound speed and $\boldsymbol{S}_{\mathrm{mag}}$ is the magnetic term (see § (3.2.2)). $\boldsymbol{\nabla}\cdot\boldsymbol{F}_{\mathrm{stir}}$ is the divergence of the turbulent forcing, which is 0 for a solenoidal driving, and $\Theta(t)$ is the Heaviside step function ensuring that gravity is plugged in at $t = 0$. In all runs, the Mach number $\mathcal{M}$ increases slightly with time due to collapsing regions (see §3.2.6). In most cases, this only amounts to changes by a few percents except for the $\mathcal{M} \simeq 3$ simulation which starts at $\mathcal{M} \simeq 2$ and ends up at $\mathcal{M} \simeq 3-4$ because the virial parameter

$$\alpha_{\mathrm{vir},0} = \frac{5\,\sigma_v^2}{6\,G\,L_{\mathrm{b}}^2\,\rho_0} \text{ is very small (see Table 1).} \tag{4.117}$$

We note that the aforementioned definition of $\alpha_{\mathrm{vir},0}$, which is taken from Federrath & Klessen (2012, 2013), differs from that of Sec. 3.2.2 by a factor $\pi/6 \simeq 1/2$, if the cloud size L_{c} is taken to be the box size L_{b}. As there is no unique way to turn the dimension of a cubic box into that of an equivalent spherical cloud and in order to simplify the comparison between simulations and our calculations, we keep their notation and definition.

Finally, to be consistent with the authors, we describe the time evolution of the simulations by means of the reduced time $\tilde{t} = t/\tau_{\mathrm{ff},0}$, which is time in units of the mean free fall time $\tau_{\mathrm{ff},0} \equiv \sqrt{\frac{3\pi}{32G\rho_0}}$, and by means of the star formation efficiency (SFE), which is set at 0% at the formation of the first sink particle. The authors only extracted density PDFs up to the time when SFE= 20%, which we will refer to as the "long time" of the runs.

4.1.2 Resolution and limitations on the resolution of the PDFs

Truelove et al. (1997) have shown that, in a box with density ρ, the resolution Δx should be at least 4 times smaller than the associated Jeans length in order to avoid artificial fragmentation:

$$\Delta x \leq \frac{1}{4}\sqrt{\frac{\pi c_{\mathrm{s}}^2}{G\rho}}. \tag{4.118}$$

This yields the critical density value ρ_{max} above which collapse events are not resolved with sufficient accuracy and simulations do not properly describe the cloud statistics:

$$\rho_{\mathrm{max}} = \rho_0\, e^{s_{\mathrm{max}}} = \frac{\pi c_{\mathrm{s}}^2}{16G\Delta x_{\mathrm{min}}^2}, \tag{4.119}$$

with Δx_{min} the size of the most resolved cell. Thus, the effects of gravity on density PDFs can only be properly studied for densities $s < s_{\mathrm{max}}$ (see Chap. **1**). According to Eq. (4.93), we expect gravity to have a dominant contribution at densities $s > s_{\mathrm{G}}$, which yields here for the non magnetized runs (see

Eq. (4.93)):

$$|e^{s_{\rm G}} - 1| \equiv (b\mathcal{M})^2 \times \alpha_{\rm vir,0} \times \left| \frac{s_{\rm G} + \frac{1}{2}\sigma_s^2}{\sigma_s^2} \right|, \tag{4.120}$$

where $\alpha_{\rm vir,0} = 5\sigma_v^2/(6GL_{\rm b}^2\rho_0)$ as in Federrath & Klessen (2012, 2013) and $L_{\rm b}$ is the size of the simulation box. To compare $s_{\rm G}$ with $s_{\rm max}$ we recast Eq. (4.119) as:

$$s_{\rm max} = \ln\left(\alpha_{\rm vir,0}\right) + 2\ln\left(\frac{N_{res}}{\mathcal{M}}\right) + \ln\left(\frac{6\pi}{80}\right), \tag{4.121}$$

while Eq. (4.120) gives:

$$s_{\rm G} \gtrsim 2\ln(b\mathcal{M}) + \ln(\alpha_{\rm vir,0}). \tag{4.122}$$

Therefore, at fixed $\alpha_{\rm vir,0}$, numerical resolution must be increased consistently with the Mach number $\mathcal{M}$ to properly capture the effects of gravity on the high density tail of the PDF. For $\alpha_{\rm vir,0} \simeq 1$, simulations respectively at $\mathcal{M} = 20$ and $\mathcal{M} = 50$ need a resolution of at least $N_{\rm res} = 1024$ and $N_{\rm res} = 8192$ to resolve the density domain dominated by gravity over at least a decade. Note that $N_{\rm res} = 1024$ is still probably too small for $\mathcal{M} = 20$.

4.2 Short time evolution of the transport equations

It is worth studying the short time evolution of this numerical set up in order to grasp some of the properties derived in § (3.2). To avoid overly lengthy calculations, we restrict ourselves to non magnetized simulations ($\boldsymbol{S}_{\rm mag} = 0$).

In each simulation, gravity is switched on once fully developed and stationary turbulence has been achieved. This sets the initial conditions for the transport equation Eq. (4.116). In particular, at the initial time, one has $\langle \boldsymbol{\nabla}\cdot\boldsymbol{u}|s, t=0\rangle \equiv \langle \boldsymbol{\nabla}\cdot\boldsymbol{u}|s\rangle_0 = 0$. To obtain the short time evolution of terms $\langle\psi|s,t\rangle$ in Eq. (4.116), we perform their Taylor expansion with respect to $t \geq 0$:

$$\langle\psi|s,t\rangle = \langle\psi|s\rangle_0 + \sum_{k\geq 1} \frac{\psi^{(k)}(s)}{k!} t^k. \tag{4.123}$$

This yields at first order:

$$\begin{aligned}
\langle \boldsymbol{\nabla}\cdot\boldsymbol{u}|s\rangle^{(1)} &= -4\pi G\rho_0\left(e^s - 1\right), && (4.124)\\
\ln(f)^{(1)} &= 0, && (4.125)\\
\left\langle(\boldsymbol{\nabla}\cdot\boldsymbol{u})^2|s\right\rangle^{(1)} &= 0, && (4.126)\\
\left\langle(\boldsymbol{\nabla}\cdot\boldsymbol{u})^3|s\right\rangle^{(1)} &= 12\pi G\rho_0\left(1 - e^s\right)\left\langle(\boldsymbol{\nabla}\cdot\boldsymbol{u})^2|s\right\rangle_0. && (4.127)
\end{aligned}$$

Eqn (4.124) illustrates at first order the competing effects of the velocity field (l.h.s.) and the gravity field (r.h.s.) on the density fluctuations (PDF). This equation shows that, when gravity is present, it affects turbulence over the entire density spectrum. Gravity impacts turbulence even in the low density regions ($s < 0$) within a typical timescale $1/\sqrt{4\pi G\rho_0} = \tau_{\rm G,0} \simeq \tau_{\rm ff,0}/2$ (see §3.2.2). By enhancing the contrast between underdense and overdense regions, gravity stretches the lognormal density PDF of turbulence, increasing its variance within the aforementioned timescale.

Extending the Taylor expansion to higher orders is more involved because terms such as $S_{\rm turb}(s,t) \equiv -\langle\boldsymbol{\nabla}\boldsymbol{u} : \boldsymbol{\nabla}\boldsymbol{u}|s\rangle$ or $S_{\rm th}(s,t) = -c_{\rm s}^2\,\langle\Delta s\,|s\rangle$ must be solved for. The former one can be decomposed as follows:

$$\langle \boldsymbol{\nabla u} : \boldsymbol{\nabla u} | s \rangle = \left\langle \frac{1}{3}(\boldsymbol{\nabla} \cdot \boldsymbol{u})^2 + \boldsymbol{\sigma}_u^2 - \frac{1}{2}\boldsymbol{\omega}^2 | s \right\rangle , \tag{4.128}$$

where $\boldsymbol{\omega} \equiv \boldsymbol{\nabla} \times \boldsymbol{u}$ is vorticity and $\boldsymbol{\sigma}_u^2 = \mathrm{Tr}(\underline{\underline{\boldsymbol{\sigma}_u}}^2)$, where $\underline{\underline{\boldsymbol{\sigma}_u}} \equiv \frac{1}{2}(\boldsymbol{\nabla u} + \boldsymbol{\nabla u}^{\mathrm{T}}) - \frac{1}{3}(\boldsymbol{\nabla} \cdot \boldsymbol{u})\mathbb{I}_{\mathrm{d}}$ is the strain rate deviatoric tensor. The expansion at second order then yields:

$$\begin{aligned}
\langle \boldsymbol{\nabla} \cdot \boldsymbol{u} | s \rangle^{(2)} &= \frac{1}{2} \left\langle \boldsymbol{\omega}^2 | s \right\rangle^{(1)} - \left\langle \boldsymbol{\sigma}_u^2 | s \right\rangle^{(1)} - c_{\mathrm{s}}^2 \, \langle \Delta s \, | s \rangle^{(1)}, && (4.129)\\
\ln(f)^{(2)} &= \{1 + \partial_s\} \langle \boldsymbol{\nabla} \cdot \boldsymbol{u} | s \rangle^{(1)} + \langle \boldsymbol{\nabla} \cdot \boldsymbol{u} | s \rangle^{(1)} \, \partial_s \ln f_0, && (4.130)\\
\left\langle (\boldsymbol{\nabla} \cdot \boldsymbol{u})^2 | s \right\rangle^{(2)} &= 2 \left\{ 4\pi G \rho_0 \, (e^s - 1) \right\}^2 - 8\pi G \rho_0 \, (e^s - 1) \left\langle (\boldsymbol{\nabla} \cdot \boldsymbol{u})^2 | s \right\rangle_0 \partial_s \ln f_0 \\
&\quad - \left\langle (\boldsymbol{\nabla} \cdot \boldsymbol{u})^2 | s \right\rangle_0 \{1 + \partial_s\} \langle \boldsymbol{\nabla} \cdot \boldsymbol{u} | s \rangle^{(1)} - \left\langle (\boldsymbol{\nabla} \cdot \boldsymbol{u})(2\boldsymbol{\sigma}_u^2 - \boldsymbol{\omega}^2 + 2\, c_{\mathrm{s}}^2 \, \Delta s) | s \right\rangle^{(1)} \\
&\quad + \left\{ \frac{1}{3} + \partial_s \right\} \left\langle (\boldsymbol{\nabla} \cdot \boldsymbol{u})^3 | s \right\rangle^{(1)} . && (4.131)
\end{aligned}$$

Using transport equations for vorticity and pressure,

$$\begin{aligned}
\frac{1}{2}\partial_t \boldsymbol{\omega}^2 &= -\boldsymbol{\omega}^2(\boldsymbol{\nabla} \cdot \boldsymbol{u}) + \boldsymbol{\omega} \cdot (\boldsymbol{\omega} \cdot \boldsymbol{\nabla})\boldsymbol{u} - \frac{1}{2}(\boldsymbol{u} \cdot \boldsymbol{\nabla})\boldsymbol{\omega}^2, && (4.132)\\
\partial_t (c_{\mathrm{s}}^2 \Delta s) &= -c_{\mathrm{s}}^2 \Delta \left((\boldsymbol{u} \cdot \nabla) s + \boldsymbol{\nabla} \cdot \boldsymbol{u} \right), && (4.133)
\end{aligned}$$

stochastic fields on the right hand side of Eqs. (4.132)–(4.133) are continuous with respect to the time variable at $t = 0$, and hence we expect no discontinuity in the *first* time-derivative of $\left\langle \boldsymbol{\omega}^2 | s \right\rangle$ and $\left\langle (c_{\mathrm{s}}^2 \Delta s) | s \right\rangle$. Thus:

$$\left\langle \boldsymbol{\omega}^2 | s \right\rangle^{(1)} = c_{\mathrm{s}}^2 \, \langle \Delta s \, | s \rangle^{(1)} = 0. \tag{4.134}$$

On the right hand side of of Eq. (4.131), for $s \gtrsim 1$, each one of the last four terms is expected to be less than, or of of the same order of magnitude as, the second term ($8\pi G \rho_0 \, (e^s - 1) \left\langle (\boldsymbol{\nabla} \cdot \boldsymbol{u})^2 | s \right\rangle_0 \partial_s \ln f_0$). We thus recast Eqs. (4.129)–(4.131) as follows:

$$\begin{aligned}
\langle \boldsymbol{\nabla} \cdot \boldsymbol{u} | s \rangle^{(2)} &= - \left\langle \boldsymbol{\sigma}_u^2 | s \right\rangle^{(1)} , && (4.135)\\
\left\langle (\boldsymbol{\nabla} \cdot \boldsymbol{u})^2 | s \right\rangle^{(2)} &= 2 \left\{ 4\pi G \rho_0 \, (e^s - 1) \right\}^2 - 8\pi G \rho_0 \, (e^s - 1) \left\langle (\boldsymbol{\nabla} \cdot \boldsymbol{u})^2 | s \right\rangle_0 \partial_s \ln f_0 \\
&\quad + R(s), && (4.136)
\end{aligned}$$

where $R(s)$ is a residue that contains the last 3 terms of Eq. (4.131). Equation (4.136) allows us to distinguish 2 regimes.

1. At high density, $\left\langle (\boldsymbol{\nabla} \cdot \boldsymbol{u})^2 | s \right\rangle^{(2)} = 2 \left\{ 4\pi G \rho_0 \, (e^s - 1) \right\}^2$. This implies that infall motions induced by pure gravitational collapse dominate and erase all traces of pre-existing turbulent motions in a critically short time $t(s) \sim (b\mathcal{M})\sqrt{\alpha_{\mathrm{vir},0}}\tau_{\mathrm{G},0} e^{-s}$.
2. At lower densities, $\left\langle (\boldsymbol{\nabla} \cdot \boldsymbol{u})^2 | s \right\rangle^{(2)} = 8\pi G \rho_0 \, (1 - e^s) \left\langle (\boldsymbol{\nabla} \cdot \boldsymbol{u})^2 | s \right\rangle_0 \partial_s \ln f_0 + R(s)$. In this regime, gravity enhances pre-existing turbulent motions and essentially acts as a driver of turbulence, leading to an increase of the PDF variance within a typical timescale $\tau_{\mathrm{ff},0}$, as mentioned above.

The transition between these two regimes occurs when:

$$\boxed{|4\pi G \rho_0 \, (e^s - 1)| \gtrsim \left| \left\langle (\boldsymbol{\nabla} \cdot \boldsymbol{u})^2 | s \right\rangle_0 \partial_s \ln f_0 \right| ,} \tag{4.137}$$

which is exactly the criterion derived in Eq. (4.89).

The Taylor expansion, at this order, allows insights on *where the transition between gravity-enhanced turbulence and pure gravity occurs.* According to Eq. (4.130) (see also §3.3.2), the characteristic timescale for significant changes of the s-PDF in the highest s regions, where gravity dominates, is that for the Poisson Equation (4.9), $\tau_{\mathrm{G}}(s) = \tau_{\mathrm{G},0} e^{-s/2}$. The characteristic timescale for significant changes of the variance in lower s regions is $\tau_{\mathrm{ff},0}$[7]. Unfortunately, neither the asymptotic scaling for $\langle \boldsymbol{\nabla} \cdot \boldsymbol{u} | s \rangle$ in high s regions nor the characteristic time scale to achieve it can be derived exactly, but the latter is expected to scale as $e^{s/2}$, as seen in §3.3.2.

4.3 Evolution of the s-PDF

4.3.1 Effects of gravity on the low-s-part of the s-PDF

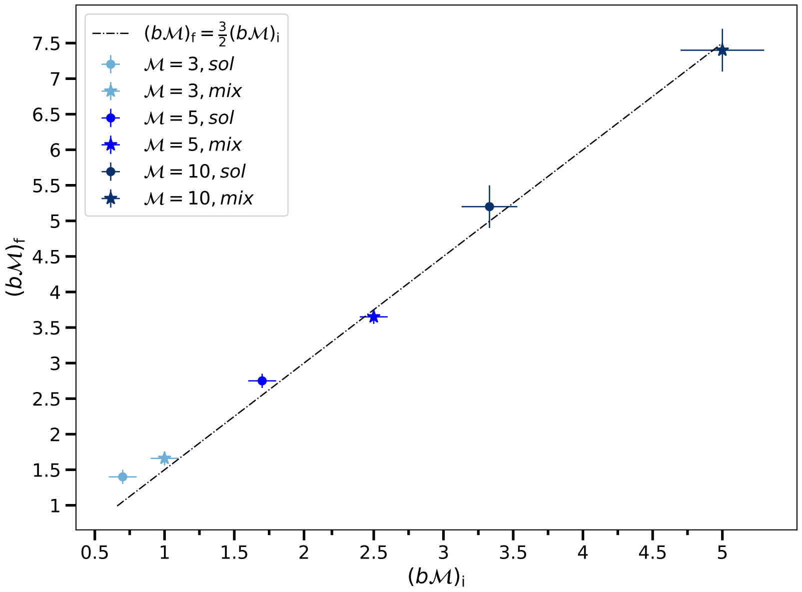

FIGURE 4.1 $(b\mathcal{M})_{\mathrm{i}}$ measured at $t = 0$ vs $(b\mathcal{M})_{\mathrm{f}}$ measured for SFE=20% for non magnetized runs. Both $(b\mathcal{M})$ values are obtained by inverting the relation $\sigma_s^2 = \ln\left(1 + (b\mathcal{M})^2\right)$ in the lognormal part of the PDF. This highlights the increase of the variance due to the impact of gravity.

At low densities ($s < 0$), the PDF is observed to be lognormal-like, indicating that gas motions are mostly governed by the statistics of "inertial" turbulence. Then, according to the calculations in §3.2 and §4.2, we expect that the variance in the lognormal part of the PDF ($s < s_{\mathrm{G}}$) increases because of the growing impact of gravity. The reason can be two fold. On the one hand, gravity acts as a compressive driver of turbulence, so that b increases in Eqs. (4.91)-(4.95). On the other hand, the velocity of the flow and hence the Mach number can increase in these "low" density regions, resulting overall in a larger $(b\mathcal{M})$ value than in the absence of gravity. As shown in §4.2, the characteristic timescale for this enhancement of the variance increase is $\tau_{\mathrm{ff},0}$. For regions that already are barely gravitationally stable, where star formation is imminent, like *e.g.* in the compressive run where an SFE of 20% is reached in a relatively short time $\tilde{t}$, we may not expect to have time to detect a significant change of the variance in the lognormal part (see Fig. 4.5).

In almost all simulations, save for the compressive run, the variance in the log-normal part of the PDFs increases with time. Fig. 4.1 displays the increase of variance σ_s *in the lognormal part* of the s-PDF of non magnetized runs as a function of the parameter $(b\mathcal{M})$ obtained from inverting the relation $\sigma_s^2 = \ln\left(1 + (b\mathcal{M})^2\right)$. In all these calculations, the parameter $(b\mathcal{M})_{\mathrm{f}}$ that is determined at the SFE value of = 20% is larger than the initial one at $t = 0$, $(b\mathcal{M})_{\mathrm{i}}$. For solenoidal simulations with $\mathcal{M} = 5$ and

---

[7] We recall that $\tau_{\mathrm{ff},0} \simeq 2\,\tau_{\mathrm{G},0}$

$\mathcal{M} = 10$, where $\alpha_{\mathrm{vir},0} \simeq 1$, we expect that the b parameter, which is initially equal to 1/3, increases up to 1/2 (close to an equipartition of solenoidal and compressive modes). In these simulations, the Mach number does not change appreciably (Federrath & Klessen, 2013) so that $(b\mathcal{M})_{\mathrm{f}} \simeq 3/2(b\mathcal{M})_{\mathrm{i}}$. The $\mathcal{M} \sim 3$ simulations are expected to lie above the best-fit relationship in Fig. (4.1) because $\alpha_{\mathrm{vir},0} \ll 1$, resulting in a final b value $b_f > 0.5$ in Eq. (4.91). Magnetized runs are not included in this analysis due to the additional β parameter in Eq. (4.95), because one would need to account for the behavior of the magnetic pressure in these regions. In both magnetized cases, however, the variance grows by 6% and 20% for the runs with $\mathcal{M}_A = 13$ and $\mathcal{M}_A = 2.7$, respectively. In all these simulations, gravity increases the variance of the PDF and mostly acts as an extra compressive driver.

4.3.2 Departure from lognormal statistics and formation of power law tails

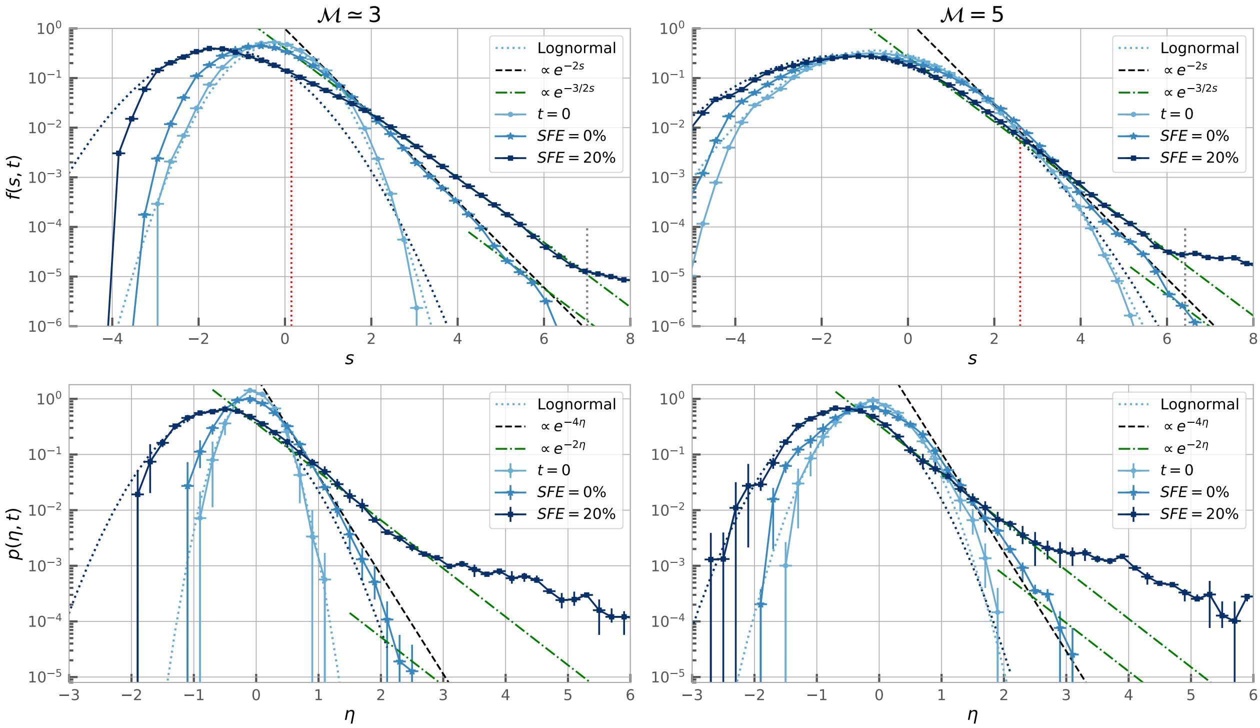

FIGURE 4.2 Evolution of the s (top row) and η-PDFs (bottom row) for solenoidal simulations with $\mathcal{M} \simeq 3$, $N_{\mathrm{res}} = 512$ (left) and $\mathcal{M} = 5$, $N_{\mathrm{res}} = 256$ (right) at $t = 0$ (light blue circles), SFE= 0% (blue stars) and SFE= 20% (dark blue squares). Horizontal error-bars represent the bin spacing and vertical error-bars indicate the uncertainty in the η-PDFs corresponding to 3 different projection directions. Lognormal fits of the low density parts of PDFs at $t = 0$ and SFE= 20% are shown in dotted lines. The s-PDFs and η-PDFs develop power-law tails with exponents $\alpha_\eta = 2$, $\alpha_\eta = 4$ (black dashed lines) and then with $\alpha_s = 3/2$, $\alpha_\eta = 2$ (green dot-dashed lines) at higher density. The vertical dotted red lines corresponds to the value of s_{G} calculated from Eqs. (4.120) with values of σ_s computed at SFE= 20%. The vertical dotted grey lines at $s > 6$ correspond to the maximum density value for well-resolved results $s_{\max}$ from Eq. (4.121).

In high-s regions of the PDF, departures from lognormal statistics are expected to occur for $s > s_{\mathrm{G}}$. Above this thershold value, a power-law tail is expected to develop, with an exponent that is initially $\alpha_s = 2$ and then tends to $\alpha_s = 3/2$ (see Sec. 3.3). It is worth emphasizing that, for this $\mathcal{M} \sim 3$ simulation, $s_{\mathrm{G}} \sim 0.1$ as $\alpha_{\mathrm{vir}} \ll 1$, so that we do not expect the power law tail with exponent $\alpha_s = 3/2$ to develop up to s_{G} in a time $\tilde{t} \simeq 1$ (since this typically occurs over a few times $\tau_{\mathrm{ff},0}$). Departures from a lognormal behavior are however indeed observed to start at about $s \sim 0.1$. Figure (4.2) displays the PDF of the s-PDF of solenoidal turbulence forcing for $\mathcal{M} \simeq 3$ and for two different grids $N_{\mathrm{res}} = 512$ and $\mathcal{M} = 5$, $N_{\mathrm{res}} = 256$ at three different evolution stages: at the initial time $t = 0$ (light blue), and

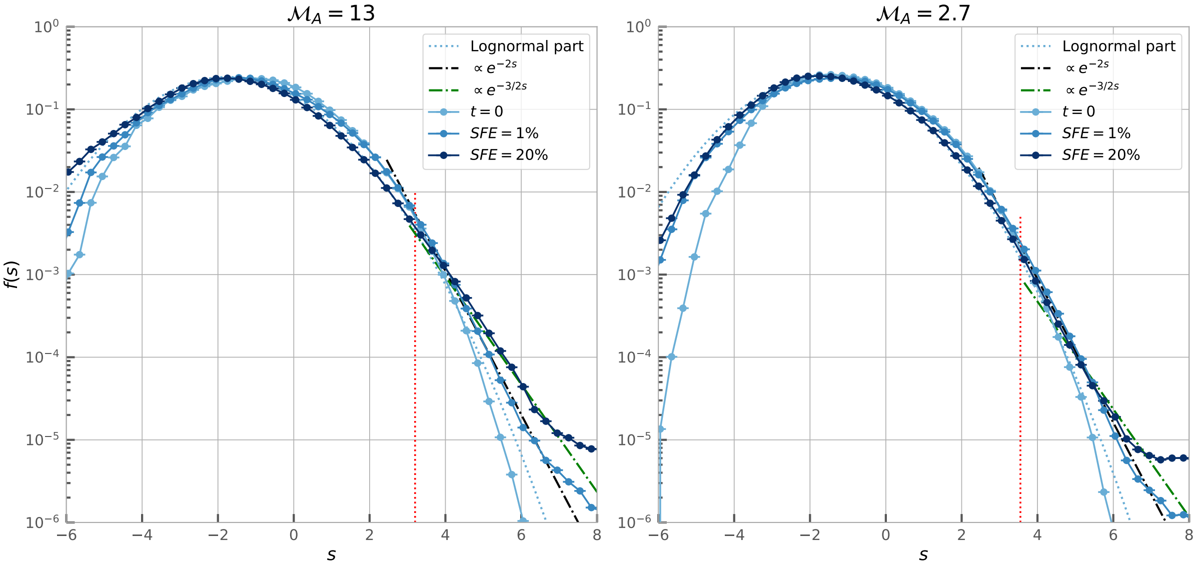

FIGURE 4.3 Same as for Fig. (4.2) for the magnetized simulation with mixed turbulence forcing. The blue line corresponds to SFE= 1%.

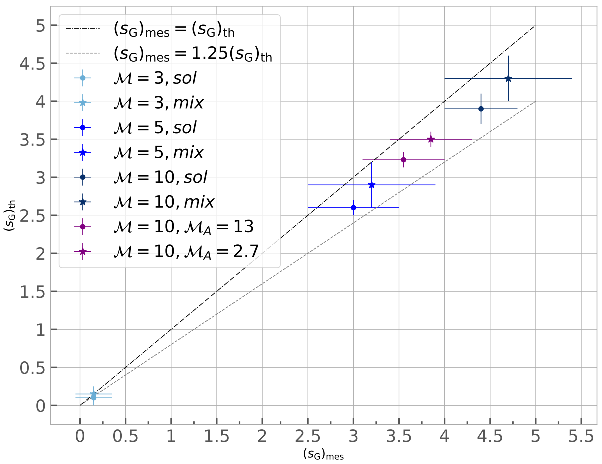

FIGURE 4.4 $(s_G)_{mes}$, directly measured on the s-PDF, as a function of $(s_G)_{th}$ derived from Eq. (4.120) (and Eq. (4.98) for the magnetized runs) with the values of $(b\mathcal{M})$ and σ_s that are deduced from a lognormal fits to the PDFs at low densities. Results for simulations with solenoidal and mixed turbulence forcing with Mach numbers $\mathcal{M} \in \{3, 5, 10\}$ are included as well as for two magnetized simulations with Alfvenic Mach numbers $\mathcal{M}_A = 2.7$ and 13. Theoretical $(s_G)_{th}$ values are close to the measured ones ($(s_G)_{mes}$).

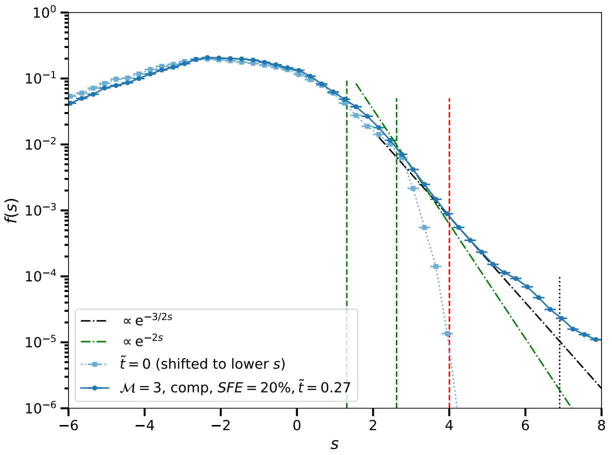

FIGURE 4.5 s-PDFs of the compressive simulation with $\mathcal{M} \sim 3$. Dark-blue solid line: at time $\tilde{t} = 0.27$, corresponding to a SFE=20%. Light-blue dotted line: at the initial time $\tilde{t} = 0$, shifted to lower s to account for mass conservation and to allow a comparison with theoretical results. Power law profiles are shown as green and black dash-dotted lines. The green vertical dashed lines correspond to s values such that $t = \tau_G(s)$ and $t = 2\tau_G(s)$, respectively, i.e. $s = -2\ln\left(2\tilde{t}\right)$ and $s = -2\ln\left(\tilde{t}\right)$. The red vertical dashed line corresponds to $s = -2\ln\left(\tilde{t}/2\right)$.

then at star formation efficiency (SFE) values of =0% (blue) and =20% (dark blue). Fig. 4.3 displays the s-PDF of the magnetized runs with mixed turbulence forcing and $\mathcal{M} = 10$. The PDFs develop a power-law tail with exponent $\alpha_s = 2$ at short times and exponent $\alpha_s = 3/2$ at large times. Departures from a purely lognormal distribution occur at a value of s close to the s_G estimate calculated from Eq. (4.120) for values of $(b\mathcal{M})$ and σ_s at time $\tilde{t} = t/\tau_{\rm ff,0}$, when gravity has acted to increase them.

Fig. 4.4 compares values of $(s_G)_{mes}$ that are directly inferred from the s-PDF to theoretical ones $(s_G)_{th}$ derived from Eqs. (4.120) (and Eq. (4.98)) with the values of $(b\mathcal{M})$ and σ_s deduced from a lognormal fit to the PDF at low densities. We note that, as mentioned in Sec. 3.2.2, $s_{\rm G}$ evolves over a *global* timescale $\tau_{\rm ff,0}$, which is the characteristic time for an increase of variance σ_s (or of $(b\mathcal{M})$). The measured $(s_{\rm G})_{\rm mes}$ values are close to theoretical ones $(s_{\rm G})_{\rm th}$. Moreover, save for the $\mathcal{M} \sim 3$ simulations, the measured $(s_{\rm G})_{\rm mes}$ values agree very well with the predicted onset of a power law tail.

Furthermore, in all runs, the development of power-law tails in the PDF at a given s is observed to occur at a characteristic time of the order of the "local" free fall time $\tau_{\rm ff}(s)$, as expected from § 3.3. To illustrate this, we show results from compressive simulations for $\mathcal{M} \sim 3$ in Fig. 4.5. Indeed, because $\alpha_{\rm vir,0} \ll 1$ in this run, every region where $s > s_{\rm G} \simeq 0.1$ (see Eq. (4.122)) starts to collapse as soon as gravity is switched on, leading to fast star formation. This allows us to evaluate the timescales for the development of PLTs. A first, steeper PLT with exponent $\alpha_s \simeq 2$ appears in a typical time $\tau_{\rm G}(s)$ whereas the shallower "asymptotic" PLT appears in a typical time equal to a few times $\tau_{\rm ff}(s)$.

4.3.3 Evolution of the η-PDF

The η-PDF, $p(\eta)$ ($\eta = \ln(\Sigma/\overline{\Sigma})$), evolves from a lognormal form and develops power-law tails just like the s-PDF $f(s)$. Likewise, at high logarithmic column densities $\eta > \eta_{\rm max}$, shallow power-law tails appear due to the artificial fragmentation of regions with density over the resolution limit $s > s_{\rm max}$ (see Sec. 4.1.2). Fig. 4.2 displays the η-PDF of solenoidal simulations with $\mathcal{M} \sim 3$ and $\mathcal{M} = 5$ at initial time $t = 0$, and star formation efficiency (SFE) values of =0% and SFE=20%. The η-PDF displays a power law tail with exponent $\alpha_\eta \simeq$=4 and α_η=2 when the s-PDF develops a power-law tail with exponent $\alpha_s = 2$ and $\alpha_s = 3/2$ respectively.

4.4 Evolution of the correlation length

We now study how the correlation length evolves. To this aim, we use Eq. (2.11) defined in Chapter **2**, which gives an estimate of the ratio $l_c(\rho)/R$ in terms of the ratio of the variances of the column density Σ and density ρ:

$$\mathrm{Var}\left(\frac{\Sigma}{\mathbb{E}\left(\Sigma\right)}\right) \simeq \mathrm{Var}\left(\frac{\rho}{\mathbb{E}\left(\rho\right)}\right)\frac{l_c(\rho)}{R}.$$

Eq. (2.11) thus yields the estimate $\hat{l}_c/R$ of the ratio of the correlation length $l_c(\rho)$ to the half size of the simulation box $R = L/2$:

$$\frac{\hat{l}_c}{R} \equiv \frac{\mathrm{Var}\left(\frac{\Sigma}{\mathbb{E}(\Sigma)}\right)}{\mathrm{Var}\left(\frac{\rho}{\mathbb{E}(\rho)}\right)} \simeq \frac{l_c(\rho)}{R}. \tag{4.138}$$

As shown in Sec. 3.4, the increase of the variance of ρ that is associated with the development of power-law tail is expected to be accompanied by a decrease of the correlation length $l_c(\rho)$ and thus of the estimate $\hat{l}_c/R$, as $\overline{\rho} = \rho_0 = cst$ (see Eq. (4.111)).

Had Eq. (4.138) led to an *exact* value of ratio $l_c(\rho)/R$, we would expect that $\hat{l}_c/R \propto \mathrm{Var}\left(\rho\right)^{-1/3}$. Eq. (4.138), however, is only a proxy to derive an estimate of $l_c(\rho)$ to within a factor of order unity which depends on the shape of the auto-covariance function (ACF) of the density field (see Chap. **2**). For example, for an exponential ACF ($\propto e^{-r/\lambda}$), we had $\hat{l}_c \simeq \pi^{-1/3} l_c(\rho)$ whereas $\hat{l}_c \simeq l_c(\rho)$ for a gaussian ACF ($\propto e^{-(r/\lambda)^2}$). Furthermore, the ACF is initially that of *inertial* turbulence and evolves towards an ACF whose shape at short lags is determined by gravity induced dynamics. We thus expect the ACF to change with time. At late times, when the dynamics in high density regions (short scales) is dominated by gravity, one can expect that the ACF at short lags does change as time increases but preserving its functional form. We therefore expect that $\hat{l}_c/R \propto \mathrm{Var}\left(\rho\right)^{-1/3}$ only at late times, i.e. for $\mathrm{Var}\left(\rho\right)_t \gg \mathrm{Var}\left(\rho\right)_{t=0}$. Finally, as the simulations can only resolve structures that are larger than $\Delta x_{\rm min} = L/N_{\rm res}$, we expect that values of $\hat{l}_c/R$ inevitably level off at some point.

Fig. 4.6 displays estimated values of $\hat{l}_c/R$ as a function of ratio $\mathrm{Var}\left(\rho\right)_t/\mathrm{Var}\left(\rho\right)_{t=0}$ (which grows

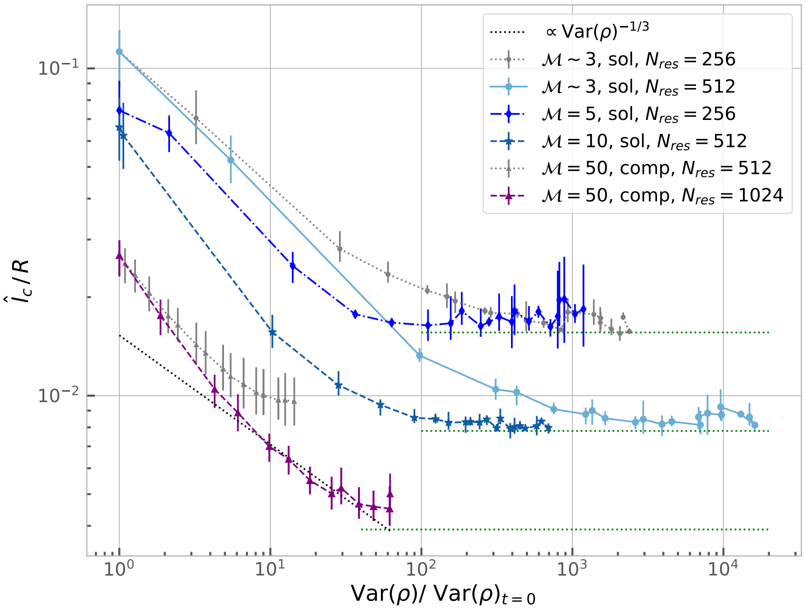

FIGURE 4.6 Estimate of correlation length $\hat{l}_c/R$ (Eq. (4.138)) as a function of ratio $\mathrm{Var}\,(\rho)_t\,/\mathrm{Var}\,(\rho)_{t=0}$, for Mach numbers $\mathcal{M} \in \{3, 5, 10, 50\}$ (from light blue to blue, dark blue and purple lines). Two lower resolutions are displayed in grey for $\mathcal{M} = 3$ and $\mathcal{M} = 10$, in order to highlight the limitations due to the numerical resolution (as measured by N_{res}). The black dotted line corresponds to scaling $\hat{l}_c/R \propto \mathrm{Var}\,(\rho)^{-1/3}$. Green horizontal dotted lines indicate the value of ratio $\lambda_J(\rho_{\max})/2R$ for which $\hat{l}_c/R$ levels off.

with time due to the development of PLTs) from hydrodynamic simulations for various Mach number $\mathcal{M}$ and resolution N_{res}. As expected, the $\hat{l}_c/R$ ratio decreases as the variance $\mathrm{Var}\,(\rho)$ increases. At high variance values (late times), the correlation length is observed to level off at a value that depends on the resolution N_{res}, corresponding to $\hat{l}_c \simeq 2\Delta x_{\min} = \lambda_J(\rho_{\max})/2$ where $\lambda_J(\rho_{\max})$ is the Jeans length at density $\rho_{\max}$ above which cloud collapse features are not resolved (Truelove et al., 1997), as defined in Eq. (4.119). For simulations at $\mathcal{M} = 50$ at the highest resolution $N_{\mathrm{res}} = 1024$, we observe that the scaling $\hat{l}_c/R \propto \mathrm{Var}\,(\rho)^{-1/3}$ holds over a decade for $\mathrm{Var}\,(\rho)_t\,/\mathrm{Var}\,(\rho)_{t=0} \geq 5$. In the other simulations, this scaling law is inhibited by the levelling off of $\hat{l}_c$ (save perhaps for the $\mathcal{M} = 10$ one where it holds for half a decade). It would thus be interesting to carry out all simulations with the same highest resolution ($N_{\mathrm{res}} = 1024$ for example).

The initial values of $\hat{l}_c/R$ yield $\hat{l}_c/L = 0.056^{+0.01}_{-0.013}$, $\hat{l}_c/L = 0.037^{+0.009}_{-0.006}$, $\hat{l}_c/L = 0.025^{+0.005}_{-0.003}$, and $\hat{l}_c/L = 0.013^{+0.0015}_{-0.0018}$ for $\mathcal{M} = 3$, 5, 10, 50 respectively. For simulations with $\mathcal{M} \in \{3, 5, 10\}$, one finds that, within a factor of order unity, $\hat{l}_c \simeq L/\mathcal{M}^2 = \lambda_{\mathrm{s}}$, where λ_{s} is the sonic length, close to the average width of filamentary structures in isothermal turbulence (Federrath, 2016b). This is not surprising because $l_c(\rho)$ describes the average size of the most correlated substructures (see Chap. **1**). For the $\mathcal{M} = 50$ simulations, however, $\hat{l}_c$ is about 30 times larger that $\lambda_{\mathrm{s}} = L/2500$. λ_{s} is not resolved in these simulations ($N_{\mathrm{res}} = 512$ or 1024), which may account for the large discrepancy between $\hat{l}_c$ and its expected value λ_{s}.

The above results show that Eq. (4.138) allows a good approximation of the actual value of ratio $l_c(\rho)/R$. They also emphasize that correlated substructures are only resolved down to the smallest Jeans length that can be achieved in the simulations. In addition, $l_c(\rho) \simeq \lambda_{\mathrm{s}}$ is the initial average width of filamentary structures, so that $l_c(\rho)$ describes the average size of the densest and most correlated substructures (see Chap. **1**). This does not imply that structures larger than $l_c(\rho)$ are not correlated. Such large correlated structures can exist (e.g; filaments) but they are less correlated than structures that are smaller than $l_c(\rho)$ (i.e. they are associated to a lower correlation coefficient $C_\rho/\mathrm{Var}\,(\rho)$). Finally, simulations for the highest resolutions suggest that quantity $l_c(\rho)^3\mathrm{Var}\,(e^s)$ is indeed conserved, as expected from our theoretical analysis.

5 Comparison with Observations

In this section, we confront our theory to data from several MCs. Observations show the column density PDF has a lognormal shape in regions where star formation has not occurred yet and develops power-law tails at high column densities in regions with numerous pre-stellar cores (Kainulainen et al., 2009; Schneider et al., 2013). In the latter regions, we expect that the exponent of the power-law tail is $\alpha_\eta = 2$, corresponding to an underlying s-PDF with a power-law exponent $\alpha_s = 3/2$, which is a signature of fully developed gravity powered dynamics. In regions where detectable star formation has not occurred yet, we expect that the η-PDFs has an extended lognormal part and perhaps power-law tails with an exponent $2 < \alpha_\eta \simeq 4$, corresponding to an underlying s-PDF power-law exponent $\alpha_s \simeq 2$, as detailed in the previous sections.

We use a simple model with one or two power-law tails, characterized by 1 or 2 transition densities between lognormal and power law tails, noted s_1 and s_2, as described in Sec. 3.5 of Chap. 2. This allows us to characterize the physical processes governing the shape of the s and η-PDFs in the clouds. We neglect magnetic field effects. Thus, we derive an estimate of the product $(b\mathcal{M})$ (Eq. (4.91)) from the variance $\sigma_{\mathrm{s},\eta}$ in the lognormal parts of the PDF. In addition, the values of s_1 and s_2 allow an estimate of $\alpha_{\mathrm{vir}} = 5\sigma_v^2/(\pi G L_{\mathrm{c}}^2\bar{\rho})$ (Eq. (4.93)) and of the time at which the first regions started to collapse, expressed in units of the mean free-fall time $\tilde{t}_{\mathrm{coll}} = t_{\mathrm{coll}}/\tau_{\mathrm{ff},0}$. Values are given in Tab. 1.

We apply our methods to four different clouds: Orion B (Schneider et al., 2013; Orkisz et al., 2017), Aquila (Könyves et al., 2010, 2015; André et al., 2010; Schneider et al., 2013), Polaris (André et al., 2010; Miville-Deschênes et al., 2010; Schneider et al., 2013) and Draco (Miville-Deschênes et al., 2017). All these data come from the Herschel Gould Belt survey (André et al., 2010) and were kindly provided by Nicola Schneider. They have been corrected for line of sight contamination (Schneider et al., 2015). For Orion B, the cloud's total mass and area above an extinction $A_v \geq 1$ are $M_{c,A_v\geq 1} = 29.69 \times 10^3 M_\odot$ and $A_{c,A_v\geq 1} = 651$ pc^2. For Aquila, Polaris and Draco, $(M_{c,A_v\geq 1}, A_{c,A_v\geq 1}) = (25.94 \times 10^3 M_\odot, 393\,\mathrm{pc}^2)$, $(1.21 \times 10^3 M_\odot, 3.9\,\mathrm{pc}^2)$ and $(8.04 \times 10^3 M_\odot, 1500\,\mathrm{pc}^2)$, respectively.

5.1 Clouds with active star formation

The two first clouds, Orion B and Aquila, are known to contain numerous pre-stellar cores. Line of sight contamination is negligible in the Orion B data but leads to an artificial deviation from a lognormal distribution in the low density regions in the Aquila data, which has been corrected for (Schneider et al., 2015). As seen in Figs. 4.7, their η-PDFs display a lognormal part at low column densities and a power-law tail at high densities with exponent $\alpha_\eta \simeq 2$, corresponding to an underlying s-PDF with a power-law tail with exponent $\alpha_s = 3/2$, a signature of collapsed regions. Using the procedure of Sec. 3.5, we obtain that both cloud PDFs develop power-law tails consistent with the expected asymptotic exponent $\alpha_s = 3/2$ for $s > s_1$ with $1 < s_1 < 2$. We can thus estimate that in these clouds, (statistically significant) collapse events have occurred in the densest regions since $\tilde{t}_{\mathrm{coll}} \approx (2-5) \times e^{-s_1/2} \gtrsim 1$ (see Sec. 3.3.2). Note here that $\tau_{\mathrm{ff},0}$ corresponds to the *region under study* in the cloud, and not to the whole cloud. Stated differently, the present age of the region of interest is such that $t - t_0 \gtrsim \tau_{\mathrm{ff},0}$, where one should recall the definition of t_0 (§3.3).

Assuming that power-law tails develop for $s \geq s_{\mathrm{G}}$ (see Sec. 4.3.2), estimates of s_1 combined with estimates of $(b\mathcal{M})$ from the determination of σ_s (see Sec. 3.5) yield values of the virial parameter $\alpha_{\mathrm{vir}} \sim 1$ from Eqs. (4.93) and (4.120). Estimates of $(b\mathcal{M})$ for Orion B lead to mean Mach-numbers $\mathcal{M} = 5.4^{+0.8}_{-0.8}$ and $\mathcal{M} = 3.6^{+0.5}_{-0.5}$ for $b = 1/3$ and $b = 1/2$, respectively, in good agreement with the results

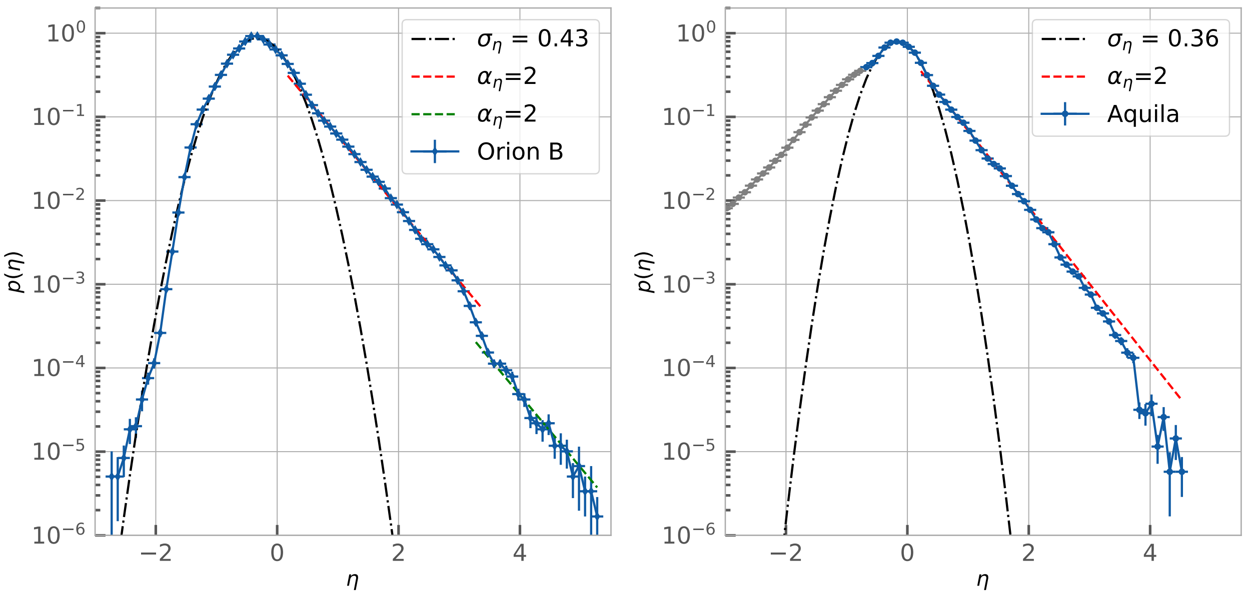

FIGURE 4.7 Dark blue: observed η-PDF of the Orion B (Left) and Aquila (Right) clouds. Dash-dotted black line: lognormal fit of the low η part of the PDF. Dashed red and green lines: power-law with exponent $\alpha_\eta = 2$, corresponding to an underlying s-PDF with a power-law exponent $\alpha_s = 3/2$, a signature of collapsed regions. The data in grey at low densities in the Aquila PDF are contaminated by line of sight contamination effects.

of Orkisz et al. (2017). In Aquila, we obtain $\mathcal{M} = 4.0^{+0.5}_{-0.5}$ and $\mathcal{M} = 2.7^{+0.3}_{-0.3}$, reflecting the smaller variance σ_η. This is consistent with the estimate of Schneider et al. (2013), $\mathcal{M} \sim 6$ with a $\sim$ 30-40% error.

5.2 "Young" clouds with little or no sign of star formation activity

In the two other clouds, Polaris and Draco, detectable star formation does not seem to have occurred yet. There are only pre-stellar nuclei in Polaris. These clouds are therefore good candidates to probe the statistics of the initial phases of cloud dynamics and star formation. Their η-PDFs exhibit either extended lognormal forms, covering a wide range of $p(\eta)$ (Draco), and/or an extended domain of power-law tails with a steep exponent, $\alpha_\eta \simeq 4$, corresponding to a s-PDF power-law tail exponent $\alpha_s = 2$, before reaching asymptotic values $\alpha_s = 3/2$ at high density. This can be seen in Fig. 4.8. According to our theory, the steep power-law tails or extended lognormal distributions suggests *a short time* $\tilde{t}_{\mathrm{coll}}$ *since the initiation of collapse.*

5.3 Polaris

The Polaris PDF exhibits an extended power-law tail with a steep exponent, $\alpha_\eta \simeq 4$, corresponding to a s-PDF power-law tail of exponent $\alpha_s = 2$ for $s > s_1$, before reaching the asymptotic values $\alpha_\eta \simeq 2$, i.e. $\alpha_s = 3/2$ at high density, $s > s_2$ (see Fig. 4.8 left). Carrying out the same analysis as before and using Sec. 3.5, we get $(s_1, s_2) = (1.68^{+0.38}_{-0.34}, 6.3^{+0.1}_{-0.15})$. The value of s_1 implies that $\tilde{t}_{\mathrm{coll}} \gtrsim 0.5\, e^{-s_1/2} = 0.22^{+0.03}_{-0.04}$ (see Sec. 3.3.1). The value of the second density threshold s_2, which corresponds to collapsing regions, yields $\tilde{t}_{\mathrm{coll}} \approx$(2-5)$\times e^{-s_2/2} \approx 0.09 - 0.21$ (see Sec. 3.3.2 and 4.3.2), which is consistent with the above estimate of $\tilde{t}_{\mathrm{coll}}$. A final estimate is $\tilde{t}_{\mathrm{coll}} = 0.2 \pm 0.1$.

The estimated $(b\mathcal{M})$ value for Polaris yields mean Mach numbers $\mathcal{M} = 3.8^{+0.4}_{-0.4}$ and $\mathcal{M} = 2.5^{+0.3}_{-0.3}$ for $b = 1/3$ and $b = 1/2$, respectively, consistent with the estimation of Schneider et al. (2013). Taking $s_1 = s_{\mathrm{G}}$, we obtain an upper bound $\alpha_{\mathrm{vir}} \lesssim 1.2$.

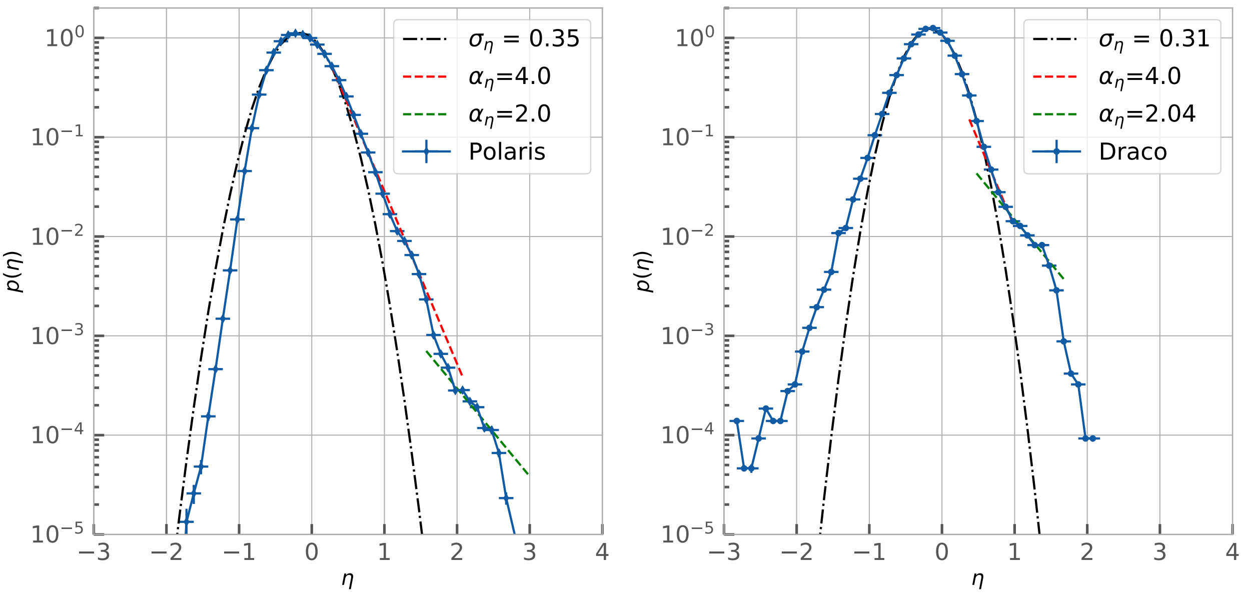

FIGURE 4.8 Observed η-PDF of the Polaris (Left) and Draco(Right) clouds. Dash-dotted black line: lognormal fit of the low η part of the PDF. Dashed red and green lines: power-law tails with exponents $\alpha_\eta = 4$ and 2, corresponding to power law tail exponents $\alpha_s = 2$ and $3/2$ in the underlying s-PDF, respectively.

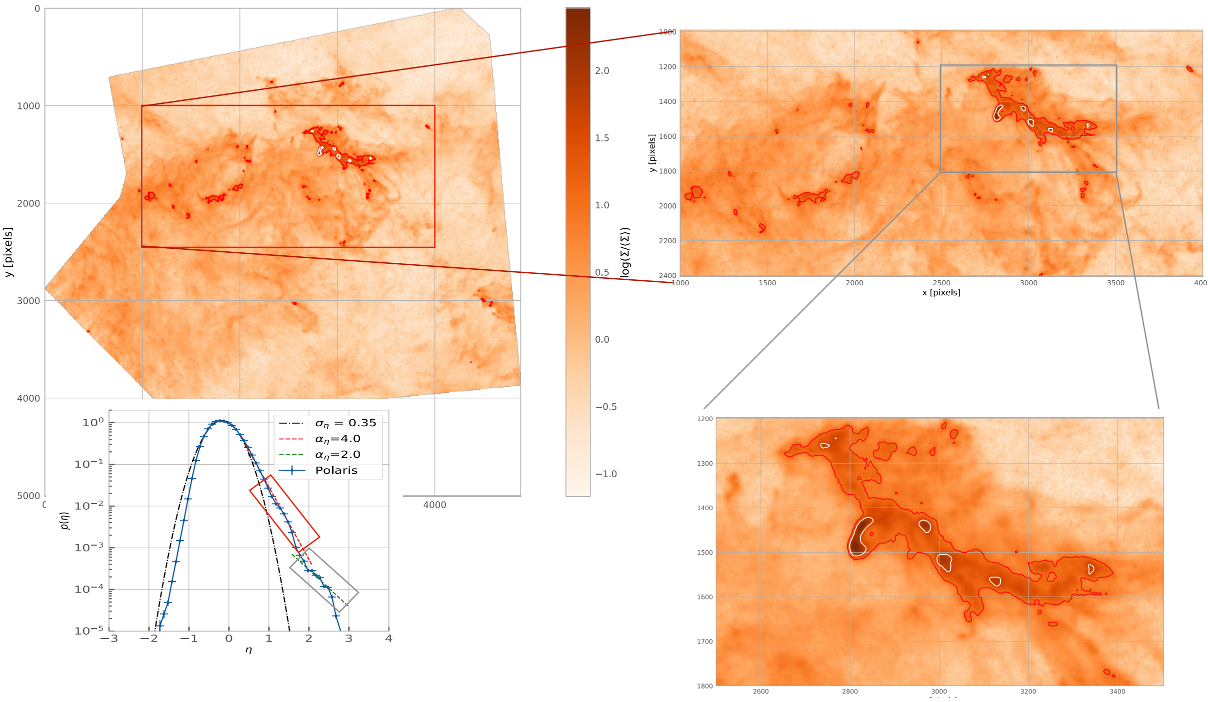

FIGURE 4.9 Column density maps of the Polaris Flare. Top Left panel: full observed field. Bottom Left panel: η-PDF. Top Right panel: zoom in on regions with $\eta > 1$ which make up the first PLT in the η-PDF (in red on the PDF). Bottom Right panel: Zoom in on regions with $\eta > 1.7$ which make up the second PLT (in green on the PDF). Red contours display regions with $\eta > 1$ while white ones display regions with $\eta > 1.7$. The "Saxophone" region (bottom right panel) hosts most of both power-law tail contributors and the second PLT comes from clump-like structures that are nested in it.

5.3.1 Localisation of regions entailing the PLTs

We observe that most of the PLT contributors come from the "Saxophone" filamentary region (Schneider et al., 2013). and that regions which make up the second, high density, PLT are small clump-like structures entirely nested in the "Saxophone", as shown in Fig. 4.9. This is consistent with scenarios of star formation where pre-stellar cores form inside larger filamentary structures (André, 2017; André et al., 2019). This scenario also indicates that gravity is at the origin of these PLTs.

5.3.2 Is gravity the origin of the PLT in Polaris ?

Polaris shows little or no sign of star formation activity, so that it is difficult to attribute departures from lognormal statistics to the effects of gravity as in Orion B and Aquila. Thus, the Polaris PLT may be due to the other mechanisms mentioned earlier, the superposition of cold and warm phases (Brunt, 2015) or departures from an isothermal equation of state (e.o.s) (Passot & Vázquez-Semadeni, 1998; Audit & Hennebelle, 2010).

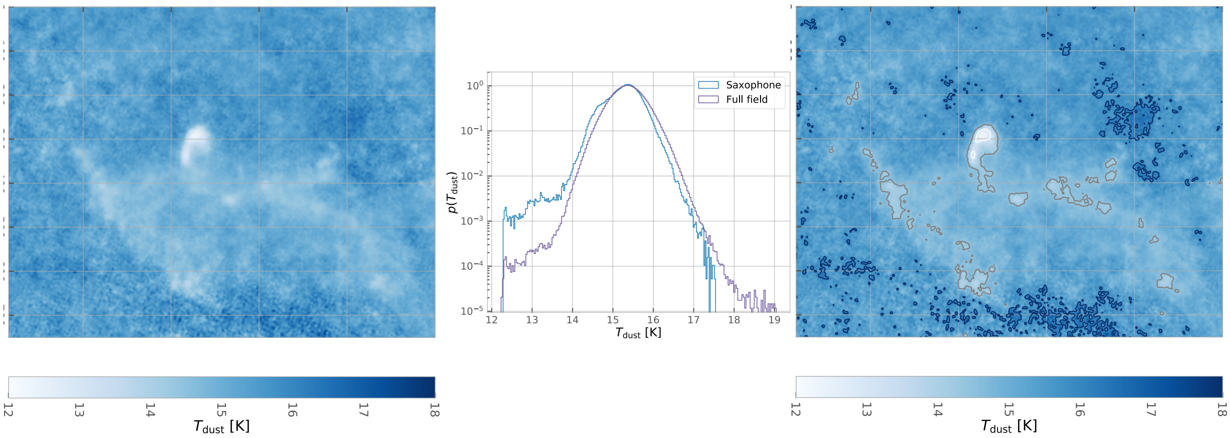

FIGURE 4.10 Dust temperature maps of the "Saxophone" structure in the Polaris cloud. Middle panel: Dust temperature PDF of the full observed field of Polaris (displayed above) in purple and of the "Saxophone" subregion in blue. Top panels: Undressed heat map and heat map with contours of the "Saxophone". White contours display regions with $12.3\,\mathrm{K} < \mathrm{T_{dust}} < 13\,\mathrm{K}$, grey ones region with $T_{\rm dust} < 14.4\,\mathrm{K}$ and blue ones regions with $16\,\mathrm{K} < \mathrm{T_{dust}} < 18\,\mathrm{K}$. The "Saxophone" is marginally colder than the average.

In Polaris, measurements of CO excitation temperatures (from ^{12}CO 1↔0) and dust temperatures fall within a narrow range $T_{\rm ex}(\mathrm{CO}) = 13 \pm 2$ K, $T_{\rm dust} = 15.3 \pm 1.3$ K, indicating fairly isothermal conditions (Shimoikura et al., 2012; Schneider et al., 2013). At such (high) densities, we expect dust and gas to be thermalized, which is consistent with the fact the two independent temperature estimates, $T_{\rm ex}(\mathrm{CO})$ and $T_{\rm dust}$, are close to one another. There is therefore little evidence for the presence of cold and warm phases. The second possibility would imply a sub-isothermal polytropic equation of state $T_{\rm dust} = T_{\rm gas} \propto \rho^{\gamma-1}$ with $\gamma < 1$ in higher density regions. Fig. 4.10 displays the dust temperature maps of a selected subregion of Polaris containing the "Saxophone" structure, as well as the temperature PDF of both the whole cloud and the subregion. The average temperature of both the whole cloud and the subregion are $\overline{T}_{\rm dust} = 15.3$ K with a standard deviation $\sigma(T) = 0.4$ K. The "Saxophone" filament therefore appears marginally colder than the average with temperatures $13\,\mathrm{K} \leq \mathrm{T_{sax}} \leq 15.3\,\mathrm{K}$. The majority of this structure is at relatively high temperatures ($> 14.4\,\mathrm{K}$) and contains only one low temperature clump at $12.3 - 13$ K. The "Saxophone" filament is a large coherent structure both in terms of its high density and low temperature, so that we cannot completely rule out the sub-isothermal model. However, in the molecular phase and at such high densities ($n > 10^2$ /cc) and low temperatures ($T \sim 10$ K), cooling from dust or molecular transitions are expected to be compensated by various sources of heating (Klessen & Glover, 2016) and the e.o.s. is better described by isothermal conditions with perhaps over-isothermal polytropic exponents ($\gamma > 1$) at high density values (see e.g. Hennebelle et al. 2020). In these isothermal or over-isothermal conditions, gravity appears as the favored origin of high density PLTs.

From these arguments, we infer that the quiescent Polaris cloud is quite young and has not even reached half of its mean free-fall time. We expect that it will eventually form detectable pre-stellar cores, in a timescale of the order of its mean-free fall time, most probably in the "Saxophone" region.

5.4 Draco

At Draco, the PDF displays an extended lognormal part with potentially two power-law tails, a first one with a steep exponent, $\alpha_\eta \simeq 4$, corresponding to a s-PDF power-law tail exponent $\alpha_s = 2$ for $s > s_1$, and a second one with the asymptotic exponent value $\alpha_\eta \simeq 2$, i.e. $\alpha_s = 3/2$ at high density, $s > s_2$ (see Fig. 4.8 left). Using the procedure of Sec. 3.5 we get $(s_1, s_2) = (3.18^{+0.1}_{-0.1}, 4.05^{+0.08}_{-0.1})$. The value of s_1 yields $\tilde{t}_{\mathrm{coll}} \gtrsim 0.1$. The threshold density value s_2 implies that $\tilde{t}_{\mathrm{coll}}$ in a $0.2 - 0.6$ range and we finally estimate that $\tilde{t}_{\mathrm{coll}} = 0.4 \pm 0.2$. This agrees with a scenario such that $s_{\mathrm{G}} = s_1$ and the PDF is approaching its asymptotic form with a single PLT exponent $\alpha_s = 3/2$. We then derive the value of the $(b\mathcal{M})$ parameter and find that $\mathcal{M} = 3.2^{+0.3}_{-0.3}$ and $\mathcal{M} = 2.1^{+0.2}_{-0.2}$, depending on the b value. This is consistent with the independent analysis of Miville-Deschênes et al. (2017), who estimated that $\sigma_v \sim 10$ km/s and $T \sim 8000$ K, resulting in a Mach-number $\mathcal{M} \sim 2$. Finally, we take $s_1 = s_{\mathrm{G}}$ and obtain an upper bound $\alpha_{\mathrm{vir}} \lesssim 4.2$ for Draco.

5.4.1 Other origin for departures from lognormal statistics in Draco

It has been suggested in the literature that the high density part of the Draco PDF corresponds to a second lognormal distribution, due to either an ionisation compression front (Tremblin et al., 2014) or the superposition of cold and warm phases (Brunt, 2015). Furthermore, at the high temperatures ($T \sim 8000$ K) of Draco, one expects that cooling plays a significant role, implying non isothermal thermodynamic conditions (Audit & Hennebelle, 2010). Thus, it is difficult at this stage to clearly discriminate against any of the different models. In other words, one cannot decide between a purely turbulent origin for the Draco density statistics and the increasing impact of gravity. Note that these two possibilities are not necessarily mutually exclusive.

TABLE 1 Properties of four molecular clouds

Name (1)	Func. form (2)	σ_s (3)	$(b\mathcal{M})$ (4)	μ (5)	α_1 (6)	α_2 (7)	s_1 (8)	s_2 (9)	α_{vir} (10)	$\tilde{t}_{\mathrm{coll}}$ (11)
Orion B	Ln+1Pl	$1.2^{+0.09}_{-0.1}$	$1.8^{+0.26}_{-0.26}$	$-0.92^{+0.13}_{-0.11}$	2	–	$1.73^{+0.25}_{-0.23}$	–	$0.88^{+0.26}_{-0.23}$	$\gtrsim 1$
Aquila	Ln+1Pl	$1.0^{+0.08}_{-0.07}$	$1.33^{+0.16}_{-0.16}$	$-0.76^{+0.09}_{-0.17}$	2	–	$1.31^{+0.15}_{-0.13}$	–	$0.88^{+0.12}_{-0.12}$	$\gtrsim 1$
Polaris	Ln+2Pl	$0.98^{+0.07}_{-0.08}$	$1.27^{+0.16}_{-0.15}$	$-0.55^{+0.08}_{-0.07}$	4	2	$1.68^{+0.38}_{-0.34}$	$6.3^{+0.1}_{-0.15}$	$\lesssim 1.2$	0.2 ± 0.1
Draco	Ln+2Pl	$0.87^{+0.07}_{-0.06}$	$1.07^{+0.12}_{-0.11}$	$-0.4^{+0.06}_{-0.05}$	4	2	$3.18^{+0.1}_{-0.1}$	$4.05^{+0.08}_{-0.1}$	$\lesssim 4.2$	0.4 ± 0.2

NOTE—Columns: (1) cloud's name; (2) functional form: Ln+1Pl, Ln+2Pl (Lognormal and 1 power law, Lognormal and 2 power laws); (3) standard deviation of the lognormal part σ_s; (4) $(b\mathcal{M})$ associated to σ_s; (5) most probable s-value μ; (6) exponent of the first power-law α_1; (7) exponent of the second power-law α_2; (8) transition between the Lognormal part and the first power-law s_1; (9) transition between the two power-laws s_2; (10) virial parameter α_{vir} associated to s_1; (11) time since the first region started to collapse in units of mean free-fall time, $\tilde{t}_{\mathrm{coll}}$.

6 Discussion

The present study clearly shows that the interplay between turbulence and gravity lies at the heart of the evolution of MCs and of the star formation process.

6.1 The scale-dependent dynamics of molecular clouds and the suggested explanations

At the largest cloud scale, the total mass and the velocity dispersion shows that MCs are close to an equipartition between gravitational and kinetic energies, indicating that MCs are gravitationally bound and are not collapsing globally and rapidly. This points to a virial parameter $\alpha_{\rm vir} = 2E_{\rm kin}/E_g \simeq 1$, where $E_{\rm kin}$ and E_g denote the cloud's kinetic and gravitational energy, respectively[8] (Larson 1981; Solomon et al. 1987; Myers & Goodman 1988; Bertoldi & McKee 1992; McKee & Tan 2003). Note that Ballesteros-Paredes (2006) have argued that equipartition between kinetic energy and gravitational energy does not necessarily imply virial equilibrium for the cloud (which strictly speaking implies that the second time derivative of the moment of inertia is zero). In contrast, at smaller scales, the densest regions are expected to collapse on timescales shorter than the average turbulence crossing time, $\sim L_c/2v_{\rm rms}$. Further support for the important impact of gravity at *small scales* ($\lesssim 0.1$ pc) comes from the positive correlation between velocity dispersion and density in *dense massive star formation clumps*, the former increasing together with the latter. This is the exact opposite of the observed Larson relations of supersonic turbulence driven from large scales (e.g. Caselli & Myers 1995; Plume et al. 1997). The Larson relation is found to break down for massive clumps, and spectral line widths at a given radius are systematically larger than predictions from this relation. The inner parts of massive star forming regions thus tend to have higher velocity at given radius than predicted by the Larson relation, pointing to an excess kinetic energy compared to Larson's scaling. These regions (including notably the so-called infrared dark clouds (IRDC)) may not be typical of most star-forming MCs, but they are representative of regions forming most of the massive stars in the Galaxy and therefore deserve attention.

Enhanced velocity dispersion at small scales in dense star-forming regions has been explained in three different ways. Some authors have invoked the impact of a (stabilising) external pressure upon clumps.

More recently, others have proposed the adiabatic heating of turbulence by gravitational collapse at small scales (Robertson & Goldreich, 2012). This yields that $\sigma_t \propto R^{0.2-0.3}$ outside the free-fall collapsing core, instead of $\sigma_t \propto R^{0.5}$, which is consistent with observations on dense massive clumps (Murray & Chang 2015; Murray et al. 2017). The basic principle is that, at scales that are small enough, the local contraction time is shorter than the eddy turnover time, implying that the energy cascade from large to small scales is inhibited and dissipation becomes inefficient, allowing random bulk motions to "heat" (amplify) adiabatically gas velocities. At larger scales, this cascade operates efficiently and turbulent energy decays as usual. The fact that gravity affects the velocity structure of turbulence, and even drives turbulence, has been found in various simulations (e.g. Sur et al. 2010; Federrath et al. 2011; Lee et al. 2015). As shown by the latter studies, turbulent velocities are enhanced near local density peaks, with more power at small scales than in the global power spectrum (see e.g. Fig. 10 of Lee et al. 2015). This stems from the conversion of infall kinetic energy and gravitational energy induced by collapse into turbulent kinetic energy through shock formation (Scalo & Pumphrey, 1982). The amounts of energy that go into turbulent motions and radial infall, respectively, seem to depend

---

[8] For sake of simplicity, we will not consider the magnetic field in the present discussion. At first order, this latter can be included by a rescaling of the non thermal velocity, $v_{\rm nt} = (v_{\rm rms}^2 + v_A^2)^{1/2}$, where $v_{\rm rms}$ and v_A denote the turbulent (rms) and Alfven velocities, respectively. Since these two velocities have a similar scale dependence (Basu, 2000), such a rescaling appears to be reasonable.

on the initial conditions of the numerical simulations, however (Lee et al., 2015). The net result is to increase the magnitude of turbulent velocities and to flatten the turbulent power spectrum at small scales (see also Collins et al. 2012), and hence the local (small scale) line width-size relation. At scales ~0.1 to a few pc, the rms and free-fall velocities are of comparable magnitudes, i.e. accelerations due to the Reynolds stress and to gravity are close to one another. At the same time, the bulk velocity is significantly smaller (see e.g. Fig. 8 of Murray & Chang 2015, Fig. 13 of Murray et al. 2017 or Fig. 9 of Lee et al. 2015), suggesting that, at these scales, the gas in overdense structures is bound but not necessarily collapsing. Note, however, that the infall velocity is significantly smaller than the free-fall velocity, a consequence of the support provided by random gas motions. At even smaller scales ($\lesssim$0.1 pc), which is about the sonic scale for usual MC conditions, i.e. near the density maxima where prestellar cores will eventually form, the local rms velocity peaks below the free-fall velocity, illustrating a loss of support against collapse at these scales. The signature of collapse is the line-velocity relation in reverse, with $\sigma \propto R^{-1/2}$. Furthermore, Robertson & Goldreich (2012) showed that compression also drives turbulence in a gas. In a converging flow, turbulent gas gets compressed, which tends to increase the turbulent velocity. More precisely, compression alters the balance between the compressive modes of turbulence that are responsible for density enhancements, and the solenoidal modes, which is usually prescribed by the value of prefactor b in front of the Mach number, $b\mathcal{M}$, in the variance-velocity relation (see Eq. (4.91)). It is worth emphasizing again that, in these simulations, turbulence is found to follow the usual Larson relation away from collapsing regions.

A third, and more extreme, explanation for enhanced velocity dispersion at small scales (e.g. Ballesteros-Paredes et al. 2018; Vázquez-Semadeni et al. 2019 and references therein) is that gravitational collapse occurs at *all scales*, including that of the whole cloud. This would imply that the observed relationship between velocity dispersion and size arises from the global free-fall of the cloud, yielding fragmentation at smaller scales, rather than from virial equilibrium and a large-scale turbulence cascade (as in Larson relations). Indeed, one cannot distinguish between free-fall and virial velocities from observations, because $\sigma \propto (M/R)^{1/2}$ in both cases. In this model, turbulence plays no important role in the dynamics of MCs and the star formation process, and only serves to generate density fluctuations that prevent the homologous collapse of the cloud. This interesting idea certainly deserves attention, but it seems difficult to reconcile it with the global turbulent properties of the ISM and MCs at large scales (or low densities) as well as for *all* clouds (see §1). Moreover, if a substantial fraction of a whole cloud is collapsing, we expect that gas compression leads to the development of small-scale shocks that convert kinetic energy into either heat or turbulence. Turbulence has two opposite effects. On the one hand, converging compressive modes, which are the only modes coupled to the gravitational field in overdense regions ($s > 0$), promote collapse. On the other hand, energy modes with a positive or zero velocity divergence ($\nabla \cdot \mathbf{u} \geq \mathbf{0}$), which include the expansional parts of compressive and solenoidal components, act against collapse. Thus, these two modes continually exchange energy. Oblique shocks, notably, turn compressible components into solenoidal ones through vorticity generation due to the misalignment of the pressure and density gradients (e.g. Elmegreen & Scalo 2004). Thus, it is very difficult to determine the net energy balance at all scales in a cloud and to avoid the impact of large-scale turbulence on cloud dynamics. The fact that regions where massive stars are forming, and hence where collapse is occurring, and those that host no stars or only low mass stars have different velocity dispersions at all scales seems to argue against a “universal" gravity dominated picture for all clouds. At any rate, in a model where cloud evolution and star formation are solely due to gravity at all scales, a probabilistic approach loses significance and so does the concept of a relationship between the gas PDF, star formation and the resulting initial mass function (IMF).

One aspect that has not been discussed yet is the impact of the galaxy on turbulence in MCs. As shown by Meidt et al. (2018), the amplitudes of gas motions due to the galaxy gravity generally exceeds those that are generated by the cloud self-gravity, providing another support for the gas besides turbulence (see their Fig. 1 and 2). Some turbulent motions may thus emerge as coherent orbital motions driven by the host galaxy. This acts to increase spectral line widths at all column densities and affects low-Σ clouds most, in agreement with observations (Heyer et al., 2009).

As mentioned above, at very small scales, $R \lesssim 0.1$ pc, numerical simulations of self-gravitating fluids predict not only a quantitative, but a qualitative change in the relationship between line width and size, such that the former increases with decreasing size. Small scales pertain to stellar cores rather than to clumps or clouds, and hence are relevant to the *ultimate* stages of star formation, not to early ones, which are aimed at in the present study. At these scales, turbulent energy has been dissipated, stellar cores are collapsing so that gravitational energy is entirely being converted into kinetic energy, which is the Larson relation in reverse. Thus, the Larson relation is no longer expected to hold for collapsing structures. As mentioned above, at such scales, a probabilistic approach of turbulence and thus the very concept of a probability density function (PDF) loses significance.

6.2 Physical picture: towards a consistent gravito-turbulent paradigm ?

6.2.1 Dynamical regimes

As derived in the previous sections, a major result of the present study is the determination of a density threshold, $s_{\rm G} \equiv s_{\rm G}(t)$, given in Eqs. (4.93) and (4.120), above which gravity has a *measurable* impact on the flow dynamics. A direct consequence of the increasing impact of gravity on turbulence is the onset, above $s > s_{\rm G}$, of a *first power law tail* in the s-PDF, $f(s,t) \propto e^{-\alpha_s s}$, i.e. $p(\eta,t) \propto e^{-\alpha_\eta \eta}$ for the η-PDF of the surface density. This occurs over a characteristic timescale $t_{\rm coll} \sim \tau_{\rm G}(s)$, with $\alpha_s \simeq 2$, i.e. $\alpha_\eta = -2/((1-3/\alpha_s) \simeq 4$. At later times (larger than a few times $\tau_{\rm ff}(s)$) and/or at higher density, i.e. smaller scales, a *second power law* develops, with $\alpha_s = 3/2$, i.e. $\alpha_\eta = 2$. This is the signature of regions in "free-fall" collapse where the dynamics induced by gravity is fully developed. We recall that $s_{\rm G}$ varies on the *"slow " global* timescale, $\bar{\tau}$, of variations of the global mean properties of the cloud (see Sec. 3.3.1 and 3.3.2).

In high density regions such that $s > s_{\rm G}$, the dominant control on cloud dynamics shifts from inertia to gravity over a *local* time scale of the order of the *local* free fall time $\tau_{\rm ff}(s)$. In other words, these regions begin to contract due to their self gravity over the *local* free fall time scale. The velocity divergence becomes negative and its scaling changes from $\langle \boldsymbol{\nabla} \cdot \boldsymbol{u} | \rho \rangle \propto -G\rho$ at small times to $\langle \boldsymbol{\nabla} \cdot \boldsymbol{u} | \rho \rangle \propto \tau_{\rm ff}(\rho)^{-1} \propto -\sqrt{G\rho}$ at later times, when gravity-controlled dynamics is fully developed. This transition is associated with the growth of high density power-law tails in the density PDF (see 3.1), which are therefore a *signature* of the late dynamical regime. In this way, the density PDF provides information on the underlying dynamics of the velocity divergence. Power law tails with exponent $\alpha_s \simeq 2$ and $\alpha_s = 3/2$ then reflect the scalings for $\langle \boldsymbol{\nabla} \cdot \boldsymbol{u} | \rho \rangle$ at high densities. Such scalings are in fact not surprising as they are expected to be found in the isothermal phase of collapsing clumps (Larson, 1969), at the smallest scales in the hierarchy of MC structures (see Sec. 3.3.1 and 3.3.2). We recall that these scalings correspond to conditional *expectations*, and *do not* imply that, at *any* point of the flow with density ρ, the divergence of the velocity field will exactly be $\boldsymbol{\nabla} \cdot \boldsymbol{u} = \langle \boldsymbol{\nabla} \cdot \boldsymbol{u} | \rho \rangle$. Fluctuations about the aforementioned conditional expectation must be expected. What these scalings entail is that, *on average*, the dynamics of high density regions is dominated by gravitational infall.

At lower density ($s \leq s_{\rm G}$), a fraction of the gravitational energy is converted into random gas motions and promotes compressive modes of turbulence that are responsible for local density enhancements. The dynamics is mostly that of inertial turbulence (*i.e.* dominated by the advection term in the Navier-Stokes equation) and gravity essentially acts to change prefactor b in front of the Mach number ($b\mathcal{M}$) in the variance-velocity relation (see Eq. (4.91)). As mentioned earlier, this prefactor describes the ratio of contributions from compressive and solenoidal modes, in agreement with Robertson & Goldreich (2012).

The general features of the density PDF are essentially the same in all star-forming clumps/clouds, but we have shown that, at any given time, the density threshold $s_{\mathrm{G}}(t)$ decreases substantially from low-density regions to high-density ones. In regions where massive stars form, notably IRDCs, this threshold can even be located close to the peak of the PDF, i.e. $s_{\mathrm{G}} \approx 0$. These results demonstrate that gravity changes the structure of turbulence in clouds as they are condensing.

6.2.2 Size of the densest correlated structures

This study shows that, as dense regions contract due to gravity and power-law tails develop in the ρ-PDF at high density over a short *local* timescale, the variance of the density field increases, resulting in a decrease of the correlation length $l_c(\rho)$. This correlation length corresponds to the average size of the densest and most correlated substructures of the flow (see Chap. **1**). A fundamental result of our analysis is the conservation of the $\overline{\rho}(t)\mathrm{Var}\left(e^s\right) l_c(\rho)^3$ quantity (Sec. 2.5.2), which encapsulates the interrelationships between the key physical processes. For example, it specifies how the correlation length varies as the other variables change values.

Physically, our results are consistent with scenarios of star formation where pre-stellar cores form within larger filamentary structures (André, 2017; André et al., 2019). In the terminology of this study, this is expressed as follows: dense and short scale correlated substructures (*i.e.* stellar cores) appear in larger correlated structures (*i.e.* filaments). In our framework, the former correspond to objets of average size $l_c(\rho)(t)$ whereas the latter correspond to objects of average *radial* size equal to the "initial" correlation length $l_c(\rho)(t_0)$ (see Sec. 4.4). Here, t_0 corresponds to the time at which some dense and significant regions start to collapse and deviate from the *global* evolution (contraction or expansion) of the cloud (see Sec. 3.3). The theory predicts not only that gravity is responsible for the growth of power-law tails in the density PDFs, but also that this occurs at shorter and shorter scales $l_c(\rho)$ corresponding to the formation of smaller and clumpier structures. This emphasizes that this theory, which is based on the hypothesis of *statistical* homogeneity, does not rely on any assumption regarding the magnitude of deviations from the average and is *able* to describe *simultaneously* a hierarchy of structures spanning a large range of size and densities.

6.2.3 The averaged correlated mass and the averaged mass to form bound stellar cores

Quantity $\overline{\rho}(t)\mathrm{Var}\left(e^s\right) l_c(\rho)^3$ has the dimensions of mass (Sec. 2.5.2) and is proportional to the averaged mass in the most correlated structures M_{corr}:

$$M_{\mathrm{corr}} \propto \overline{\rho}\mathrm{Var}\left(e^s\right) l_c(\rho)^3, \tag{4.139}$$

with a proportionality coefficient that depends on geometrical characteristics. Conservation of the averaged correlated mass stems from mass conservation and the assumption of statistical homogeneity only. M_{corr} is initially nested inside correlated filamentary structures of average size $l_c(\rho)(t_0)$ and gets distributed, as collapse proceeds, in shorter scale correlated substructures of average size $l_c(\rho)(t) < l_c(\rho)(t_0)$. Some of these structures ultimately become pre-stellar cores where stars emerge from. Thus, M_{corr} is ultimately a measure of the average mass that is available to form bound (pre-stellar) cores and it is important to relate this mass to the initial cloud properties.

Observations show that regions where star formation has not occurred yet exhibit lognormal-like PDFs (Schneider et al., 2013). For example, the Draco, Polaris and also Chamaelon III (De Oliveira et al., 2014) quiescent clouds are in various, more or less advanced states of evolution. They appear to indicate that initially, *i.e.* before the onset of star formation, variance $\mathrm{Var}\left(e^s\right)$ is that of isothermal "inertial" turbulence, such that $\mathrm{Var}\left(e^s\right)(t_0) = (b\mathcal{M})^2$. Density $\overline{\rho}(b\mathcal{M})^2$, which appears in the definition of M_{corr}, is the average post shock density from the Rankine-Hugoniot relations (with the b^2 factor possibly reflecting the obliquity of shocks). A final step is to determine the correlation length $l_c(\rho)(t_0)$.

In inertial isothermal turbulence (without gravity), the natural length scale, which is associated with the average thickness of shock layers, is the sonic length $\lambda_\mathrm{s} \simeq R/\mathcal{M}^2$, where R is the cloud size, as shown in Sec. 4.4. For typical clouds in the Milky-Way, using the Larson relation, one finds that this length scale is approximately constant and of the order $\lambda_\mathrm{s} \sim 0.05 - 0.16$ pc, for $c_\mathrm{s} = 0.2$ km/s (Federrath, 2016b).

In gravo-turbulent conditions (i.e. turbulence with gravity), another natural length scale arises, which is the Jeans length $\lambda_\mathrm{J} \propto c_\mathrm{s}/\rho^{1/2}$. We are interested in the averaged post shock densities (as mentioned earlier), and hence introduce the post shock Jeans length $\lambda_\mathrm{J,ps}$:

$$\lambda_\mathrm{J,ps} = \sqrt{\frac{\pi c_\mathrm{s}^2}{G\overline{\rho}(b\mathcal{M})^2}} = \sqrt{\frac{\pi c_\mathrm{s}^2}{G\overline{\rho}}}\frac{1}{b\mathcal{M}}. \tag{4.140}$$

Post shock velocities are subsonic due to mass conservation (as shown by the Rankine-Hugoniot relations), the post shock Jeans length is a measure of the stability of shock layers against gravitational collapse. An important feature of this characteristic length is that it varies little in many clouds where the Larson conditions hold. In these cases, the Mach number $\mathcal{M}$ and density $\overline{\rho}$ are related to the cloud size R through the following relations: $\mathcal{M}(R) \propto R^{\sim 1/2}$ and $\overline{\rho}(R) \propto R^{\sim -1}$. This implies that $\overline{\rho}\mathcal{M}^2$ is nearly constant. For typical Milky-Way conditions, the post shock Jeans length is:

$$\boxed{\lambda_\mathrm{J,ps} = 0.3\,\mathrm{pc} \times \left(\frac{c_\mathrm{s}}{0.2\,\mathrm{km/s}}\right)\left(\frac{2.0}{\mu_\mathrm{mol}}\,\frac{10^3\,\mathrm{cc}^{-1}}{\overline{n}}\right)^{1/2}\left(\frac{0.5 \times 5}{b \times \mathcal{M}}\right),} \tag{4.141}$$

implying that $\lambda_\mathrm{J,ps} \sim \lambda_\mathrm{s}$.

One may envision two situations depending on the respective values of the two Jeans lengths, $\lambda_\mathrm{J,ps}$ and λ_s. If $\lambda_\mathrm{J,ps} < \lambda_\mathrm{s}$, shock layers would on average be unstable against gravitational collapse and break up in small structures of average half (radial) size $\lambda_\mathrm{J,ps}/2$ (Chandrasekhar, 1951a). Conversely, if $\lambda_\mathrm{J,ps} > \lambda_\mathrm{s}$, shock layers would on average be stable against gravitational collapse and the average half (radial) size of dense correlated structures would be λ_s.

In Milky-Way like conditions, the two characteristic lengths are of the same order of magnitude so that it is impossible to discriminate between these two possibilities. However, we may infer that:

$$l_c(\rho)(t_0) = \min(\lambda_\mathrm{J,ps}/2,\, \lambda_s) \simeq 0.1 - 0.2\,\mathrm{pc}. \tag{4.142}$$

Taking the observed averaged *radial* size of correlated filamentary structures as a reasonable estimate of the "initial" correlation length $l_c(\rho)(t_0)$, we find a characteristic size of the order ~ 0.1 pc, which is surprisingly independent of the environments of these structures and which is of the order of $\lambda_\mathrm{J,ps}$ and λ_s (Arzoumanian et al. 2011, see also Hennebelle & Falgarone 2012; Hennebelle & Inutsuka 2019 for a more complete discussion). This yields a correlated mass

$$\boxed{M_\mathrm{corr} = a_\mathrm{g}\overline{\rho}\mathrm{Var}\left(e^s\right)\, l_c(\rho)^3 = 1.56 M_\odot\, \left(\frac{a_\mathrm{g}}{2^3}\right)\left(\frac{\mu_\mathrm{mol}}{2.0}\right)\left(\frac{\overline{n}}{10^3\ \mathrm{cc}^{-1}}\right)\left(\frac{b\,\mathcal{M}}{0.4 \times 5}\right)^2\left(\frac{l_c(\rho)(t_0)}{0.1\ \mathrm{pc}}\right)^3,} \tag{4.143}$$

where μ_mol is the mean molecular weight and a_g is a geometrical factor. a_g is taken to be equal to 2^3 from the definition of $l_c(\rho)$, in order to account for the half size of correlated structures.

At this stage, it must be emphasized that the M_corr mass is calculated for initial turbulence conditions, implying that it is *not* necessarily the average mass of filaments in star forming clouds. It may be interpreted as the correlated mass nested inside the *initial* filamentary structures generated by turbulence but may not be relevant to caracterize evolved filamentary structures in star forming clouds. In those clouds, filaments, and most importantly unstable ones, have probably had time to accrete material from their surroundings and hence are probably *not* identical to those of the initial *turbulence*. The M_{corr} mass is truly the average mass present in correlated substructures of size $l_c(\rho)(t)$, some of which are already bound stellar cores.

An important feature of M_{corr} is that we do not expect that it varies by large amounts in clouds which meet typical Larson conditions. In these clouds, if $l_c(\rho)(t_0)$ is the average radial size of filamentary structures, potentially the sonic or post shock Jeans lengths, it is constant (see also Hennebelle & André 2013; Hennebelle & Inutsuka 2019 for an explanation in terms of ambipolar diffusion). Variations of M_{corr} can only be due to changes of quantity $\overline{n}\mathcal{M}^2$, but it is also approximately constant. This remarkable behaviour has been used to explain, with a different approach, the apparent universality of the peak of the Core Mass Function for a wide range of stellar cluster conditions (Hennebelle & Chabrier, 2008).

As Eq. (4.143) is calculated for typical Larson conditions, this theory predicts that the average mass available to form bound (pre-stellar) cores is of the order of $\sim 1 M_{\odot}$. This available mass, which is located in structures of size $l_c(\rho)$, will not necessarily be entirely distributed into pre-stellar cores. Thus, it must be considered as an upper bound for the average mass of pre-stellar cores of the order of $\sim 1 M_{\odot}$, in agreement with observations (André et al., 2019).

6.2.4 Concluding remarks

The general interpretation of the PDF and ACF properties that is proposed here is consistent with the local collapse of star-forming clumps on ∼pc scales, but not necessarily with the global collapse of the whole cloud. It is consistent with the general concept of “turbulent fragmentation" (Padoan & Nordlund 2002; Mac Low & Klessen 2004; Hennebelle & Chabrier 2008; Hopkins 2012b) in which compressive turbulence provides seeds for local collapse through shocks. In this case, prestellar clump formation does not necessarily require regions encompassing a large number of thermal Jeans masses but results from down-scale cascades in large scale supersonic turbulence. The global collapse of structures generated by turbulence is avoided because the gravitational and turbulent energies are quickly transferred to motions of individual substructures on smaller and smaller scales, so that only the densest substructures eventually collapse instead of the whole cloud. The collapse to high densities occurs on short timescales, but the cloud itself may survive for much longer.

It is important, at this stage, to clarify some confusion that exists in the literature. Turbulence does not provide a *static* steady support against collapse but acts instead as a dynamical statistical process *at the very early stages of star formation* which interacts with gravity at all scales, as formalized in the present study. At all scales, turbulence constantly generates regions with density higher than the average but also sweeps them away on a dynamical time, which limits the amount of accreted mass. Only regions that are dense enough for self-gravity to dominate within this timescale will collapse, giving birth to prestellar cores that get decoupled from the (non collapsing) large scale structure (see e.g. Chabrier & Hennebelle 2011). Thus, one should not consider that turbulence prevents global collapse because of some "turbulent pressure", as discussed by some authors. The conditions that are required for such a representation are very restrictive (Bonazzola et al., 1992) and requiring a scale separation for turbulent fluctuations (e.g. Elmegreen & Scalo 2004). The nature of the turbulent energy spectrum implies that most of the energy lies at the largest scales, so that, because the spectrum is continuous, there can be no real scale separation. Bonazzola et al. (1992) has shown that turbulence effects can be represented as a pressure only if the dominant scale is much smaller than the size of the potentially collapsing region. This is not the case for most star-forming MCs where the energy injection scale is much larger than that of collapsing structures. Supersonic turbulence is also likely to be dominated by highly intermittent shocks whose impact is definitely not akin to that of a pressure.

A basic feature of the present theory is that the density scale at which gravity starts to affect turbulence decreases as the average density increases. Predictions of the gas density statistics and how they change from quiescent regions to star-forming ones are consistent with observations in many molecular clouds. Different statistical properties can be analyzed within the same *general gravo-turbulent framework*.

7 Conclusion

In this chapter, we have developed in detail an analytical theory for the statistics of density fluctuations in star-forming molecular clouds under the combined effects of supersonic turbulence and self-gravity. The theory relies on general properties of solutions to the coupled Navier-Stokes equations for fluid motions and the Poisson equation for gravity. It extends previous approaches (Chandrasekhar, 1951b; Pope, 1981, 1985; Pan et al., 2018, 2019a,b) by accounting for gravity and by treating the PDF as a dynamical variable, not a stationary one. We derive rigorously transport equations for the PDF and ACF with a magnetic field present, determine how they evolve with time and solve for the density threshold above which gravity strongly affects and eventually dominates the flow dynamics. The theoretical results and diagnostics reproduce very well numerical simulations of gravo-turbulent collapsing clouds (Sec. 4) as well as observations on several molecular clouds (Sec. 5). In qualitative terms, the most basic features of the theory are that the same *general gravo-turbulent framework* allows the analysis of several different statistical properties and that the density scale at which gravity starts to affect turbulence decreases as the average density increases.

A first result of this chapter is a relation between the statistics of the velocity divergence and the behavior of the non stationary density PDF at high densities (see Sec. 3.1). This allows one to attribute the development of PLTs in the PDF and the values of their exponents to typical regimes of gravity-influenced flow dynamics. Early stages of gravitational infall induce departures from a lognormal PDF towards a transient power law tail attractor of exponent $\alpha_s = 2$. Subsequently, when the effects of gravity on the flow dynamics are fully developed, further departures take the form of a second power law tail with exponent $\alpha_s = 3/2$.

A major result of the theory is the identification of two density domains in the PDF (see Sec. 3.2). At low density, gravity does not affect *significantly* the flow dynamics, implying that the PDF is that of pure "inertial" turbulence, which is close to a lognormal distribution form for isothermal, dominantly solenoidal turbulence. In these conditions, the impact of gravity is essentially to redistribute the energy (or momentum) between solenoidal and compressive turbulence modes with only a small impact on the velocity dispersion. The end result is in an enhanced b value ($\geq 1/3$) in the $\mathcal{M} - \sigma_s$ Mach-variance relation (Eq. (4.91)). The other density domain lies above a density threshold, $s_{\rm G}$, given by Eqs. (4.93), (4.98) and (4.120). At such high density values, gravity starts to *significantly* impact the flow dynamics, essentially by increasing the velocity dispersion. Above this threshold density value, $s > s_{\rm G}$, power-law tails develop over time in the s-PDF, $f(s,t) \propto e^{-\alpha_s s}$, and in the the η-PDF of the surface (column) density, $p(\eta,t) \propto e^{-\alpha_\eta \eta}$. Both are a direct consequence of the increasing impact of gravity upon turbulence (see Sec. 3.3). Within a typical timescale $\sim \tau_{\rm G}(s) = \tau_{{\rm G},0}\, e^{-s/2}$, this leads to a *first power law tail* with $\alpha_s \geq 2$, such that $\alpha_\eta = -2/((1-3/\alpha_s) \geq 4$. Later on, after a few times $\tau_{\rm ff}(s)$ for a given density s and/or at higher density, *i.e.* at smaller scales for a given time, a *second power law tail* develops, with $\alpha_s = 3/2$ and $\alpha_\eta = 2$. This is the signature of regions in what we called the "free-fall" collapse regime, where the dynamics induced by gravity are fully developed. These general features of the PDF are the same for all star-forming regions, but we have shown that, at any given time in the cloud evolution, the density threshold $s_{\rm G}$ decreases substantially from low-density clouds/clumps to high-density ones. This emphasizes that one must avoid a lumped approach and pay attention to two key features. One is that properties of *individual cloud regions* are likely to be different from those of the whole cloud. In addition, these properties depend on evolutionary phase the cloud lies (*i.e.* on its age, assuming one can unambiguously define an initial time $t = 0$).

A third important result of this theory deals with the evolution of the correlation length $l_c(\rho)$ of the density field (see Sec. 2.5.2 and 3.4). As collapse progresses in high density regions, the variance of the density field increases and the correlation length $l_c(\rho)$ decreases. The correlation length is the average size of the most correlated structures (see Chap. **1**), which illustrates the fact that, as time goes on, collapse affects shorter and shorter scales in association with the formation of increasingly smaller and clumpier structures. According to this framework, dense and short scale correlated substructures (cores) of average size $l_c(\rho)(t)$ form in larger correlated structures (filaments) of average size $l_c(\rho)(t_0) \sim 0.1$ pc. Thus, this theory, which is based on *statistical* homogeneity, does not constrain fluctuations around the average to be small and is *able* to *simultaneously* describe a hierarchy of structures spanning a large range of size and densities in various environments. Moreover the size of correlated structures decreases whilst some average mass in correlated structures remains constant (see Sec. 2.5.2 and 6.2). This mass is the averaged mass from which will eventually feed bound (pre-stellar) cores and is estimated to be on the order of $\sim 1\ M_\odot$ in typical Milky-Way like conditions.

The results of Chap. **2**, in combination with the results of Sec. 3.2 and Sec. 3.3, allow one to infer, *from column-density data*, the values of various physical parameters characterizing a molecular cloud, and notably the virial parameter α_{vir}. With this theory, one is able to date the clouds in units of $\tilde{t}_{\mathrm{coll}}$, *i.e.* the time since the onset of collapse in a statistically significant proportion of dense regions in the cloud normalized to the cloud mean free-fall time. This explains why clouds that exhibit η-PDFs with steep power laws ($\alpha_\eta \geq 3$) or extended lognormal parts are quiescent, because they are "young" ($\tilde{t}_{\mathrm{coll}}$). This applies to the quiescent Polaris cloud (André et al., 2010; Miville-Deschênes et al., 2010; Schneider et al., 2013) (Sec. 5) and probably also to the cloud Chamaelon III cloud (De Oliveira et al., 2014).

The theory derived of this study allows the determination of both the volume and column density thresholds, s_G, η_G, as well as the characteristic timescales $\tau_{\mathrm{G}}(s), \tilde{t}_{\mathrm{coll}}$ (Eqns (4.93),(2.23),(4.120)). This allows *quantitative and predictive diagnoses*, from either numerical simulations or observations, on the importance of the impact of gravity on turbulence in the cloud and its evolutionary status. A precise scale and clock is now at the disposal of numerical specialists and observers exploring star formation in MCs. The theoretical framework allows a new vision on how gravitational collapse gets initiated and evolves within dense MCs. It provides a sound theoretical foundation and quantitative diagnostics to analyze both observations and numerical simulations of star-forming regions and to characterize the evolution of the density PDFs and ACFs. It is hoped that such a sound basis for the statistical properties of turbulence in the presence of gravity will help improve our understanding of star formation in dense turbulent star-forming regions.

Chapter

5 Towards the stellar initial mass function (IMF)

Contents

1 Introduction

A mass function (MF) describes the number density of objects per mass interval. These functions are the cornerstones as well as the starting points of statistical studies of cosmological and astrophysical populations. In his pioneering study, Salpeter (1955) defined the stellar mass function as follows:

$$\xi(m) = \frac{\mathrm{d}n}{\mathrm{dlog}(m)}. \tag{5.1}$$

where n is the the number of stars per unit volume at time t and per mass interval m.

1.0.1 The observable luminosity function and the two regimes of the MF

One major difficulty with the stellar mass function (MF) is that it cannot be obtained directly by observations. One *can only calculate the mass of a star* by studying the trajectories and periods of revolution of planets and objects that orbit it, which requires measurements over long time spans. The data set that is currently available is not large enough to be statistically significant and one has to resort to an indirect method. What can be measured instead is the total amount of electromagnetic energy (light) emitted by an astronomical object or its surface brightness, *i.e.* luminosity. One therefore determines the luminosity function and turns it into a mass function using theories of stellar evolution. More precisely, one uses the theoretical relationship between mass and luminosity, which varies as a function of age. At the time of his study, Salpeter (1955) could only rely on so-called super-solar stars, whose mass m ($\gtrsim 1M_\odot$) and age were known with sufficient accuracy. He showed that the MF could be fit with a power law, such that $\xi(m) \propto m^{-x}$ with $x = 1.35$.

Since that time, there have been huge improvements in the number of observations and in our understanding of the thermodynamics of low mass stars and brown dwarfs (see *e.g.* Chabrier & Baraffe 2000) and the stellar MF has been extended down to small mass values. At masses below $\sim 1M_\odot$, the MF becomes shallower than the Salpeter trend and flattens out at a mass of $\approx 0.3M_\odot$. At still lower mass values, in the brown dwarf domain ($m \lesssim 0.1M_\odot$), the MF is expected to decay in order to account for the small number of detections (see (Chabrier, 2003) for a thorough review on stellar mass function). All in all, the stellar MF can be described by a Salpeter power-law at large mass values and a lognormal function in the small mass domain.

1.0.2 Present day MF and the initial mass function (IMF)

Models of star evolution are used to determine the MF from luminosity measurements. They describe how stars evolve with time and predict that they eventually deviate from the main luminosity vs. mass sequence once they reach a certain age. Thus, the present day mass function (observed at time t) differs from the initial mass function (IMF), which pertains to stars created initially, and one has to make a correction for age.

1.1 Observational features

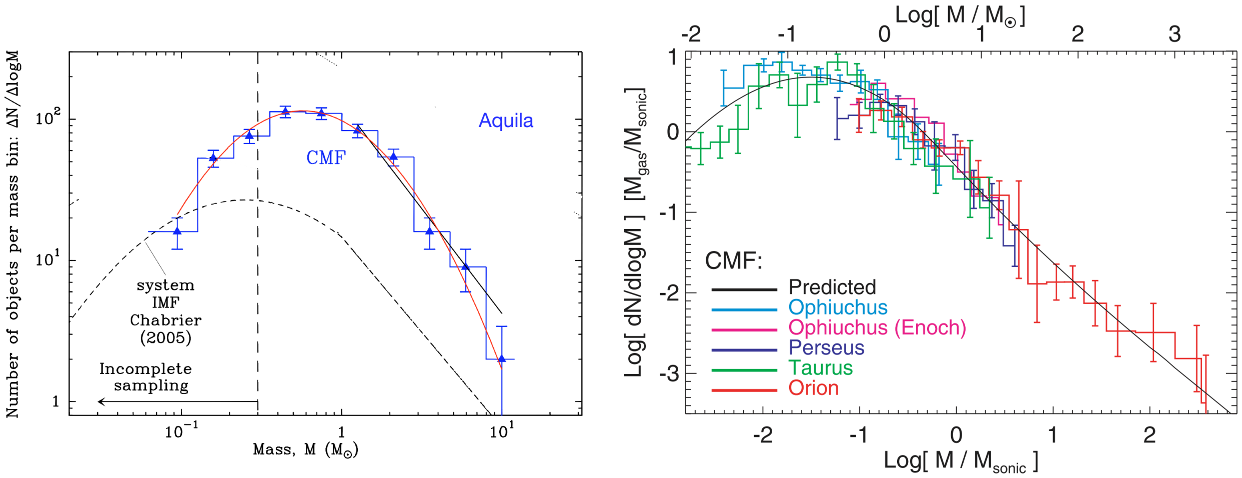

Figure 5.1 Observed Core Mass Function (CMF). Left panel: CMF of the Aquila cloud, from (André et al., 2010). Right panel: CMF of the Ophiuchus, Perseus, Taurus and Orion clouds, taken from Hopkins (2012b). These CMFs are remarkably close to one another as well as to the stellar IMF (Chabrier, 2005).

Remarkably, the Salpeter power-law IMF holds for massive stars and objects in almost all galactic and extra-galactic environments with an uncertainty range of ±0.3 for the exponent. Observations over the whole mass range are more limited, but, in the Milky Way, the IMFs of many regions conform to that same power-law at large mass values and to the same lognormal form at masses $<\sim 1 M_\odot$. In star forming clouds, *i.e* in early stages of star formation, the mass function of prestellar cores, from which young protostars emerge, called the core mass function (CMF), is remarkably similar to the stellar IMF (André et al., 2008; André et al., 2010). The only part of the CMF that is not firmly established is its tail at small mass values, because data fall bellow the completeness limit[9] (see Fig. 5.1). Taken together, these observations indicate that, at least in the large mass domain, the CMF and IMF gets set at a very early stage and is not affected by the generation of protostars.

1.2 Motivation

The initial mass function provides an essential link between the evolutions of galaxies and stars and determines the chemical, light and baryonic contents of the universe (Chabrier, 2003). It is used in almost all numerical models of star formation as a closure equation for the evolution of sub-grid regions. Two key questions remain: *what determines the IMF and does the IMF remain unchanged as the universe evolves ?* These questions have motivated us to work on an analytical theory for the generation of the IMF allowing a robust, explicit and quantitative understanding of the physical mechanisms involved.

Mass functions were first investigated in cosmology (see Monaco 1998; Zentner 2007 for reviews), and the formalism that was developed to that end was adapted to stellar scales by Hennebelle & Chabrier (2008); Hopkins (2012a,b). These models are successful in explaining the shape and the rather universal character of the IMF over a wide range of stellar cluster conditions in Milky-Way like environments. They are based on an *initial* lognormal distribution for the statistically homogeneous fluctuating density field, which is appropriate for compressible turbulence. Observations have shown, however, that, in star forming clouds, the probability density functions (PDF) deviate from a lognormal form and develop preeminent power law tails at high density values, a feature which has been identified as the signature of gravity (see the previous chapters). We thus seek to assess whether (1) one must account for this feature and if so, (2) whether or not it impacts the IMF.

The purpose of this chapter is to retrace all the steps that are required to derive the IMF. We review the key studies of Hennebelle & Chabrier (2008) and Hopkins (2012a) and shed light on the assumptions that had to be made and their consequences. We add several new derivations and theoretical arguments in order to set up a robust framework for further developments. We then consider the mechanisms leading to core and star formation. This allows us to evaluate the impact of conditions that are more relevant to describe the evolution of clouds at an advanced stage of core formation than those of Hennebelle & Chabrier (2008) and Hopkins (2012a), which are adapted to earlier stages. Finally, we discuss how to improve the counting procedure which extracts the number of collapsing objects from density statistics.

This chapter is organized as follows. The framework developed for cosmology is the cornerstone of all efforts to understand the star formation process and it is worth evaluating thoroughly how it has been extended beyond its initial domain of application. This is done in section 2. In the next section (3), we review existing models of star formation and their key assumptions (Hennebelle & Chabrier, 2008; Hopkins, 2012a,b). We then give preliminary answers to the two questions raised above and discuss perspectives for future work in Section 4. Section. 5 concludes the chapter.

---

[9] The completeness limit is the smallest average fraction of the total number of objects that can be identified by the detection algorithm

2 Cosmological mass functions

In cosmology, one is interested in the mass function of (dark matter) halos that are generated by the condensation of the primordial matter density field ρ.

2.1 Gaussian and homogeneous primordial fluctuations

Density fluctuations γ are defined as follows:

$$\rho(\boldsymbol{x},t)=\overline{\rho}(t)(1+\gamma), \tag{5.2}$$

where $\overline{\rho}(t)$ is the average density of the universe. According to the standard paradigm, primordial density fluctuations arise in a phase of cosmological inflation and the *primordial* γ field is a *statistically homogeneous* and isotropic *Gaussian* random field (see Chap. **1**). By definition, γ is centered, such that $\overline{\gamma}=0$.

2.1.1 Smoothed density field

As we will see below, a quantity of great physical interest is the density contrast smoothed over some scale R, $\gamma(\boldsymbol{x};R)$:

$$\gamma(\boldsymbol{x};R)\equiv\gamma * W_R=\int W_R(\boldsymbol{x}-\boldsymbol{x'})\gamma(\boldsymbol{x'})\mathrm{d}\boldsymbol{x'}, \tag{5.3}$$

where W_R is some appropriate window function (see below). An important feature of a Gaussian field is that, by definition, its convolution with *any window* function is also Gaussian. This implies that $\gamma(\boldsymbol{x};R)$ is also statistically homogeneous, Gaussian and centered. The variance of $\gamma(\boldsymbol{x};R)$ can be calculated easily. Using Parseval formula, one obtains that:

$$\sigma_\gamma(R)^2\equiv\mathrm{Var}\left(\gamma(\boldsymbol{x};R)\right)=\int\mathcal{P}_\gamma(\boldsymbol{k})\left|\hat{W}_R(\boldsymbol{k})\right|^2\mathrm{d}\;\boldsymbol{k}, \tag{5.4}$$

where $\mathcal{P}_\gamma(\boldsymbol{k})$ is the power spectrum of γ and $\hat{W}_R(\boldsymbol{k})$ is the Fourier transform of function W_R. This illustrates that a Gaussian field is completely determined by its first moment (its expectation) and its power spectrum (or its ACF).

2.1.2 Delta correlated Fourier modes

It is useful to introduce the Fourier modes of the density contrast γ, $\hat{\gamma}(\boldsymbol{k})$:

$$\hat{\gamma}(\boldsymbol{k})=\frac{1}{(2\pi)^{3/2}}\int\gamma(\boldsymbol{x})\exp(-i\boldsymbol{k}\cdot\boldsymbol{x})\mathrm{d}\boldsymbol{x}, \tag{5.5}$$

where we either assume some some very large cut off scale L to ensure convergence or use the above expression as a formal one. An interesting feature of the Fourier modes $\hat{\gamma}(\boldsymbol{k})$ is that they are delta-correlated:

$$\begin{aligned}
\mathbb{E}\left(\hat{\gamma}(\boldsymbol{k}_1)\,\hat{\gamma}(\boldsymbol{k}_2)\right) &= \frac{1}{(2\pi)^3}\iint\mathrm{d}\boldsymbol{x}_1\,\mathrm{d}\boldsymbol{x}_2\,\mathbb{E}\left(\gamma(\boldsymbol{x}_1)\gamma(\boldsymbol{x}_2)\right)\exp\left(-i\{\boldsymbol{k}_1\cdot\boldsymbol{x}_1+\boldsymbol{k}_2\;\cdot\boldsymbol{x}_2\}\right) && (5.6)\\
&= \frac{1}{(2\pi)^3}\iint\mathrm{d}\boldsymbol{x}_1\,\mathrm{d}\boldsymbol{x}_2\,C_\gamma(\boldsymbol{x}_1-\boldsymbol{x}_1)\exp\left(-i\{\boldsymbol{k}_1\cdot\boldsymbol{x}_1+\boldsymbol{k}_2\;\cdot\boldsymbol{x}_2\}\right) && (5.7)\\
&= \frac{1}{(2\pi)^3}\iint\frac{\mathrm{d}\boldsymbol{u}\,\mathrm{d}\boldsymbol{v}}{8}C_\gamma(\boldsymbol{u})e^{-i\left(\frac{\boldsymbol{k}_1+\boldsymbol{k}_2}{2}\right)\cdot\boldsymbol{u}}\,e^{-i\left(\frac{\boldsymbol{k}_2-\boldsymbol{k}_1}{2}\right)\cdot\boldsymbol{v}} && (5.8)\\
&= (2\pi)^{3/2}\,\mathcal{P}_\gamma\left(\frac{\boldsymbol{k}_1+\boldsymbol{k}_2}{2}\right)\,\delta(\boldsymbol{k}_2-\boldsymbol{k}_1), && (5.9)
\end{aligned}$$

where C_γ is the ACF of the γ field (see Chap. **1**). Thus, Fourier modes of different wave numbers $\boldsymbol{k}$ are *uncorrelated*, a property that is entirely due to the assumption of homogeneity. In terms of its Fourier modes, the smoothed density field $\gamma(\boldsymbol{x}; R)$ is such that:

$$\hat{\gamma}(\boldsymbol{k}; R) = \hat{\gamma}(\boldsymbol{k}) \hat{W}_R(\boldsymbol{k}) \tag{5.10}$$

2.1.3 Particular choices of window functions

There are two obvious types of window functions. One is the indicator function of a sphere in real space (or top hat window), $W_R^{(S)}$, such that:

$$W_R^{(S)}(\boldsymbol{x}) = \frac{3}{4\pi R^3} \Theta \left(1 - |\boldsymbol{x}|/R\right), \tag{5.11}$$

where Θ is the Heaviside step function. The other common window function is the Gaussian one, $W_R^{(G)}$:

$$W_R^{(G)}(\boldsymbol{x}) = \frac{1}{(2\pi)^{3/2} R^3} \exp\left(-\frac{\boldsymbol{x}^2}{2\,R^2}\right). \tag{5.12}$$

Both window functions operate over finite volumes equal to $4/3\pi R^3$ and $(2\pi)^{3/2} R^3$, respectively. In the following, we use the normalized, dimensionless, functions given above. The Fourier transforms of these functions are:

$$\hat{W}_R^{(S)}(\boldsymbol{k}) = \frac{3}{(2\pi)^{3/2}} \frac{\sin(|\boldsymbol{k}|\,R) - |\boldsymbol{k}|\,R \cos(|\boldsymbol{k}|\,R)}{(|\boldsymbol{k}|\,R)^3}, \tag{5.13}$$

$$\hat{W}_R^{(G)}(\boldsymbol{k}) = \exp\left(-\frac{(|\boldsymbol{k}|\,R)^2}{2}\right). \tag{5.14}$$

Another useful window function is the sharp k-space filter, defined in Fourier space and which filters out all wavenumbers greater than $1/R$:

$$\hat{W}_R^{sks}(\boldsymbol{k}) = \theta(1 - |\boldsymbol{k}|R), \tag{5.15}$$

which, in real space, corresponds to the following function:

$$W_R^{sks}(\boldsymbol{x}) = \sqrt{\frac{2}{\pi}} \frac{1}{R^3} \frac{\sin(|\boldsymbol{x}|/R) - |\boldsymbol{x}|\,R^{-1} \cos(|\boldsymbol{x}|/R)}{(|\boldsymbol{x}|\,R^{-1})^3}. \tag{5.16}$$

One drawback of this window function is that it does not operate over a well-defined volume, but its properties in Fourier space make it very useful, as we shall see. For example, the variance of the filtered field, $\mathrm{Var}\left(\gamma(\boldsymbol{x}; R)\right)$, can be calculated easily for a standard power-law power spectrum $\mathcal{P}_\gamma \propto k^{-n}$ (see Eq. (5.4)).

2.2 Press-Schechter formalism and mass functions

Press & Schechter (1974) (PS) were the first to propose an analytical model for the mass function of galaxy clusters. They went after the mass functions of structures that have collapsed and are at virial equilibrium (see Introduction) at some specific cosmological time t (often described as redshift z). In essence, their approach amounts to (1) determining the volume fraction *initially* occupied by unstable regions prone to collapse and virialization at scale R and (2) attributing a mass to each of these regions.

2.2.1 Initial volume fraction of region exceeding some density contrast at scale R

In step (1) of the PS approach, one focusses on the *initial* density contrast smoothed over scale R, $\gamma(\boldsymbol{x};R)$, and determines the volume fraction of regions where it exceeds some threshold value γ_c. This threshold value is deduced from the evolution of overdensities using a linear perturbation theory for example. γ_c depends on the cosmological time t (or redshift z) that is chosen and possibly also on the smoothing scale R. In the original PS calculations, γ_c is a function of time t (or redshift z) only, but later efforts have shown that it does also depend on R. $\gamma(\boldsymbol{x};R)$ is *Gaussian* and *homogeneous*, and hence the probability that $\gamma(\boldsymbol{x};R) \geq \gamma_c(t)$ is independent of position $\boldsymbol{x}$, such that:

$$\mathbb{P}(\gamma(\boldsymbol{x};R) \geq \gamma_c(t)) = \int_{\gamma_c}^{\infty} \frac{1}{\sqrt{2\pi\sigma(R)^2}} e^{-\frac{\gamma^2}{2\,\sigma(R)^2}}\,\mathrm{d}\gamma. \tag{5.17}$$

Assuming *ergodicity*, the volume fraction occupied by unstable regions at scale R, $F(R;t)$, is equal to $\mathbb{P}(\gamma(\boldsymbol{x};R) \geq \gamma_c)$:

$$F(R;t) = \mathbb{P}(\gamma(\boldsymbol{x};R) \geq \gamma_c(t)) = \frac{1}{2}\mathrm{erfc}\left(\frac{\gamma_c(t)}{\sqrt{2}\sigma(R)}\right), \tag{5.18}$$

where erfc is the complementary error function. Two important features of Eq. (5.18) deserve attention. First, for infinitely large values of the smoothing scale R, variance $\sigma(R)^2$ becomes vanishingly small and so does $F(R;t)$. This illustrates that, at an infinitely large scale, the universe is considered to be homogeneous and its dynamics are described by the standard Friedman and Lemaitre equations. Second, after an infinitely long time t, all regions with a positive density contrast γ are expected to have undergone collapse. Thus, at an infinitely large time t, $F(R;\infty)$, the volume fraction, is $F(R;\infty) = 1/2$ because $\gamma_c = 0$. We shall come back to this point later.

There is a one to one correspondence between the filter radius R and variance $\sigma(R)^2$, such that the latter decreases towards 0 as the former increases. This is why cosmologists usually describe their analyses in terms of $S = \sigma(R)^2$, which they refer to as "resolution", instead of R. At an infinite filter radius R, everything is blurred and S is 0, which explains why S has been called resolution. The PS procedure is thus carried out for increasing resolutions S, corresponding to decreasing radii R.

2.2.2 Mass attributed to unstable regions and the PS mass function

In order to determine the mass function, one must attribute a mass to unstable regions at scale R. One must first realize that if the smoothed density field exceeds the threshold value $\gamma_c(R_1)$ for some filter radius R_1, (*i.e.*$\gamma(\boldsymbol{x};R_1) > \gamma_c(R_1)$), it will also exceed the threshold at a larger scale $R_2 \geq R_1$, $\gamma(\boldsymbol{x};R_2) = \gamma_c(R_2)$. Thus, the probability $F(R;t)$ that the smoothed density of a region is above the threshold value at time t (or redshift z) (see Eq. (5.18)) corresponds in fact to the initial volume fraction occupied by objects of initial scale larger than R that have collapsed and are virialized. The relationship between mass $M(R)$ and the smoothing scale R is thus set by the operating volume of the window function W_R and the density threshold attached to that scale. For example, for the top hat window function, $M(R) = 4\pi\rho_{c,R}R^3/3$, where $\rho_{c,R} = \overline{\rho}(1+\gamma_c(R))$ is the threshold density contained inside the filter. We note that the value $\rho_{c,R} = \overline{\rho}$ is frequently chosen in cosmology, but this yields little change of mass as long as $\gamma_c \lesssim 1$.

The mass function $n(M)$ is given by the so called "golden rule" (following Cavaliere et al. 1991; Monaco 1998):

$$Mn(M)\mathrm{d}M = \rho_{c,R}\left|\frac{\mathrm{d}F}{\mathrm{d}R}\right|\mathrm{d}R(M), \tag{5.19}$$

where R and M are related by the above relationship between mass and the smoothing scale. Due to this $M \leftrightarrow R$ correspondence, the above equation is usually written as:

$$Mn(M) = \rho_{c,R}(M) \left| \frac{\mathrm{d}F}{\mathrm{d}M} \right| . \tag{5.20}$$

Physically, the left hand side of Eq. (5.19) represents the average total mass per unit volume in structures whose masses are in the $[M, M + \mathrm{d}M[$ interval, and the right hand side represents the volume fraction of unstable structures at scales in the $[R, R + \mathrm{d}R[$ interval multiplied by density.

2.2.3 The cloud-in-cloud problem

In their original calculations, PS noted that Eq. (5.18) yields a volume fraction of 1/2 in virialized objects at an infinitely large time. They attributed this to a failure to account for underdense regions. Underdense regions can be included in larger overdense ones, or, more generally, there is a finite probability that non-collapsed regions are included in larger collapsed ones. This is commonly called the cloud-in-cloud problem. PS argued that underdense regions would eventually collapse into overdense regions and multiplied F in Eq. (5.18) by a factor of 2 to account for all the mass. Although there can be little doubt that more mass must be present in bound objects than allowed for by the PS procedure, that this should lead to a correction factor of exactly two is far from obvious.

2.2.4 Summary of the PS formalism

To obtain the mass function of collapsed structures (which are galaxy clusters), PS essentially assumed that objects collapse once the smoothed density contrast at their initial scale exceeds some threshold value. They further assumed that the nonlinearities that are associated with virialization do not affect the collapse of overdense regions at larger scales. Strictly speaking, this is not correct. These assumptions, however, allowed PS to winnow all the ingredients required for the generation of nonlinear structures down to two critical ones. The first ingredient is the statistical properties of the primordial density fluctuations, which are assumed to be *Gaussian* and *ergodic* (implying statistical homogeneity). The second ingredient is a description of how overdensities evolve, *e.g.* according to linear perturbation theory, which determines the density threshold for collapse into a virialized object.

The PS formalism proved successful when compared to N-body simulations, and has been a powerful starting point for all subsequent works on the subject. It suffers from a number of problems, however. The first one is the cloud-in-cloud issue, which has been introduced above and which is of a statistical nature. A second one is of a dynamical nature. The heuristic derivation of the MF bypasses all the complications associated with the highly non-linear dynamics of gravitational collapse. The procedure completely ignores important features of the collapse process, such as the role of tidal forces and the transient filamentary shape of collapsed structures. A third problem is of a geometrical nature and deals with the need to relate the mass of a structure to the smoothing radius R. The relation that is given is reasonable but cannot be considered as better than an order-of-magnitude estimate. In practice, the true geometry of collapsed regions in Lagrangian space (i.e. as mapped in the initial configuration) can be quite complex, especially at intermediate and small masses. For those objects, a different and more sophisticated mass assignment procedure ought to be developed.

2.3 The excursion-set formalism and mass functions

Many authors have extended the PS approach in many different ways in order to understand why it is successful in spite of its rather heuristic character (see Monaco 1998 and reference therein). Bond et al. (1991) introduced the term "excursion set approach" in order to indicate that the MF determination is based on the statistics of regions where density contrast γ is larger than some threshold γ_c. The PS procedure is obviously an attempt to determine these statistics.

2.3.1 Back to the cloud-in-cloud problem

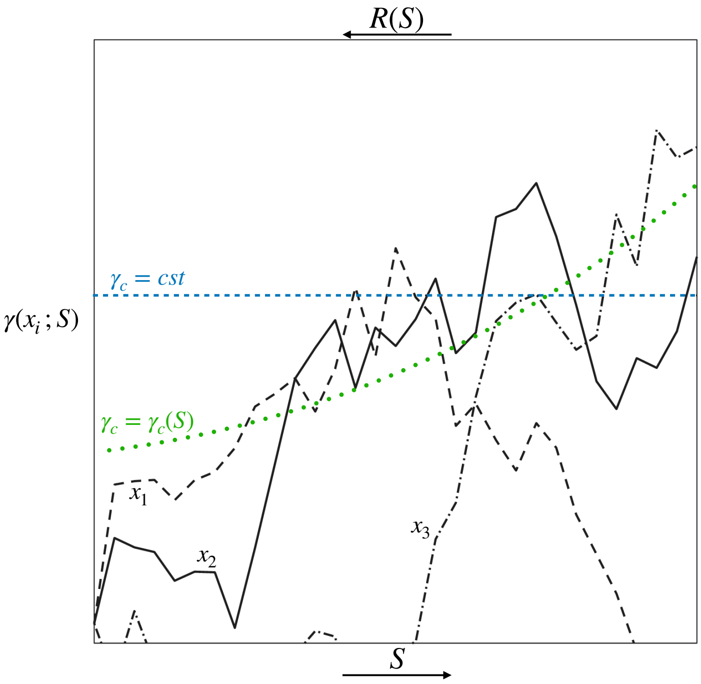

FIGURE 5.2 Trajectories of 3 random walks $\gamma(\boldsymbol{x}_i; S)$ in the $S - \gamma$ plane attached to three different positions $\boldsymbol{x}_i$. The filter function is the sharp k-space filter W^{sks}. A constant threshold (barrier) $\gamma_c = cst$ is shown in blue and a moving one $\gamma_c = \gamma_c(S)$ is shown in green. The axes are arbitrary as are just meant to be illustrative. Trajectories taken from Zentner (2007) can cross barriers several times.

The cloud-in-cloud problem originates from an inconsistency in the original PS procedure. For any filtering length R, a collapse prediction is assigned to any point $\boldsymbol{x}$ by comparing $\gamma(\boldsymbol{x}; R)$ yo $\gamma_c(t)$. In other words, a whole trajectory in the $R - \gamma$ plane is attached to point $\boldsymbol{x}$ by the $\gamma = \gamma(\boldsymbol{x}; R)$ parameterization. Alternatively, one can choose resolution $S = \sigma(R)^2$ instead of radius R and describe trajectories in the $S - \gamma$ plane. In this picture, all trajectories start from $\gamma = 0$ at $S = 0$ (or $R = \infty$), wander around as S increases (i.e as R decreases) and eventually cross the threshold boundary $\gamma = \gamma_c$ (see Fig. 5.2). In the PS procedure, if the trajectory lies above the threshold at some resolution S_1 (or filtering radius $R_1(S_1)$), point $\boldsymbol{x}$ is taken to be part of a collapsed region at larger radius (lesser resolution) $R_2(S_2) \geq R_1(S_1)$. However, if the trajectory lies below the threshold at some resolution S_3 (or radius R_3), point $\boldsymbol{x}$ is not included in regions of lower resolution $S < S_3$ (or size $R > R_3$). Thus, the PS procedure *does not* account for possible *down-crossing* of the barrier γ_c. The consequence is that underdense regions that exist in larger overdense and unstable ones are excluded from the tally (underdense clouds inside an unstable cloud, hence the cloud-in-cloud term).

This formulation of the cloud-in-cloud problem in terms of trajectories in the $S - \gamma$ plane was introduced by Bond et al. (1991) a few decades after the PS study. From the above description, it is clear that the unstable structure to which point $\boldsymbol{x}$ must be attached is of size R, such that the corresponding resolution $S(R)$ corresponds to the *first* up-crossing of the barrier γ_c in the S-γ plane. In the R-γ plane and starting from $R = 0$, this corresponds to the *last* up-crossing of the barrier, *i.e.* $\boldsymbol{x}$ is attached to the largest unstable structure that includes it. However, as cosmologists speak in terms of resolution S, we will refer to this up-crossing as the *first* crossing of the barrier.

In order to solve the cloud-in-cloud problem, one must track trajectories in the S-γ plane attached to all points $\boldsymbol{x}$ in order to detect excursions into the unstable region $\gamma \geq \gamma_c$ (hence the name excursion-set).

2.3.2 Random walks

As explained above, we aim to determine the distribution of the resolution (or radius) for which the first crossings of the barrier occur in the S-γ plane. Each trajectory appears as a random walk where resolution S acts as pseudo-time (see Fig. 5.2). One then has to determine the fraction of random walks that have crossed the barrier at least once at "time" S. In this fashion, a random walk that has up-crossed the threshold boundary is considered to be collapsed at that scale, regardless of potential subsequent downcrossings. One proceeds as follows. An absorbing barrier is put in correspondence with the threshold boundary, so as to eliminate any downcrossing event (Bond et al., 1991). The mathematical nature of the problem, and the resulting MF, strongly depend on the shape of the window function. Indeed, discretizing the pseudo-time variable S (the resolution) in an infinite number of steps $S_n = n \times \Delta S$ yields a discretized random walk $\gamma_n = \gamma(S_n)$. It is useful to express this in recursive form in order to discuss the random walk properties:

$$\gamma_n = \gamma_{n-1} + \Delta\gamma_{n-1,n}. \tag{5.21}$$

The increment $\Delta\gamma_{n-1,n} = \gamma(\boldsymbol{x}, R_n) - \gamma(\boldsymbol{x}, R_{n-1})$ is, in terms of Fourier coefficients:

$$\Delta\gamma_{n-1,n} = \frac{1}{(2\pi)^{3/2}} \int \hat{\gamma}(\boldsymbol{k}) \left(\hat{W}_{R_n}(\boldsymbol{k}) - \hat{W}_{R_{n-1}}(\boldsymbol{k}) \right) e^{i\boldsymbol{k}\cdot\boldsymbol{x}} \mathrm{d}\boldsymbol{k}, \tag{5.22}$$

and is such that $\mathbb{E}\left(\Delta\gamma_{n-1,n}\right) = 0$. The cross correlation of the increment $\Delta\gamma_{n-1,n}$ and γ_{n-1} is:

$$\begin{aligned} \mathbb{E}\left(\Delta\gamma_{n-1,n}\, \gamma_{n-1}\right) &= \frac{1}{(2\pi)^3} \int \mathbb{E}\left(\hat{\gamma}(\boldsymbol{k}_1)\, \hat{\gamma}(\boldsymbol{k}_2)\right) \left(\hat{W}_{R_n}(\boldsymbol{k}_1) - \hat{W}_{R_{n-1}}(\boldsymbol{k}_1) \right) \hat{W}_{R_{n-1}}(\boldsymbol{k}_2) e^{i(\boldsymbol{k}_1+\boldsymbol{k}_2)\cdot\boldsymbol{x}} \mathrm{d}\boldsymbol{k}_1\, \mathrm{d}\boldsymbol{k}_2 \\ &= \frac{1}{(2\pi)^{3/2}} \int \mathcal{P}_\gamma(\boldsymbol{k}) \left(\hat{W}_{R_n}(\boldsymbol{k}) - \hat{W}_{R_{n-1}}(\boldsymbol{k}) \right) \hat{W}_{R_{n-1}}(\boldsymbol{k}) e^{2\, i\boldsymbol{k}\cdot\boldsymbol{x}} \mathrm{d}\boldsymbol{k}, \end{aligned} \tag{5.23}$$

where we have used the fact that Fourier modes are δ-correlated. Thus, the random walks are in general correlated in S in a manner that depends on the window fonction W_R, as for general filters $\mathbb{E}\left(\Delta\gamma_{n-1,n}\, \gamma_{n-1}\right) \neq 0$. In that case, one must know the N-point correlations of the process at all resolutions.

2.3.3 Brownian walks

As discussed above, for a general window function, determining the fraction of random walks that have crossed the barrier at least once at "time" S is not straightforward. Several methods have been put forward to achieve this (see e.g. Monaco 1998; Zentner 2007). The problem is greatly simplified if one uses the sharp k-space filter W^{sks}. As seen from Eq. 5.23, uncorrelated modes get added as the resolution increases and the random walk has uncorrelated steps. The γ field is Gaussian, implying that these random walks are gaussian and more precisely Brownian, which have been studied extensively in statistical mechanics. Putting this in the perspective of Brownian random walks with an absorbing barrier allows one to benefit from advances in statistical mechanics. According to Chandrasekhar (1943), the distribution of the positions z of brownian particles that have not met the *fixed* absorbing barrier $z_c = cst$ (and are thus in the half space $z < z_c$) at time t is:

$$\Pi(z, t; z_c) = \frac{1}{\sqrt{2\pi t}} \left(\exp\left[-\frac{z^2}{2t} \right] - \exp\left[-\frac{(2z_c - z)^2}{2t} \right] \right). \tag{5.24}$$

In the cosmological excursion set framework, this amounts to determining the distribution of walks that *have never crossed* the *constant* $\gamma_c = cst$ barrier and for which the density contrast is γ (the position) at resolution S (the time t). From this, one deduces that the fraction of walks that have been absorbed,

$F(S)$, is:

$$F(S) = 1 - \int_{-\infty}^{\gamma_c} \Pi(\gamma, S; \gamma_c)\,\mathrm{d}\,\gamma = \mathrm{erfc}\left(\frac{\gamma_c}{\sqrt{2S}}\right), \tag{5.25}$$

which is exactly the PS formula Eq.5.18 *including* the multiplicative factor of 2 that had been added in an ad-hoc manner. Thus, the excursion-set formalism naturally corrects the PS one. In addition, one should note that these results suggest that the PS formula probably holds for the sharp k-space filter only.

2.3.4 The first crossing distribution

The differential probability for a first crossing of barrier $f_\mathrm{f}(S)$ is obtained from the cumulative distribution of absorbed walks:

$$f_\mathrm{f}(S) = \frac{\mathrm{d}F}{\mathrm{d}S}, \tag{5.26}$$

and is termed *first-crossing* distribution. It accounts for the fraction of walks that have crossed the barrier *for the first time* at resolution S in the $[S, S + \mathrm{d}S[$ interval.

2.3.5 General moving barriers

In general, the inclusion of more dynamical aspects in the determination of the γ_c barrier leads to a threshold that depends on the filter scale R, or equivalently on resolution S, $\gamma_c \equiv \gamma_c(S)$. In such conditions, and for general barriers $\gamma_c(S)$, there is no easy solution for the first crossing distribution. Restricting ourselves to the sharp k-space filter for the sake of simplicity, we obtain this distribution using two complementary methods.

One method follows directly from the previous calculations. MonteCarlo simulations of discretized random walks that start at $\gamma_0 = 0$ can be generated. At step n (corresponding to resolution S_n), position γ_n is given by:

$$\gamma_n = \sum_{i=1,n} \Delta\gamma_i, \tag{5.27}$$

where the $\Delta\gamma_i$ are uncorrelated Gaussian variables. Thus, for each walk, one can extract the resolution S_n at which the trajectory first crosses the barrier.

A second method, which is faster and more precise, has been proposed by Zhang & Hui (2006). They have shown that the first crossing distribution $f_\mathrm{f}(S)$ is the solution of a Volterra integral equation of the second kind:

$$f_\mathrm{f}(S) = g_1(S) + \int_0^S f_\mathrm{f}(S')g_2(S, S')\mathrm{d}S', \tag{5.28}$$

where

$$g_1(S) = \left(\frac{\gamma_c(S)}{S} - 2\frac{\mathrm{d}\gamma_c(S)}{\mathrm{d}S}\right)\frac{1}{\sqrt{2\pi S}}\exp\left(-\frac{\gamma_c(S)^2}{2S}\right), \tag{5.29}$$

$$g_2(S, S') = \left(2\frac{\mathrm{d}\gamma_c(S)}{\mathrm{d}S} - \frac{\gamma_c(S) - \gamma_c(S')}{S - S'}\right)\frac{1}{\sqrt{2\pi(S - S')}}\exp\left(-\frac{(\gamma_c(S) - \gamma_c(S'))^2}{2(S - S')}\right). \tag{5.30}$$

5

We detail the derivation of this equation App. A and emphasize here that it has been derived for the sharp k-space filter only. For example, the fact that the steps are uncorrelated has been used to obtain the gaussian with variance $S - S'$ in g_2. This equation has, in general, a unique solution. For a barrier that is linear in S, *i.e.* such that $\gamma_c(S) = a + bS$, the solution is:

$$f_\mathrm{f}(S) = \frac{a}{S\sqrt{2\pi S}}\exp\left(-\frac{\gamma_c(S)^2}{2S}\right), \tag{5.31}$$

which gives exactly Eq. 5.25 for $b = 0$.

2.3.6 The golden rule and the mass function

As in the PS procedure, the excursion set one leads to the volume fraction *initially* occupied by unstable regions that are prone to collapse and form virialized objects at scale R and time t. This is achieved through the determination of the first crossing distribution $f_{\mathrm{f}}(S)$. The next step consists in attributing a mass to these regions. As before, the mass of regions that are unstable at scale R is the mass that is contained within the sampling volume of filter W_R. This mass is well defined for the top hat and gaussian window functions, but not for the sharp k-space filter. In the latter case, it is still reasonable to consider it to be proportional to R^3. For this reason, the mass chosen is often that which is sampled by a top hat window:

$$M(R) = \frac{4\pi}{3}\rho_{c,R}R^3 = \frac{4\pi}{3}\overline{\rho}(1+\gamma_c(R))R^3. \tag{5.32}$$

Some authors have added a proportionality constant to this relation, which they treat as a free parameter to be determined from numerical simulations.

A general problem with excursion set-based approaches, including the original PS one, is that the geometry of collapsed regions (i.e. of the excursion sets) is not taken into account properly. The volume of excursion sets as a function of resolution S (or radius R), and hence the mass of structures, is deduced from the "golden rule" described earlier, which can be rewritten in terms of the first crossing distribution:

$$Mn(M)\mathrm{d}M = \rho_{c,R}(S)\, f_{\mathrm{f}}(S)\, \mathrm{d}S(M) \tag{5.33}$$

In practice, the golden rule is a reasonable approximation, which may be expected to give estimates with the correct order of magnitude.

2.4 Summary and caveats

The key assumptions that have been used to derive MFs are (1) that the stochastic fields are ergodic (and therefore statistically homogenenous), (2) that the fields are Gaussian so that smoothed fields remain gaussian.

2.4.1 Relevance of the statistical procedures

The assumption of ergodicity is extremely important. Indeed, the aim is to describe the statistics of "physical" random walks in the $S-\gamma$ plane attached to positions $\boldsymbol{x}$ obtained by smoothing the density contrast field with increasing resolution S (decreasing filtering radius R). If the $\gamma(\boldsymbol{x})$ field was known exactly, *i.e.* if one could specify the precise value of $\gamma(\boldsymbol{x})$ at all points $\boldsymbol{x}$ in the universe, one could indeed perform the smoothing procedure at each point $\boldsymbol{x}$ and for each resolution S. One could then construct all the trajectories in the S-γ plane. This not feasible in practice , so that one can only infer the statistical characteristics of the γ field. Fortunately, the assumption of ergodicity allows (1) to recast the procedure in terms of a set of independent random walks where only the statistical characteristics of the field γ are needed, and (2) to circumvent the issue of carrying out an infinitely large number of convolutions. This is reflected in the use of PDFs in the PS and excursion-set formalisms. As explained in Chapter **3**, this procedure can accurately predict the observed MF if the Universe itself or some relevant subdomain is large enough compared to the correlation length of the density field ρ (or the contrast γ). In the cosmological context, we have shown that this could be assessed with the homogeneity scale λ_H (see Chapter **3**). At the scale of the observable universe ($L \sim 10$ Gpc/h), one has $\lambda_H/L \sim 10^{-2}$, ensuring that the statistical procedure is correct.

2.4.2 Gaussian simplifications

The assumption of Gaussian fields allows huge simplifications in the calculation of random walks in the excursion-set procedure. For a gaussian field, knowledge of the power spectrum (or ACF) is indeed sufficient to characterize all N points correlations. Furthermore, the statistics of increments in the random walk are also gaussian which makes the actual computation doable. If the stochastic fields are not gaussian, the derivation of the MF is considerably more difficult but some effort has been made to obtain convincing results (see e.g. Musso & Sheth 2014). We will come back to this point in the next section. As explained above, the derivation of a mass function is achieved in 3 steps.

2.4.3 Caveats regarding the various steps of the procedure

The first step is a dynamical study of the evolution of structures to obtain a threshold value γ_c (the barrier). The second one is the statistical counting of random walks crossing that barrier. Simple models of the primordial universe lead to an instability criterion in the form of a constant density threshold. More realistic descriptions of the environments of overdensities in the primordial universe show that collapse conditions depend on several stochastic quantities. For example, including a more realistic model of triaxial collapse, Sheth et al. (2001); Shen et al. (2006) have shown that the collapse condition depends on density contrast γ and on 3 eigenvalues λ_i of a quantity called the deformation tensor. In this case, one has to deal with trajectories and barriers in a space of higher dimensions than before. These authors showed that a huge simplification is to use suitably chosen representative values for the eigenvalues, which are their conditional expectations for a given density contrast γ. In this manner, the excursion set approach reduces to finding the first crossing distribution of one-dimensional random walks in γ, with a threshold γ_c that depends on the resolution. This is a key point. One should study the conditional expectations of the various stochastic quantities of interest for given γ values in order to obtain a representative average MF over all possible realizations.

The third step in the procedure consists in assigning a mass to a resolution through the "golden rule". In practice, this golden rule is just a reasonable approximation expected to be correct at the order of magnitude level. To derive a more rigorous relationship between resolution and mass, the geometry of the excursion sets ought to be taken into account properly. This raises an important difficulty. With the absorbing-barrier procedure, it is possible to determine the fraction of the total mass that lies in collapsed structures at a given resolution, but no information is provided on how the collapsed structures fragment into clumps. We also note that, for this procedure to be valid, there must be a one to one correspondence between mass and resolution (radius).

3 From the cosmological to the stellar mass functions

As shown above, theories of mass functions have been developed and studied extensively in cosmology. In this context, primordial fluctuations are believed to be well described by gaussian fields. At sub-galactic scales, however, the initial conditions in star-forming clouds are believed to be those of isothermal turbulence for which the density field ρ is not Gaussian but lognormal. One therefore loses the many advantages of gaussian fields that have been used extensively in cosmological studies. The logarithm of density, $s = \ln(\rho/\overline{\rho})$, is a Gaussian field, however, so that one may hope to overcome the difficulty. We will come back to this later.

Hennebelle & Chabrier (2008) and Hopkins (2012b) have relied on the cosmological framework to determine MFs at stellar scales using the PS and excursion set formalisms, respectively. In both cases, there are again three major steps in the procedure, as in the cosmology. A first step consists in determining a suitable density threshold (barrier) to describe the condition for star formation. A second step consists in the statistical counting of unstable regions at scale R, *i.e* where density values are above the threshold value. The third step is a procedure to assign a mass to unstable regions at scale R, which relies on a "golden rule" for turning the counting of regions into the counting of the mass in bound objects. As discussed above, the MF that is obtained is the mass function of the reservoirs from which stars emerge, *i.e.* the Core Mass Function (CMF). We will return to this point later.

3.1 Step 1: Density threshold in a turbulent medium

Before addressing the issue of statistical counting for a non gaussian field, we first address the problem of determining the density threshold for collapse at a given scale. In cosmology, dynamical studies of the evolution of structures is relatively easy because, as a first approximation, gravity is the only active force. Linear perturbation theory in a Lagrangian description of Zel'Dovich (1970) is sufficient to capture the essential features of the dynamics. We must bear in mind here that MFs that are derived from an excursion-set procedure are only approximate. In this situation, the time dependence of the MF is accounted for by linking the collapse of the perturbation (i.e. the time at which it is virialized) to its *initial* density contrast. In the context of star formation, where turbulence is believed to provide the seeds of collapse, the dynamics is significantly more complicated and linking the collapse time to some specific density contrast is not straightforward. At best, one can only hope to obtain the MF of all the objects that will eventually collapse regardless of the precise time at which this occurs.

To obtain a collapse condition, Hennebelle & Chabrier (2008) used the condition of virial equilibrium of an homogeneous *isolated* cloud (Chandrasekhar & Lee, 1968):

$$\frac{\mathrm{d}^2 I}{\mathrm{d}t^2} = 2E_K + 2U_i + E_G < 0 \tag{5.34}$$

where I is the moment of inertia (the trace of the inertia matrix) and U_i is the total (thermal) internal energy of the isothermal cloud:

$$U_i = \frac{3}{2} M c_\mathrm{s}^2, \tag{5.35}$$

where c_s is the thermal sound speed, E_G is the gravitational binding energy of an homogeneous cloud of half size R and mass M:

$$E_G \propto -G\frac{M^2}{R} \tag{5.36}$$

and E_K is the total kinetic energy of the homogeneous cloud, calculated with the velocity $\boldsymbol{v}$ *in the center of mass frame*:

$$E_K = \rho \int \frac{1}{2}\boldsymbol{v}^2 \mathrm{d}\boldsymbol{x} = \frac{M}{2}\left\langle \boldsymbol{v}^2 \right\rangle_\mathrm{cloud} \tag{5.37}$$

It is usually admitted that *isolated* structures such that $\mathrm{d}^2 I/\mathrm{d}t^2 < 0$ collapse into roughly spherical object. This criterion is not entirely rigorous as it does not account for a possible tri-axial collapse mechanism. Moreover, it is based on the "acceleration" of I and hence does not take into account the initial "velocity" of I which may be positive and may prevent collapse. Finally, it is clear that subregions in a star forming cloud are not really isolated. Casting aside all these complicating factors, this criterion is a workable one for very large populations. This yields the density threshold:

$$\rho_c = a\frac{c_\mathrm{s}^2 + \frac{1}{3}\left\langle \boldsymbol{v}^2 \right\rangle_\mathrm{cloud}}{GR^2} \tag{5.38}$$

where a is a constant that accounts for geometrical factors. In the original article of Hennebelle & Chabrier (2008), this quantity is equal to the term $a_J^{2/3}$ stemming from the definition of Jeans mass, and is taken to be of order unity. In order to obtain a reasonable estimate of $\left\langle \boldsymbol{v}^2 \right\rangle_\mathrm{cloud}$ and the expected average kinetic energy in structures of size R, a phenomenological model of hydrodynamic turbulence is used. This yields the scale dependance

$$\left\langle \boldsymbol{v}^2 \right\rangle_{\text{cloud}} (R) = V_0^2 \left(\frac{R}{l_0} \right)^{2\eta}, \tag{5.39}$$

where V_0 and l_0 are characteristic velocity and length that can be deduced from the Larson cloud characteristics, for example ($V_0 \sim 1$ km/s, $l_0 \sim 1$ pc), and where η is the exponent for compressible turbulence ($\eta \simeq 0.5$, see e.g. Lemaster & Stone 2009). This implies a weak correlation between velocity and density. In isothermal turbulence, $\boldsymbol{v}^2$ is indeed weakly correlated to ρ. Written in terms of conditional expectations, this is expressed as:

$$\left\langle \boldsymbol{v}^2 | \rho \right\rangle \simeq v_{\text{rms}}^2, \tag{5.40}$$

where v_{rms} is the r.m.s. velocity (see e.g. Federrath & Banerjee 2015 Fig.7). In the end, one obtains the following density threshold:

$$\rho_c = \overline{\rho} e^{s_c} = a \frac{c_{\text{s}}^2 + \frac{1}{3} V_0^2 \left(\frac{R}{l_0} \right)^{2\eta}}{G R^2}, \tag{5.41}$$

or in terms of the logarithmic density s:

$$e^{s_c} = a \frac{c_{\text{s}}^2 + \frac{1}{3} V_0^2 \left(\frac{R}{l_0} \right)^{2\eta}}{G \overline{\rho} R^2}. \tag{5.42}$$

Hopkins (2012a,b) used a different approach but ultimately obtained similar results. He took his condition for collapse from a linear stability analysis of turbulent discs (Begelman & Shlosman, 2009), which generalized the study of Toomre (1964) to a disk with finite thickness. For disk thickness h ($h \sim 100$ pc in the Milky Way) and surface density $\Sigma \equiv 2h\rho$, the dispersion relation reads:

$$\omega^2 = \kappa^2 + (v_t^2 + c_{\text{s}}^2) k^2 - \frac{2\pi G \Sigma |k|}{1 + |k| h} = \kappa^2 + (v_t^2 + c_{\text{s}}^2) k^2 - \frac{4\pi G \rho\, h\, |k|}{1 + |k| h}, \tag{5.43}$$

where ω and k are the usual wave-numbers, κ is the epicyclic frequency and v_t is an average turbulent velocity. For infinitely thin discs ($h = 0$), this reduces to the Toomre fragmentation criterion:

$$Q = \frac{\kappa \sqrt{(v_t^2 + c_{\text{s}}^2)}}{\pi G \Sigma} < 1. \tag{5.44}$$

Without much justification, Hopkins (2012a,b) then introduced a scale dependence by setting v_t equal to the turbulent velocity dispersion at scale k, $v_t = \sigma_v(k) \propto k^{-\eta}$. In a proper *linear stability analysis* taking into account the scale dependence of the background turbulent field, there should be a non trivial coupling of Fourier modes and one would not expect such a simple rescaling of the equation. That being said, in order to scale the turbulent velocity dispersion, Hopkins (2012a,b) assumed that the galactic disk is marginally stable according to the Toomre criterion Eq. 5.44 (i.e $Q(k) = 1$ at scale $k \sim h^{-1}$). The short scale behaviour $R \ll h$ (or $kh \gg 1$) of the instability criterion of Hopkins (2012a,b) then reduces to:

$$\rho_c = \frac{(\sigma_v(R)^2 + c_{\text{s}}^2)}{4\pi G R^2}. \tag{5.45}$$

This criterion is similar to the one obtained by Chandrasekhar (1951a) in his linear stability analysis, save for the scale dependence of the turbulent velocity dispersion $\sigma_v(R)$. Even though it is still not fully satisfactory for the same reasons as above, this criterion is, in essence, similar to the criterion obtained in Hennebelle & Chabrier (2008) with $a = \pi/4$. Given that different approaches and different sets of hypotheses lead to similar criteria, one can make do with them for want of a more rigourous and comprehensive theoretical derivation, . Moreover, using the Toomre criterion to scale the turbulent velocity dispersion at the galactic disk scale $h \sim 100$ pc, one is able to get around the empirical Larson relations for our galaxy and extend the calculation to other less well resolved galaxies (see e.g. Chabrier et al. 2014). The big leap behind this procedure, however, is the assumption that gas dynamics in star-forming clumps are affected only marginally by the transition from $\mathrm{H_I}$ to $\mathrm{H_2}$ or by large scale gradients, so that atomic and molecular gases follow the same turbulent cascade from galactic to cloud scales.

The two different thresholds derived above conform to the same scaling in R but can differ by a factor that may well be of order 10. We recall that the MFs that will be obtained are only expected to allow reasonable estimates of the mean number of objects generated in a mass interval. The calculations rely on the simplest ingredients for the formation of structures in molecular clouds and the resulting density criteria involve scaling factors that appear somewhat arbitrary. These criteria allow a global analysis over a very large range of scales and, unless they miss out on key processes, their validity may be assessed *a posteriori* by comparing predicted and observed MFs.

3.2 Step 2 and 3: Statistical counting and the Press-Schechter approach of Hennebelle & Chabrier (2008)

Now that a density threshold has been obtained for the occurrence of collapse at scale R, we must carry out the statistical counting of unstable reservoirs at that same scale. As mentioned earlier, difficulties arise because ρ is not Gaussian but lognormal.

3.2.1 Statistical counting

Hennebelle & Chabrier (2008) used the PS formalism to carry out the counting. In order to benefit from the same simplifications as for Gaussian fields, they assumed that the density field ρ smoothed at scale R with the sharp k-space filter W_R^{sks}, $\rho_R = \rho * W_R^{sks}$, is lognormal at all scales. Turbulence is a scale independent process in the inertial domain, *i.e.* from the viscous to the integral scale l_i (see Chapter **1** and Frisch 1995), but this is a strong assumption as there is no particular reason for a lognormal field to meet this condition with the specific window function W_R^{sks}. As discussed in Chapter **2**, obtaining robust conclusions on the PDF of a linear combination of lognormal variables is challenging and the validity of the Hennebelle & Chabrier (2008) assumption can only be assessed from the end results of the derivation.

Following Hennebelle & Chabrier (2008), the PDF of the logarithmic density field $s^{(R)} = \ln(\rho_R/\overline{\rho_R})$, is taken to be Gaussian at all scales, such that:

$$f_{s^{(R)}}(s) = \frac{1}{\sqrt{4\pi\sigma(R)^2}}\exp\left(-\frac{(s+\sigma(R)^2/2)^2}{2\sigma(R)^2}\right), \tag{5.46}$$

(their Eq. 6). One then needs to specify the variance $\sigma(R)$ to go further, a point that will be discussed later. We note here an issue that was not raised in the original paper of Hennebelle & Chabrier (2008). The (statistical) average of the density field smoothed at scale R with the sharp k-space filter W_R^{sks} is not well defined as the sampling volume of the window function is not defined (see Sec 2.1.3). One has indeed:

$$\overline{\rho_R} = \mathbb{E}\left(\rho * W_R^{sks}\right) = \overline{\rho}\int W_R^{sks}(\boldsymbol{x})\mathrm{d}\boldsymbol{x}. \tag{5.47}$$

For almost all other window functions with finite volumes, the averaged density is $\overline{\rho_R} = \overline{\rho}$ and this is the logical choice adopted by Hennebelle & Chabrier (2008). One is then able to count the total mass of gas per unit volume with a density larger than $\rho_c(R) = \overline{\rho} e^{s_c(R)}$ at scale R, $M_{tot}(R)$. This is the total mass (per unit volume) that will be found in collapsed objects at scale R:

$$M_{tot}(R) = \int_{s_c(R)}^{\infty} \overline{\rho} e^s f_{s(R)}(s) \,\mathrm{d}\, s = \overline{\rho}\, \frac{1}{2} \left(1 + \mathrm{erf} \left[\frac{\frac{1}{2}\sigma(R)^2 - s_c(R)}{\sqrt{2}\sigma(R)} \right] \right), \tag{5.48}$$

where erf is the error function.

3.2.2 The cloud-in-cloud problem and the mass assignment procedure

The above procedure is of course subject to the same cloud-in-cloud issue as in cosmology. Here, the problem is slightly different because one is interested in obtaining the MF of pre-stellar cores, *i.e.* the smallest objects that collapse without no further fragmentation, at least not before the star-formation stage. Let us consider a region which is self-gravitating on some large scale R_0. If it contains multiple subregions that are themselves self-gravitating on a smaller scale $R < R_0$, then the entire R_0 region will not behave as a single core. Since the mean density for self-gravitation at the smaller scale R is larger than that at R_0 (see Sec. 3.1), such subregions collapse more rapidly, *i.e.* the "parent cloud" fragments into smaller objects. This can be continued in iterative fashion inside R. Only when a region is self-gravitating on scale R and not on smaller scales does collapse proceed without fragmentation.

Hennebelle & Chabrier (2008) took into account this problem and realized that, if the smoothed density at scale R, $\rho_R \equiv \rho(\boldsymbol{x}; R)$, is larger than threshold $\rho_c(R)$, it almost certainly exceeds the threshold at a lower filter radius $R' < R$. This implies that smaller unstable subregions get included in the scale R region. In terms of a random walk crossing a barrier moving with time (resolution $S(R)$), this amounts to assuming that, if the trajectory is above the barrier at time t (resolution $S(R)$), it will also be above the moving barrier at a later time $t' > t$ (*i.e.* at resolution $S' > S$ corresponding to $R' < R$). This is true for continuous random walks (and thus for Brownian walks) with continuous moving barriers.

Attributing a volume $V_W(R)$ to the window function W_R, as before, one defines the associated mass as follows:

$$M_W(R) = V_W(R) \times \rho_R. \tag{5.49}$$

As in cosmology, this mass is well defined for the top hat and gaussian window functions, but not for the sharp k-space filter. In the latter case, it is still reasonable to consider that the mass is proportional to R^3 and the authors chose:

$$M_W(R) = \rho_R R^3, \tag{5.50}$$

which allows an order of magnitude estimate. We can now re-cast the cloud-in-cloud problem in terms of mass instead of density and define the following threshold mass at scale R:

$$M_c(R) = \rho_c(R) R^3 = a\, R\, \frac{c_\mathrm{s}^2 + \frac{1}{3} V_0^2 \left(\frac{R}{l_0}\right)^{2\eta}}{G}. \tag{5.51}$$

Thus, if $M_W(R) > M_c(R)$, the R scale structure probably contains a smaller substructure at scale $R' < R$ such that $M_W(R') = M_c(R')$. This implies that the parent structure of scale R will most probably fragment into smaller masses $M_c(R')$ with $R' < R$. Interestingly, even if the density threshold increases as the filter scale decreases, the threshold mass $M_c(R)$ increases with R because of the volume compensation. Thus, the smallest mass corresponds to the largest over-densities. All in all, this implies that structures of scale R with density $\rho_R > \rho_c(R)$ fragment into substructures with mass $M_c(R') < M_c(R)$. Thus, the total mass per unit volume $M_{tot}(R)$, which corresponds to the whole unstable reservoir at scale R (per unit volume), is entirely redistributed in objects of mass *smaller* than $M_c(R)$. In this fashion, a significant number of objects with mass $M \leq M_c(R)$ originates from the fragmentation of the unstable mass at scale R, $M_{tot}(R)$. In order to account for this, Hennebelle & Chabrier (2008) introduced the probability that an unstable cloud of mass M' is embedded in a larger unstable one of size R, noted $P(R, M')$.

3.2.3 Golden rule

To obtain the mass function in pre-stellar cores, Hennebelle & Chabrier (2008) used the following golden rule:

$$\begin{aligned}\int_0^{M_c(R)} P(R,M')n(M')M'\mathrm{d}M' &= M_{tot}(R) = \int_{s_c(R)}^{\infty} \overline{\rho} e^s \, f_{s(R)}(s) \, \mathrm{d}\ s \\ &= \overline{\rho}\,\frac{1}{2}\left(1+\mathrm{erf}\left[\frac{\frac{1}{2}\sigma(R)^2 - s_c(R)}{\sqrt{2}\sigma(R)}\right]\right), \qquad (5.52)\end{aligned}$$

where $n(M')\mathrm{d}M'$ is the number density of cores with mass $M \in [M', M' + \mathrm{d}M'[$. Estimating the probability $P(R, M')$ in this equation is not straightforward. In a first approach, these authors took $P(R, M') = 1$, implying that any self-gravitating cloud of mass smaller than $M_c(R)$ is embedded in a cloud which is unstable when smoothed at scale R. This yields:

$$\int_0^{M_c(R)} n(M')M'\mathrm{d}M' = \overline{\rho}\,\frac{1}{2}\left(1+\mathrm{erf}\left[\frac{\frac{1}{2}\sigma(R)^2 - s_c(R)}{\sqrt{2}\sigma(R)}\right]\right). \qquad (5.53)$$

The validity of this result can be assessed with a more precise counting procedure, as will be done with the excursion-set formalism in the next section.

3.2.4 Mass function

Differentiating the previous equation (Eq. 5.53) with respect to R yields the following mass function:

$$\begin{aligned}n(M_c(R))\,M_c(R)\frac{\mathrm{d}M_c}{\mathrm{d}R} &= \overline{\rho}\,\frac{\mathrm{d}}{\mathrm{d}R}\left(\frac{\frac{1}{2}\sigma(R)^2 - s_c(R)}{\sqrt{2}\sigma(R)}\right)\frac{1}{\sqrt{\pi}}\mathrm{exp}\left(-\frac{\left(s_c(R)-\frac{1}{2}\sigma(R)^2\right)^2}{2\sigma(R)^2}\right) \\ &= \overline{\rho} e^{s_c(R)} f_{s(R)}(s_c(R))\left(-\frac{\mathrm{d}s_c}{\mathrm{d}R} + \frac{\mathrm{d}\sigma(R)}{\mathrm{d}R}\,[s_c(R)+\sigma(R)]\right). \qquad (5.54)\end{aligned}$$

A last step is to specify variance $\sigma(R)^2$. But before doing so, we first simplify Eq. 5.54 in the short R limit. We compare the two terms that appear in a parenthesis in the r.h.s. of this equation. The first term is:

$$\frac{\mathrm{d}s_c}{\mathrm{d}R} \simeq -\frac{2}{R} \text{ for } R \ll \lambda_{\mathrm{s}} = l_0\left(\frac{c_{\mathrm{s}}}{V_0}\right)^{1/2\eta} \text{ where } \lambda_{\mathrm{s}} \text{ is the sonic length.} \qquad (5.55)$$

The second term is, in the limit $R \ll \lambda_{\mathrm{s}}$,

$$\frac{\mathrm{d}\sigma(R)}{\mathrm{d}R}\,[s_c(R)+\sigma(R)] \simeq -2\frac{\mathrm{d}\sigma(R)}{\mathrm{d}R}\ln(R) = \mathcal{O}\left(\ln(R)\right). \qquad (5.56)$$

Thus, in the $R \ll \lambda_{\mathrm{s}}$ limit, we need not specify the behavior of $\sigma(R)$ as we can neglect this second term. We therefore obtain:

$$n(M_c(R))\,M_c(R)\frac{\mathrm{d}M_c}{\mathrm{d}R} = \overline{\rho} e^{s_c(R)} f_{s(R)}(s_c(R))\left(-\frac{\mathrm{d}s_c}{\mathrm{d}R}\right). \qquad (5.57)$$

3.2.5 The variance at scale R

With the sharp k-space filter, the variance of ρ is given by:

$$\mathrm{Var}\,(\rho_R) = \int \mathrm{d}\Omega \int_{1/L_c}^{1/R} \mathcal{P}_\rho(\boldsymbol{k}) k^2 \mathrm{d}k, \tag{5.58}$$

where $\mathrm{d}\Omega$ is the infinitesimal solid angle, L_c is the size of the cloud and $\mathcal{P}_\rho$ is the power spectrum of ρ. In principle, the lower limit of integration should be 0 but we study a cloud of finite size L_c , so there can be no power in length-scales larger than L_c. For the statistical counting to be significant, the cloud must be large enough compared to the correlation length of ρ, $l_c(\rho)$. In that case, the density power spectrum for $k \sim 1/L_c \ll 1/l_c(\rho)$ scales as:

$$\mathcal{P}_\rho(\boldsymbol{k}) \simeq 8\mathrm{Var}\,(\rho)\, l_c(\rho)^3, \;\; k \sim 1/L_c \ll 1/l_c(\rho), \tag{5.59}$$

and

$$\mathcal{P}_\rho(\boldsymbol{k})k^2 = \mathcal{O}\left((k\, l_c(\rho))^2\right), \;\; k\, l_c(\rho) \sim l_c(\rho)/L_c \ll 1, \tag{5.60}$$

so that the lower limit of integration in the integral can be set at $1/L_c$ or 0 indifferently. Then, given the density variance $\mathrm{Var}\,(\rho_R)$, $\sigma(R)^2$, the variance of the Gaussian field $s^{(R)}$ is given by:

$$\sigma(R)^2 = \ln\left(1 + \mathrm{Var}\,(\rho_R/\overline{\rho})\right). \tag{5.61}$$

To overcome the difficulties in obtaining the $\mathcal{P}_\rho$ power spectrum, Hennebelle & Chabrier (2008) used the following phenomenological model for $\sigma(R)^2$:

$$\sigma(R) = \sigma_0 \left(1 - \left(\frac{R}{L_c}\right)^n\right) \tag{5.62}$$

where σ_0 is the standard deviation of the unfiltered field s,

$$\sigma_0^2 = \ln\left(1 + (b\mathcal{M})^2\right) \text{ with } \mathcal{M} \text{ the r.m.s Mach number and } b \text{ the forcing parameter,} \tag{5.63}$$

and $n \simeq 2/3 - 1$ is related to the exponent of the power-spectrum of (the unfiltered) $s = \ln(\rho/\overline{\rho})$ (see the bottom of page 3 in Hennebelle & Chabrier 2008).

Technically, one cannot claim that the demonstration is foolproof because the authors have relied on the smoothing of $\rho = \overline{\rho}e^s$ instead of s. Had the smoothing procedure been applied to s, the PDF that enters equations (5.46), (5.48), (5.54) and (5.57) would have been that of the following field :

$$s_R = s * W_R^{sks} \text{ instead of that of } s^{(R)} = \ln(\rho_R/\overline{\rho}) = \ln\left(\frac{\rho}{\overline{\rho}} * W_R^{sks}\right), \tag{5.64}$$

and would therefore have been

$$f_{s_R}(x) = \frac{1}{\sqrt{2\pi\sigma(R)^2}} \exp\left(-\frac{(x - s_0)^2}{2\sigma(R)^2}\right), \tag{5.65}$$

where $s_0 = \overline{s} = -\sigma_0^2/2$. This would change all the calculations leading to Eqs. (5.54) and (5.57). Nevertheless, the functional form adopted in Eq. 5.62 accounts for the decrease of variance $\sigma(R)$ with increasing radius R. The theory that would specify the exact relationship is not available yet and this assumption allows one to continue with the derivation of the IMF. With that parameterization, Hennebelle & Chabrier (2008) were able to show that neglecting the second term in the parenthesis of Eq. (5.54) is valid unless for $R \simeq L_c$. Eq. (5.57) then allows an analytical expression for the CMF

$n(M)$ and a study of its properties.

3.2.6 Dynamical regimes and properties of the CMF

Developing each term in Eq. (5.57) , one obtains:

$$n(\tilde{M}(\tilde{R})) = \frac{2\overline{\rho}}{M_{J,0}} \frac{\exp(-\sigma(R)^2/8)}{\sqrt{2\pi}\sigma(R)} \frac{1}{\tilde{R}^6} \frac{1+(1-\eta)\mathcal{M}_*^2\tilde{R}^{2\eta}}{1+(1+2\eta)\mathcal{M}_*^2\tilde{R}^{2\eta}} \left(\frac{\tilde{M}}{\tilde{R}^3}\right)^{-\frac{3}{2}-\frac{1}{2\sigma^2}\ln(\tilde{M}/\tilde{R}^3)}. \tag{5.66}$$

where

$$\tilde{R} = \frac{R}{\lambda_{J,0}} \text{ with } \lambda_{J,0} = a^{1/2}\frac{c_{\rm s}}{\sqrt{G\overline{\rho}}} \text{ a typical Jeans length and,} \tag{5.67}$$

$$\tilde{M} = \frac{M_c}{M_{J,0}} \text{ with } M_{J,0} = a^{3/2}\frac{c_{\rm s}^3}{\sqrt{G^3\overline{\rho}}} \text{ a typical Jeans mass and,} \tag{5.68}$$

$$\mathcal{M}_* = \frac{1}{\sqrt{3}}\frac{V_0}{c_{\rm s}}\left(\frac{\lambda_{J,0}}{l_0}\right)^{\eta} \simeq (0.8-1)\left(\frac{\lambda_{J,0}}{l_0}\times 10\right)^{\eta}\frac{0.2 \text{ km s}^{-1}}{c_{\rm s}}, \text{ for } \eta = 0.5, \tag{5.69}$$

is the Mach number at the Jeans length $\lambda_{J,0}$.

- Thermal regime:

For scales R such that $\mathcal{M}_*^2\tilde{R}^{2\eta} \ll 1$, *i.e.* in the regime where the thermal support is the dominant one (characterized by the sound speed $c_{\rm s}$), the equation can be simplified because

$$\tilde{M} \simeq \tilde{R}. \tag{5.70}$$

Thus, in the thermal regime,

$$n(\tilde{M}) \simeq \frac{2\overline{\rho}}{M_{J,0}} \frac{\exp(-\sigma_0^2/8)}{\sqrt{2\pi}\sigma_0} \tilde{M}^{-3} e^{-\frac{2}{\sigma_0^2}\ln(\tilde{M})^2}. \tag{5.71}$$

In this regime, the MF is made of two contributions, namely, a power law with an index of 3 and a lognormal term, $\ln(\tilde{M})^2$. The former contribution is dominant when $M_{\sigma-} \ll \tilde{M} \ll M_{\sigma+}$, where

$$M_{\sigma\pm} = \exp\left(\pm\frac{3}{2}\sigma_0^2\right) \tag{5.72}$$

whereas the latter contribution eventually becomes dominant at both large ($M \geq M_{\sigma+}$) a and small ($M \leq M_{\sigma-}$) masses, where it is responsible for a lognormal cutoff. The range of the power-law domain is $M_{\sigma+} - M_{\sigma-}$ which is expressed in term of the r.m.s. Mach number $\mathcal{M}$ as follows:

$$M_{\sigma+} - M_{\sigma-} = \left(1+(b\mathcal{M})^2\right)^{3/2} - \left(1+(b\mathcal{M})^2\right)^{-3/2}. \tag{5.73}$$

For small values of the turbulent forcing term $(b\mathcal{M})^2$, *i.e.* for moderately supersonic to subsonic turbulence, this range is very small and the MF is essentially lognormal.

- Turbulent regime:

For scales R such that $\mathcal{M}_*^2\tilde{R}^{2\eta} \gg 1$ and $R \ll L_c$, *i.e.* in the regime where turbulent support is dominant, the MF can be simplified as follows:

$$n(\tilde{M}) \propto \tilde{M}^{-\frac{3(\eta+1)}{2\eta+1}+4\frac{(\eta-1)^2}{(2\eta+1)^2\sigma(R)^2}\ln(\mathcal{M}_*)} e^{-\frac{2}{\sigma(R)^2}\frac{(\eta-1)^2}{(2\eta+1)^2}\ln(\tilde{M})^2}. \tag{5.74}$$

As before, the MF is made of two contributions. One is a power law with index

$$\alpha = \frac{3(\eta+1)}{2\eta+1} - 4\frac{(\eta-1)^2}{(2\eta+1)^2\sigma(R)^2}\ln(\mathcal{M}_*) \simeq 2.25 \text{ for } \eta = 0.5 \text{ and } \mathcal{M}_* = 1 \tag{5.75}$$

and the other one is a lognormal cutoff. Interestingly, the exponent of the power law is smaller than in the thermal regime and is close to the Salpeter value for $\mathcal{M}_* \simeq 1$. As in the thermal regime, the mass range in which the power-law contribution is dominant depends on $\sigma(R)$, which depends on R in a non-trivial manner. The power law contribution is the dominant one for

$$\tilde{M}(\tilde{R}) \ll e^{-2\ln(\mathcal{M}_*)} \exp\left(\frac{3(\eta+1)\sigma(R)^2}{2}\frac{(2\eta+1)}{(\eta-1)^2}\right) = \mathcal{M}_*^{-2}\left(1+(b\mathcal{M})^2\right)^{18\left(1-\tilde{R}^n\left(\frac{\lambda_{J,0}}{Lc}\right)^n\right)^2}, \tag{5.76}$$

where we chose $\eta = 0.5$.

- Global:

The transition between the two regimes occurs at scale R such that $\mathcal{M}_*^2\tilde{R}^{2\eta} \simeq 1$, *i.e.* for $\tilde{R} \simeq \mathcal{M}_*^{-1/\eta}$. This corresponds to $R \sim \lambda_\mathrm{s}$ where λ_s is the sonic length. Thus, for $\mathcal{M}_* \ll 1$, the MF is essentially that of the thermal regime. For $\mathcal{M}_* \gg 1$, the MF is that of turbulent regime. In that case, however, the exponent of the power-law is smaller than the Salpeter value and produces a CMF tail that is too shallow. For typical Milky Way conditions, such that $\mathcal{M}_* \simeq 1-2$, the MF is that of the thermal regime at small masses and that of the turbulent one at large masses with an exponent close to the Salpeter value. In principle, some caution is warranted as the $\mathcal{M}_* \simeq 1-2$ estimate depends on conditions for star formation that are not known accurately. The fact that this estimate leads to the observed CMF, however, is a strong argument in its favour.

For $\mathcal{M}_* \simeq 1-2$, the peak of the CMF occurs in the thermal regime and yields:

$$\tilde{M}_\mathrm{peak} \simeq \frac{1}{(1+(b\mathcal{M})^2)^{3/4}}, \tag{5.77}$$

where the running of $\sigma(R)$ has been ignored. This peak mass is the most probable pre-stellar core mass, which must not be mistaken with the average mass. For supersonic turbulence, this is roughly :

$$M_\mathrm{peak} \simeq \frac{M_{J,0}}{(b\mathcal{M})^{3/2}} \propto \frac{1}{\sqrt{\overline{\rho}\mathcal{M}^3}}. \tag{5.78}$$

For typical clouds of size L_c that meet the following Larson conditions $\overline{\rho} \propto L_c^{\sim -1}$, $\mathcal{M} \propto L_c^{\sim 0.5}$, this peak mass scale as $M_\mathrm{peak} \propto L_c^{-1/4}$. Thus, even for cloud size variations that are as large as a factor of 100, the peak mass is only affected by a factor of 3. This partial compensation between the increasing and decreasing scale dependences of the Mach number and the Jeans mass may be one of the reasons why the peak of the CMF (IMF) appears to be almost constant over a wide range of stellar cluster conditions.

3.2.7 From the CMF to the IMF

As mentioned throughout the above derivation, the MF that is obtained is really the pre-stellar Core Mass Function (CMF) instead of the Initial Mass Function (IMF). However, observations of prestellar condensates, as identified in dust continuum surveys, show that the CMF and the IMF have similar shapes and that the CMF peaks at a mass that is about 3 times larger than that of the observed IMF, notwithstanding the large uncertainties that affect both (André et al., 2008; André et al., 2010). It is therefore tempting to assume that the transformation of gravitationally bound prestellar cores into genuine stars or brown dwarfs involves some uniform efficiency factor, $M_*/M_{\rm core}$, which is estimated to be in the range $30\%, 50\%$ from observations. It is not clear, however, how this comes about. Magnetically driven outflows, which are expected to produce a mass-independent star formation efficiency factor in the appropriate range (Matzner & McKee, 2000), are an attractive proposition that deserve further study. For want of a firm theoretical basis, Hennebelle & Chabrier (2008) simply assumed that the IMF is obtained from their CMF by rescaling the mass of stars M_* with a star formation efficiency factor, $M_*/M_{\rm core} \simeq 30\%, 50\%$.

3.2.8 Summary of the model

We have made an in-depth presentation of the Hennebelle & Chabrier (2008) model. It is worth summarizing its underlying assumptions and successful outcomes.

- Assumptions:

By construction, the model relies on the same assumptions as the PS model: ergodicity (and hence statistical homogeneity) of the random field ρ and a Gaussian $s = \ln(\rho/\overline{\rho})$ field. Additional assumptions are as follows.

In order to handle the fact that ρ is not Gaussian but lognormal, it is assumed that ρ_R, the PDF of the smoothed density field at some scale R, is also lognormal. This implies that the PDF of the density logarithm $s^{(R)} = \ln(\rho_R/\overline{\rho})$ is Gaussian.

The counting procedure relies on a density threshold (Eq. (5.38)), which is deduced from the condition of virial equilibrium for a homogeneous *isolated* cloud and a phenomenological model of turbulence. This condition is not entirely rigorous as it accounts for neither a possible tri-axial collapse nor a possible initial cloud expansion. Further, it does not account for the fact that subregions in a star forming cloud are far from being isolated and are subjected to external tides. A final assumption that the density and velocity fields are weakly correlated in isothermal "inertial" turbulence which is shown to be sufficiently accurate by numerical simulations. More refined models that account for possible tri-axial collapse, as in cosmology, might change quantitatively the MF (see Sec. 2.4.3). In cosmological models, tidal forces enhance collapse along one axis and hamper collapse along the other axes relative to spherical conditions (Sheth et al., 2001; Shen et al., 2006). Smaller objects are particularly sensitive to external tides and must have a greater internal density to hold themselves together as they collapse. In cosmology, allowing for tri-axial collapse modifies quantitatively only the low mass part of the MF and leaves the high mass part almost unaffected (Sheth et al., 2001). It is thus reasonable to assume that this will also be true for star formation. In any case, as mentioned earlier, the dynamics in this context is far more complex and would require extensive investigations. In the absence of a comprehensive theoretical framework, the density threshold criterion is a first approximation that allows progress and it does lead to a MF with the required characteristics.

A second assumption is in the statistical counting of unstable regions, which involves the cloud-in-cloud problem. This has been addressed by the golden rule (Eq. (5.52)) and factor $P(R; M')$. This last term is taken to be equal to 1 for lack of suitable information, which circumvents the problem but does not solve it completely.

A third, and perhaps less important, assumption, at least for low masses, deals with how the variances of ρ_R and $s^{(R)} = \ln(\rho_R/\overline{\rho})$ vary as a function of the filter radius R (Eq. 5.62). The functional form that was adopted is not exact but accounts for the decrease of the variance with increasing R. In addition, in order to avoid large artefacts, the CMF is truncated before going to scales $R \sim L_c$.

Thus, one cannot generalize the current IMF model without due attention to all these assumptions, because they may be inconsistent with the additional processes and constraints that are introduced.

- Success:

This theory reproduces the observed properties of the CMF and IMF. It shows that the Salpeter value for the exponent in the IMF power-law can be attributed to turbulence (Chabrier & Hennebelle, 2011). Further, it accounts for the apparent universality of the IMF over a wide range of stellar cluster conditions. We have identified clearly the steps that take us to a solution and all the assumptions that are needed with our current level of understanding. For example, the theory introduces the probability that an unstable cloud of mass M' is embedded in a larger unstable one of size R ($P(R, M')$). At present, this probability is not known. Thus, Hennebelle & Chabrier (2008) had to take it equal to some constant value, but this can be upgraded as more information becomes available. In other words, the theory allows one to winnow the list of all the necessary steps down to a few select ones. Notably, the theory has been extended further to describe conditions in Early Type Galaxies by Chabrier et al. (2014).

3.3 Steps 2 and 3: Statistical counting and the excursion-set of Hopkins (2012a,b)

As shown in the previous section, the Hennebelle & Chabrier (2008) model is successful in predicting the observed properties of the CMF in various stellar cluster conditions, but relies on a number of assumptions. The cloud-in-cloud problem is only solved partially in relation to the choice of probability $P(R; M') = 1$. Moreover, the model deals with scales that are smaller than the cloud scale L_c, so that the properties of the parent cloud (of size L_c) must be specified in an ad hoc manner, *e.g.* in this case through the empirical Larson relations. This not-so-fondamental issue is related to a perhaps more important one, which is that the proper calculation of variance $\sigma(R)$ cannot be done properly, at least at scales comparable to the cloud scale L_c.

Hopkins (2012a,b) sought to improve this model and adopted the excursion set formalism. We will show that this author has not come up with a complete solution either. More importantly, we will show that (1) this author did bring a genuine improvement to the statistical counting of Hennebelle & Chabrier (2008) but (2) made an ambiguous calculation and (3) did not really solve the variance problem ($\sigma(R)$).

3.3.1 The cloud-in-cloud problem

Hopkins (2012a,b) addressed the cloud-in-cloud problem with the excursion-set formalism. He performed the thought experiment detailed earlier, which is briefly recapitulated here for the sake of convenience. Consider a region which is self-gravitating at some large scale R_0. This region will not form a single core if it contains multiple subregions that are themselves self-gravitating on a smaller scale $R < R_0$. The reason is that such subregions are bound to collapse more rapidly because the mean density for self-gravitation at scale R is larger than that at R_0 (see Sec. 3.1). Thus, the parent cloud is bound to break up into smaller objects. This can be continued iteratively inside R. Only when a region is self-gravitating at the R scale, and not self-gravitating on any smaller scales, can collapse proceed without fragmentation. Hopkins (2012a,b) thus realized that the CMF was given by the "last crossing" distribution $f_{\mathrm{last}}(R)$ instead of the "first crossing" one used in cosmology (see Fig. 5.3). This last crossing distribution corresponds to random walks that cross the barrier for the last time at resolution $S(R)$ (see the previous section).

As in the cosmological case, the last crossing distribution is deduced from a set of random walks for a *centered Gaussian field* γ. For the sharp k-space filter, *and only for this filter*, random walks obtained by smoothing the *centered Gaussian field* γ are Brownian (see Sec 2). This allowed Hopkins (2012b) to follow the derivation of Zhang & Hui (2006) and to obtain a Volterra equation of the second kind for $f_{\mathrm{last}}(S(R))$, where again $S(R) = \sigma^2(R)$ is the variance of the smoothed field γ. To do so, he considered walks in the opposite pseudo-time direction, *i.e* going back in time, corresponding to decreasing S (thus increasing R). A trajectory begins at γ_0 at $S(0)$ and its position γ is evaluated at increasingly smaller

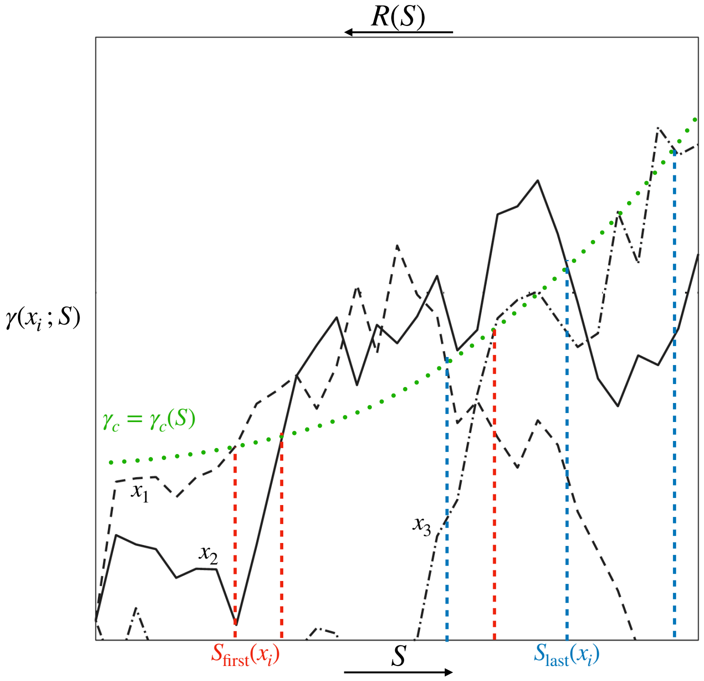

FIGURE 5.3 Trajectories of 3 random walks $\gamma(\boldsymbol{x}_i; S)$ in the $S-\gamma$ plane attached to three different positions $\boldsymbol{x}_i$. The filter function is the sharp k-space filter W^{sks}. A moving barrier $\gamma_c = \gamma_c(S)$ is represented in green. The resolution S_{first} at which the walks cross the barrier for the first time is shown in red. The resolution S_{last} at which the walks cross the barrier for the last time is shown in blue.

values of S (larger R). The Moving barrier is located at $B(S)$. We thus see that for the last crossing distribution to be meaningful, the probability that γ_0 exceeds $B(S(0))$ must vanish as $R \to 0$. This is indeed the case here, because $\rho_c(R) \to \infty$ when $R \to 0$ (see Sec. 3.1). The derivation of the Volterra equation for the last crossing distribution f_{last} is very similar to that of Zhang & Hui (2006) (described in App. A). The end result is the following:

$$f_{\text{last}}(S) = g_1(S) + \int_S^0 \mathrm{d}S'\, f_{\text{last}}(S')\, g_2(S,S'), \tag{5.79}$$

where

$$\begin{aligned} g_1(S) &= \left(2\frac{\mathrm{d}B}{\mathrm{d}S} - \frac{B(S)}{S}\right)\frac{1}{\sqrt{2\pi S}}\exp\left(-\frac{B(S)^2}{2S}\right), & (5.80)\\ g_2(S,S') &= \left(\frac{B(S)-B(S')}{S-S'} + \frac{B(S)}{S} - 2\frac{\mathrm{d}B}{\mathrm{d}S}\right) P_{2,1}\left(B(S), S; B(S'), S'\right) & (5.81)\end{aligned}$$

where $B(S)$ is the moving barrier and $P_{2,1}\left(\gamma_1, S_1; \gamma_2, S_2\right)$ is the conditional density function for starting at γ_2 at S_2 and arriving at γ_1 at $S_1 < S_2$ going back in time. Stated differently, $P_{2,1}\left(\gamma_1, S_1; \gamma_2, S_2\right) \mathrm{d}\gamma$ it is the infinitesimal probability of having started at $\gamma \in [\gamma_1, \gamma_1 + \mathrm{d}\gamma[$ at S_1, knowing that the present position at $S_2 > S_1$ is γ_2. This conditional probability is not obtained as easily as the conditional probability that the trajectory is at position $\gamma \in [\gamma_2, \gamma_2 + \mathrm{d}\gamma[$ at resolution S_2 knowing that it was at position $\gamma = \gamma_1$ at $S_1 < S_2$, $P_{1,2}\left(\gamma_2, S_2; \gamma_1, S_1\right) \mathrm{d}\gamma$, which is the one encountered in cosmology (see App. A). Thanks to the continuous Bayes' relation (see Chapter **1**), we may write that:

$$P_{2,1}\left(\gamma_1, S_1; \gamma_2, S_2\right) = P_{1,2}\left(\gamma_2, S_2; \gamma_1, S_1\right)\sqrt{\frac{S_2}{S_1}}\exp\left(-\frac{\gamma_1^2}{2S_1} + \frac{\gamma_2^2}{2S_2}\right) \tag{5.82}$$

$$= \frac{1}{\sqrt{2\pi(S_2 - S_1)\frac{S_1}{S_2}}}\exp\left(-\frac{\left(\gamma_1 - \gamma_2\frac{S_1}{S_2}\right)^2}{2(S_2 - S_1)\frac{S_1}{S_2}}\right). \tag{5.83}$$

Here, we have again made extensive use of the fact that the steps of the random walk are uncorrelated (for increasing S), a property which stems from the use of the sharp k-space filter. As before, the Volterra equation has as a unique solution that can be calculated by standard numerical methods. For a linear barrier $B(S) = B_0 + \beta S$, the solution is:

$$f_{\text{last}}(S) = \frac{\beta}{\sqrt{2\pi S}}\exp\left(-\frac{B^2}{2S}\right). \tag{5.84}$$

For a constant barrier $B(S) = B_0$, $f_{\text{last}}(S) = 0$ because, as explained earlier, the probability that γ_0 exceeds $B(S(0))$ must vanish at $R \to 0$.

3.3.2 The Hopkins (2012a,b) model and the variance problem

The next step in the Hopkins (2012a,b) derivation involves a somewhat hybrid smoothing procedure. One must first specify the field to be smoothed and its statistical properties (e.g. his variance and power-spectrum). Following Hennebelle & Chabrier (2008), Hopkins (2012a,b) assumed that the density field ρ filtered at scale R, $\rho_R \equiv \rho * W_R$, is lognormal, on the grounds that simulations determine a density field that is smoothed over a window function corresponding to the numerical resolution limit. In studies of numerical resolution, the PDF is always found to be close to lognormal. However, in general, the coarsest resolution in these studies is already small enough so that the PDF is well resolved, at least around the peak. If the resolution gets degraded further, would it still produce lognormal PDFs? It is difficult to answer this question because, the coarsest the resolution is, the smaller the sample size is and the lower the accuracy of the PDF estimation is for high and low density events (see Chap. **3**). Furthermore, even if the answer to the above question is positive, the window function corresponding to the numerical resolution limit is some sort of top hat function and it is not clear whether or not results would hold for other window functions, and in particular for the sharp k-space one. As in Hennebelle & Chabrier (2008), the assumption can only be justified *a posteriori* through a comparison with observations.

Taking on board that the density field ρ_R is lognormal at all scales $R \simeq 1/k$, the variance is:

$$\text{Var}\,(\rho_R) = \overline{\rho}(b\mathcal{M}(R \simeq 1/k))^2. \tag{5.85}$$

corresponding to a Gaussian logarithmic density $s^{(R)} \equiv \ln(\rho_R/\overline{\rho})$ with variance

$$\text{Var}\left(s^{(R)}\right) \equiv \sigma_k^2 = \ln\left(1 + (b\mathcal{M}(k))^2\right) \quad \text{and expectation} \quad \overline{s^{(R)}} = -\frac{\sigma_k^2}{2} \tag{5.86}$$

where we recall that $k \simeq 1/R$ (Eq (6)-(9) in Hopkins (2012a)). Hopkins (2012a,b) then makes the additional assumption that the density field ρ is also lognormal in k-space. To quote him, "Any distribution which is lognormal in either real or k-space must be lognormal in both" (see below Eq. (12)). This is *not* true, however, for lognormal fields and can hardly be justified. As shown in Sec. 2, Fourier modes are delta-correlated and only have a formal meaning. The validity of this assumption is therefore uncertain and this concern creeps up repeatedly in what follows. One other assumption is that Eq. (5.86) is "correct on a k-by-k basis". One can then construct a quantity similar to a power-spectrum and obtain the variance $\sigma(R)^2$ of the smoothed logarithmic density field at scale R:

$$s_R \equiv s * W_R = \ln\left(\frac{\rho}{\overline{\rho}}\right) * W_R, \tag{5.87}$$

$$\sigma(R)^2 \equiv \mathrm{Var}\,(s_R) = \int \mathrm{d}\ln k\, \sigma_k(\mathcal{M}(k))^2 |W_R(k)|^2, \text{ (Eq. (10) in Hopkins (2012a)).} \tag{5.88}$$

The reasons for such a scaling are not really clear, as Hopkins (2012a) repeatedly make the confusion of identifying $s_R \equiv s * W_R$ with $s^{(R)} \equiv \ln(\rho_R/\overline{\rho})$. The author assumed that the expectation of the quantity that should be s_R is

$$\overline{s_R} = -\frac{\sigma(R)^2}{2}, \text{ (see, e.g. Eq. (13) and the top of page 6 just after Eq. (15) in Hopkins (2012a)).} \tag{5.89}$$

However, if $s_R \equiv s * W_R$, then $\overline{s_R}$ does *not* depend on the filter radius R and is:

$$\overline{s_R} = \overline{s_0} = -\frac{1}{2}\ln\left(1 + (b\mathcal{M}(0))^2\right) = -\frac{1}{2}\ln\left(1 + (b\mathcal{M})^2\right) \neq -\frac{\sigma(R)^2}{2}. \tag{5.90}$$

The relation $\overline{s_R} = -\sigma(R)^2/2$ holds for $s^{(R)}$ if its variance is $\sigma(R)^2$.

To construct the random walks and use the Volterra equation derived above for a *centered* gaussian field, Hopkins (2012a) chose the sharp-k-space filter W^{sks} and the following field:

$$\delta_R = "s_R" - "\overline{s_R}" = "s_R" + \frac{\sigma(R)^2}{2}, \text{ where it is still not clear whether "}s_R\text{" stands for the actual } s_R \text{ or } s^{(R)}.$$

Barrier ρ_c for the ρ field is then transformed into a barrier for the δ_R field as follows:

$$B_\delta(R) = \ln\left(\frac{\rho_c(R)}{\overline{\rho}}\right) + \frac{\sigma(R)^2}{2}, \text{ (see Eq. (13) in Hopkins (2012a) and Eq. (25) in Hopkins (2012b)),} \tag{5.91}$$

and the mass encompassed by the window function is taken to be :

$$M_R = \frac{4\pi}{3}R^3 e^{B_\delta(R)} = \frac{4\pi}{3}R^3 \rho_c(R), \text{ at least for } R < h \text{ (see Eq (14) and (15) of Hopkins (2012a)).} \tag{5.92}$$

With this confusion, one sidesteps a series of problems that are due to the fact that :

$$\boxed{s_R \equiv s * W_R = \ln\left(\frac{\rho}{\overline{\rho}}\right) * W_R \neq \ln\left(\frac{\rho}{\overline{\rho}} * W_R\right) = s^{(R)}.} \tag{5.93}$$

3.3.3 Proper lay out of the Hopkins (2012a,b) assumptions and overlooked issues.

From the previous sections, it is clear that $s = \ln(\rho/\overline{\rho})$ is the field to be smoothed. Only trajectories that are described by the smoothed s with the sharp k-space filter W^{sks} are Brownian walks. For a random walk with the field $s^{(R)} = \ln(\rho_R/\overline{\rho})$, where ρ_R is the density field smoothed with W_R^{sks}, the steps are correlated in a non trivial manner and one cannot use the Volterra equation to derive the last crossing distribution. This is precisely because the filtering and logarithm-taking operations do not commute :

$$s_R \equiv s * W_R = \ln\left(\frac{\rho}{\overline{\rho}}\right) * W_R \neq \ln\left(\frac{\rho}{\overline{\rho}} * W_R\right) = s^{(R)}. \tag{5.94}$$

If the smoothing procedure is applied to $s = \ln(\rho/\overline{\rho})$, which is gaussian by assumption, there is no need to make the stronger assumption that ρ_R is lognormal for all R. By definition, s is Gaussian, and hence s_R is also Gaussian. The centered field to be taken for the random walk is:

$$\delta = s - s_0, \text{ with } s_0 = -\frac{1}{2}\ln\left(1 + (b\mathcal{M})^2\right) = -\frac{\sigma(0)^2}{2}, \tag{5.95}$$

which is evidently Gaussian. The barrier for the field s, $B_s(R)$, then naturally becomes a barrier for δ, $B_\delta(R)$ as follows:

$$B_\delta(R) = B_s(R) - s_0. \tag{5.96}$$

The derivation made by Hopkins (2012a,b) relies on the following assumptions.

- The variance $\sigma(R)^2$:

The author assumes that the power spectrum of s is related to $\sigma_k(\mathcal{M}(k))^2$, which leads to the variance of s_R for all R:

$$\sigma(R)^2 = \int \mathrm{d}\ln k\, \sigma_k(\mathcal{M}(k))^2 |W_R(k)|^2 = \int \mathrm{d}\ln k \ln\left(1 + (b\mathcal{M}(k))^2\right) |W_R(k)|^2. \tag{5.97}$$

Hopkins (2012a,b) used the Toomre criterion to extend the calculation of σ_k^2 and $\rho_c(R)$ to the galactic scale height $h \sim 100$pc (see Sec.3.1). He was thus able to normalize the turbulent velocity dispersion and to get around the empirical Larson relations. Moreover, he could continue with the calculation of $\sigma(R)$ at scales comparable to cloud ones. The end result is an averaged CMF over all cloud conditions in the Milky Way, provided that they belong to the same turbulent cascade. As mentioned earlier, the big leap in this procedure is the assumption that the dynamical properties of the gas in star-forming clumps are affected only marginally by the transition from $\mathrm{H_I}$ to $\mathrm{H_2}$ and by large scale gradients, in order for the atomic and molecular gas to belong to the same turbulent cascade from galactic to cloud scales. Due to the rather ad hoc derivation of $\sigma(R)$, the Hopkins (2012a) model is therefore as phenomenological as that of Hennebelle & Chabrier (2008) and is not a definitive improvement.

- The chosen barrier and the overlooked issue:

The author assumes that the moving barrier for δ is given by

$$B_\delta(R) = \ln\left(\frac{\rho_c(R)}{\overline{\rho}}\right) + \frac{\sigma(R)^2}{2}, \tag{5.98}$$

which corresponds to the following barrier for s:

$$B_s(R) = \ln\left(\frac{\rho_c(R)}{\overline{\rho}}\right) + \frac{\sigma(R)^2}{2} + s_0 = \ln\left(\frac{\rho_c(R)}{\overline{\rho}}\right) - \frac{\sigma(0)^2 - \sigma(R)^2}{2}, \text{ for } s. \tag{5.99}$$

This amounts to ignoring that $s_R \neq s^{(R)}$ (see Eq. (5.94)). The collapse condition derived by Hopkins (2012a,b) and Hennebelle & Chabrier (2008) applies to the density field ρ (see Sec. 3.1). In general, however,

$$\rho_R = \overline{\rho} e^{s^{(R)}} \neq \overline{\rho} e^{s_R}, \quad \text{because } s_R \neq s^{(R)}. \tag{5.100}$$

Fortunately, the exponential is a (strictly) convex function. Thus, for a positive window function W_R with a *finite volume* which is properly normalized to one:

$$\int W_R(\boldsymbol{x})\mathrm{d}\boldsymbol{x} = 1, \tag{5.101}$$

one can endow $\mathbb{R}^3$ with the finite measure $W_R\mathrm{d}\boldsymbol{x}$. In such conditions, the Jensen inequality of convexity applies and yields:

$$\rho_R(\boldsymbol{x}) \equiv \rho * W_R = \overline{\rho} \int \exp\left[s(\boldsymbol{x}-\boldsymbol{x}')\right] W_R(\boldsymbol{x}')\mathrm{d}\,\boldsymbol{x}' \;\; > \;\; \overline{\rho}\exp\left[\int s(\boldsymbol{x}-\boldsymbol{x}')W_R(\boldsymbol{x}')\mathrm{d}\,\boldsymbol{x}'\right], \\ > \;\; \overline{\rho}\exp(s * W_R) = \overline{\rho}\exp(s_R(\boldsymbol{x})). \quad (5.102)$$

For well behaved window functions (such as the top hat or gaussian windows):

$$\boxed{s_R = \ln(\rho_c(R)/\overline{\rho}) \text{ implies } \rho_R > \rho_c(R).} \quad (5.103)$$

In this case, the collapse criterion is in fact only a sufficient condition. There may well be regions where $\rho_R \geq \rho_c(R)$ but where $s_R < \ln(\rho_c(R)/\overline{\rho})$, and they would not be regarded as unstable and included in the tally. Collapse criteria are admittedly rather gross simplifications of true conditions, and one can argue that, given that one is dealing with a very large population of objects, the only workable strategy is to make do with a sufficient condition. But one should bear in mind that the consequence is an underestimate of the number of unstable regions. This concern worsens when one uses the sharp k-space window function because it is not positive and does not encompass a finite volume. For this function, the Jensen inequality does not hold and one cannot, in practice, deduce anything about ρ_R from the knowledge of s_R. While Hopkins (2012a) never mentioned this problem he actually perform a calculation that allowed to address it as follows. He performed random walks for both the sharp k-space and Gaussian window functions, determined the respective *first* crossing distributions and found that they lead to nearly identical MFs. One can then argue that this is also likely true for the *last* crossing distributions, and assume that $\rho_R > \overline{\rho}e^{s_R}$.

In their derivation, Hopkins (2012a,b) chose the following barrier:

$$B_s(R) = \ln\left(\frac{\rho_c(R)}{\overline{\rho}}\right) - \frac{\sigma(0)^2 - \sigma(R)^2}{2}, \text{ for } s. \quad (5.104)$$

Hence, when a random walk crosses this barrier, such that $s_R = B_s(R)$, one has:

$$\rho_R > \overline{\rho}e^{B_s(R)} = \rho_c(R)\exp\left(-\frac{\sigma(0)^2 - \sigma(R)^2}{2}\right). \quad (5.105)$$

For small R, this essentially reduces to $\rho_R > \rho_c(R)$. For large R, $\sigma(R) \ll \sigma(0)$ and hence $\rho_R > \rho_c(R)\left(1+(b\mathcal{M})^2\right)^{-1/2}$. At small R, the excursion step procedure may overlook unstable regions but still yields a sufficient instability condition. At large R, however, the condition on s_R does not constrain ρ_R to be above the instability threshold and the resulting MF is uncertain. Thus, the Hopkins (2012a,b) approach to extend the calculation of $\sigma(R)$ to scales comparable to cloud dimensions remains essentially approximative. The issue of the non commutating filtering and log-taking operations creeps up again in what follows.

- Mass attribution:

As detailed in the previous section, once the last crossing distribution has been obtained, one must attribute a mass to each scale R. Attaching a volume $V_W(R)$ to the window function, the mass contained within it is $M(R)$:

$$M(R) = V_W(R)\rho_R. \quad (5.106)$$

the sharp k-space window function W^{sks}, Hopkins (2012a,b) chose volume $V_{W^{sks}}(R) \simeq 4\pi R^3/3$ for $R \leq h$. Nevertheless, as before, the excursion-set procedure deals with values s_R and not ρ_R, so that when s_R is above the threshold, the only thing that can be said, using Jensen inequality, is:

$$\boxed{M(R) = V_W(R)\rho_R > V_W(R)\overline{\rho}e^{s_R},} \tag{5.107}$$

and the mass is rather ill-defined. Hopkins (2012a,b) overlooked this issue and chose to attribute the following unstable mass to each scale R :

$$M(R) = V_W(R)\rho_c(R). \tag{5.108}$$

which seems quite reasonable. However, as seen above, for small scales R such that $\sigma(R) \sim \sigma(0)$, $B_s(R) = \ln\left(\frac{\rho_c(R)}{\overline{\rho}}\right)$. Thus, when the smoothed logarithmic density field reaches the collapse threshold, the mass encompassed by the window function is:

$$M(R) = V_W(R)\rho_R > V_W(R)\overline{\rho}e^{B_s(R)} = V_W(R)\rho_c(R). \tag{5.109}$$

implying that the mass attributed to those scales R is under-estimated. This compounds the problem of overlooking unstable regions in the counting.

- The golden rule and the CMF:

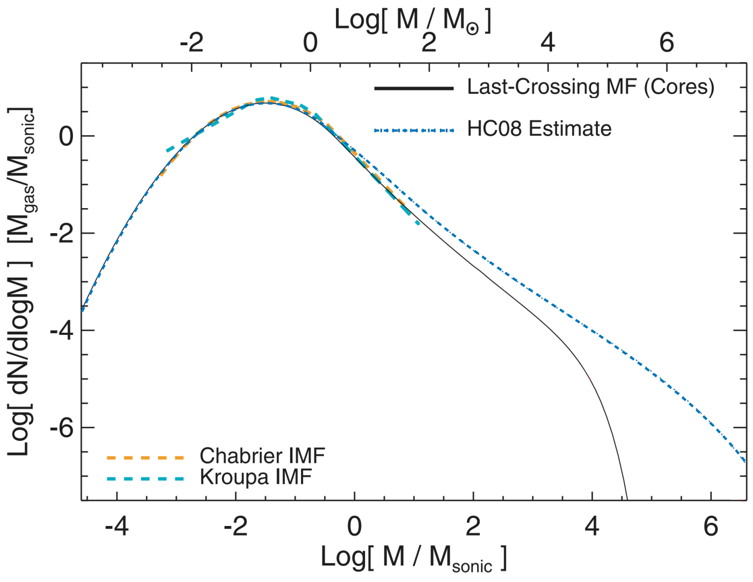

FIGURE 5.4 CMF obtained by Hopkins (2012b) (Their Fig 1). Black: the CMF obtained with the excursion set. Blue: the CMF of Hennebelle & Chabrier (2008). The functional forms of the IMFs observed by Chabrier and Kroupa are shown in orange and light blue, respectively (see Chabrier 2003) At small mass values $M \leq 10M_\odot$ (or small scales), these CMFs are remarkably close to one another.

Once he has attributed a mass to each scale R or resolution $S = \sigma(R)^2$, Hopkins (2012b) uses the golden rule:

$$M\,n(M) = \rho_c(S) f_{\mathrm{last}}(S) \left|\frac{\mathrm{d}S}{\mathrm{d}M}\right|. \tag{5.110}$$

For comparison, the CMF obtained in Hennebelle & Chabrier (2008) yields (see Eq. 5.57):

$$M\,n(M) = \rho_c(S) f_{s(R)}(s_c) \left|\frac{\mathrm{d}s_c}{\mathrm{d}S}\right| \left|\frac{\mathrm{d}S}{\mathrm{d}M}\right| \tag{5.111}$$

where $s_c = \ln(\rho_c(S)/\overline{\rho})$ and

$$f_{s^{(R)}}(x) = \frac{1}{\sqrt{4\pi\sigma(R)^2}} \exp\left(-\frac{(x+\sigma(R)^2/2)^2}{2\sigma(R)^2}\right). \tag{5.112}$$

Using Eq. 5.79, Hopkins (2012b) showed and tested numerically that, at small scales $R < h$, *i.e* large S, the last crossing distribution $f_{\mathrm{last}}(S)$ is such that:

$$f_{\mathrm{last}}(S) \simeq f_{s^{(R)}}(s_c) \left|\frac{\mathrm{d}s_c}{\mathrm{d}S}\right| \tag{5.113}$$

which leads to the Hennebelle & Chabrier (2008) result. The agreement between the two calculations is shown in Fig. 5.4, taken from Hopkins (2012b) (their Fig. 1).

3.3.4 Success of the model and summary

The Hopkins (2012b) solution reduces to that of Hennebelle & Chabrier (2008) at small scales $R < h$ (small masses), and hence both can be credited with the same degree of success. They explain that the Salpeter exponent in the IMF is due to turbulence. They account for the apparent universality of the IMF over a wide range of stellar cluster conditions. Finally, they identify the key ingredients that are needed for a global account ofs the formation of structures in star-forming clouds. By the same token, both models are subject to the same caveats (see Sec 3.2.8). The derivation of the Volterra equation for the last crossing distribution follows the same line of reasoning as Zhang & Hui (2006) for the first crossing distribution.

The excursion-set procedure provides a satisfactory solution to the cloud-in-cloud problem but the Hopkins (2012b) study remains subject to several limitations related to the fact that ρ is lognormal and not Gaussian (see Sec. 3.3.3). The instability criterion and the mass assignment procedure suffer from important uncertainties because only $s = \ln(\rho/\overline{\rho})$ is Gaussian, and because :

$$s_R \equiv s * W_R = \ln\left(\frac{\rho}{\overline{\rho}}\right) * W_R \neq \ln\left(\frac{\rho}{\overline{\rho}} * W_R\right) = s^{(R)}. \tag{5.114}$$

At small scales (or small masses), the instability criterion only yields a sufficient condition for collapse and some unstable regions are probably bypassed by the statistical counting. Assigning a mass to a scale remains fraught with uncertainties. For $s_R = s_c$, the only information that can be obtained on the mass encompassed by the window function is:

$$M(R) = V_W(R)\rho_R > V_W(R)\overline{\rho}e^{s_c}. \tag{5.115}$$

At small scales $R < h$, this leads to underestimate mass. Hopkins (2012b) did not solve the variance issue mentioned in the introduction and did not obtain a reliable CMF at scales larger than the cloud scales (see Eq. (5.105)).

The excursion-set model is useful in that it reveals hidden assumptions in the model of Hennebelle & Chabrier (2008). As in cosmology, the excursion-set formalism provides useful information on the relevance of the Press-Schechter approach, such as that of Hennebelle & Chabrier (2008).

3.4 Conclusion regarding these models

We have made a detailed presentation of the models of Hennebelle & Chabrier (2008) and Hopkins (2012a,b) based on the Press-Schechter and excursion-set formalisms, respectively. Both models rely on the ergodicity assumption and therefore on the statistical homogeneity of the density and velocity stochastic fields. In order to clarify some of the derivations, we have provided new arguments and theoretical developments.

At this stage, it is worth recapitulating the major steps involved in the derivation of the CMF, of which there are three. One step is the instability criterion that yields a density threshold for collapse (Eq. (5.38)). This simple condition does not account for tri-axial collapse and initial cloud expansion. It also glosses over the fact that subregions in a star forming cloud are not isolated and are subjected to external tides. The weak correlation between density and velocity which is required is valid for isothermal "inertial" turbulence and is found to be a reasonable approximation according to state-of-the-art numerical simulations. In cosmological models, tidal forces enhance collapse in one direction at the expense of the other directions leading to departures from radial symmetry (Sheth et al., 2001; Shen et al., 2006). Smaller objects are more influenced by external tides than larger ones: their internal density must be larger if they are to hold together. Correcting for these effects modifies quantitatively the low mass part of the MF and leaves the high mass part of the MF almost unchanged (Sheth et al., 2001). It is thus reasonable to expect that this will also be true for star formation. We have shown in Eq. (5.105) that the instability criteria for the density field ρ correspond in fact to sufficient conditions for collapse at small scales $R < h$ and to rather imprecise conditions that do not necessarily imply collapse at large scales (such that $\sigma(R) \ll \sigma(0)$). In any case, one should bear in mind that the dynamics of star formation is far more complex than in cosmology. For a statistical study of a large population of objects, the density threshold criterion must be regarded as a first approximation allowing progress.

A second step is the statistical counting of unstable regions at some scale, *i.e* such that their density exceeds the threshold derived in step 1. A source of error is the so-called cloud-in-cloud problem, which has been looked at in different ways. In the most advanced approach based on the excursion-set formalism (Hopkins, 2012a,b), the criterion that is adopted only yields a sufficient condition for collapse at small scales (see Eq. (5.105)). As a consequence, some unstable regions are likely overlooked in the counting.

The last step is a procedure to attribute a mass to each scale. The statistical procedure, which is borrowed from that for Gaussian fields, leads to lower bounds on mass estimates Eq. (5.109)), but this is probably taken over by the mass of the unstable regions that get overlooked in the counting.

In the end, the mass function that is obtained is that of unstable mass reservoirs which do not contain any smaller unstable ones and hence which are not prone to fragmentation. One last assumption is that the mass of an unstable reservoir is conserved during collapse and is entirely used up in the ensuing pre-stellar core, which glosses over complications inherent in the highly non-linear dynamics of gravo-turbulent collapse. All these assumptions should be regarded as shortcuts allowing a solution, however imperfect it may be, that is limited by our current level of understanding. *In the end*, they do lead to a Core Mass Function with the desired properties. The various assumptions that are made follow one another in a logical sequence and are intimately tied to one another, so that modifying a single one has consequences for all the others. Converting pre-stellar cores with mass $M_{\rm core}$ into stars with mass M_* with an efficiency factor such that $M_*/M_{\rm core} \simeq 30-50\%$, the CMF can be turned into an Initial Mass Function with the desired properties.

3.5 Additional potential flaws of these models.

Two other potential shortcomings have been identified. One is that the IMF can be derived from the CMF using a simple conversion factor for stars. The other is that the CMF is dictated by the physics of isothermal gravo-turbulent fragmentation. These shortcomings are mostly of concern for the low mass part of the IMF and for its peak value. The peak value is of particular importance because it shows that there is a characteristic value for the mass of newly formed stars.

3.5.1 Conversion of the CMF into the IMF

Turning the CMF into an IMF using a single conversion factor amounts to stating that a pre-stellar core does not fragment and collapses into a single star. Observations of star forming clouds show that, at large mass values, populations of pre-stellar cores define a CMF that is remarkably similar in shape to the stellar IMF (André et al., 2008; André et al., 2010). In the low mass end, the data fall below the completeness limit (defined above) and the CMF is ill defined. The theories of Hennebelle & Chabrier (2008) and Hopkins (2012a) both rely on the assumption of an isothermal thermodynamic path, which must break down for small scale structures with high density and low mass in bound structures. At large density, gas becomes opaque to its own radiation and heats up. Whether or not this affects the mapping of the CMF into the IMF has not been ascertained yet.

Resolving this issue may seem a simple matter to be tackled with numerical simulations. In practice, however, this turns out to be a formidable technical challenge. Isothermal turbulence is scale-free in the inertial domain (Frisch, 1995), implying that the proper dynamic range for the simulations is not well defined. To date, it has not been demonstrated that simulations of isothermal gravito-turbulent fragmentation lead to a distribution of point masses which does not depend on the numerical resolution (see e.g. Guszejnov et al. 2020 and reference therein). According to a majority of authors, the characteristic structures that are generated by isothermal turbulence are not singular points but singular filaments (Krumholz, 2014). Inutsuka & Miyama (1992) has carried out an analytical linear stability analysis of an isolated isothermal axisymmetric filament and shown that, under specific conditions, it collapses into a line of infinite density before it can fragment in smaller segments. It has thus been argued that numerical simulations produce unstable filaments down to the smallest scales they can handle and that a "sink particle" algorithm (see Chap. **1**) would act to break those filaments up into points at the grid scale (see e.g. Guszejnov et al. 2016, 2018a and reference therein). This would explain the non-convergence of the simulations. It is not clear whether the result of Inutsuka & Miyama (1992) applies only to the special case of an isolated isothermal axisymmetric filament, or that the lack of convergence is the real outcome of isothermal gravo-turbulent collapse. Faced with these issues, some authors have proposed that the fragmentation cascade is arrested when the gas begins to heat up, so that the characteristic star mass is determined by whatever physical process causing a deviation from isothermal conditions (see e.g. Guszejnov & Hopkins 2015). Alternatively, one may call on the presence of a magnetic field and the associated magnetic support (see e.g. Matzner & McKee 2000; Guszejnov et al. 2020).

In conclusion, one could argue that the CMF is well described by the models of Hennebelle & Chabrier (2008) and Hopkins (2012a,b) but that the IMF is not. The reason is that, if the physics behind the conversion of the CMF to the IMF are indeed that of isothermal gravo-turbulence, too many cores would fragment into smaller stellar objects resulting in too many low mass stars. Cores would sub-fragment indefinitely in self-similar fashion, which would explain the results of numerical simulations. In the end, this would imply that isothermal thermodynamic conditions and gravity alone can neither lead to a meaningful IMF nor account for the observed one.

3.5.2 Departures from lognormal statistics

Alternatively, Lee & Hennebelle (2018a) have argued that the CMF is not described correctly by the models of Hennebelle & Chabrier (2008) and Hopkins (2012a,b) on the grounds that numerical simulations of isothermal turbulent fragmentation do not lead to any characteristic core mass. They even relied on the Hennebelle & Chabrier (2008) model to explain why isothermal calculations do not converge to the proper mass spectrum. Their reasoning is the following. As explained in previous Chapters, as subregions collapse inside a cloud, the density field deviates from lognormal statistics and its PDF develops power-law tails. Lee & Hennebelle (2018a) then proceeded with the Hennebelle &

Chabrier (2008) model to count the unstable regions and determine the resulting MF at a time where the PDF has developed a power-law tail. To do so, they simply changed the PDF $f_{s(R)}(s_c(R))$ in Eq. (5.57) above:

$$n(M_c(R))\,M_c(R)\frac{\mathrm{d}M_c}{\mathrm{d}R} \;=\; \rho_c(R)f_{s(R)}(s_c(R))\left(-\frac{\mathrm{d}s_c}{\mathrm{d}R}\right). \tag{5.116}$$

These authors took a PDF of the following form:

$$f_{s(R)}(x) = C\exp\left(-\alpha x\right)\; \text{ at high } x, \tag{5.117}$$

and kept all the other steps in the derivation. In particular, they kept the same density threshold valid for the thermal regime (at short scale $R < \lambda_S$) (see Sec 3.2.6),

$$\rho_c(R) \simeq \overline{\rho}\tilde{R}^{-2} \text{ yielding,} \tag{5.118}$$

$$M(R) \propto R \propto \rho_c(R)^{-1/2}. \tag{5.119}$$

This gives for the following MF:

$$n(M)\,M \propto M^{-2}\,M^{2\alpha}M^{-1} = M^{-3+2\alpha}. \tag{5.120}$$

Hence, for $\alpha = 3/2$, as expected in late stages of collapse (see Chapter **4**),

$$n(M)\,M \propto M^{-3+2\alpha} = M^0, \text{ and } \; n(M) \propto M^{-1}. \tag{5.121}$$

This would explain why there is no characteristic mass in isothermal numerical simulations. As before, the characteristics of the IMF and even the CMF are determined by the process, or the processes, that causes a deviation from isothermal conditions. Recent studies have revived the idea that this is due to the tidal screening effect around the first (adiabatic) Larson core (Lee & Hennebelle, 2018b; Hennebelle et al., 2019; Colman & Teyssier, 2020)

The shortcomings that have been discussed in this section bear on the low mass part of the IMF and its peak. The peak is of special significance because it defines a characteristic mass for newly formed stars. In contrast, there is a general consensus on the high mass part of the IMF and it is widely accepted that the Salpeter power-law relationship is due to turbulence.

4 Perspectives and suggested explanations.

The models developed by Hennebelle & Chabrier (2008) and Hopkins (2012a,b) are relevant to the CMF and not directly to the IMF. The latter is simply deduced from the former with an efficiency conversion factor from core to star. This procedure glosses over the rather complex star formation processes (see *e.g.* Matzner & McKee 2000; Guszejnov & Hopkins 2015 for possible models) but no simple alternative is available at present. A more severe problem lies in the departure of the density statistics from lognormal ones and its impact on the CMF peak, as suggested by Lee & Hennebelle (2018a). We now address this issue.

4.1 Corrected barrier

Given the logical sequence of arguments that lead to the CMF, changing one assumption may affect the other ones. In a first step, a threshold density value must be specified. Taking a lognormal density distribution, Hennebelle & Chabrier (2008); Hopkins (2012a,b) combined the condition of virial equilibrium in an homogeneous *isolated* cloud with a phenomenological model of turbulence to arrive at a critical density value ρ_c in Eq. (5.38). This condition is not entirely rigorous as it accounts for neither a possible tri-axial collapse mechanism nor a possible initial cloud expansion. Further, it ignores the fact that, in a cloud, subregions are far from being isolated and are subjected to external tides. The final assumption, which states that the density and velocity fields are weakly correlated in isothermal "inertial" turbulence, has been shown to be sufficiently accurate by numerical simulations. In cosmological models, tidal forces enhance collapse in one direction at the expense of the other directions (Sheth et al., 2001; Shen et al., 2006). Smaller objects are particularly sensitive to external tides and must have a greater internal density to hold themselves together as they collapse. In cosmology, allowing for tri-axial collapse modifies quantitatively the low mass part of the MF and leaves the high mass part almost unaffected (Sheth et al., 2001). It is thus reasonable to assume that this will also be true for star formation. In the special case of initially lognormal turbulence statistics, this density threshold criterion serves as a first approximation that allows progress and does lead to a MF with the required characteristics.

There can be little doubt that (external) tidal forces tend to break the spherical symmetry of a collapsing structure because they generate shear stresses in relation to non radial (shearing) motions (see e.g. Sheth et al. 2001). In the initial conditions of isothermal inertial turbulence, the velocity field and its gradients are only weakly correlated to density (see Chapter **4**, Federrath & Banerjee 2015; Pan et al. 2019b):

$$\begin{aligned} \langle \mathcal{M} | \rho \rangle &\simeq \overline{\mathcal{M}}, && (5.122)\\ \langle \boldsymbol{\nabla}\cdot\boldsymbol{u} | \rho \rangle &\simeq \overline{\boldsymbol{\nabla}\cdot\boldsymbol{u}} = 0, && (5.123)\\ \left\langle (\boldsymbol{\nabla}\cdot\boldsymbol{u})^2 | \rho \right\rangle &\simeq \overline{(\boldsymbol{\nabla}\cdot\boldsymbol{u})^2}. && (5.124) \end{aligned}$$

Thus, one might argue that, in the initial phase of collapse, where conditions are close to those of isothermal inertial turbulence, external tidal forces can play a minor role. As collapse begins, however, this will probably no longer be true. The likely consequence is a decrease of the number of bound spherical structures in the low mass end of the spectrum. To understand why the result obtained by neglecting tidal forces is physically satisfactory, we return to the instability criterion. This criterion gives a threshold density $\rho_c(R)$ which increases with decreasing scale R and decreasing mass M (see Eq. (5.38)). In the conditions of initial inertial turbulence, bound objects at the low mass end of the spectrum emerge from the densest cloud region. These regions collapse on time scales related to their local free-fall times $\tau_{\mathrm{ff}}(\rho) \propto \rho^{-1/2}$, which are the smallest ones in the cloud. Therefore, these objets will probably have time, on average, to condense into spherical bound objects before external tides tear them apart. This explains why the original counting procedure of Hennebelle & Chabrier (2008); Hopkins (2012a,b) yields a satisfactory result, even though it still probably overestimates the number of bound objects at the low mass end of the spectrum.

If one now carries out the counting at a time when significant departures from lognormal turbulent conditions have set in, one must revise this assumption. We saw in in Chapter **4** that the transition from lognormal statistics to gravity-dominated statistics in high density regions occurs over the local free fall time scale $\tau_{\mathrm{ff}}(\rho)$. The presence of a high density PLT of exponent α in the density PDF is the signature of gravity-driven dynamics characterized by the following conditional expectation:

$$\langle \boldsymbol{\nabla}\cdot\boldsymbol{u} | \rho \rangle \propto \rho^{\alpha-1}. \tag{5.125}$$

This indicates that the dynamics of high density regions is governed by objects that are collapsing or have already collapsed. This implies that the environment of clump structures is completely different from the initial one. More precisely, external tidal forces must be large and probably tear small clumps apart before they can form bound objects. To properly account for these effects, one must study multi-dimensional random walks crossing a moving barrier. This would be much more difficult than in the cosmological case due to the pronounced non linearity of the physical effects involved. In the cosmological context, however, Sheth et al. (2001) have shown that choosing a suitable barrier accounting for the conditional expectation of the various quantities of interest knowing density ρ was sufficient to obtain an accurate MF.

We therefore do not plan, for now, to study properly the tri-axial collapse of objects subjected to external tides but limit ourselves to an illustration of the consequences with a simple toy model. To represent the effect of tidal shearing, the simplest approach is to modify the threshold density:

$$\rho_c(R) = a\frac{c_{\mathrm{s}}^2 + \frac{1}{3}\left\langle \boldsymbol{v}^2 \right\rangle_{\mathrm{cloud}}}{GR^2} \tag{5.126}$$

so that it takes into account the environments of clumps in high density regions. We then modify the averaged velocity $\left\langle \boldsymbol{v}^2 \right\rangle_{\mathrm{cloud}}$ at scale R and correlate it with density ρ, as expected for densities contributing to the PLT in the PDF. At short scale in the thermal regime (corresponding to high threshold densities), we use a dimensional argument to propose the following scaling:

$$\boxed{\frac{\frac{1}{3}\left\langle \boldsymbol{v}^2 \right\rangle_{\mathrm{cloud}}(\rho)}{R^2} = \frac{G\rho}{a} g(R) \propto \tau_{\mathrm{ff}}(\rho)^{-2},} \tag{5.127}$$

where $g(R)$ is some function of R. $\tau_{\mathrm{ff}}(\rho)^{-1}$ has the dimensions of a shearing rate and describes the impact of tidal shearing. This leads to a modified criterion at short scale:

$$\rho_c(R) = a\frac{c_{\mathrm{s}}^2}{GR^2} \times \frac{1}{1-g(R)}, \tag{5.128}$$

where we see that $g(R) \leq 1$, so that the threshold is properly defined because clumps cannot condense into bound spherical objects and get shredded by tidal forces if $g(R) \geq 1$. The mass associated to scale R is then:

$$M_c(R) = a\frac{c_{\mathrm{s}}^2}{G} \times \frac{R}{1-g(R)}. \tag{5.129}$$

To proceed with an analytical calculation, we give the following scaling to $g(R)$ at low R:

$$g(R) = 1 - \left(\frac{R}{R_0}\right)^{n_{\mathrm{turb}}} \tag{5.130}$$

where R_0 is some characteristic scale and n_{turb} is an exponent representing the smoothing of velocity profiles and shear deformation in turbulent flows, inspired by the study of pipe flows (see e.g. Cantwell 2019). We note that this is meant to produce some smoothing of the gradients of the average-velocity as observed in turbulent flows. The fact that $g(R) \to 1$ when $R \to 0$ leads to a drastic increase of the threshold value. We obtain:

$$\rho_c(R) = a\frac{c_{\mathrm{s}}^2}{GR_0^2}\left(\frac{R}{R_0}\right)^{-2-n_{\mathrm{turb}}}, \tag{5.131}$$

$$M_c(R) = a\frac{c_{\mathrm{s}}^2 R_0}{G}\left(\frac{R}{R_0}\right)^{1-n_{\mathrm{turb}}}. \tag{5.132}$$

To obtain a one to one correspondence between mass and scale R, *i.e* for the procedure to be meaningful, $n_{\mathrm{turb}} < 1$. This gives the following scaling at low mass values:

$$\boxed{Mn(M) \propto M^{\frac{3n_{\mathrm{turb}}}{2(1-n_{\mathrm{turb}})}}.} \tag{5.133}$$

This toy model results in a decrease of the number of bound objects at the small mass end of the spectrum. To take into account the effects of turbulent motions at high scale and mass, we then simply use the following form

$$\frac{\frac{1}{3}\left\langle \boldsymbol{v}^2 \right\rangle_{\rm cloud}(\rho)}{R^2} = \frac{G\rho}{a}\exp\left(-\left(\frac{R}{R_0}\right)^{n_{\rm turb}}\right) + \frac{\frac{1}{3}V_0^2\left(\frac{R}{l_0}\right)^{2\eta}}{R^2}. \tag{5.134}$$

The tidal shearing effect is then naturally attenuated at scales larger than R_0. We note that $n_{\rm turb} = 0$ corresponds to a case with no tidal shearing (see, e.g. Eq. (5.131)).

To illustrate how these modifications affect the CMF, we have carried out the calculation of Lee & Hennebelle (2018a) with the procedure of Hennebelle & Chabrier (2008) for a PDF with the functional form presented in Chapter **2**:

$$\begin{aligned} f_s(s_0) &= A_1\, e^{-\frac{(s_0-\mu)^2}{2\sigma_s^2}}, \; s_0 \leq s_{\rm crit}, \\ &= A_2\, e^{-\alpha_s(s_0-s_{\rm crit})}, \; s_0 \geq s_{\rm crit}. \end{aligned} \tag{5.135}$$

where A_1 and A_2 are two coefficients to be determined. Normalizing f and enforcing continuity as well as the necessary condition $\overline{e^s} = 1$ (from the definition of s), we obtain:

$$A_1 = A_2\, e^{\frac{(s_{\rm crit}-\mu)^2}{2\sigma_s^2}} \tag{5.136}$$

$$1 = \frac{1}{2}A_1\sqrt{2\pi\sigma_s^2}\left[1+{\rm erf}\left(\frac{s_{\rm crit}-\mu}{\sqrt{2}\sigma_s}\right)\right] + \frac{A_2}{\alpha_s} \tag{5.137}$$

$$\begin{aligned} 1 &= A_1\sqrt{\frac{\pi}{2}\sigma_s^2}\, e^{\mu+\frac{\sigma_s^2}{2}}\left[1+{\rm erf}\left(\frac{s_{\rm crit}-\mu-\sigma_s^2}{\sqrt{2}\sigma_s}\right)\right] \\ &\quad + \frac{A_2\, e^{s_{\rm crit}}}{\alpha_s - 1}. \end{aligned} \tag{5.138}$$

Knowing $s_{\rm crit}$ and σ_s, the above equation allows one to calculate A_1, A_2 and μ. In this procedure, parameter μ, which determines the peak of the lognormal part of the distribution, is shifted to lower density values to ensure that $\overline{e^s} = 1$. This functional form is only continuous but allows an analytical determination of parameters A_1, A_2 and μ. For sake of simplicity, we simply ignore the running of the variance $\sigma(R)$ with R. Now, to calculate the CMF in addition to the cloud properties, we need to specify $s_{\rm crit}$, R_0 and $n_{\rm turb}$. The cloud has radius $R_c = 10$ pc, an average number density $\overline{n} = 100$ cc^{-1} and an average Mach number $\mathcal{M} = 10$. We then choose 6 different transition values $s_{\rm crit} = \mu + n_{\rm crit}\sigma_s$ with $n_{\rm crit} = 1, 2, 3, 4, 5, 6$. $n_{\rm turb}$ is set at a value of 0.7 for illustration purposes and the value R_0 is chosen so that $\ln(\rho_c(R_0)/\overline{\rho}) = s_{\rm crit}$ when there is no tidal shearing ($n_{\rm turb} = 0$). Finally we take $a = 1/4\pi$ in the instability criterion.

The CMFs that are obtained with and without shearing with our simple toy model are displayed on Fig. 5.5. Here, the CMF is multiplied by the cloud volume $V_{\rm cloud}$, so that it gives the expected average number of objects generated in the cloud per mass interval. The modified CMF corresponds to the mass function for unstable reservoirs that have not collapsed yet at some time t when the PDF has developed a PLT until $s = s_{\rm crit}$. In a way, these CMFs track changes of the mass distribution of available unstable reservoirs, *i.e* that have not collapsed yet at time $t(s_{\rm crit})$. A given $s_{\rm crit}$ value corresponds to time $t \sim \tau_{\rm ff}(s_{\rm crit})$. In practice, $s_{\rm crit}$ is expected to saturate at some value s_G (see Chapter **4**), which corresponds to $n_{\rm crit} \simeq 2.5 - 3$ for the present cloud. Furthermore, from this perspective on the time evolution, we see that the majority of small mass bound objects are produced early on ($n_{\rm crit} \gg 1$), when tidal effects do not affect the dynamics significantly. Ultimately, of course, changes of the gas thermodynamic path will kick in and further impede the fragmentation of small mass objects, but it

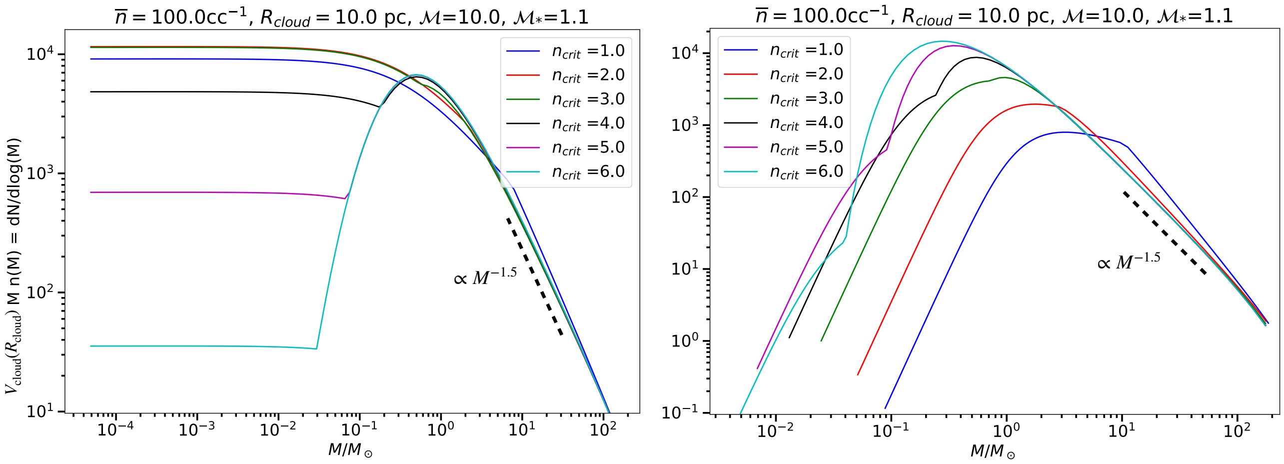

FIGURE 5.5 CMF calculated with a PDF exhibiting a PLT of exponent $\alpha_s = 3/2$. The CMF giving the number of objects per unit volume and per mass interval is multiplied here by the cloud volume $V_{\rm cloud}$. Left: Without shearing effects. Right: With shearing effects ($n_{\rm turb} = 0.7$). The inclusion of shearing reduces significantly the number of objects at the low mass end of the spectrum.

may well be that this only leads to some minor correction to the peak mass of the CMF.

Before going any further, we must bear in mind that the model developed above to account for tidal shearing is a simple toy model. It was only built to illustrate the fact that the density barrier ρ_c, and other assumptions in the derivation of the CMF must be consistent with the physical processes at work in collapsing cloud regions. Thus, the CMFs that have been calculated are only meant to be illustrative examples. In fact, before calculating such CMFs, one should completely revise the second step in the derivation of the CMF, which deals with the statistical counting of over-dense region. We now discuss how such a change of ρ statistics affects counting.

4.2 Meaning of the counting procedure for non Gaussian and non lognormal fields

As we mentioned, as gravity takes over in a collapsing region, the density field deviates from the lognormal statistics that prevailed initially. The PDF then exhibits a power-law tail at high density and the logarithmic density field s is certainly no longer Gaussian. Thus, before simply changing the PDF $f_{s(R)}(s_c(R))$ in Eq. (5.57), one must first revisit the other assumptions in the derivation of the MF.

As shown in the lognormal example studied by Hennebelle & Chabrier (2008) and Hopkins (2012a,b), the Press-Schechter (PS) approach relies on the assumption of gaussian fields, as revealed by the excursion-set formalism. The calculation made for the lognormal field $\rho = \overline{\rho}\exp(s)$ by Hennebelle & Chabrier (2008) was retrieved in the excursion set calculation performed on Gaussian field s by Hopkins (2012a,b). As shown before, the proper procedure consists in smoothing the Gaussian field at various scales to obtain the last crossing distribution. Only then can the mapping onto the density field ρ be performed to obtain a MF which is identical to that of the PS procedure, at least for small low masses. The excursion-set formalism clarifies the relevance of the Press-Schechter approach and strongly suggests that it relies on the assumption that the density field ρ can be mapped onto a gaussian field ξ with no loss of substance.

In fact the Gaussian condition can be traced back to the assumption that the functional form of the smoothed density PDF remains the same for all window functions. In the original calculation of Hennebelle & Chabrier (2008), this corresponds to the assumption that ρ_R remains lognormal for all R. With this assumption, only the variance (and average) of the smoothed density field is needed to obtain its PDF. However, this is only valid for Gaussian fields. Instead of this strong assumption, one can just assume that s is Gaussian and perform the calculation with s, as in the excursion-set method.

We assume that the PDF of the unfiltered logarithmic density field s has a lognormal part at low densities and a power-law tail at high densities. It is not at all clear what the PDFs of the smoothed density field ρ or its logarithm s would be. Lee & Hennebelle (2018a) have not addressed this issue and simply assumed that the PDF keeps the same functional form. As for the lognormal case, we can guess that the proper assumption is that s (or ρ) can be mapped into a Gaussian field ξ:

$$s = \Psi(\xi). \tag{5.139}$$

where Ψ is some deterministic function. As seen from Chapter **3**, the PDF of s and ξ are then related to each other by:

$$f_s(s_0) = \frac{f_\xi(\xi_0)}{|(\Psi^{-1})'(s_0)|} \tag{5.140}$$

where $\xi_0 = \Psi^{-1}(s_0)$ (Papoulis & Pillai, 1965). With no loss of generality, we can further assume that the ξ field is centered with unit variance. Then, since f_s and f_ξ are known, we can obtain Ψ^{-1} (and then Ψ) by solving the following differential equation:

$$|(\psi^{-1})'(s_0)| = \frac{f_\xi((\psi^{-1})(s_0))}{f_s(s_0)}. \tag{5.141}$$

If we further assume that Ψ is an increasing diffeomorphism $(\psi^{-1})' \geq 0$, we find that:

$$\xi_0 = \Psi^{-1}(s_0) = \sqrt{2}\,\mathrm{erf}^{-1}\left(-1 + 2\int_{\infty}^{s_0} f_s(x)\,\mathrm{d}x\right), \tag{5.142}$$

where erf^{-1} is the inverse of the error function. In cases such that s is already Gaussian with a non zero expectation $\overline{s}$ and variance σ_s^2, this simply reduces to:

$$\xi_0 = \frac{s_0 - \overline{s}}{\sigma_s}. \tag{5.143}$$

In order to prove that the proper assumption for the Lee & Hennebelle (2018a) calculation is that s (or ρ) is mapped to a Gaussian field ξ, we must carry out the correct excursion-set calculation and compare the results of the two calculations. This will provide some additional insight into the significance of the calculation.

4.2.1 Deterministic function of a Gaussian field

As explained in the study of the excursion-set approach of Hopkins (2012a,b), one must deal with the ξ field. Barrier $B_\rho(R)$ then corresponds to the following barrier:

$$B_s(R) = \ln\left(\frac{B_\rho(R)}{\overline{\rho}}\right) \text{ and } B_\xi(R) = \Psi^{-1}\left(B_s(R)\right). \tag{5.144}$$

For the lognormal case, we saw that, after smoothing, we only had:

$$\rho_R \equiv \rho * W_R > \overline{\rho}e^{s_R} \equiv \overline{\rho}e^{s * W_R}, \tag{5.145}$$

because $s * W_R \neq \ln(\rho/\overline{\rho} * W_R)$ and because the exponential is convex. This would turn the instability criterion into only a sufficient criterion. Here, the situation is a bit more complicated as we have:

$$\rho = \exp\left(\Psi(\xi)\right). \tag{5.146}$$

We therefore need to determine whether or not Ψ is convex and what the new instability criterion is. To do so, we use the functional form used in Chapter **2**:

$$\begin{aligned} f_s(s_0) &= A_1\, e^{-\frac{(s_0-\mu)^2}{2\sigma_s^2}},\ s_0 \leq s_{\rm crit}, \\ &= A_2\, e^{-\alpha_s(s_0-s_{\rm crit})},\ s_0 \geq s_{\rm crit}. \end{aligned} \tag{5.147}$$

As mentioned earlier, this functional form is only continuous but allows an analytical determination of parameters A_1, A_2 and μ, as well as, most importantly, Ψ^{-1}. We obtain:

$$\begin{aligned} \Psi^{-1}(s_0) &= \sqrt{2}\,\mathrm{erf}^{-1}\left(-1 + A_1\sqrt{2\pi}\sigma_s\left[1+\mathrm{erf}\left(\frac{s_0-\mu}{\sqrt{2}\sigma_s}\right)\right]\right),\ s_0 \leq s_{\rm crit}, \qquad (5.148) \\ &= \sqrt{2}\,\mathrm{erf}^{-1}\left(-1 + A_1\sqrt{2\pi}\sigma_s\left[1+\mathrm{erf}\left(\frac{s_{\rm crit}-\mu}{\sqrt{2}\sigma_s}\right)\right] + \frac{2A_2}{\alpha_s}\left[1-e^{\alpha_s(s_{\rm crit}-s_0)}\right]\right),\ s_0 \geq s_{\rm crit}. \end{aligned}$$

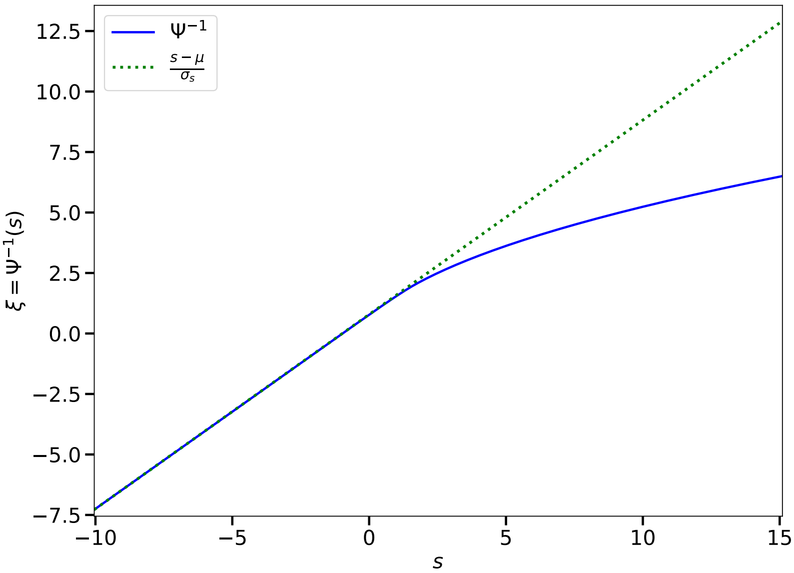

FIGURE 5.6 In blue: $\Psi^{-1}(s)$ for the specific choice of parameters $(\mu, \sigma_s, s_{\rm crit}) = (-0.98, 1.245, 1.73)$. The line corresponding to equation $\xi = (s-\mu)/\sigma_s$ is shown in green. We see that $\Psi^{-1}(s)$ is concave.

We display in Fig. 5.6 Ψ^{-1} for the specific choice of parameters $(\mu, \sigma_s, s_{\rm crit}) = (-0.98, 1.245, 1.73)$ (describing the Orion B cloud, see Chapter **4**). We see that Ψ^{-1} is concave and hence that Ψ is convex (the graphs of Ψ and Ψ^{-1} are symmetric with respect to the $y = x$ axis). We can then apply the Jensen inequality to function $\exp(\Psi)$ and obtain:

$$\boxed{\rho_R > \exp(\Psi(\xi_R)).} \tag{5.149}$$

This is reassuring because, if ξ_R is above threshold $B_\xi(R)$, then $\rho_R > B_\rho(R)$ and we can be sure that the region is unstable at scale R. This ensures that every region counted is indeed unstable, but this does not guarantee that all unstable regions are accounted for.

Now that we have shown that the mapping of ρ onto ξ does not invalidate the instability criterion, we can use the excursion-set procedure and find out whether or not it retrieves the counting of Lee & Hennebelle (2018a). The Volterra equation for the last crossing distribution is the same as the one above, and we expect to find the same MF as Lee & Hennebelle (2018a), which was obtained by the PS procedure. We plan to test this in order to understand the actual meaning of the counting procedures and the resulting CMF. This work is still in progress at the time of writing and is thus not presented here.

5 Conclusion

We have given an in-depth review of the models of Hennebelle & Chabrier (2008) and Hopkins (2012a,b) for the CMF and IMF, and examined all their steps and assumptions carefully. This was intended to provide a clear understanding of what must be done when new information becomes available and requires an updating of the assumptions. We have also identified issues that should be addressed to improve these models.

One shortcoming of these models is that they generate a CMF and then, in order to obtain the IMF, rely on a simple universal mapping that ties each core of mass $M_{\rm core}$ to a star of mass M_* through an efficiency factor such that $M_*/M_{\rm core} \simeq 30 - 50\%$. An analysis of how to turn the CMF into the IMF is beyond the scope of these models, all the more as the physical processes involved remain ill determined (see e.g. Matzner & McKee 2000; Guszejnov & Hopkins 2015 for possible models). If the CMF is predicted accurately, these models have served their purpose even if some additional physics is needed to specify the appropriate conversion to the IMF. For lack of time, we have not investigated how a pre-stellar core becomes a star, although this is obviously a fundamental and critical question.

Some authors have argued that these models do not even predict a correct CMF. Lee & Hennebelle (2018a), for example, have concluded that departures from a lognormal density distribution lead to an overprediction of the number of low mass objects. Thus, the models would probably miss out on what really sets the CMF peak and, by way of consequence, the IMF peak as well. We have addressed this key issue only partially in this chapter and more work needs to be done.

We have first shown that, in order to properly describe the MF of unstable mass reservoirs as the density field departs from lognormal statistics, one must first revise the instability criterion proposed by Hennebelle & Chabrier (2008) and Hopkins (2012a,b). There is little doubt that the initial conditions of star formation are indeed those of isothermal turbulence with lognormal statistics, but changes of density statistics are observed in mature clouds where small and dense regions are beginning to collapse (see Chapter **4**). These changes have been attributed to the growing influence of gravity. In these conditions, tidal forces that have been ignored can no longer be neglected and induce a drastic reduction of the number of spherical bound objects. We have developed a simple toy model to illustrate the impact of tidal shear deformation on the instability criterion and changed it accordingly. The CMF that is calculated corresponds to unstable reservoirs that have not collapsed yet at time t when the PDF has developed a PLT until $s = s_{\rm crit}$. To a given $s_{\rm crit}$ corresponds a time $t \sim \tau_{\rm ff}(s_{\rm crit})$. CMFs therefore track the time evolution of unstable reservoirs that have not collapsed yet. With this perspective on the time evolution of a cloud, we find that the majority of small mass bound objects are generated in initial stages ($n_{\rm crit} \gg 1$), when tidal forces are still minor contributors to collapse dynamics. Ultimately, of course, changes in the thermodynamic path of the gas will impede further the fragmentation of small mass objects, but it is not obvious that they will affect the peak mass of the CMF.

Finally, we have discussed the counting procedure that leads to a CMF. With a density field that is not lognormal, the PS counting procedure may no longer be adequate. We have given some clues on how to explore this issue and also on how to perform an adequate counting.

One way to address these questions has emerged from recent numerical simulations. In a recent article on the accuracy of calculated IMFs, Guszejnov et al. (2020) have used a different sink particle algorithm than in their previous work (Guszejnov et al., 2018a). In their earlier study, they had not been able to achieve convergence of the numerical IMF in isothermal simulations and had found that too many low mass objects were generated. Their modified sink particle algorithm did not seem to improve matters but, in an erratum, Guszejnov et al. (2021) explained that it had not been initialized properly. With a proper implementation of that algorithm, they found that "the population of low-mass sink particles is drastically reduced". Surprisingly, there is no consensus on the proper sink algorithm and different groups use different ones (see e.g. Bleuler & Teyssier 2014; Grudić et al. 2020 and reference therein). As of today, there has been no benchmark for the behaviour of sink particles in highly complex and turbulent environments, which is regrettable because this is clearly a key component of all simulations. One should make sure that the algorithms enforce not only necessary conditions for collapse but also sufficient ones. If an algorithm relies on necessary conditions only (such as virial equilibrium for example), many objects that in fact may not collapse in the three directions are artificially turned into sink particles. In that case, the output of a simulation, and in particular the statistics of sink particles, should be taken with due caution.

Appendix

A A Volterra equation of the second kind for the first crossing distribution.

We detail here the derivation of the Volterra equation of the second kind obtained by Zhang & Hui (2006) and presented in Sec. 2.3.5. We first recall that the first crossing distribution $f_{\mathrm{f}}(S)$ is such that the probability that a random walk starting from $\gamma = 0$ at $S = 0$ crosses barrier $\gamma_c(S)$ for the *first* time between S and $S + \mathrm{d}S$ is $f_{\mathrm{f}}(S)\mathrm{d}S$.

A.1 Probability that a trajectory has never crossed the barrier at resolution S

One introduces the probability, $\Pi(x, S)\mathrm{d}x$, that a trajectory (starting from $\gamma = 0$ at $S = 0$) is at position $\gamma \in [x, x + \mathrm{d}x[$ at resolution (pseudo-time) S, without having ever crossed the barrier $\gamma_c(S')$ at smaller resolution $S' < S$. Since the random walk either crosses the barrier before S or passes through point (S, γ) where $\gamma < \gamma_c(S)$, one has:

$$1 = \int_0^S f_{\mathrm{f}}(S)\mathrm{d}S + \int_{-\infty}^{\gamma_c(S)} \Pi(x, S)\mathrm{d}x. \tag{5.150}$$

The first term on the r.h.s. accounts for the probability that a trajectory has crossed the barrier for the first time between $S = 0$ and S. The second term of the r.h.s. accounts for the probability that a trajectory has position γ in $]-\infty, \gamma_c(S)[$ at time S without having ever crossed the barrier.

Without considering the problem of the barrier, the probability that a trajectory (starting from $\gamma = 0$ at $S = 0$) is at a position $\gamma \in [x, x + \mathrm{d}x[$ at resolution (pseudo-time) S, $\Pi_{\mathrm{nb}}(x, S)\mathrm{d}x$ is simply given by

$$\Pi_{\mathrm{nb}}(x, S) = \frac{1}{\sqrt{2\pi S}} \exp\left(-\frac{x^2}{2S}\right), \tag{5.151}$$

where we recall that $S = \sigma(R)^2$ is the variance of the smoothed Gaussian density contrast at scale R. Then, for a trajectory to be at position $\gamma \in [x, x + \mathrm{d}x[$ at resolution S, either event (E_1) {the walk has never crossed the barrier before}, or event (E_2) {the walk has crossed the barrier for the first time at resolution $S' < S$ and then reached position γ at resolution (time) S} occur. These two events are mutually exclusive so that:

$$\Pi_{\mathrm{nb}}(x,S)\mathrm{d}x=\mathbb{P}(E_1)+\mathbb{P}(E_2),\ \text{with}\ \mathbb{P}(E_1)=\Pi(x,S)\mathrm{d}x. \tag{5.152}$$

To derive $\mathbb{P}(E_2)$, one must first study event $(\mathrm{d}E_2)$: {a trajectory crosses the barrier for the first time at resolution $S\in[S',S'+\mathrm{d}\ S'[$ and then reaches position $\gamma\in[x,x+\mathrm{d}x[$ at resolution S}. This event is the intersection of events (see Chap. **1**) $(\mathrm{d}E_2^{(1)})$: {The trajectory crosses the barrier for the first time at resolution $S\in[S',S'+\mathrm{d}\ S'[$} and $(\mathrm{d}E_2^{(2)})$: {The trajectory arrives to $\gamma\in[x,x+\mathrm{d}x[$ at resolution S after starting at $\gamma_c(S')$ at S'}.

A.1.1 Conditional probability of arriving at $\gamma\in[x,x+\mathrm{d}x[$ knowing that the trajectory started at x'

To study event $(\mathrm{d}E_2^{(2)})$, one must go back to the construction of random walks in the excursion-set formalism. A trajectory is built by looking at the different values of the smoothed density contrast $\gamma(\boldsymbol{x},R(S))$ as resolution $S(R)$ is increased (decreasing radius $R(S)$). Starting from $S=0$ $(R=\infty)$ at $\gamma=0$, the trajectory then wanders around in the $S-\gamma$ plane as pseudo-time S increases. The trajectory describes a random walk. The step covered by the random walk attached to $\boldsymbol{x}$ between two different resolutions $S_1(R_1)<S_2(R_2)$ (corresponding to $R_2<R_1$), $\Delta\gamma_{1,2}$, is given by:

$$\Delta\gamma_{1,2}=\frac{1}{(2\pi)^{3/2}}\int\hat{\gamma}(\boldsymbol{k})\left(\hat{W}_{R_2}(\boldsymbol{k})-\hat{W}_{R_1}(\boldsymbol{k})\right)e^{i\boldsymbol{k}\cdot\boldsymbol{x}}\mathrm{d}\boldsymbol{k}. \tag{5.153}$$

Considering all the random walks attached to each position $\boldsymbol{x}$, step $\Delta\gamma_{1,2}$ appears as a centered Gaussian variable with the following variance:

$$\mathrm{Var}\left(\Delta\gamma_{1,2}\right)=\int\mathcal{P}_\gamma(\boldsymbol{k})\left|\hat{W}_{R_2}(\boldsymbol{k})-\hat{W}_{R_1}(\boldsymbol{k})\right|^2\mathrm{d}\ \boldsymbol{k}. \tag{5.154}$$

Moreover, in general, for a given random walk, the random step $\Delta\gamma_{1,2}$ is correlated to the position of the random walk at resolution S_1, $\gamma(\boldsymbol{x},S_1)$, and its correlation is given by Eq.5.23 which is worth repeating here:

$$\mathbb{E}\left(\Delta\gamma_{1,2}\,\gamma(\boldsymbol{x},S_1)\right)\ =\ \frac{1}{(2\pi)^{3/2}}\int\mathcal{P}_\gamma(\boldsymbol{k})\left(\hat{W}_{R_n}(\boldsymbol{k})-\hat{W}_{R_{n-1}}(\boldsymbol{k})\right)\hat{W}_{R_{n-1}}(\boldsymbol{k})e^{2\,i\boldsymbol{k}\cdot\boldsymbol{x}}\mathrm{d}\boldsymbol{k}. \tag{5.155}$$

Different steps of the random walk are therefore correlated in a manner that depends on the filter function W_R. However, for the *specific* case of the sharp k-space filter W^{sks}, this correlation vanishes and the steps are uncorrelated. This means that the conditional probability that the trajectory is at position $\gamma\in[x_2,x_2+\mathrm{d}x[$ at resolution S_2 knowing that it was a position $\gamma=x_1$ at S_1, $P_{1,2}\left(x_2,S_2;x_1,S_1\right)\mathrm{d}x$, with $P_{1,2}\left(x_2,S_2;x_1,S_1\right)$ the associated conditional density function (see Chap. **1**), is simply given by

$$P_{1,2}\left(x_2,S_2;x_1,S_1\right)=\frac{1}{\sqrt{2\pi\mathrm{Var}\left(\Delta\gamma_{1,2}\right)}}\exp\left(-\frac{(x_2-x_1)^2}{2\mathrm{Var}\left(\Delta\gamma_{1,2}\right)}\right)=\frac{1}{\sqrt{2\pi(S_2-S_1)}}\exp\left(-\frac{(x_2-x_1)^2}{2(S_2-S_1)}\right). \tag{5.156}$$

A.1.2 Probability $\Pi(x,S)$ for the sharp $\boldsymbol{k}$-space filter

For the special case of the sharp k-space filter and only for this filter, events $(\mathrm{d}E_2^{(1)})$ and $(\mathrm{d}E_2^{(2)})$ are independent, so that:

$$\mathbb{P}\left((\mathrm{d}E_2)\right)\ =\ \mathbb{P}\left((\mathrm{d}E_2^{(1)})\cap(\mathrm{d}E_2^{(2)})\right)=\mathbb{P}\left((\mathrm{d}E_2^{(1)})\right)\mathbb{P}\left((\mathrm{d}E_2^{(2)})\right),$$

$$= \quad f_{\mathrm{f}}(S')\, P_{1,2}\left(x, S; x' = \gamma_c(S'), S'\right) \mathrm{d}x \mathrm{d}S'. \tag{5.157}$$

We are then able to obtain the probability $\mathbb{P}(E_2)$ from $\mathbb{P}\left((\mathrm{d}E_2)\right)$:

$$\mathbb{P}(E_2) = \int_0^S f_{\mathrm{f}}(S')\, P_{1,2}\left(x, S; x' = \gamma_c(S'), S'\right) \mathrm{d}S'\, \mathrm{d}x. \tag{5.158}$$

This finally yields, from Eq. 5.152 :

$$\Pi(x, S) = \Pi_{\mathrm{nb}}(x, S) - \int_0^S f_{\mathrm{f}}(S')\, P_{1,2}\left(x, S; x' = \gamma_c(S'), S'\right) \mathrm{d}S'. \tag{5.159}$$

A.2 The sharp *k*-space filter and the Volterra equation for the first crossing distribution

Using the sharp k-space filter, one derives the two equations 5.150 and 5.159 repeated here :

$$\begin{aligned} 1 &= \int_0^S f_{\mathrm{f}}(S)\mathrm{d}S + \int_{-\infty}^{\gamma_c(S)} \Pi(x, S)\mathrm{d}x \\ \Pi(x, S) &= \Pi_{\mathrm{nb}}(x, S) - \int_0^S f_{\mathrm{f}}(S')\, P_{1,2}\left(x, S; x' = \gamma_c(S'), S'\right) \mathrm{d}S'. \end{aligned}$$

Deriving Eq. 5.150 with respect to S and then injecting Eq. 5.159 in it, we obtain, after some algebra, the following equation:

$$f_{\mathrm{f}}(S) = g_1(S) + \int_0^S f_{\mathrm{f}}(S')g_2(S, S')\mathrm{d}S', \tag{5.160}$$

where

$$g_1(S) = \left(\frac{\gamma_c(S)}{S} - 2\frac{\mathrm{d}\gamma_c(S)}{\mathrm{d}S}\right) \frac{1}{\sqrt{2\pi S}} \exp\left(-\frac{\gamma_c(S)^2}{2S}\right), \tag{5.161}$$

$$g_2(S, S') = \left(2\frac{\mathrm{d}\gamma_c(S)}{\mathrm{d}S} - \frac{\gamma_c(S) - \gamma_c(S')}{S - S'}\right) \frac{1}{\sqrt{2\pi(S - S')}} \exp\left(-\frac{(\gamma_c(S) - \gamma_c(S'))^2}{2(S - S')}\right). \tag{5.162}$$

This equation is called the Volterra equation of the second kind and has, in general, a unique solution. For a barrier linear in S, *i.e.* $\gamma_c(S) = a + bS$, this equation has the following closed-form solution:

$$f_{\mathrm{f}}(S) = \frac{a}{S\sqrt{2\pi S}} \exp\left(-\frac{\gamma_c(S)^2}{2S}\right), \tag{5.163}$$

which is exactly Eq. 5.25 for $b = 0$.

A.3 Key ingredients

To obtain the Voltera equation of the second kind, we used the properties of the sharp k-space filter, which generates an uncorrelated (Brownian) random walk. Attempts to obtain this equation with other filters are likely to fail, as the properties of uncorrelated walks are used extensively in the derivation.

Conclusion

In this PhD thesis, I presented my work on the study of the statistics of astrophysical flows and their evolution. It is hoped that this thesis is one step toward a description of the statistics of random (turbulent) fluid motions under the influence of gravity. In one sense, this work connects formalisms that have been developed in the distinct fields of turbulence and cosmology. In another sense, it is aimed at improving our understanding of the role played by turbulent structures in the star formation process. It is focussed on the statistics of density and velocity in molecular clouds and more specifically on how they evolve with time. On the one hand, it leads to new tools for studying and describing the statistics of astrophysical flows which should be useful to both observers and numerical specialists. On the other hand, it aims to improve our understanding of the evolution of the statistics of velocity and density fields and to develop a new approach on how gravitational collapse gets initiated and proceeds in dense Molecular Clouds. We will now present a short summary of its content

Summary

In Chapter **1** we presented relevant tools used throughout this thesis. More precisely we introduced various statistical quantities useful to describe stochastic fields such as the density field in molecular clouds. We defined the Probability Density Function (PDF), Auto-covariance function (ACF), and correlation length of the density field. The correlation length represent the average size of most correlated structures in the flow.

In Chapter **2** we have studied the statistics of the observed column-density fields and the information on the underlying density field that can be obtained from such observations. In this chapter, we first noted that the statistics of the column-density field are affected by systematic biases due to integration effects along the line of sight. Specifically, these effects are likely to generate large scale gradients in the column density field which may therefore appear to be statistically heterogeneous. They are also responsible for anisotropy in the ACFs. We have then shown that, provided that these biases are avoided, the correlation length of the column density field which is calculated from its ACF allows the determination of the correlation length of the underlying density field. In a next step, we have developed a method to derive the correlation length, or more exactly the ratio of the correlation length over the size of the cloud (or the box for numerical simulations), from the variances of the density and column-density fields (Sec. 2.2). Finally, we have proposed a strategy to derive the (volume) density PDF from the column density PDF in Sec. 3. We were then equipped with a set of statistical tools to study the statistics of star forming clouds and to assess whether a statistical approach based on ergodicity is relevant.

In Chapter **3**, we have examined the validity of statistical homogeneity and ergodicity when deriving general properties of star-forming molecular clouds from observations or numerical results of some of their properties. Notably we focused on the field of density fluctuations and its PDF. This is a fundamental question since these fluctuations are believed to be at the root of the star formation process. It is thus essential to examine the validity of a statistical approach in order to assess the accuracy of the determination of the statistical properties of the cloud from the observations or simulations of a limited number of samples. To fulfill this goal, we first use the ergodic theory for any random field X to derive some rigorous statistical results. We show that the estimation of the correlation length allows one to define an effective number of samples, N, such that a space (or time) average of a single realisation is formally equivalent to averaging over N independent samples. When it is difficult to determine the correlation length, we have shown how it can still be estimated by performing several identical trials in Sec. 2.2.

We then apply this statistical approach and the results of ergodic theory to astrophysical systems characterized by a field of density fluctuations, which may be used in cosmology for the formation of structures and in star-forming clouds for star formation. Focussing on the latter, we apply our results to the observed column-density field, which is related to the (volume) density field in the cloud. Using the results of Chapter **2**, we have devised a method to determine the correlation length, or more exactly the ratio of the correlation length over the size of the cloud (or the box of numerical simulations), from the variances of both the density and column-density fields. Estimating the variance of the underlying density field, $\mathrm{Var}\left(\rho/\left<\rho\right>\right)$, and computing the variance of the column-density field, $\mathrm{Var}\left(\Sigma/\left<\Sigma\right>\right)$, we are able to derive an estimate of the correlation length l_c. The statistics of the PDF ergodic estimator for positive column-density contrasts enables us to get rid of most of the integration anisotropy bias. It also allows a proper evaluation of statistical error bars and shows that these (i) can *not* be derived from simple Poisson statistics and (ii) become increasingly large for increasing density contrasts ($|\eta| \geq 1$), severely reducing the accuracy of the high end part of the PDF because of the small sample size (see Sec. 4.3.2). We provide a method that can be used by observers and numerical simulation specialists to determine approximate, but robust, error bars in Sec. 4.3.3.

We have examined in detail the Polaris cloud, which serves as a template for initial stages of star formation in MCs. Using the data available, we have calculated the density ACF and correlation length in this cloud and show that the latter is of about $\sim$1% of the size of the cloud ($l_c(\rho)/R \sim 10^{-2}$). We have also examined the more complex Orion B cloud to confirm result obtained on Polaris.

In a next section, we have applied the same statistical formalism to the determination of the total gravitational energy and virial parameter of the cloud. We have demonstrated that the contribution of the (undetermined) internal structure of the clouds has only a small impact on these determinations. The cloud's gravitational energy and virial parameter can thus be safely estimated from the observed total mass and size, with no knowledge of its internal structure. This is an important result because the virial parameter determines the dynamics of a cloud, equilibrium, expansion or gravitational contraction.

Examining the same problem in a tore geometrical configuration, which is characteristic of numerical simulations in a periodic box, we have shown that, in contrast to the real space, only the inner structure of the density fluctuations in the box contributes to the determination of the gravitational potential and the virial parameter. In that case, the (dominant) average contribution is indeed absent, a consequence of the ill-posed problem of solving the Poisson equation in $\mathbb{T}^3$. This explains the puzzling large discrepancy found in Federrath & Klessen (2012, 2013) between the gravitational potential and virial parameter values inferred from the global characteristics of the simulation box and those that are inferred from the numerical results.

These calculations provided a rigorous framework for analyses of the global properties of star-forming clouds from limited statistical observations of their density and surface properties. Moreover this framework is a powerful tool to explore the general statistical properties of star-forming molecular clouds from a limited number of data. In particular, this may be applied to determinations of the global gravitational energy and virial parameter, thus the magnitude of binding in the cloud. Finally these calculations show that *for typical star-forming clouds at the onset of the star formation process, the correlation length of density fluctuations is much smaller than the size of the cloud.* This justifies the relevance of a statistical approach based on the assumption of statistical homogeneity when studying the statistics of the cloud, as done e.g. in cosmology or in the study of turbulence.

In Chapter **4**, we have developed in detail an analytical theory for the statistics of density fluctuations in star-forming molecular clouds under the combined effects of supersonic turbulence and self-gravity. The theory relies on general properties of solutions to the coupled Navier-Stokes equations for fluid motions and the Poisson equation for gravity. We derive rigorously transport equations for the PDF and ACF with a magnetic field present, determine how they evolve with time and solve for the density threshold above which gravity strongly affects and eventually dominates the flow dynamics. The theoretical results and diagnostics reproduce very well numerical simulations of gravo-turbulent collapsing clouds as well as observations on several molecular clouds (Sec. 5). In qualitative terms, the most basic features of the theory are that the same *general gravo-turbulent framework* allows the analysis of several different statistical properties and that the density scale at which gravity starts to affect turbulence decreases as the average density increases.

A first result of this chapter is a relation between the statistics of the velocity divergence and the behavior of the non stationary density PDF at high densities (see Sec. 3.1). This allows one to attribute the development of PLTs in the PDF and the values of their exponents to typical regimes of gravity-influenced flow dynamics. Early stages of gravitational infall induce departures from a lognormal PDF towards a transient power law tail attractor of exponent $\alpha_s = 2$. Subsequently, when the effects of gravity on the flow dynamics are fully developed, further departures take the form of a second power law tail with exponent $\alpha_s = 3/2$.

A major result of the theory is the identification of two density domains in the PDF (see Sec. 3.2). At low density, gravity does not affect *significantly* the flow dynamics, implying that the PDF is that of pure "inertial" turbulence, which is close to a lognormal distribution form for isothermal, dominantly solenoidal turbulence. The other density domain lies above a density threshold, $s_{\rm G}$. At such high density values, gravity starts to *significantly* impact the flow dynamics, essentially by increasing the velocity dispersion. Above this threshold density value, $s > s_{\rm G}$, power-law tails develop over time in the s-PDF, $f(s,t) \propto e^{-\alpha_s s}$, and in the the η-PDF of the surface (column) density, $p(\eta, t) \propto e^{-\alpha_\eta \eta}$. Both are a direct consequence of the increasing impact of gravity upon turbulence.Within a typical timescale $\sim \tau_{\rm G}(s) = \tau_{\rm G,0}\, e^{-s/2}$, this leads to a *first power law tail* with $\alpha_s \geq 2$, such that $\alpha_\eta = -2/((1-3/\alpha_s) \geq 4$. Later on, after a few times $\tau_{\rm ff}(s)$ for a given density s and/or at higher density, *i.e.* at smaller scales for a given time, a *second power law tail* develops, with $\alpha_s = 3/2$ and $\alpha_\eta = 2$. This is the signature of regions in what we called the "free-fall" collapse regime, where the dynamics induced by gravity are fully developed. These general features of the PDF are the same for all star-forming regions, but we have shown that, at any given time in the cloud evolution, the density threshold $s_{\rm G}$ decreases substantially from low-density clouds/clumps to high-density ones. In addition, these properties depend on the evolutionary phase in which the cloud lies (*i.e.* on its age, assuming one can unambiguously define an initial time $t = 0$).

A third important result of this theory deals with the evolution of the correlation length $l_c(\rho)$ of the density field (see Sec. 2.5.2 and 3.4). As collapse progresses in high density regions, the variance of the density field increases and the correlation length $l_c(\rho)$ decreases. The correlation length is the average size of the most correlated structures (see Chap. **1**), which illustrates the fact that, as time goes on, collapse affects shorter and shorter scales in association with corresponding the formation of increasingly smaller and clumpier structures. According to this framework, dense and short scale correlated substructures (cores) of average size $l_c(\rho)(t)$ form in larger correlated structures (filaments) of average size $l_c(\rho)(t_0) \sim 0.1$ pc. Moreover the size of correlated structures decreases whilst some average mass in correlated structures remains constant (see Sec. 2.5.2 and 6.2). This mass is the averaged mass from which will eventually feed bound (pre-stellar) cores and is estimated to be on the order of ~ 1 $M_\odot$ in typical Milky-Way like conditions.

The results of Chapter **2**, in combination with the results of Sec. 3.2 and Sec. 3.3, allow one to infer, *from column-density data*, the values of various physical parameters characterizing a molecular cloud, and notably the virial parameter $\alpha_{\rm vir}$. With this theory, one is able to date the clouds in units of $\tilde{t}_{\rm coll}$, *i.e.* the time since the onset of collapse in a statistically significant proportion of dense regions in the cloud normalized to the cloud mean free-fall time.

The theory derived of this study allows the determination of both the volume and column density thresholds, s_G, η_G, as well as the characteristic timescales $\tau_{\rm G}(s), \tilde{t}_{\rm coll}$ (Eqns (4.93),(2.23),(4.120)). This allows *quantitative and predictive diagnoses*, from either numerical simulations or observations, on the importance of the impact of gravity on turbulence in the cloud and its evolutionary status. A precise scale and clock is now at the disposal of numerical specialists and observers exploring star formation in MCs. The theoretical framework allows a new vision on how gravitational collapse gets initiated and evolves within dense MCs. It provides a sound theoretical foundation and quantitative diagnostics to analyze both observations and numerical simulations of star-forming regions and to characterize the evolution of the density PDFs and ACFs. It is hoped that such a sound basis for the statistical properties of turbulence in the presence of gravity will help improve our understanding of star formation in dense turbulent star-forming regions.

In Chapter **5**, we gave an in-depth review of the models of Hennebelle & Chabrier (2008) and Hopkins (2012a,b) for the Core Mass Function and Initial Mass Function, and examined all their steps and assumptions carefully. This was intended to provide a clear understanding of what must be done when new information becomes available and requires an updating of the assumptions. We have also identified issues that should be addressed to improve these models. One shortcoming of these models is that they generate a CMF and then, in order to obtain the IMF, rely on a simple universal mapping that ties each core of mass $M_{\rm core}$ to a star of mass M_* through an efficiency factor such that $M_*/M_{\rm core} \simeq 30-50\%$. Some authors have argued that these models do not even predict a correct CMF. Lee & Hennebelle (2018a), for example, have concluded that departures from a lognormal density distribution lead to an overprediction of the number of low mass objects. Thus, the models would probably miss out on what really sets the CMF peak and, by way of consequence, the IMF peak as well. We have addressed this key issue only partially in this chapter and more work needs to be done.

We have first shown that, in order to properly describe the MF of unstable mass reservoirs as the density field departs from lognormal statistics, one must first revise the instability criterion proposed by Hennebelle & Chabrier (2008) and Hopkins (2012a,b). We have developed a simple toy model to illustrate the impact of tidal shear deformation on the instability criterion and changed it accordingly. The CMF that is calculated corresponds to unstable reservoirs that have not collapsed yet at time t when the PDF has developed a PLT until $s = s_{\rm crit}$. To a given $s_{\rm crit}$ corresponds a time $t \sim \tau_{\rm ff}(s_{\rm crit})$. CMFs therefore track the time evolution of unstable reservoirs that have not collapsed yet. With this perspective on the time evolution of a cloud, we find that the majority of small mass bound objects are generated in initial stages ($n_{\rm crit} \gg 1$), when tidal forces are still minor contributors to collapse dynamics. Ultimately, of course, changes in the thermodynamic path of the gas will impede further the fragmentation of small mass objects, but it is not obvious that they will affect the peak mass of the CMF.

Finally, we have discussed the counting procedure that leads to a CMF. With a density field that is not lognormal, the Press-Schechter counting procedure developed by Hennebelle & Chabrier (2008) may no longer be adequate. We have given some clues on how to explore this issue and also on how to perform an adequate counting.

Perspectives

After this work, many direct prospects could be imagined.

A first one follows directly from Chapter **5** and is the proper realisation of an excursion-set counting for non lognormal fields, independent of the barrier shape.

A second related prospect concerns the determination of the density threshold (barrier) used as an input for the determination of mass functions. To properly include tides one should indeed extend the triaxial excursion set approach developed in cosmology to the non linear astrophysical context. I plan to study the evolution of the deformation tensor, by drawing inspiration from the work developed in part by teams from the physics laboratory of my host university for incompressible turbulence. A first pedagocical approach could be the study of the rate of strain tensor in 1D spherical collapse to describe spaghettification of fluid patches. This approach would naturally lead to the study of more complex geometry. Moreover, it would take great advantage of the facilities offered by the use of a code solving fluid dynamics with a Lagrangian description like the PHANTOM code (Price et al., 2018).

A last perspective concerns the study of the algorithm used in numerical simulations, and most precisely the ones associated to sink particles. As of today, there has been no benchmark for the behaviour of sink particles in highly complex and turbulent environments, which is regrettable because this is clearly a key component of all simulations. One should make sure that the algorithms enforce not only necessary conditions for collapse but also sufficient ones. If an algorithm relies on necessary conditions only (such as virial equilibrium for example), many objects that in fact may not collapse in the three directions are artificially turned into sink particles. In that case, the output of a simulation, and in particular the statistics of sink particles, should be taken with due caution.

Bibliography

Alfvén, H. 1942, Nature, 150, 405

André, P. 2017, Comptes Rendus Geoscience, 349, 187

André, P., Arzoumanian, D., Könyves, V., Shimajiri, Y., & Palmeirim, P. 2019, Astronomy & Astrophysics, 629, L4

André, P., Ward-Thompson, D., & Barsony, M. 2000, Protostars and Planets IV, 59

André, P., Men'shchikov, A., Bontemps, S., et al. 2010, Astronomy & Astrophysics, 518, L102

André, P., Basu, S., & ichiro Inutsuka, S. 2008, The Formation and Evolution of Prestellar Cores. `https://arxiv.org/abs/0801.4210`

Arzoumanian, D., André, P., Didelon, P., et al. 2011, Astronomy & Astrophysics, 529, L6

Audit, E., & Hennebelle, P. 2010, Astronomy & Astrophysics, 511, A76

Bachiller, R. 1996, Annual Review of Astronomy and Astrophysics, 34, 111

Ballesteros-Paredes, J. 2006, Monthly Notices of the Royal Astronomical Society, 372, 443

Ballesteros-Paredes, J., Hartmann, L., & Vázquez-Semadeni, E. 1999, The Astrophysical Journal, 527, 285

Ballesteros-Paredes, J., Vázquez-Semadeni, E., Gazol, A., et al. 2011, Monthly Notices of the Royal Astronomical Society, 416, 1436

Ballesteros-Paredes, J., Vázquez-Semadeni, E., Palau, A., & Klessen, R. S. 2018, Monthly Notices of the Royal Astronomical Society, 479, 2112

Ballesteros-Paredes, J., André, P., Hennebelle, P., et al. 2020, Space Science Reviews, 216, 1

Basu, S. 2000, The Astrophysical Journal Letters, 540, L103

Batchelor, G. K. 1953, The theory of homogeneous turbulence (Cambridge university press)

Beaulieu, N. C. 2011, IEEE transactions on communications, 60, 23

Begelman, M. C., & Shlosman, I. 2009, The Astrophysical Journal Letters, 702, L5

Berger, M. J., & Colella, P. 1989, Journal of computational Physics, 82, 64

Bertoldi, F., & McKee, C. F. 1992, The Astrophysical Journal, 395, 140

Bleuler, A., & Teyssier, R. 2014, Monthly Notices of the Royal Astronomical Society, 445, 4015

Bonazzola, S., Perault, M., Puget, J., et al. 1992, Journal of Fluid Mechanics, 245, 1

Bond, J., Cole, S., Efstathiou, G., & Kaiser, N. 1991, The Astrophysical Journal, 379, 440

Brunt, C. 2015, Monthly Notices of the Royal Astronomical Society, 449, 4465

Brunt, C. M., Federrath, C., & Price, D. J. 2010a, Monthly Notices of the Royal Astronomical Society, 403, 1507

—. 2010b, Monthly Notices of the Royal Astronomical Society: Letters, 405, L56

Buchert, T., & Ehlers, J. 1997, Astronomy & Astrophysics, 320, 1. `https://arxiv.org/abs/astro-ph/9510056`

Burkhart, B., & Lazarian, A. 2012, The Astrophysical Journal, 755, L19, doi: `10.1088/2041-8205/755/1/l19`

Burkhart, B., Stalpes, K., & Collins, D. C. 2016, The Astrophysical Journal Letters, 834, L1

Cantwell, B. J. 2019, Journal of Fluid Mechanics, 878, 834

Caselli, P., & Myers, P. 1995, The Astrophysical Journal, 446, 665

Cavaliere, A., Colafrancesco, S., & Scaramella, R. 1991, The Astrophysical Journal, 380, 15

Chabrier, G. 2003, PASP, 115, 763

—. 2005, Astrophysics and Space Science Library, Vol. 327, The Initial Mass Function 50 Years Later, Springer

Chabrier, G., & Baraffe, I. 2000, Annual Review of Astronomy and Astrophysics, 38, 337

Chabrier, G., & Hennebelle, P. 2011, Astronomy & Astrophysics, 534, A106

Chabrier, G., Hennebelle, P., & Charlot, S. 2014, The Astrophysical Journal, 796, 75

Chandrasekhar, S. 1943, Reviews of modern physics, 15, 1

—. 1949, The Astrophysical Journal, 110, 329

—. 1951a, Proceedings of the Royal Society of London. Series A. Mathematical and Physical Sciences, 210, 26

—. 1951b, Proceedings of the Royal Society of London. Series A. Mathematical and Physical Sciences, 210, 18

—. 1969, Ellipsoidal figures of equilibrium (Yale Univ. Press)

Chandrasekhar, S., & Lee, E. P. 1968, Monthly Notices of the Royal Astronomical Society, 139, 135

Cho, W., & Kim, J. 2011, Monthly Notices of the Royal Astronomical Society: Letters, 410, L8

Collins, D. C., Kritsuk, A. G., Padoan, P., et al. 2012, The Astrophysical Journal, 750, 13

Colman, T., & Teyssier, R. 2020, Monthly Notices of the Royal Astronomical Society, 492, 4727

Dame, T. M., Hartmann, D., & Thaddeus, P. 2001, The Astrophysical Journal, 547, 792

De Oliveira, C. A., Schneider, N., Merín, B., et al. 2014, Astronomy & Astrophysics, 568, A98

Dickman, R., & Kleiner, S. 1985, The Astrophysical Journal, 295, 479

Donkov, S., & Stefanov, I. Z. 2018, Monthly Notices of the Royal Astronomical Society, 474, 5588

Elmegreen, B. G., & Scalo, J. 2004, Annu. Rev. Astron. Astrophys., 42, 211

Federrath, C. 2016a, Monthly Notices of the Royal Astronomical Society, 457, 375

—. 2016b, Monthly Notices of the Royal Astronomical Society, 457, 375

Federrath, C., & Banerjee, S. 2015, Monthly Notices of the Royal Astronomical Society, 448, 3297

Federrath, C., & Klessen, R. S. 2012, The Astrophysical Journal, 761, 156, doi: `10.1088/0004-637X/761/2/156`

—. 2013, The Astrophysical Journal, 763, 51

Federrath, C., Klessen, R. S., & Schmidt, W. 2008, The Astrophysical Journal Letters, 688, L79

Federrath, C., Roman-Duval, J., Klessen, R., Schmidt, W., & Mac Low, M.-M. 2010, Astronomy & Astrophysics, 512, A81

Federrath, C., Sur, S., Schleicher, D. R., Banerjee, R., & Klessen, R. S. 2011, The Astrophysical Journal, 731, 62

Field, G., Goldsmith, D., & Habing, H. 1969, The Astrophysical Journal, 155, L149

Fleck Jr, R. 1981, The Astrophysical Journal, 246, L151

Foster, P. N., & Chevalier, R. A. 1993, The Astrophysical Journal, 416, 303

Frisch, U. 1995, Turbulence: the legacy of AN Kolmogorov (Cambridge university press)

Fryxell, B., Olson, K., Ricker, P., et al. 2000, The Astrophysical Journal Supplement Series, 131, 273

Girichidis, P., Konstandin, L., Whitworth, A. P., & Klessen, R. S. 2014, The Astrophysical Journal, 781, 91

Grudić, M. Y., Guszejnov, D., Hopkins, P. F., Offner, S. S., & Faucher-Giguère, C.-A. 2020, arXiv preprint arXiv:2010.11254

Guillet, T., & Teyssier, R. 2011, Journal of Computational Physics, 230, 4756

Guszejnov, D., Grudić, M. Y., Hopkins, P. F., Offner, S. S., & Faucher-Giguère, C.-A. 2020, Monthly Notices of the Royal Astronomical Society, 496, 5072

—. 2021, Monthly Notices of the Royal Astronomical Society, 500, 1125

Guszejnov, D., & Hopkins, P. F. 2015, Monthly Notices of the Royal Astronomical Society, 450, 4137

Guszejnov, D., Hopkins, P. F., Grudić, M. Y., Krumholz, M. R., & Federrath, C. 2018a, Monthly Notices of the Royal Astronomical Society, 480, 182

Guszejnov, D., Hopkins, P. F., & Grudić, M. Y. 2018b, Monthly Notices of the Royal Astronomical Society, 477, 5139, doi: `10.1093/mnras/sty920`

Guszejnov, D., Krumholz, M. R., & Hopkins, P. F. 2016, Monthly Notices of the Royal Astronomical Society, 458, 673

Hartmann, L., Ballesteros-Paredes, J., & Bergin, E. A. 2001, The Astrophysical Journal, 562, 852

Heinesen, A. 2020, Journal of Cosmology and Astroparticle Physics, 2020, 052

Hennebelle, P. 2013, Astronomy & Astrophysics, 556, A153

Hennebelle, P., & André, P. 2013, Astronomy & Astrophysics, 560, A68

Hennebelle, P., & Chabrier, G. 2008, The Astrophysical Journal, 684, 395

Hennebelle, P., Commercon, B., Lee, Y.-N., & Chabrier, G. 2020, The Astrophysical Journal, 904, 194

Hennebelle, P., & Falgarone, E. 2012, The Astronomy and Astrophysics Review, 20, 55

Hennebelle, P., & Inutsuka, S.-i. 2019, Frontiers in Astronomy and Space Sciences, 6, 5

Hennebelle, P., Lee, Y.-N., & Chabrier, G. 2019, The Astrophysical Journal, 883, 140

Heyer, M., Krawczyk, C., Duval, J., & Jackson, J. M. 2009, The Astrophysical Journal, 699, 1092

Heyer, M. H., & Brunt, C. M. 2004, The Astrophysical Journal Letters, 615, L45

Hopkins, P. F. 2012a, Monthly Notices of the Royal Astronomical Society, 423, 2016

—. 2012b, Monthly Notices of the Royal Astronomical Society, 423, 2037

—. 2013, Monthly Notices of the Royal Astronomical Society, 430, 1880

Inutsuka, S.-I., & Miyama, S. M. 1992, The Astrophysical Journal, 388, 392, doi: `10.1086/171162`

Jaupart, E., & Chabrier, G. 2020, The Astrophysical Journal Letters, 903, L2

Jaupart, É., Parizot, É., & Allard, D. 2018, Astronomy & Astrophysics, 619, A12

Jeans, J. H. 1902, Philosophical Transactions of the Royal Society of London. Series A, Containing Papers of a Mathematical or Physical Character, 199, 1

Kainulainen, J., Beuther, H., Henning, T., & Plume, R. 2009, Astronomy & Astrophysics, 508, L35

Kainulainen, J., Lehtinen, K., & Harju, J. 2006, Astronomy & Astrophysics, 447, 597

Kleiner, S., & Dickman, R. 1984, The Astrophysical Journal, 286, 255

—. 1985, The Astrophysical Journal, 295, 466

Klessen, R. S. 2000, The Astrophysical Journal, 535, 869

Klessen, R. S., & Glover, S. C. 2016, in Star Formation in Galaxy Evolution: Connecting Numerical Models to Reality (Springer), 85–249

Kolmogorov, A. N. 1941, Cr Acad. Sci. URSS, 30, 301

Könyves, V., André, P., Men'Shchikov, A., et al. 2010, Astronomy & Astrophysics, 518, L106

Könyves, V., André, P., Men'Shchikov, A., et al. 2015, Astronomy & Astrophysics, 584, A91

Kritsuk, A. G., Lee, C. T., & Norman, M. L. 2013, Monthly Notices of the Royal Astronomical Society, 436, 3247

Kritsuk, A. G., Norman, M. L., Padoan, P., & Wagner, R. 2007, The Astrophysical Journal, 665, 416

Kritsuk, A. G., Norman, M. L., & Wagner, R. 2010, The Astrophysical Journal Letters, 727, L20

Kritsuk, A. G., Ustyugov, S. D., & Norman, M. L. 2017, New Journal of Physics, 19, 065003

Krumholz, M. R. 2014, Physics Reports, 539, 49

Larson, R. B. 1969, Monthly Notices of the Royal Astronomical Society, 145, 271

—. 1981, Monthly Notices of the Royal Astronomical Society, 194, 809

Ledoux, P., & Walraven, T. 1958, in Astrophysics II: Stellar Structure/Astrophysik II: Sternaufbau (Springer), 353–604

Lee, E. J., Chang, P., & Murray, N. 2015, The Astrophysical Journal, 800, 49

Lee, Y.-N., & Hennebelle, P. 2018a, Astronomy & Astrophysics, 611, A88

—. 2018b, Astronomy & Astrophysics, 611, A89, doi: `10.1051/0004-6361/201731523`

Lemaster, M. N., & Stone, J. M. 2008, The Astrophysical Journal Letters, 682, L97

—. 2009, The Astrophysical Journal, 691, 1092

Mac Low, M.-M., & Klessen, R. S. 2004, Reviews of modern physics, 76, 125

Machida, M. N., Inutsuka, S.-i., & Matsumoto, T. 2006, The Astrophysical Journal Letters, 647, L151

Marquis de Laplace, P. S. 1835, Exposition du système du monde (Bachelier)

Masunaga, H., & Inutsuka, S.-i. 2000, The Astrophysical Journal, 531, 350

Matzner, C. D., & McKee, C. F. 2000, The Astrophysical Journal, 545, 364

McKee, C. F., & Ostriker, E. C. 2007, Annu. Rev. Astron. Astrophys., 45, 565

McKee, C. F., & Ostriker, J. P. 1977, The Astrophysical Journal, 218, 148

McKee, C. F., & Tan, J. C. 2003, The Astrophysical Journal, 585, 850

McKee, C. F., & Zweibel, E. G. 1992, The Astrophysical Journal, 399, 551

Meidt, S. E., Leroy, A. K., Rosolowsky, E., et al. 2018, The Astrophysical Journal, 854, 100

Miville-Deschênes, M.-A., Martin, P., Abergel, A., et al. 2010, Astronomy & Astrophysics, 518, L104

Miville-Deschênes, M.-A., Salomé, Q., Martin, P., et al. 2017, Astronomy & Astrophysics, 599, A109

Molina, F., Glover, S. C., Federrath, C., & Klessen, R. S. 2012, Monthly Notices of the Royal Astronomical Society, 423, 2680

Monaco, P. 1998, FCPh, 19, 157

Murray, D. W., Chang, P., Murray, N. W., & Pittman, J. 2017, Monthly Notices of the Royal Astronomical Society, 465, 1316, doi: `10.1093/mnras/stw2796`

Murray, N., & Chang, P. 2015, The Astrophysical Journal, 804, 44

Musso, M., & Sheth, R. K. 2014, Monthly Notices of the Royal Astronomical Society, 439, 3051, doi: `10.1093/mnras/stu165`

Myers, P., & Goodman, A. 1988, the Astrophysical Journal, 326, L27

Orkisz, J. H., Pety, J., Gerin, M., et al. 2017, Astronomy & Astrophysics, 599, A99

Ossenkopf-Okada, V., Csengeri, T., Schneider, N., Federrath, C., & Klessen, R. S. 2016, Astronomy & Astrophysics, 590, A104

Padoan, P., & Nordlund, Å. 2002, The Astrophysical Journal, 576, 870

Pan, L., Padoan, P., & Nordlund, Å. 2018, The Astrophysical Journal Letters, 866, L17

—. 2019a, The Astrophysical Journal, 876, 90

—. 2019b, The Astrophysical Journal, 881, 155

Panopoulou, G., Psaradaki, I., Skalidis, R., Tassis, K., & Andrews, J. 2017, Monthly Notices of the Royal Astronomical Society, 466, 2529

Papoulis, A., & Pillai, S. 1965, Variables Stochastic Processes. Mc Graw McGraw-Hill, New York, NY

Passot, T., & Vázquez-Semadeni, E. 1998, Physical Review E, 58, 4501

Peebles, P. J. E. 1973, The Astrophysical Journal, 185, 413, doi: `10.1086/152431`

Plume, R., Jaffe, D. T., Evans II, N. J., Martin-Pintado, J., & Gomez-Gonzalez, J. 1997, The Astrophysical Journal, 476, 730

Pope, S. 1981, The Physics of Fluids, 24, 588

Pope, S., & Ching, E. S. 1993, Physics of Fluids A: Fluid Dynamics, 5, 1529

Pope, S. B. 1985, Progress in energy and combustion science, 11, 119

Press, W. H., & Schechter, P. 1974, The Astrophysical Journal, 187, 425

Price, D. J., Wurster, J., Tricco, T. S., et al. 2018, Publications of the Astronomical Society of Australia, 35

Reinke, N., Fuchs, A., Hölling, M., & Peinke, J. 2016, in Fractal Flow Design: How to Design Bespoke Turbulence and Why (Springer), 165–177

Reinke, N., Fuchs, A., Nickelsen, D., & Peinke, J. 2018, Journal of Fluid Mechanics, 848, 117–153, doi: `10.1017/jfm.2018.360`

Ricker, P. 2008, The Astrophysical Journal Supplement Series, 176, 293

Robertson, B., & Goldreich, P. 2012, The Astrophysical Journal Letters, 750, L31

Salpeter, E. E. 1955, The Astrophysical Journal, 121, 161

Scalo, J. 1984, The Astrophysical Journal, 277, 556

Scalo, J., & Pumphrey, W. 1982, The Astrophysical Journal, 258, L29

Schneider, N., André, P., Könyves, V., et al. 2013, The Astrophysical Journal Letters, 766, L17

Schneider, N., Ossenkopf, V., Csengeri, T., et al. 2015, Astronomy & Astrophysics, 575, A79

Schneider, N. e. a., Csengeri, T., Hennemann, M., et al. 2012, Astronomy & Astrophysics, 540, L11

Shen, J., Abel, T., Mo, H., & Sheth, R. K. 2006, The Astrophysical Journal, 645, 783

Sheth, R. K., Mo, H., & Tormen, G. 2001, Monthly Notices of the Royal Astronomical Society, 323, 1

Shimoikura, T., Dobashi, K., Sakurai, T., et al. 2012, The Astrophysical Journal, 745, 195, doi: `10.1088/0004-637x/745/2/195`

Solomon, P., Rivolo, A., Barrett, J., & Yahil, A. 1987, The Astrophysical Journal, 319, 730

Stevens, A. 2020, Nature Astronomy, 4, 811

Sur, S., Schleicher, D. R. G., Banerjee, R., Federrath, C., & Klessen, R. S. 2010, The Astrophysical Journal Letters, 721, L134, doi: `10.1088/2041-8205/721/2/L134`

Szyszkowicz, S. S., & Yanikomeroglu, H. 2009, IEEE Transactions on Communications, 57, 3538

Toomre, A. 1964, The Astrophysical Journal, 139, 1217, doi: `10.1086/147861`

Tremblin, P., Schneider, N., Minier, V., et al. 2014, Astronomy & Astrophysics, 564, A106

Truelove, J. K., Klein, R. I., McKee, C. F., et al. 1997, The Astrophysical Journal Letters, 489, L179

Vaytet, N., Chabrier, G., Audit, E., et al. 2013, Astronomy & Astrophysics, 557, A90

Vaytet, N., Commerçon, B., Masson, J., González, M., & Chabrier, G. 2018, Astronomy & Astrophysics, 615, A5

Vazquez-Semadeni, E. 1994, The Astrophysical Journal, 423, 681

Vazquez-Semadeni, E., & Garcia, N. 2001, The Astrophysical Journal, 557, 727, doi: `10.1086/321688`

Vázquez-Semadeni, E., Palau, A., Ballesteros-Paredes, J., Gómez, G. C., & Zamora-Avilés, M. 2019, Monthly Notices of the Royal Astronomical Society, 490, 3061

Vigneron, Q. 2021, Physical Review D, 103, 064064

von Mises, R. 1957, Richard von Mises, probability, statistics, and truth, Dover Publications (reprint, original Springer: 1928), New York

von Plato, J. 2005, in Landmark Writings in Western Mathematics 1640-1940 (Elsevier), 960–969

Von Weizsäcker, C. 1951, The Astrophysical Journal, 114, 165

Zel'Dovich, Y. B. 1970, Astronomy and astrophysics, 5, 84

Zentner, A. R. 2007, International Journal of Modern Physics D, 16, 763

Zhang, J., & Hui, L. 2006, The Astrophysical Journal, 641, 641